



This is to certify that the

dissertation entitled

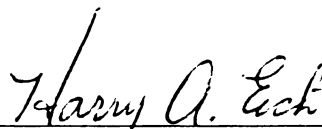
- I. Syntheses, Structures and Formation Mechanisms of Metastable Modifications of Metal Dihalides
- II. Magnetic and Electrical Properties of Oxidenitrides

presented by

Guo Liu

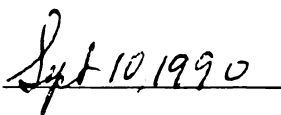
has been accepted towards fulfillment
of the requirements for

Ph.D. _____ degree in Chemistry



Major professor

Date


Sept 10, 1990

LIBRARY
Michigan State
University

PLACE IN RETURN BOX to remove this checkout from your record.
 TO AVOID FINES return on or before date due.

DATE DUE	DATE DUE	DATE DUE
_____	_____	_____
_____	_____	_____
_____	_____	_____
_____	_____	_____
_____	_____	_____
_____	_____	_____
_____	_____	_____

**I. SYNTHESSES, STRUCTURES AND FORMATION MECHANISMS OF
METASTABLE MODIFICATIONS OF METAL DIHALIDES**

and

II. MAGNETIC AND ELECTRICAL PROPERTIES OF OXIDENITRIDES

By

Guo Liu

A DISSERTATION

**Submitted to
Michigan State University
in partial fulfillment of the requirements
for the degree of**

DOCTOR OF PHILOSOPHY

Department of Chemistry

1990

ABSTRACT

I. SYNTHESSES, STRUCTURES AND FORMATION MECHANISMS OF
METASTABLE MODIFICATIONS OF METAL DIHALIDES

By

Guo Liu

Among the various low temperature chemical methods utilized for the synthesis of crystalline solids, those based on topochemical reactions uniquely allow the synthesis of metastable phases not accessible by conventional methods because the low temperature preserves the essential features of the precursor structures. Three types of metastable phases have been produced by combination of a new topochemical reaction, solvolytic decomposition of mixed-valence halides LnX_{2+x} and mixed alkaline earth- Ln^{3+} halides, with low temperature dehydration. These are: fluorite-type high-temperature modifications of LnCl_2 ($\text{Ln}=\text{Sm}, \text{Eu}$), anti- Fe_2P -type 'high-pressure' modifications of BaX_2 ($\text{X}=\text{Cl}, \text{Br}$), and SrI_2 -IV-type 'high-temperature' forms of MI_2 ($\text{M}=\text{Sr}, \text{Sm}, \text{Eu}$). New vernier- and cluster-type mixed(-valent) halide precursors were also prepared. The metastable SrI_2 -IV structure was refined by the X-ray Rietveld procedure. Reactions that yield these metastable phases are analyzed in thermodynamic and kinetic terms and are shown through layer descriptions to be topotactic. Although low-temperature high-vacuum dehydrations do not involve major structural changes, those that occur during solvolytic decompositions incur significant changes. In-layer atomic rearrangements of the intermediate lattice lead to formation of the fluorite-type structure; further out-of-layer displacements yield the anti- Fe_2P -type structure.

1. The
2. The
3. The
4. The
5. The
6. The
7. The
8. The
9. The
10. The
11. The
12. The
13. The
14. The
15. The
16. The
17. The
18. The
19. The
20. The
21. The
22. The
23. The
24. The
25. The
26. The
27. The
28. The
29. The
30. The
31. The
32. The
33. The
34. The
35. The
36. The
37. The
38. The
39. The
40. The
41. The
42. The
43. The
44. The
45. The
46. The
47. The
48. The
49. The
50. The
51. The
52. The
53. The
54. The
55. The
56. The
57. The
58. The
59. The
60. The
61. The
62. The
63. The
64. The
65. The
66. The
67. The
68. The
69. The
70. The
71. The
72. The
73. The
74. The
75. The
76. The
77. The
78. The
79. The
80. The
81. The
82. The
83. The
84. The
85. The
86. The
87. The
88. The
89. The
90. The
91. The
92. The
93. The
94. The
95. The
96. The
97. The
98. The
99. The
100. The

II. MAGNETIC AND ELECTRICAL PROPERTIES OF OXIDENITRIDES

Studies of high T_c superconductors have been centered on oxides. Reports of anion substitution in these ceramic superconductors are far less extensive than those of cation substitution. Some of the properties of N^{3-} suggest it to be a likely candidate for O^{2-} substitution. Three types of oxidenitrides were then synthesized and their magnetic susceptibilities and electrical conductivities determined. (1) Pyroovskite-related $\underline{M}Mo(O,N)_3$ (\underline{M} =Ba, Sr) exhibit complex magnetic behavior at low temperatures and are probably metallic; (2) $CaFe_2O_4$ -type $BaCe\underline{Ln}(O,N)_4$ (\underline{Ln} =La, Ce) are insulating and paramagnetic with Ce exhibiting mixed-valent states; (3) NaCl-type LaO_xN_{1-x} are metallic above 6 K for $x=0.45$ and 5 K for $x=0.28$ and become superconducting below these temperatures.

ACKNOWLEDGMENTS

I gratefully acknowledge the instructions, suggestions, support, and encouragement of Professor Harry A. Eick throughout my studies at Michigan State University. I would like to express my appreciations to Dr. Wieslaw Lasocha for his friendly help and instructions at the very beginning of my research work, and to Professor Shi-Hua Wang and Stanislaw A. Hodorowicz for their suggestions and discussions. I thank Professor Mercouri Kanatzidis and Daniel Nocera for their inspirations.

Many thanks to Reza Loloee and Kevin Moeggenborg for their assistance in the magnetic and electrical measurements.

Support of the Division of Materials Research, Solid State Chemistry Program, National Science Foundation, Grant DMR-84-00739 for the first part of this work, and support of the Center for Fundamental Materials Research at Michigan State University for the second part, are gratefully acknowledged.

Finally, I thank my wife, Ying Yang, for her patience, encouragement, and support.

TABLE OF CONTENTS

LIST OF TABLES	viii
----------------------	------

LIST OF FIGURES	xi
-----------------------	----

PART I	SYNTHESES, STRUCTURES AND FORMATION MECHANISMS OF METASTABLE MODIFICATIONS OF METAL DIHALIDES	1
---------------	--	----------

CHAPTER 1	INTRODUCTION	2
------------------	---------------------------	----------

1.1	Low-Temperature Routes to Solid State Compounds	3
1.1.1	Synthesis Based on Topochemical Reactions	3
1.1.2	Synthesis Based on Low Temperature Chemical Decompositions	5
1.2	Solvolytic Decompositions and Metastable Phases	8

CHAPTER 2	BACKGROUND INFORMATION	10
------------------	-------------------------------------	-----------

2.1	Structural Chemistry of Lanthanide and Alkaline Earth Halides	11
2.1.1	Characteristics of Lanthanide and Alkaline Earth Halides ..	11
2.1.2	Mixed and Mixed-Valent Halides	12
2.2	Crystal Structures of Related Halides	17
2.2.1	The PbCl ₂ -Type Structure	17
2.2.2	The Anti-Fe ₂ P-Type Structure	22
2.2.3	The Fluorite (CaF ₂)-Type Structure	25
2.2.4	Fluorite-Related Cluster Type Superstructures	31
2.3	The X-ray Rietveld Refinement Procedure	37
2.3.1	Introduction	37
2.3.2	The Rietveld Refinement XRS-82 System	38

CHAPTER 3	EXPERIMENTAL	44
------------------	---------------------------	-----------

3.1	Synthesis Procedures	45
3.1.1	Synthesis of Individual Halides	47
3.1.2	Synthesis of Precursors	49
3.1.3	Decomposition of Precursors	52
3.2	Instrumentation and Data Processing	55
3.2.1	Powder X-ray Diffraction Examinations	55
3.2.2	Automated Powder X-ray Data Collection	55
3.2.3	Data Processing	55
3.2.4	Rietveld Refinement of the SrI ₂ -IV Structure	56

CHAPTER 4	RESULTS	60
4.1	Precursors and Structures	62
4.2	Decomposition Products and Structures	74
4.2.1	High-Temperature Forms of LnCl_2 ($\text{Ln} = \text{Sm}, \text{Eu}$)	74
4.2.2	High-Pressure Forms of BaX_2 ($\text{X} = \text{Cl}, \text{Br}, \text{I}$)	77
4.2.3	High-Temperature Forms of Ml_2 ($\text{M} = \text{Sr}, \text{Sm}, \text{Eu}$)	83
4.3	The Structure of $\text{SrI}_2\text{-IV}$ by X-ray Rietveld Refinement	88
4.4	Thermal Stabilities of Metastable Phases	95
4.5	Solvolytic Decomposition Intermediates	95
CHAPTER 5	DISCUSSION	100
5.1	Solvolytic Decomposition	101
5.1.1	Energetics	101
5.1.2	Solvent Effect	103
5.2	Low-Temperature Dehydration	104
5.3	Metastable Structures and Low Temperature Decompositions	105
5.4	Formation Mechanism of the Metastable Forms	107
5.4.1	Kinetics vs. Thermodynamics	107
5.4.2	Topochemical Transformations	107
5.4.3	Geometric Correlations	118
CONCLUDING REMARKS		121
PART II	MAGNETIC AND ELECTRICAL PROPERTIES OF OXIDENITRIDES	122
CHAPTER 1	INTRODUCTION	123
1.1	An Overview of Transition Metal Oxidenitrides	125
1.1.1	Perovskite-Type	125
1.1.2	NaCl-Type	126
1.2	Goals	127
1.2.1	$\text{MMo}(\text{O},\text{N})_3$	127
1.2.2	$\text{BaCeLn}(\text{O},\text{N})_4$	128
1.2.3	$\text{LaO}_x\text{N}_{1-x}$	128
CHAPTER 2	MAGNETIC PROPERTIES OF SOLIDS	129
2.1	Magnetization and Magnetic Susceptibility	130
2.2	Five Basic Types of Magnetic Order	131
2.2.1	Diamagnetism	131
2.2.2	Paramagnetism	131
2.2.3	Ferromagnetism	134
2.2.4	Anti-ferromagnetism	135
2.2.5	Ferrimagnetism	136
CHAPTER 3	ELECTRICAL PROPERTIES OF SOLIDS	138
3.1	The Band Theory of Solids	139
3.2	Electrical Conductivity	141

3.2.1	Temperature Dependence of Metallic Electrical Conductivity	142
3.2.2	Semiconductors	142
3.3	Superconductivity	144
CHAPTER 4	EXPERIMENTAL	146
4.1	Synthesis and Structural Characterization of Oxidenitrides	147
4.1.1	List of Chemicals	147
4.1.2	Synthesis Procedure	148
4.2	Magnetic and Electrical Measurements	150
4.3	Data Analysis	152
4.3.1	Magnetic Data	152
4.3.2	Electrical Resistivities	154
CHAPTER 5	RESULTS AND DISCUSSION	156
5.1	Pseudo-Ternary BaCeLn(O,N) ₄ Systems (Ln = La, Ce)	157
5.1.1	Chemical Characterization	157
5.1.2	Magnetic and Electrical Properties	157
5.1.3	Crystal Structures	160
5.2	Pseudo-Ternary MMo(O,N) ₃ Oxidenitrides (M = Sr, Ba)	165
5.2.1	Crystal Structures	165
5.2.2	Reaction Conditions	168
5.2.3	Magnetic and Electrical Properties	169
5.3	Pseudo-Binary LaO _x N _{1-x} Oxidenitrides	176
5.3.1	Electrical Properties	176
5.3.2	Magnetic Properties	180
	CONCLUDING REMARKS	187
	GENERAL REFERENCE BOOKS	188
	REFERENCES	189

LIST OF TABLES

Table	Page
1. Structural modifications of lanthanide halides LnX_2	13
2. Structural modifications of alkaline earth halides MX_2	14
3. Space groups and lattice parameters of mixed-valent lanthanide halides (excluding fluorides)	15
4. Space groups and lattice parameters of alkaline earth-related mixed halides (excluding fluorides)	16
5. Atomic positions of the fluorite-type SrCl_2 in cubic and hexagonal unit cells	30
6. List of atomic positions for $\text{Nd}_{14}\text{Cl}_{33}$	32
7. Miller indices, and observed and calculated interplanar d-spacings and intensities for Eu_4Cl_9	63
8. Miller indices, and observed and calculated interplanar d-spacings and intensities for $\text{Eu}_5\text{Cl}_{11}$	64
9. Miller indices, and observed and calculated interplanar d-spacings and intensities for $\text{Eu}_{14}\text{Cl}_{33}$	65
10. Transformation of " Ba_2LnCl_7 ," hexagonal lattice parameters into cubic lattice parameters	67
11. Miller indices, observed intensities, and observed and calculated interplanar d-spacings for $\text{Ba}_{17}\text{Sm}_{10}\text{Cl}_{64}$	68
12. Miller indices, and observed (Guinier) and calculated interplanar d-spacings and intensities for $\text{Ba}_9\text{La}_3\text{Br}_3$	70
13. Miller indices, and observed (Guinier) and calculated interplanar d-spacings and intensities for $\text{Ba}_9\text{Nd}_5\text{Br}_{33}$	72
14. Lattice parameters and calculated densities of LnCl_2 ($\text{Ln} = \text{Sm}, \text{Eu}$)	74

15.	Miller indices, and observed and calculated interplanar d-spacings and intensities for fluorite-type SmCl_2	75
16.	Miller indices, and observed and calculated interplanar d-spacings and intensities for fluorite-type EuCl_2	76
17.	Miller indices, and observed and calculated interplanar d-spacings and intensities for anti- Fe_2P -type BaCl_2	79
18.	Miller indices, and observed and calculated interplanar d-spacings and intensities for anti- Fe_2P -type BaBr_2	80
19.	Miller indices, and observed and calculated interplanar d-spacings and intensities for anti- Fe_2P -type BaI_2	81
20.	Structure types and lattice parameters of BaCl_2	82
21.	Structure types and lattice parameters of BaBr_2	82
22.	Miller indices, and observed (Guinier) and calculated interplanar d-spacings and intensities for SrI_2 -IV	84
23.	Miller indices, and observed (Guinier) and calculated interplanar d-spacings and intensities for SrI_2 -IV-type SmI_2	85
24.	Miller indices, and observed (Guinier) and calculated interplanar d-spacings and intensities for SrI_2 -IV-type EuI_2	86
25.	Comparison of selected crystallographic data of MI_2 and $\text{MI}_2 \cdot \text{H}_2\text{O}$	87
26.	Crystallographic and Rietveld refinement data for SrI_2 -IV	93
27.	Positional and thermal parameters for SrI_2 -IV	94
28.	Comparison of selected SrI_2 -IV and SrI_2 -I bond distances	94
29.	Miller indices, observed (Guinier) intensities, and observed and calculated interplanar d-spacings for triclinic $\text{NdBr}_3(\text{THF})_4$	98
30.	Comparison of atomic coordinates of $\text{SrI}_2 \cdot \text{H}_2\text{O}$ and SrI_2 -IV	112
31.	Structure-ionic radius ratio relationships for metastable dihalides	116
32.	Crystallographic data of metastable BaX_2 ($\text{X} = \text{Cl}, \text{Br}$) prepared from various precursors	117
33.	Geometrical correlation of the metastable LnCl_2 (cubic) with their precursors $\text{Ln}_4\text{Cl}_{33}$ (hexagonal)	120

34.	Geometrical correlation of the metastable BaBr_2 with its precursors $\text{Ba}_9\text{Ln}_5\text{Br}_{33}$ (both hexagonal)	120
35.	Units of quantities related to electrical conductivity	141
36.	Typical electrical conductivities for various materials at room temperature	141
37.	Lattice parameters for selected (<u>Pbnm</u> , Z=4) CaFe_2O_4 -type oxides and oxidenitrides	160
38.	Miller indices, and observed and calculated interplanar d-spacings and intensities for <u>Pbnm</u> CaFe_2O_4 -type $\text{BaCe}_2(\text{O,N})_4$	161
39.	Miller indices, and observed and calculated interplanar d-spacings and intensities for $\text{BaMo}(\text{O,N})_3$	167
40.	Estimated Mobilities of Oxidenitrides $\text{LaO}_x\text{N}_{1-x}$	177

LIST OF FIGURES

Figure	Page
1. A 9-coordinated tricapped trigonal prism	19
2. Projections of the PbCl_2 -type structure down the c axis	20
3. Cation arrangement of various structures illustrating their derivations from hexagonally close-packed layers	21
4. Projection of the anti- Fe_2P -type structure down the c axis	23
5. Two different layers of the anti- Fe_2P -type structure	24
6. The fluorite-type structure	26
7. Anion arrangement in $\text{Ln}_{14}\text{X}_{33}$ showing the formation of a Ln_6X_{37} cluster . . .	33
8. Two adjacent cation layers with Ln_6X_{37} clusters	35
9. Schematic illustration of layer stackings of various structure types	36
10. Apparatuses for the solvolytic decomposition experiment	54
11. Standard peak for SrI_2 -IV	59
12. Observed (a), calculated (b), and difference (c) X-ray diffraction patterns for SrI_2 -IV	90
13. Comparison of several metal coordination polyhedra	91
14. C-axis projection of the SrI_2 -IV structure illustrating the atomic packing . . .	92
15. FTIR spectrum of $\text{EuCl}_3(\text{THF})_n$ (KBr pressed pellet)	97
16. Projection of $\text{SrI}_2 \cdot \text{H}_2\text{O}$ (a) and SrI_2 -IV (b) structures down the b axis	111
17. Proposed structural changes during solvolytic decomposition in a single cation layer of $\text{Ln}_{14}\text{Cl}_{33}$	114

18.	Lattice parameter relationships between the $M_{14}X_{33}$ superstructure and the anti- Fe_2P -type structure (upper left), and between the superstructure and the fluorite-type structure (lower right)	119
19.	The low temperature ordering (if any) of neighboring dipoles and the consequent behavior of spontaneous magnetization and/or susceptibility	137
20.	Schematic band structures of solids	140
21.	Ratio of the resistivity of metallic sodium at T to that at 273 K vs. T	143
22.	An illustration of the difference between a normal conductor (a) that allows magnetic flux penetration and a superconductor (b) that expels magnetic flux from its interior	145
23.	Simple arrangement for four-probe electrical conductivity measurements . .	151
24.	The magnetic susceptibility of $BaCeLa(O,N)_4$ plotted against reciprocal temperature at 5-300 K	159
25.	Magnetic behavior of $SrMo(O,N)_3$ at 5-300 K	171
26.	Magnetic behavior of $BaMo(O,N)_3$ at 10-300 K	172
27.	Magnetic susceptibility of $SrMo(O,N)_3$ vs. reciprocal temperature	173
28.	Conductivity data of $SrMo(O,N)_3$ at 86-294 K plotted as $\ln \sigma$ against reciprocal temperature	174
29.	Conductivity data of $BaMo(O,N)_3$ at 85-295 K plotted as $\ln \sigma$ against reciprocal temperature	175
30.	Electrical resistivity of $LaO_{0.28}N_{0.72}$ vs. temperature at 5-300 K	178
31.	Electrical resistivity of $LaO_{0.45}N_{0.55}$ vs. temperature at 2-300 K	179
32.	Magnetic susceptibility of $LaO_{0.28}N_{0.72}$ vs. temperature at 2-300 K ($H_0 = 200$ gauss)	182
33.	Magnetic susceptibility of $LaO_{0.45}N_{0.55}$ vs. temperature at 2-300 K ($H_0 = 200$ gauss)	183
34.	Magnetic susceptibility of $LaO_{0.28}N_{0.72}$ plotted against reciprocal temperature to illustrate the Curie behavior at low temperatures ($H_0 = 200$ gauss)	184

35.	Magnetic susceptibility of $\text{LaO}_{0.45}\text{N}_{0.55}$ plotted against reciprocal temperature to illustrate the Curie behavior at low temperatures ($H_0 = 200$ gauss)	185
36.	Magnetic field and temperature dependences of the magnetic susceptibility of $\text{LaO}_{0.45}\text{N}_{0.55}$ above T_c	186

PART I

SYNTHESES, STRUCTURES AND FORMATION MECHANISMS OF METASTABLE MODIFICATIONS OF METAL DIHALIDES

CHAPTER 1 INTRODUCTION

SYNOPSIS

Some low temperature methods important for the synthesis of solid state compounds are summarized briefly. The new topochemical method developed in this work, solvolytic decomposition on mixed-valence halides LnX_{2+x} and mixed alkaline earth-lanthanide halides, is introduced.

1.1 Low-Temperature Routes to Solid State Compounds

Conventional high temperature ceramic methods are most widely used for the synthesis of solid state compounds. However, due to the well-known diffusion problem, stoichiometries are hard to control and compounds prepared by these methods are sometimes inhomogeneous. In addition, high temperature reactions usually preclude the synthesis of metastable phases. To overcome these limitations, low temperature chemical methods have been developed. These new methods have both enabled the synthesis of known solids with higher purity and homogeneity and resulted in the synthesis of new and metastable phases. Compounds synthesized at low temperatures are usually finely divided with large surface areas essential for catalysis and desirable for other applications.

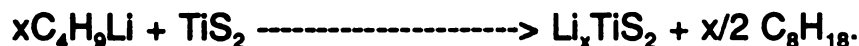
Some recent experimental results on this subject have been reviewed by Rao and Gopalakrishnan in their book (listed in the end as General Reference Books).

1.1.1 Synthesis Based on Topochemical Reactions

Among the various chemical methods, those based on topochemical (topotactic) reactions uniquely allow the synthesis of metastable phases that cannot be obtained by conventional methods since low temperature synthesis preserves the essential features of the parent (precursor) structures. The previously known topochemical reactions can be mainly classified into three categories:

a. Topochemical Redox Reactions

Examples include the well-known intercalations of alkali metals into layered transition metal oxides and chalcogenides. There are numerous papers and review articles on this subject. One example (1) is shown here.



The process involves insertion of lithium into the layer spacings of the sulphide; in the process a redox reaction occurs. This reaction is topotactic because the structure of the product, Li_xTiS_2 , is directly related to that of the precursor, TiS_2 . The only major change is expansion of the interlayer distance.

b. **Topochemical Ion-Exchange Reactions (2)**

Some transition metal oxides with layered or tunnel structures can accommodate mobile ions between the layers or tunnels. The resulting compounds are usually ionic conductors. Due to their mobility, the guest ions can be exchanged in aqueous solutions or/and molten salts. Since the reaction temperature is usually far lower than the structure-breaking temperature, the basic structure is retained except for minor changes required to accommodate the different-sized incoming ions.

c. **Topotactic Dehydrations**

Traditionally the dehydration process has been studied by thermal (DTA and TG) analysis in a flowing nonreacting gas. The products attracted chemists' attention; the structures of the products did not. In recent years, however, occasional reports on the crystal structures of dehydration products have surfaced. Low temperature dehydrations interest solid state scientists because in some instances they offer a unique procedure for preparing metastable solid state compounds. Dehydration of $\text{MoO}_3 \cdot 2\text{H}_2\text{O}$ to yield metastable MoO_3 (3), and related compounds (4,5) are known topotactic reactions. By this reaction metastable phases such as metastable bronzes A_xMoO_3 , where A is an alkali metal (6), metastable forms of AlF_3 ($\beta\text{-AlF}_3$) (7) and MCl_2 ($\text{M}=\text{Ba}, \text{Eu}$) (8,9), have been prepared.

1.1.2 Synthesis Based on Low Temperature Chemical Decompositions

a. Solid State Precursor Method

This method takes advantage of the low decomposition temperatures of precursors that can be isolated from solutions as homogeneous solids with stoichiometric compositions. The precursors most frequently used are complexes containing organic ligands that can be decomposed or removed easily. Since it is not always possible to obtain precursors of all desired compositions, solid solutions including coprecipitated hydroxides, oxalates and nitrates have also been used. Sol-gel processing is a technique based on this method. It has been used for the synthesis of many homogeneous ceramic oxides as Rao and Gopalakrishnan (see GENERAL REFERENCE BOOKS in the end) have reviewed. Compounds other than oxides can also be prepared by the precursor method. The preparation of anhydrous rare earth halides by the ammonium halide procedure, first introduced by Taylor and Carter (10) and later studied carefully by Meyer and coworkers (11,12,13), also involves solid state precursors such as $(\text{NH}_4)_3\text{LnCl}_6$. It is a simple but effective method for the synthesis of anhydrous halides both in high yields and in high purities. Other examples include the cubic form of TaN prepared by thermal decomposition of a molecular precursor $[\text{Np}_2\text{TaN}]_6 \cdot \text{NH}_3 \cdot 2\text{C}_6\text{H}_6$ isolated from a benzene solution (14), and single phase alloy $\text{Cu}_{4-x}\text{Ni}_x$ prepared by thermolysis of hetero-polymetallic molecules $(\mu_4\text{-O})\text{N}_4\text{Cu}_{4-x}(\text{Ni}(\text{H}_2\text{O}))_x\text{Cl}_6$ (N=N, N-diethylnicotinamide) (15).

b. Soluble Deposition or Precipitation

Isolation of insoluble compounds from solutions through precipitation is one of the oldest techniques used to prepare solid state compounds. The products are usually either

micro crystalline or amorphous materials. Some recent reports indicate that interesting materials that usually require high preparation temperatures can be isolated from molecular precursors in organic solutions. For example, NiTe containing Ni(0) was isolated from a toluene solution of Ni(COD)₂, Et₃P and Et₃PTe (COD=cyclooctadiene) (16), and FeTe and FeTe₂ from [Cp(Et₃P)(CO)Fe]Te_n (17). Polycrystals of semiconducting MSe₂ (M=Hg, Cd, Cu), FeSe_x, Ti₂Se and CuInSe₂ were isolated by warming DMF solutions of the polyselenide complexes [M(Se₄)₂]²⁻ (M=Cd, Hg), [Fe₂Se_{1,2}]²⁻, [Cu₂Se_{1,4}]²⁻, and [M₃Se_{1,3}]³⁻ (M=Ti, In) with Se-abstracting reagents such as CN⁻ and n-Bu₃P (18). Preparation of solid LnCl₂ (Ln=Sm, Eu) from THF solutions of LnCl₃(THF)_x by metal reduction, an interesting low temperature synthesis, also involves precipitation (19).

c. Solvolytic Decomposition

Solvolytic decomposition (leaching) is selective dissolution of one component from a solid with the remaining component(s) retained in the solid state. Use of such reactions as a solid state preparation method has not received much attention because of solubility requirement limitations. In 1963 Clifford (20,21) reported decomposition of mixed valence oxides by an acid. One such reaction is shown below:

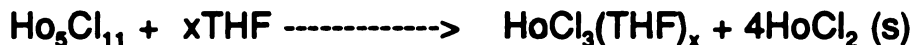


In this reaction the lower valent oxide is soluble and removed from the mixed-valent oxide lattice; the more covalent higher oxide is insoluble and is left in the solid state. Since elements like praseodymium do not readily form single high valent oxides by thermal reactions, acid leaching provides a convenient and unique preparatory

procedure. There have been a few reports of acid leaching on Mn_2O_3 and other mixed-valent oxides (22,23,24). Some deintercalation reactions are also solvolytic decompositions. For example, acid leaching of the Chevrel phase $\text{Cu}_x\text{Mo}_6\text{S}_8$ results in Mo_6S_8 (25).

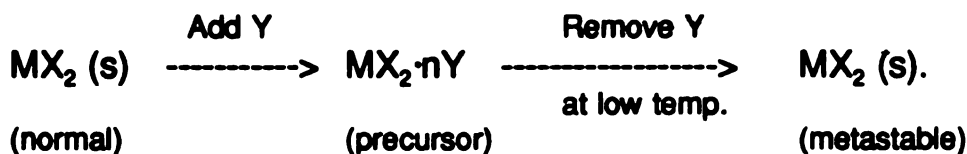
1.2 Solvolytic Decompositions and Metastable Phases

The lanthanide trihalides have long been known to be soluble in tetrahydrofuran (THF) (26) while the dichlorides LnCl_2 ($\text{M}=\text{Sm}, \text{Eu}$) are insoluble in this solvent (19). It is possible to prepare compounds of the lower valent cation by selectively dissolving the trivalent halide from a mixed valent compound. Our original goals were to apply solvolytic decompositions to mixed halide systems as a synthetic method. Since for Ho and Gd only mixed-valent halides have been synthesized, if the solvolytic decomposition



could occur, it would be a unique way of preparing the yet unknown HoCl_2 . However, our results on SmCl_2 and EuCl_2 systems indicated that low temperature leaching forms metastable phases (27). Therefore, we concentrated on the synthesis, characterization and formation mechanisms of metastable phases.

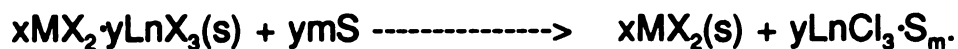
Our goals can be summarized by the following two-step reactions:



The first step is the synthesis of appropriate precursors whose structures are closely related to those of the metastable forms of MX_2 . The second step is the decomposition that yields the metastable forms. When the added component Y is a trihalide, LnX_3 , the precursor is a mixed or mixed-valent halide and the decomposition reaction is solvolytic; when Y is water (or an organic solvent), the precursor is a hydrate

(or a solvate) and the decomposition is dehydration (desolvation). Since the structure of a final metastable product is closely related to that of the precursor, this procedure is called template synthesis.

Since a thermodynamically less stable (metastable) phase is the expected product in a successful solvolytic decomposition, solvent (S) must both dissolve the added component from the mixed halide selectively, and form a strong and stable solvate capable of overcoming lattice energies. The main driving force for the decomposition is formation of the soluble solvate:



CHAPTER 2 BACKGROUND INFORMATION

SYNOPSIS

Important structural features of lanthanide and alkaline earth halides and their mixed or mixed valent halides are summarized. Crystal structures of the PbCl_2 -type, the anti- Fe_2P -type and the fluorite-type for AX_2 and the fluorite-related cluster-type $\text{M}_{14}\text{X}_{33}$ compounds are described with emphasis on layer stackings. A hexagonal unit cell of the fluorite-type structure is introduced. The Rietveld refinement procedure is briefly reviewed and the XRS-82 system set of programs is described.

2.1 Structural Chemistry of Lanthanide and Alkaline Earth Halides

Brown's book on "Halides of the Lanthanides and Actinides", though somewhat outdated, is a comprehensive and important source of information. Numerous papers and review articles dealing with the synthesis and structures of the lanthanide halides have appeared since its publication. References are given when specific compounds are mentioned. Some important points are summarized below.

2.1.1 Characteristics of Lanthanide and Alkaline Earth Halides

- a. Ionic radius of Ln^{3+} decreases across the lanthanide series steadily but slightly (La^{3+} :1.172 --- Lu^{3+} :1.001 Å);
- b. The 2+ oxidation state has been achieved mainly with those elements with configurations of f^7 or f^14 or close thereto; those that form divalent halides are: Nd, Sm, Eu, Dy, Tm, Yb. Among them, Sm, Eu and Yb divalency can be achieved by hydrogen reductions; others can only be obtained by metal reductions. Relative stabilities are: $\text{Eu}^{2+} (f^7) > \text{Yb}^{2+} (f^{14}) > \text{Sm}^{2+} (f^6)$;
- c. Ln^{2+} ions are similar to the alkaline earth ions with respect to ionic radius, acidity, and ionicity;

Ionic radius (28):	Sm^{2+}	Eu^{2+}	Sr^{2+}	Yb^{2+}	Ca^{2+}
(CN=8) Å	1.41	1.39	1.40	1.28	1.26

Halides of these elements, especially the fluorides and chlorides, are typical ionic compounds. The similarity in ionic radii makes comparative studies of LnX_2 and MX_2 (M=alkaline earth) possible because we can take advantage of the stability of the alkaline earth ions.

- d. Both LnX_2 and alkaline earth halides exhibit polymorphism (Tables 1 and 2). Among them, the PbCl_2 -type is a frequently observed form.

- e. Both Ln^{2+} and alkaline earth M^{2+} form large numbers of mixed and mixed-valent halides with Ln^{3+} . Structural information is listed in Tables 3 and 4.

2.1.2 Mixed and Mixed-Valent Halides

The mixed (-valent) fluorides have been reviewed by Greis and Haschke (29). More recently the crystal chemistry of Ca_2YbF_7 and related structures have been examined extensively by Bevan and coworkers (30,31,32). In the past decade a large number of mixed and mixed-valent chlorides and bromides have been prepared (33,34,35,36,37,38,39,40,41,42,43). Known mixed halides can be classified into two series:

- a. The vernier-type compounds that are M^{2+} -rich and have the general formula $\text{M}_n\text{X}_{2n+1}$ where $n=4, 5, 6, 7, 11$ are known for chlorides and bromides.
- b. The Ln_6X_{37} cluster-type compounds have the general formula $\text{M}_6\text{Ln}_5\text{X}_{33}$ where M is a divalent alkaline earth or lanthanide ion and Ln is a trivalent lanthanide ion (35,44). A common feature of the mixed halides is a fluorite-related superstructure discussed in 2.2.4.

Table 1. Structural modifications of lanthanide halides LnX_2 .

$\text{Ln} \setminus \text{X}$	F	Cl	Br	I
Nd		PbCl_2 (9)	PbCl_2 (9)	SrBr_2 (8)
Sm	CaF_2 (8)	PbCl_2 (9) CaF_2 (8, H)*	PbCl_2 (9) SrBr_2 (8)	PbCl_2 (9, P) EuI_2 (7) $\text{SrI}_2\text{-IV}$ (7, M)*
Eu	CaF_2 (8) PbCl_2 (9, P)	PbCl_2 (9) CaF_2 (8, H)*	PbCl_2 (9, P) SrBr_2 (8) SrI_2 (7)	PbCl_2 (9, P) EuI_2 (7) SrI_2 (7) $\text{SrI}_2\text{-IV}$ (7, M)*
Dy		SrBr_2 (8)	SrI_2 (7)	CdCl_2 (6)
Tm	CaF_2 (8)	SrI_2 (7)	SrI_2 (7) CaCl_2 (6) $\alpha\text{-PbO}_2$ (6) TiO_2 (6, H)	CdI_2 (6)
Yb	CaF_2 (8)	SrI_2 (7)	SrI_2 (7) CaCl_2 (6) $\alpha\text{-PbO}_2$ (6) TiO_2 (6, H)	CdI_2 (6)

Note. (): cation coordination number;
P: high-pressure form;
H: high-temperature form;
M: metastable form;
*: prepared in this work.

Table 2. Structural modifications of alkaline earth halides MX_2 .

M \ X	F	Cl	Br	I
Ba	PbCl ₂ (9, P) CaF ₂	PbCl ₂ (9) anti-Fe ₂ P (9, M) [*] CaF ₂ (8, H)	PbCl ₂ (9) anti-Fe ₂ P (9, M) [*]	PbCl ₂ (9) anti-Fe ₂ P (9, P) [*]
Sr	PbCl ₂ (9, P) CaF ₂ (8)	PbCl ₂ (9, P) CaF ₂ (8)	PbCl ₂ (9, P) SrBr ₂ (8)	PbCl ₂ (9, P) SrI ₂ -I (7) SrI ₂ -IV (7, M) [*]
Ca	PbCl ₂ (9, P) CaF ₂ (8)	SrI ₂ (7, P) CaCl ₂ (6) α -PbO ₂ (6, M)	CaCl ₂ (6) α -PbO ₂ (6, M) TiO ₂ (6, H)	CdI ₂ (6)

Note. (): cation coordination number;
P: high-pressure form;
H: high-temperature form;
M: metastable form;
*: prepared in this work.

Table 3. Space groups and lattice parameters of mixed-valent lanthanide halides (excluding fluorides).

n	Formula	S. G.	a(Å)	b(Å)	c(Å)	angle (°)	Reference
Vernier-type: $\text{Ln}_n\text{X}_{2n+1}$							
4	Nd_4Br_9	P 2/b	7.741(2)	30.16(1)	7.125(1)	$\gamma=91.80(5)$	<u>38,92</u>
	Eu_4Cl_9	P 2/b	7.2338(6)	28.299(3)	6.7167(6)	$\gamma=91.775(5)$	<u>35</u>
5	$\text{Sm}_5\text{Br}_{11}$	P 2 ₁ /m	7.652(2)	37.21(2)	7.121(2)	$\beta=90.26(5)$	<u>93,94</u>
	$\text{Eu}_5\text{Cl}_{11}$	P 2 ₁ /m	7.214(2)	35.17(1)	6.775(2)	$\beta=90.34(1)$	<u>35</u>
	$\text{Dy}_5\text{Cl}_{11}$	P 2 ₁ /m	7.108(1)	34.68(2)	6.632(1)	$\beta=90.23(4)$	<u>33,39</u>
	$\text{Ho}_5\text{Cl}_{11}$	P 2 ₁ /m	7.078(2)	34.57(2)	6.603(3)	$\beta=90.19(5)$	<u>40</u>
	$\text{Cf}_4\text{GdCl}_{11}$	P 2 ₁ /m	7.130	34.83	6.685	$\beta=90.24$	<u>43</u>
	$\text{Cf}_4\text{GdBr}_{11}$	P 2 ₁ /m	7.619	36.97	7.040	$\beta=90.18$	<u>43</u>
6	$\text{Sm}_6\text{Br}_{13}$	I 2/a ⁱ⁾	7.649(2)	44.44(2)	7.139(2)	$\gamma=91.30(5)$	<u>93,94</u>
	$\text{Dy}_6\text{Cl}_{13}$	I 2/a ⁱ⁾	7.099	41.41(2)	6.667(1)	$\gamma=91.35(3)$	<u>33</u>
	$\text{Tm}_6\text{Cl}_{13}$	I 2/a ⁱ⁾	7.009(3)	41.04(1)	6.557(3)	$\gamma=91.30(3)$	<u>33</u>
	$\text{Yb}_6\text{Cl}_{13}$	I 2/a ⁱ⁾	6.958(11)	40.98(6)	6.539(11)	$\gamma=91.2(2)$	<u>41,42</u>
	$\text{Yb}_5\text{ErCl}_{13}$	I 2/a ⁱ⁾	7.004(5)	41.00(2)	6.537(5)	$\gamma=91.2(1)$	<u>41,42</u>
7	$\text{Dy}_7\text{Cl}_{18}$	P n m a	7.097(1)	48.18(1)	6.674(1)		<u>33</u>
	$\text{Tm}_7\text{Cl}_{18}$	P n m a	7.001(1)	47.68(1)	6.571(3)		<u>33</u>
8	$\text{Tm}_8\text{Cl}_{17}$?	6.995(2)	54.26(2)	6.580(1)		<u>33</u>
11	$\text{Sm}_{11}\text{Br}_{24}$	P 2 ₁ /n	7.652(2)	81.62(6)	7.130(3)	$\beta=90.19(7)$	<u>93,94</u>
Cluster-type: $\text{Ln}_{14}\text{X}_{33}$ with Ln_6X_{37} clusters							
14	$\text{Sm}_{14}\text{Cl}_{33}$	R $\bar{3}$	12.864(2)		24.72(8)		this work ⁱⁱ⁾
	$\text{Sm}_9\text{Nd}_5\text{Cl}_{33}$	R $\bar{3}$	12.894(2)		24.850(6)		this work ⁱⁱ⁾
	$\text{Sm}_9\text{Gd}_5\text{Cl}_{33}$	R $\bar{3}$	12.845(2)		24.694(8)		this work ⁱⁱ⁾
	$\text{Eu}_{14}\text{Cl}_{33}$	R $\bar{3}$	12.815(4)		24.768(8)		<u>35</u>
	$\text{Nd}_{14}\text{Cl}_{33}$	R $\bar{3}$	12.987(1)		24.822(3)		<u>44</u>

- i) Non-conventional setting of space group C 2/c (# 15):
Standard setting: $\underline{a}_0, \underline{b}_0, \underline{c}_0$; transformation: $\underline{a} = -\underline{c}_0, \underline{b} = \underline{a}_0 + \underline{c}_0, \underline{c} = -\underline{b}_0$.
- ii) Directly indexed c values were half those reported here.

Table 4. Space groups and lattice parameters of alkaline earth-related mixed halides (excluding fluorides).

n	Formula	S. G.	a(Å)	b(Å)	c(Å)	angle (°)	Reference
Vernier-type: $M_{n-1}LnX_{2n+1}$							
5	Sr_4DyCl_{11}	P n m a	7.210(1)	35.18(1)	6.768(1)		<u>40</u>
	Sr_4NdBr_{11}	P n m a	7.662(1)	37.35(2)	7.140(3)		<u>95</u>
	Sr_4EuCl_{11}	P n m a	7.220(2)	35.15(1)	6.790(4)		<u>37</u>
	Sr_4NdCl_{11}	P n m a	7.230(5)	35.29(2)	6.826(4)		<u>36</u>
6	Sr_5NdBr_{13}	I 2/a ⁱ⁾	7.642	44.62(2)	7.177(6)	$\gamma=91.11(20)$	<u>95</u>
Cluster-type: $M_9Ln_5X_{33}$ with MLn_5X_{37} clusters							
14	$Sr_9Eu_5Cl_{33}$	R $\bar{3}$	12.854(4)		24.702(8)		<u>37</u>
	$Sr_9Nd_5Cl_{33}$	R $\bar{3}$	12.908(6)		24.823(10)		<u>36</u>
	$Ba_9La_5Br_{33}$	R $\bar{3}$	14.098(2)		26.678(6)		this work
	$Ba_9Nd_5Br_{33}$	R $\bar{3}$	14.039(1)		26.477(4)		this work
Unknown structures							
	"Ba ₂ LaCl ₇ "	?	17.637(6)		12.495(5)	$\gamma=120$	this work
	Ba ₁₇ Sm ₁₀ Cl ₆₄	P a 3	21.366(2) ⁱⁱ⁾				this work

- i) Non-conventional setting of space group C 2/c (# 15):
Standard setting: $\underline{a}_0, \underline{b}_0, \underline{c}_0$; transformation: $\underline{a} = -\underline{c}_0, \underline{b} = \underline{a}_0 + \underline{c}_0, \underline{c} = -\underline{b}_0$.
- ii) Single crystal parameter.

2.2 Crystal Structures of Related Halides

A crystal structure can be described a number of ways, each of which emphasizes different perspectives. Of course, the most accurate, but the least descriptive representation of a crystal structure is a set of lattice parameters, a space group and the atomic coordinates. Descriptions in terms of close packing of atoms and space filling highlight the geometric relationships and the extended nature of crystals while those based on coordination polyhedra that share edges, vertices, or faces pay more attention to the local structures and the chemical nature of central atoms. Even though it is possible to describe a structure in both terms, for an ionic inorganic solid, close packing is more convenient; while for a covalent solid, coordination polyhedra are more meaningful.

Crystal structures of some halides of importance to this work have been described. For the convenience of later discussions on reaction mechanisms, selected structures are summarized briefly. Symmetries of the close packings and correlations with hexagonal close packing layers are emphasized.

2.2.1 The PbCl_2 -Type Structure

The normal forms of LnCl_2 ($\text{Ln}=\text{Nd}, \text{Sm}, \text{Eu}$) and BaX_2 ($\text{X}=\text{Cl}, \text{Br}, \text{I}$), among many other AB_2 -type compounds, exhibit this structure. It has been described by Wyckoff (see GENERAL REFERENCE BOOKS). The EuCl_2 structure was refined by Bärnighausen (45).

Space group: Pbnm (# 62); orthorhombic.

$a = 8.965(2)$, $b = 7.538(1)$, $c = 4.511(1) \text{ \AA}$; $Z=4$.

All atoms are in the 4c special positions:

$$\pm (u, v, 1/4) \quad \pm (1/2-u, v+1/2, 1/4)$$

with $u(\text{Eu}) = 0.11510(3)$, $v = 0.24952(3)$, $B(\text{Eu}) = 1.28(1)$; $u(\text{Cl}_1) = 0.4279(1)$, $v(\text{Cl}_1) = 0.1434(1)$, $B(\text{Cl}_1) = 1.32(3)$; and $u(\text{Cl}_2) = 0.1668(1)$, $v(\text{Cl}_2) = 0.0238(2)$, $B(\text{Cl}_2) = 1.56(4)$.

The cation coordination number is hard to define. The coordination polyhedron can be described approximately as irregular 9-coordinated tricapped trigonal prism as shown in Figure 1. The three capping Eu-Cl bond lengths are: 2.916(1), 2.994(1) and 3.046(1)Å; the remaining six Eu-Cl bond lengths are: two 2.925(1), two 3.090(1) and two 3.440(1)Å. It has a mirror plane of symmetry (defined by the capping and the central atoms in Figure 1).

This structure can also be thought of as a considerably distorted close-packing of the halogen atoms with the metal atoms accommodated in the same plane. The layers are stacked in an ABAB... fashion. Figure 2(a) illustrates a single layer and Figure 2(b) is the projection of the structure down the c axis, showing the double layer feature. The two layers have identical packings and stack such that inversion centers are formed between them.

The arrangement of the metal atoms in this structure can be derived from a single hexagonally close-packed layer as depicted in Figure 3(a). Exactly half of the cations are displaced from the layer by $c/2$ such that the 6-fold axes are destroyed while zigzag metal-metal chains are formed in each layer and inversion centers are created between any two adjacent layers.

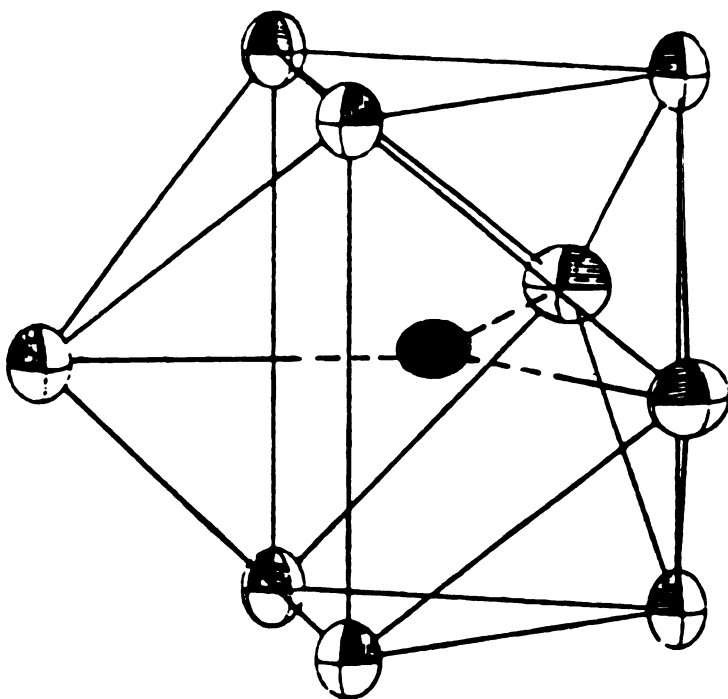


Figure 1. A 9-coordinated tricapped trigonal prism.

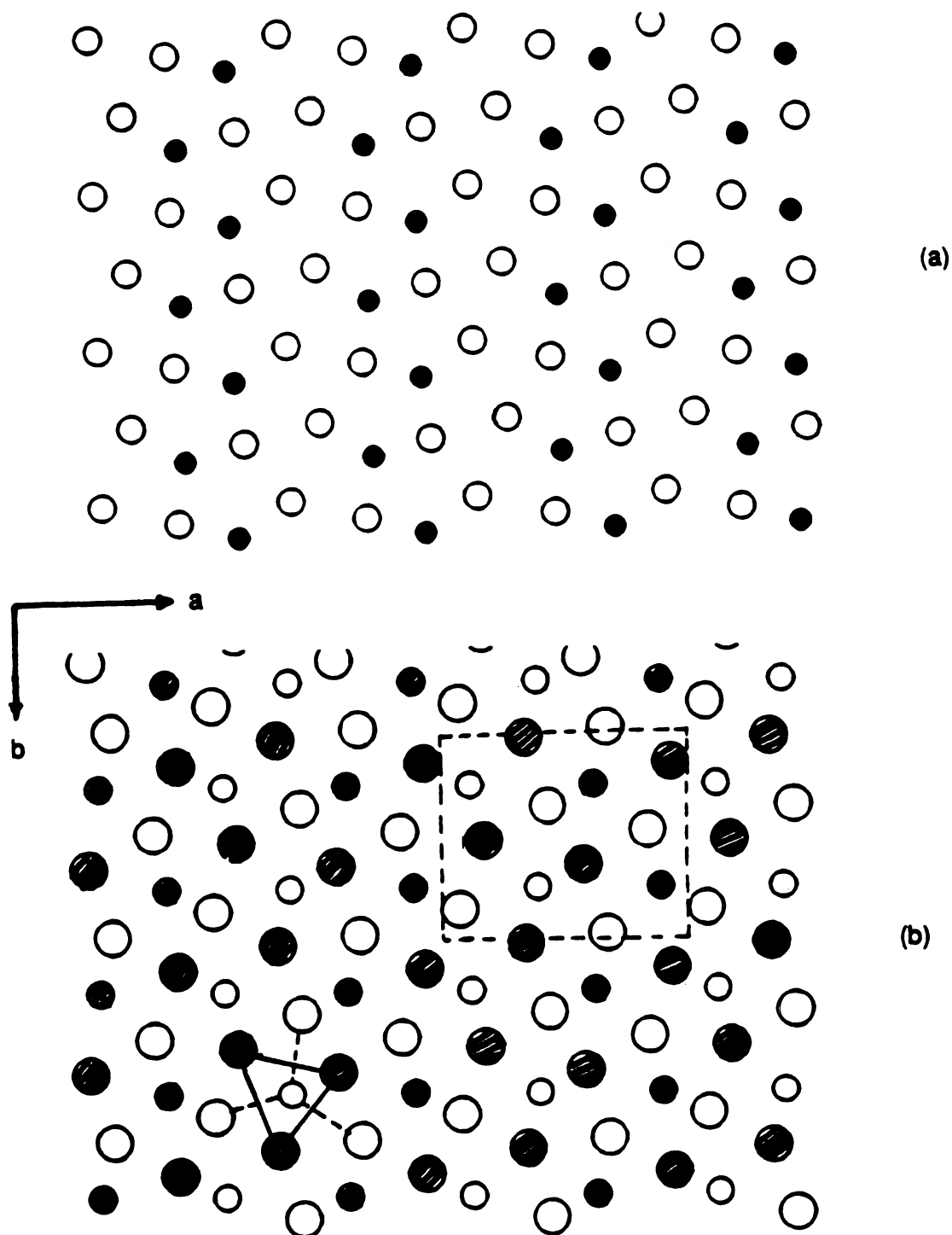


Figure 2. Projections of the PbCl_2 -type structure down the c axis. Small circles represent cations and large circles represent anions. (a) A single layer showing the roughly close-packed anions and the accommodated cations; (b) a double layer projection with one 9-coordinated polyhedron outlined (Open circles: $z = 0.25$; shaded circles: $z = \pm 0.75$).

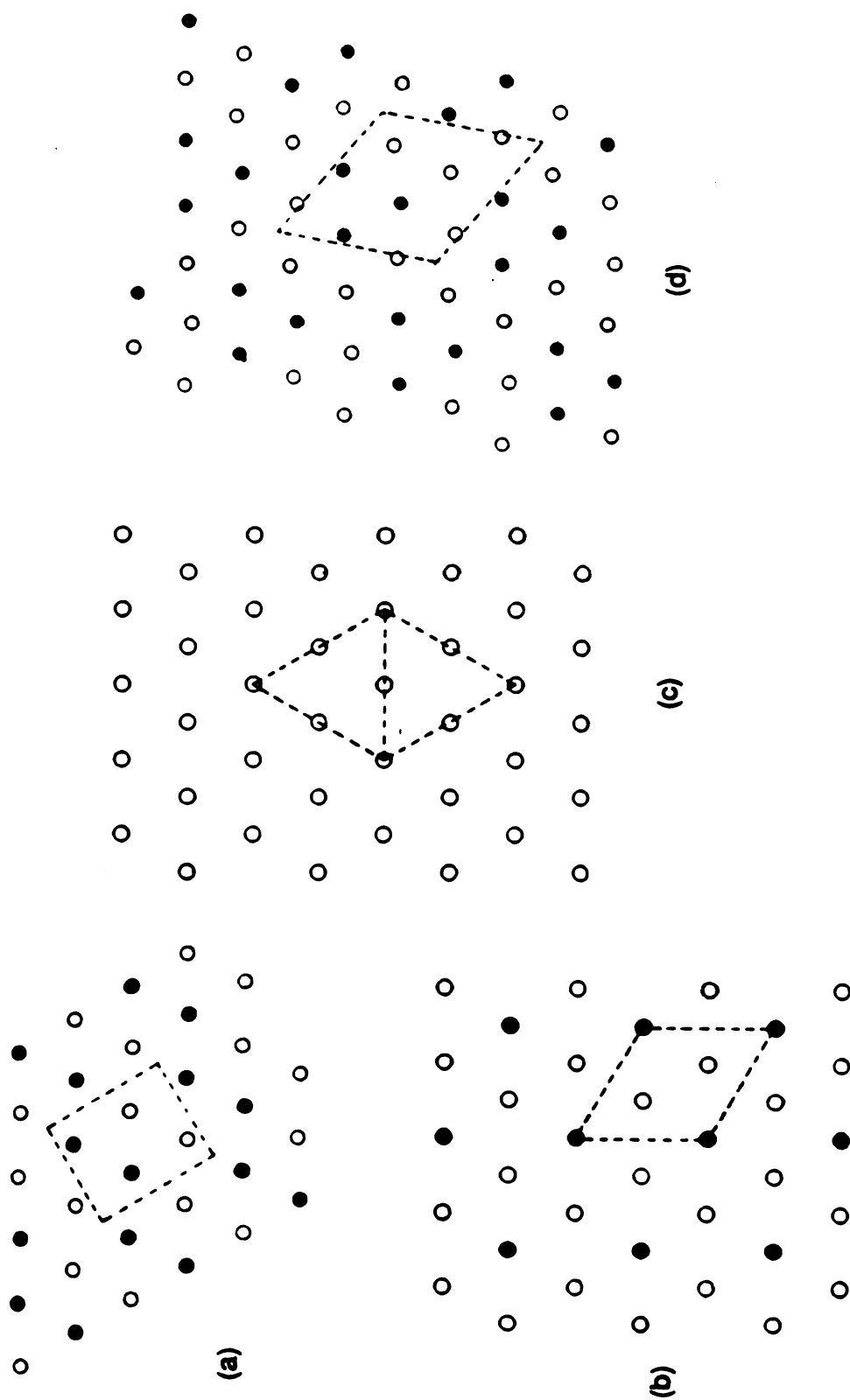


Figure 3.

Cation arrangement of various structures illustrating their derivations from hexagonally close-packed layers. (a) The PbCl_2 -type double (solid and open circle) layer structure; (b) the anti- Fe_2P -type double (solid and open circle) layer structure; (c) the fluorite-type structure; and (d) a typical layer of the cluster type $\text{Ln}_{14}\text{X}_{33}$ structure. In (d) the $1/6$ solid circles and all open circles represent Ln^{2+} , and the $5/6$ solid circles represent Ln^{3+} .

2.2.2 The Anti-Fe₂P-Type Structure

The normal Fe₂P structure was described by Wyckoff. Anti-Fe₂P-type BaI₂ was prepared under high pressures and the structure was refined by Beck using single crystal data (46).

Space group: $P\bar{6}2m$ (# 189), hexagonal.

$a = 9.142(6)$, $c = 5.173(3)$ Å; $Z = 3$.

Atomic positions:

Ba(1):	(1b)	(0,	0,	1/2)
Ba(2):	(2c)	(1/3,	2/3,	0)
I(1):	(3f)	(0.2563(2),	0,	0)
I(2):	(3g)	(0.5918(2),	0,	1/2).

In this anti-Fe₂P-type structure the metal atoms are 9-coordinated in a way similar to those in the PbCl₂-type structure shown in Figure 1. However, there are two major differences. First, the cation coordination polyhedra of the anti-Fe₂P-type have D_{3h} symmetry while those of the PbCl₂-type are less symmetric (C_{2v}); secondly, there are two types of cation coordination polyhedra in the anti-Fe₂P-type structure while there is only one type in the PbCl₂-type. The apical and equatorial (capping) Ba-I bond distances of Ba(1) differ from those of Ba(2). Ba(1) has six shorter apical (3.491(1) Å) and three longer equatorial (3.734(2) Å) bonds, while Ba(2) has six longer apical (3.791(1)) and three shorter equatorial (3.456(1) Å) bonds.

The atoms in the anti-Fe₂P-type structure are slightly more densely packed (0.8% higher packing efficiency for BaI₂ (46)) than those in the PbCl₂-type structure. Therefore, there is a slight increase in effective coordination numbers in the former structure.

The anti-Fe₂P-type structure exhibits close packing similar to that of the PbCl₂-type.

It is a double layer structure (Figure 4), but unlike the PbCl_2 -type structure the layer packings are not identical (Figure 5). Therefore a center of symmetry is absent.

The cation positions can also be derived from hexagonal close-packing as shown in Figure 3(b). Displacing $1/3$ of the metal atoms from a hexagonal close-packed layer by $c/2$ in such a way that 6-fold inversion axes are retained results in the cation arrangement of the anti- Fe_2P -type structure.

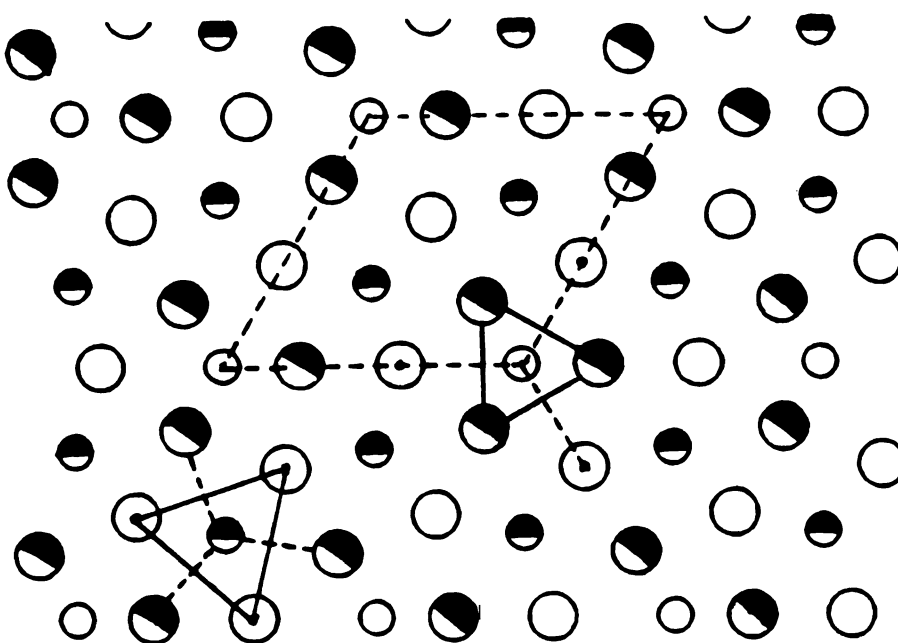


Figure 4. Projection of the anti- Fe_2P -type structure down the c axis. Open circles are at $z = \pm 0.5$ and semi-shaded circles are at $Z = 0$ and 1 ; small circles represent cations and large circles represent anions. Two types of 9-coordinated polyhedra are depicted (----: equatorial bonds).

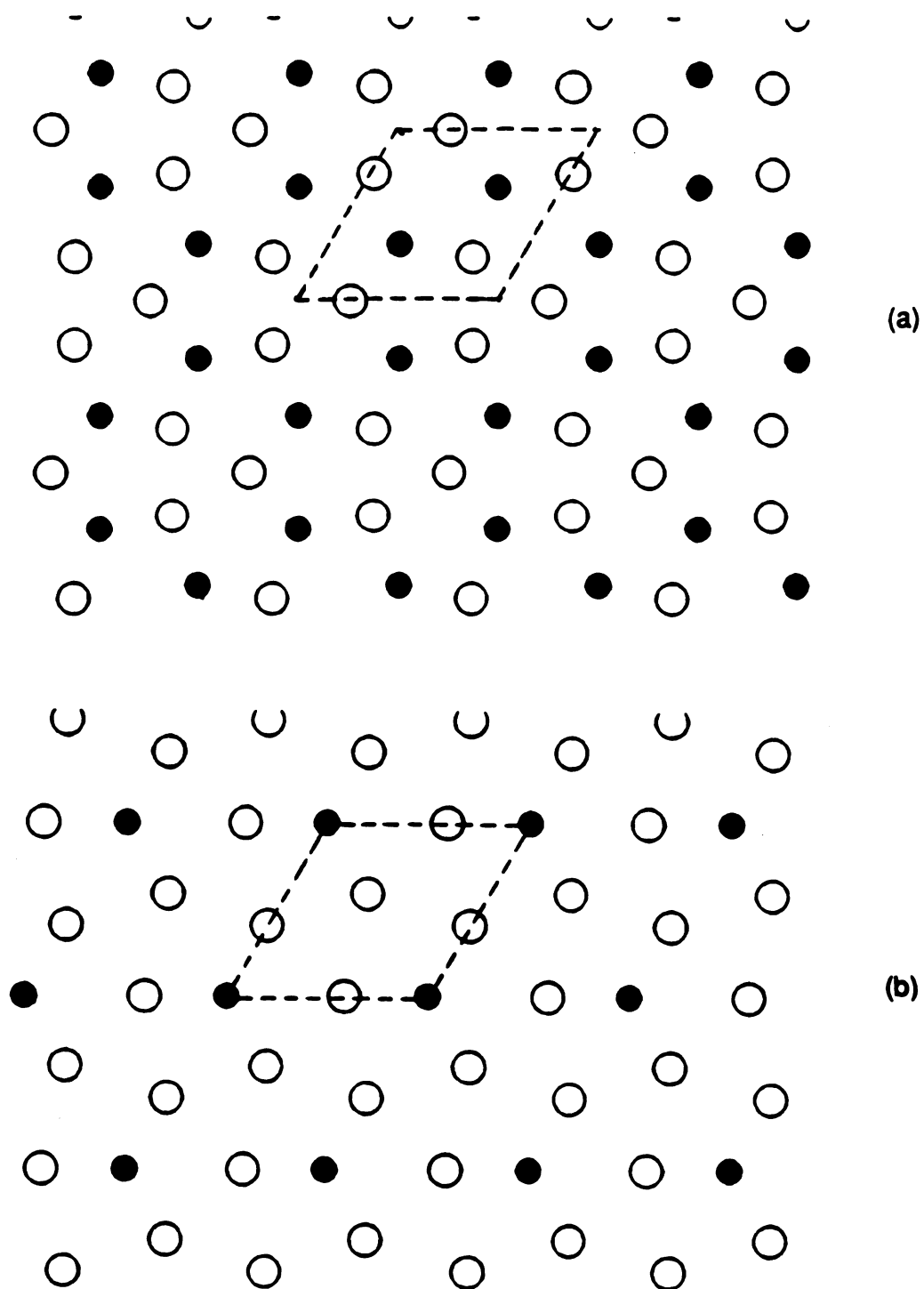


Figure 5. Two different layers of the anti- Fe_2P -type structure. Solid circles represent cations and open circles anions. (a) $z = 0$; (b) $z = 0.5$.

2.2.3 The Fluorite (CaF₂)-Type Structure

This is one of the most commonly found structure types for AB₂-type compounds. Among them are the alkaline earth and divalent rare earth fluorides, SrCl₂, and the high temperature forms of MCl₂ (M=Ba, Sm, Eu).

Space group: F m 3 m (# 225), face-centered cubic.

Unit cell dimension for SrCl₂: $a = 6.9767 \text{ \AA}$, $Z = 4$.

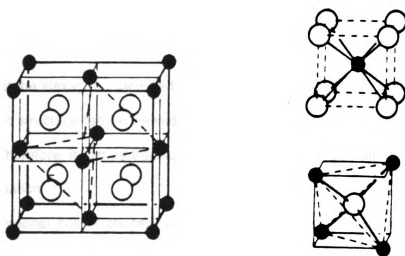
Atomic positions:

Sr:	(4a)	(0, 0, 0)
Cl:	(8c)	$\pm (1/4, 1/4, 1/4)$.

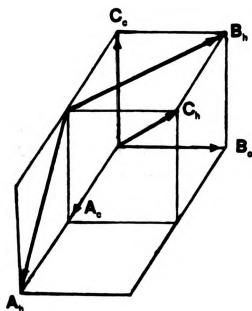
Since all the atoms occupy special positions, the coordination polyhedra of the metal atoms are ideal cubic (CN=8, symmetry O_h), and those of the anions are ideal tetrahedra (CN=4, symmetry T_d) (Figure 6(a)). The cubes are linked together by sharing faces. From a cubic coordination polyhedron the ionic radius ratio for the fluorite-type structure can be evaluated. Assume the cation (A) and anions (B's) are in close contact, then the body diagonal is $2(r_A + r_B)$. The cubic edge must be $\geq 2r_B$ for a compound AB₂ to adapt this coordination. Therefore $2(r_A + r_B) \geq \sqrt{3}(2r_B)$; that is, $r_A/r_B \geq 0.732$.

This structure is commonly described in terms of cation close-packings. When we view down a three-fold inversion axis (the body diagonal) of a cubic cell, the cations are arranged in hexagonally close-packed layers normal to the three-fold axis, with the layers stacked in the ABCABC... sequence (i.e. face centered cubic stacking). The anions occupy all the tetrahedral holes to form separate hexagonal close-packed layers parallel to the cation layers. (Here the term "layer" is used only for description purposes and does not imply a layer structure in which inter-layer interactions are weak.)

Many mixed halides have fluorite-related rhombohedral superstructures as will be described later. To facilitate comparisons between the fluorite cell and the hexagonal



(a)



(b)

Figure 6. The fluorite-type structure. (a) the cubic unit cell, and the cation (O_h) and anion (T_d) coordination polyhedra; (b) the choice of the hexagonal unit cell.

supercell, we introduce a "hexagonal unit cell" of the fluorite-type structure. This unit cell is more effective for describing the fluorite structure layer stackings.

a. Choice of the Hexagonal Unit Cell

The cubic structure can be viewed as a special case of rhombohedral structures with $\alpha = 90^\circ$. Therefore, it can be transformed into a hexagonal cell without any loss of structural information.

The hexagonal cell is chosen such that the C_h axis coincides with the body diagonal of the cubic cell, and A_h and B_h are then the face diagonals as shown in Figure 6(b). Unit cell parameters are transformed according to the following equations:

$$A_h = A_c - C_c,$$

$$B_h = -A_c + B_c,$$

$$C_h = A_c + B_c + C_c$$

or

$$\begin{pmatrix} A_h \\ B_h \\ C_h \end{pmatrix} = \begin{pmatrix} 1 & 0 & -1 \\ -1 & 1 & 0 \\ 1 & 1 & 1 \end{pmatrix} \begin{pmatrix} A_c \\ B_c \\ C_c \end{pmatrix}$$

The transformation matrix is $S = \begin{pmatrix} 1 & 0 & -1 \\ -1 & 1 & 0 \\ 1 & 1 & 1 \end{pmatrix}$.

Since the determinant of S is $|S| = 3$, the volume relationship is

$$V_h = 3V_c.$$

From $A_c = B_c = C_c$ and the ortho-normality of these cubic lattice parameters we have

$$A_h = B_h = \sqrt{2}A_c, \quad \text{and} \quad C_h = \sqrt{3}A_c.$$

It can be shown that the newly chosen unit cell is indeed hexagonal.

$$\begin{aligned} A_h \times B_h &= (A_c - C_c) \times (-A_c + B_c) = -A_c \times A_c + C_c \times A_c + A_c \times B_c - C_c \times B_c \\ &= 0 + B_c + C_c - (-A_c) = C_h \end{aligned}$$

therefore both A_h and B_h are orthogonal to C_h .

$$\begin{aligned} A_h \cdot B_h &= -A_c \cdot A_c + C_c \cdot A_c + A_c \cdot B_c - C_c \cdot B_c \\ &= -A_c^2 + 0 + 0 + 0 = -A_c^2. \end{aligned}$$

Note $A_h \cdot B_h = A_h B_h \cos \gamma = 2A_c^2 \cos \gamma$. Thus $\cos \gamma = -1/2$, and $\gamma = 120^\circ$.

b. Atomic Coordinate Transformation

The inverse matrix of S is

$$T = S^{-1} = \begin{pmatrix} 1/3 & -1/3 & 1/3 \\ 1/3 & 2/3 & 1/3 \\ -2/3 & -1/3 & 1/3 \end{pmatrix}$$

The coordinate transformation matrix is the transposed inverse matrix of S, or T^t

$$T^t = \begin{pmatrix} 1/3 & 1/3 & -2/3 \\ -1/3 & 2/3 & -1/3 \\ 1/3 & 1/3 & 1/3 \end{pmatrix}$$

The space group $Fm\bar{3}m$ has 192 general positions. Because the cations occupy the 4(a) and anions occupy the 8(c) special positions in the cubic cell, we can avoid unnecessary transformations by defining the following 8 positions as the general position set (subscript c for cubic) of the cubic unit cell:

$$\begin{array}{ll}
\pm (X_c, & Y_c, & Z_c) & \pm (X_c, & 1/2+Y_c, & 1/2+Z_c) \\
\pm (1/2+X_c, & Y_c, & 1/2+Z_c) & \pm (1/2+X_c, & 1/2+Y_c, & Z_c).
\end{array}$$

For the cations $X_c = Y_c = Z_c = 0$ and for the anions $X_c = Y_c = Z_c = 1/4$.

By applying the coordinate transformation matrix (subscript h for hexagonal) we have

$$\begin{pmatrix} X_h \\ Y_h \\ Z_h \end{pmatrix} = \begin{pmatrix} 1/3 & 1/3 & -2/3 \\ -1/3 & 2/3 & -1/3 \\ 1/3 & 1/3 & 1/3 \end{pmatrix} \begin{pmatrix} X_c \\ Y_c \\ Z_c \end{pmatrix}$$

or

$$X_h = 1/3 (X_c + Y_c - 2Z_c)$$

$$Y_h = 1/3 (-X_c + 2Y_c - Z_c)$$

$$Z_h = 1/3 (X_c + Y_c + Z_c)$$

The corners of the cubic unit cell have the following coordinates:

(0,0,0; 1,0,0; 0,1,0; 0,0,1; 1,1,1; 0,1,1; 1,0,1; 1,1,0). These coordinates can be transformed into hexagonal coordinates according to the above equations:

$$(0,0,0; \frac{1}{3}, -\frac{1}{3}, \frac{1}{3}; \frac{1}{3}, \frac{2}{3}, \frac{1}{3}; -\frac{2}{3}, -\frac{1}{3}, \frac{1}{3}; 0,0,1; -\frac{1}{3}, \frac{1}{3}, \frac{2}{3}; -\frac{1}{3}, -\frac{2}{3}, \frac{2}{3}; \frac{2}{3}, \frac{1}{3}, \frac{2}{3}).$$

Of the eight hexagonal coordinates, only three, (0,0,0), ($\frac{1}{3}, \frac{2}{3}, \frac{1}{3}$), and ($\frac{2}{3}, \frac{1}{3}, \frac{2}{3}$) lie within the hexagonal unit cell and correspond to the coordinates of Bravais-lattice points.

8 general positions of the hexagonal unit cell can be generated by applying the same transformations to the previously defined 8 general positions of the cubic unit cell. When the 8 hexagonal general positions are combined with the three Bravais-lattice point

translations, we finally obtain the 24 general positions of the hexagonal unit cell:

$$(0, 0, 0; \quad \frac{1}{6}, \frac{2}{6}, \frac{1}{6}; \quad \frac{2}{6}, \frac{1}{6}, \frac{2}{6}) +$$

$$\begin{aligned} \pm (X_h, \quad Y_h, \quad Z_h) & \quad \pm (-1/6+X_h, \quad 1/6+Y_h, \quad 1/3+Z_h) \\ \pm (-1/6+X_h, \quad -1/3+Y_h, \quad 1/3+Z_h) & \quad \pm (1/3+X_h, \quad 1/6+Y_h, \quad 1/3+Z_h). \end{aligned}$$

The atomic coordinates of SrCl_2 in both unit cells are listed in Table 5.

In the hexagonal cell it is apparent that the fluorite-type structure is made up of three cation layers at $Z=0, 1/3, 2/3$ and six anion layers at $Z=1/12 (1, 3, 5, 7, 9, 11)$. Projections down the c axis indicate that every cation or anion layer is hexagonally close-packed. A single layer is shown in Figure 3(c) (Page 21).

Table 5. Atomic positions of the fluorite-type SrCl_2 in cubic and hexagonal unit cells.

Atom	(X_c, Y_c, Z_c)	Multiplicity	(X_h, Y_h, Z_h)	Multiplicity
Sr:	(0 0 0)	4	(0 0 0)	12
Cl:	(1/4 1/4 1/4)	8	(0 0 1/4)	24

2.2.4 Fluorite-Related Cluster Type Superstructures

Mixed and mixed-valent halides of alkaline earth and rare earth halides with fluorite-related structures are compiled in Tables 3 (Page 15) and 4 (Page 16). The cluster-type $M_6Ln_5X_{33}$ compounds are of special interest to us because many precursors used in this work have this structure. The structure of the oxygen contaminated $Nd_{14}Cl_{32}O$ was solved by single crystal work (38) and later the structure of $Nd_{14}Cl_{33}$ was solved from triply-twinned crystals (44). The real symmetry of the triply-twinned crystals is triclinic, but it can be approximated as rhombohedral.

Space group: $R\bar{3}$ (# 148), rhombohedral.

Hexagonal lattice parameters for $Nd_{14}Cl_{33}$: $a = 12.987(1)$, $c = 24.822(3)$ Å; $Z=3$.

Unit cell contents: 27 LnX_2 and 15 LnX_3 ; or 3 formula units containing 3 M_6X_{37} ($Ln_1^{2+}Ln_5^{3+}Cl_{37}$) clusters.

List of atomic positions: Table 6.

Apparently, clustering of the trivalent cations in the superstructure is due to the "extra" halide anions brought in by Ln^{3+} . Each Ln^{3+} introduces one "extra" X^- when compared to LnX_2 , thus there are 15 "extra" X 's in a unit cell. Eitel (44), and Bevan and coworkers (30,47) have described the formation of clusters from the fluorite coordination polyhedra. Figure 7 illustrates the changes anions undergo when a $Ln_1^{2+}Ln_5^{3+}X_{37}$ cluster is derived from six face-sharing cubes. The cluster comprises six square anti-prisms of anions whose centers are occupied by cations, corresponding to $6(LnX_4) + 12X = Ln_6X_{36}$. The center of the cuboctahedron formed by the 12X anions is occupied by another X, thus making it Ln_6X_{37} . In the fluorite structure, however, six cubes of anions only represent Ln_6X_{32} , 5 anions less than that in a cluster group. Therefore, each unit cell contains $15/5 = 3$ clusters.

Table 6. List of atomic positions for Nd₄Cl₃₃.

Atom	Site	X	Y	Z
Nd(1)*	6(c)	0	0	0.75614(2)
Nd(1')	6(c)	0	0	0.72865(10)
Nd(2)	18(f)	0.09902(2)	0.44864(2)	0.57930(1)
Nd(3)*	18(f)	0.26385(24)	0.21241(26)	0.58792(12)
Nd(3')	18(f)	0.24689(37)	0.19776(40)	0.58061(18)
Cl(1)	6(c)	0	0	0.87855(6)
Cl(2)	18(f)	0.31452(7)	0.43630(7)	0.62907(3)
Cl(3)	18(f)	0.48795(6)	0.39243(6)	0.54437(3)
Cl(4)	18(f)	0.23341(7)	0.18049(7)	0.70356(3)
Cl(5)	18(f)	0.21869(8)	0.33109(9)	0.49998(3)
Cl(6)	18(f)	0.03893(8)	0.18417(9)	0.61225(5)
Cl(7)**	18(f)	0.0495(16)	0.0583(11)	0.4936(6)

* Partial occupancies: 0.812(2) for Nd(1) and 0.188(2) for Nd(1'); 0.591(5) for Nd(3) and 0.409(5) for Nd(3');

** Eitel (44) did not indicate partial occupancy. This position is very close to the special 3(b) site. To be consistent with the formula the occupancy factor should be 0.1667.

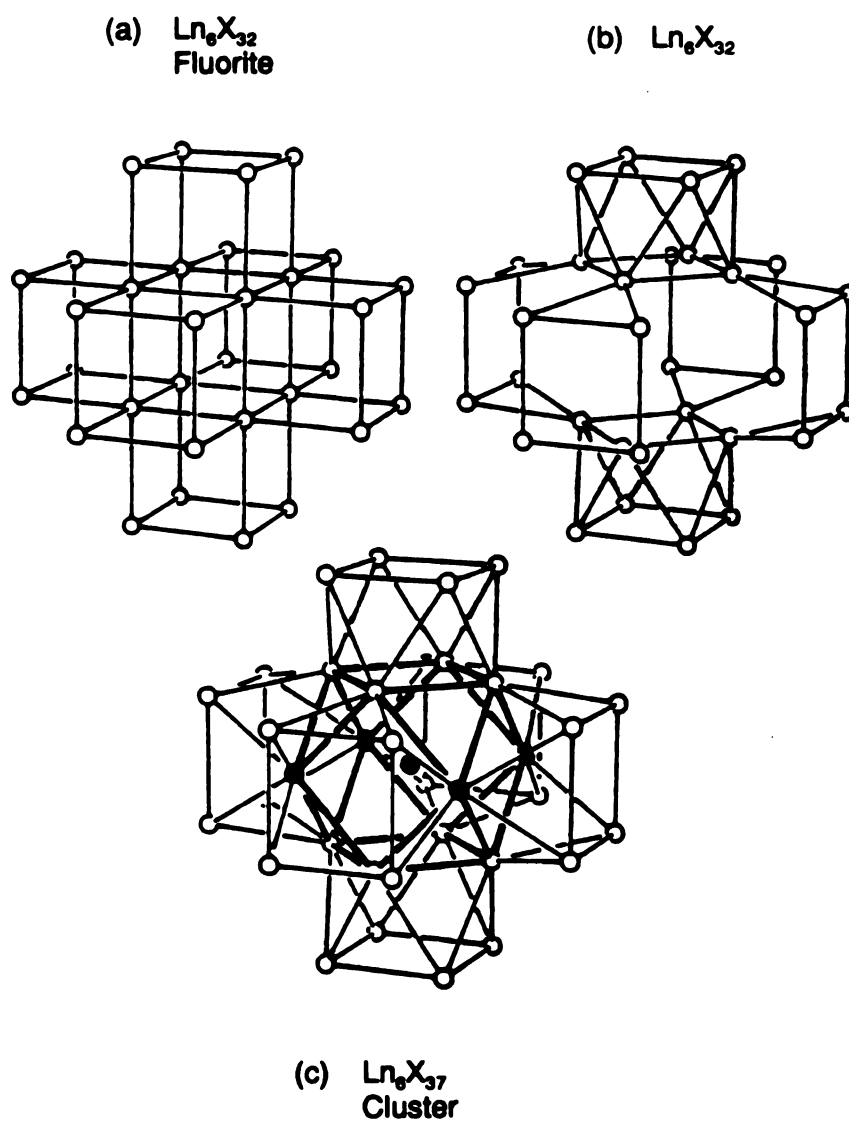
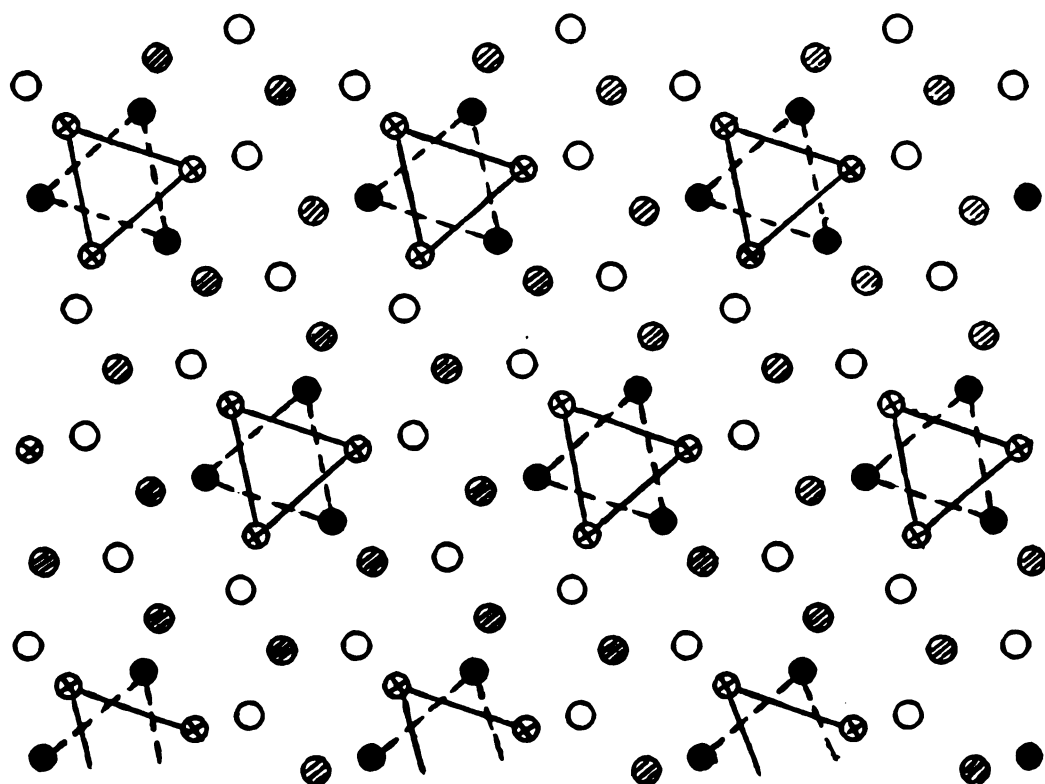


Figure 7. Anion arrangement in Ln_6X_{37} showing the formation of a Ln_6X_{37} cluster. (a) 6 LnX_6 cubes sharing faces in the fluorite structure; (b) rotation of two opposite shared faces forms two square anti-prisms; (c) addition of four "equatorial" anions and a central anion (solid circles) yields a Ln_6X_{37} cluster with an anion cuboctahedron.

Projections down the 3-fold axis can better illustrate the fluorite-related features of this superstructure. A single cation layer of $\text{Ln}_{14}\text{Cl}_{33}$ is shown in Figure 3(d) (Page 21). The hexagonally close packed character is apparent despite minor positional shifts in and out of the layer plane. Due to clustering trivalent cations are ordered along 3-fold axes in each layer. Formation of clusters occurs to two adjacent cation layers as shown in Figure 8. The rhombohedral supercell corresponds to 6-cation layers compared to 3-cation layers in the fluorite structure.

The layer stackings of the cluster-type structure, together with those of the other structure types described above, are illustrated in Figure 9. It should be noted that the cations and anions in Figure 9(a) are not exactly at the designated Z positions and at the same planes as shown. Displacements of 0.02-0.5 Å from the ideal Z positions are calculated. It is interesting to note that the "extra" anions in this superstructure are the main differences between the fluorite- and the cluster-type structures.



⊗ Ln^{3+} at $z=0.083$

● Ln^{2+} at $z=0.083$

● Ln^{3+} at $z=0.25$

○ Ln^{2+} at $z=0.25$

Figure 8. Two adjacent cation layers with Ln_6X_{37} clusters.

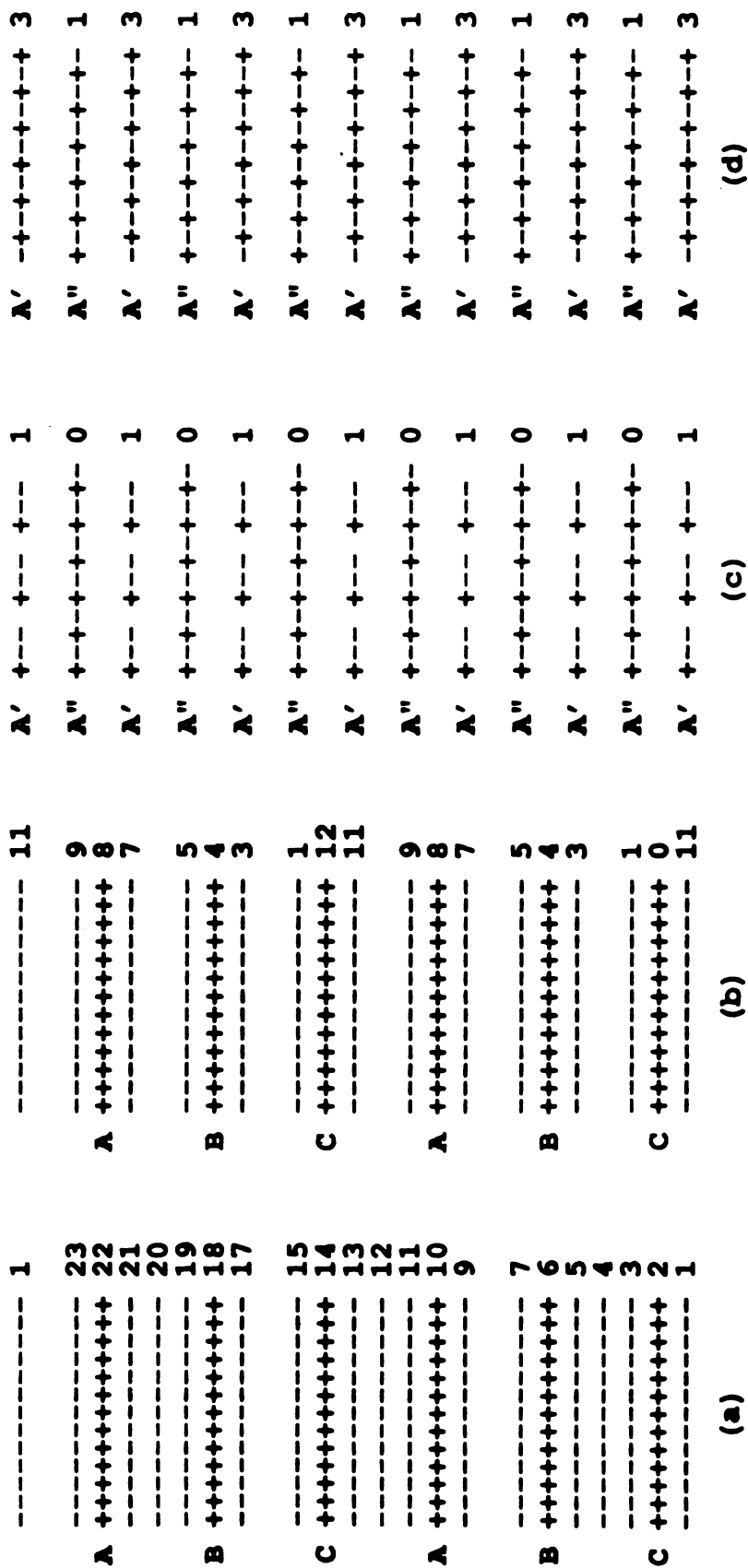


Figure 9. Schematic illustration of layer stackings of various structure types. Numbers adjacent to layers represent Z coordinates. +++: cation layer; ----: anion layer; +---, +---+ or -++-: cations and anions in the same layer. (a) Ln_1X_{33} cluster type. Z coordinates in 24th; (b) fluorite-type in hexagonal setting. Z coordinates in 12th; (c) anti- Fe_2P -type. Z coordinates in 4th. Note that the number of cations in A' layers is half that in A'' layers; (d) PbCl_2 -type. Z coordinates in 4th. The packings of A' and A'' are identical but the stacking order is different. (a), (b) and (d) are centro-symmetric; (c) is not. The anion-anion and the A'-A'' layer spacings for BaCl_2 are: (b) 2.11 Å, (c) 2.308 Å, and (d) 2.366 Å.

2.3 The X-ray Rietveld Refinement Procedure

2.3.1 Introduction

Traditionally, X-ray powder data had been used for many purposes other than structure solutions because the overlapping reflections limit information content. However, there does exist a large number of compounds such as metastable phases obtained by low temperature dehydrations for which it is difficult, if not impossible, to grow single crystals. Introduction of the whole pattern refinement procedure for neutron powder data (48) by Rietveld in 1967 and his detailed description of a computer program (49) in 1969 marked a significant advance in powder crystallography. In this method it is assumed that a powder pattern is the sum of a number of Gaussian-shaped Bragg reflections centered at their respective Bragg angle positions. The intensity counts actually observed are then used as the least-squares data points. In fact, neutron powder diffractometers give peaks that are accurately described by a Gaussian function; thus the information in neutron powder patterns are best used in Rietveld refinements. Since then numerous compounds have been studied by this technique. Cheetham and Taylor had reviewed this subject (50). A more recent review by Albinati and Willis (51) also included the practice of powder X-ray pattern refinement.

The success of the Rietveld method with powder neutron data has stimulated a great interest in applying this technique to powder X-ray data because of the easy availability and relatively low cost of X-ray facilities. The main difficulty in adapting the method for X-rays is determining a function to describe the peak shape. Generally applicable and accurate peak shape functions are not available for X-ray patterns. Furthermore, X-ray data usually contain less information than neutron patterns because of the angular dependence of X-ray scattering factors.

Nonetheless, great progress has been made during the past decade to make it possible to acquire accurate X-ray intensities from powder data. Various ways of extracting intensity information from powder patterns have been reported. These include intensity data from microdensitometer measurements of Guinier-Hägg films (52,53,54,55,56), and of Debye-Scherrer films (57) but more accurate X-ray pattern intensities are obtained by the currently most widely used automated diffractometers (58,59,60).

The Rietveld method is essentially a refinement method. It requires a good model structure. Several methods leading to solutions of unknown structures have been introduced, such as model building (61,62), structural isomorphs (53), isostructural compounds (63,60), new structures (64), and topologically-related structures (65). Probably the most exciting progress for powder X-ray crystallography is the combination of the Rietveld refinement technique and the standard Patterson and Fourier techniques (66,59) or the Direct and Fourier methods used for single crystal structure solutions (67). Such combinations make *ab initio* structure solutions possible and have been used successfully in recent years for some systems. In these methods integrated intensities of unambiguously indexed peaks in the pattern are used. Partially overlapping reflections are deconvoluted by employing an appropriate peak shape function (68).

2.3.2 The Rietveld Refinement XRS-82 System

This system is the 1982 version and was edited by Ch. Bärlocher, A. Hepp and L. B. McCusker at Institut für Kristallographie und Petrographie, ETH, Zurich, Switzerland. It was used in this work for refinement of the metastable structure of SrI_2 ($\text{SrI}_2\text{-IV}$) and is described here.

a. **Peak Shape Function**

As pointed out earlier, the principal problem one encounters in applying the Rietveld method to X-ray data is the difficulty in describing the peak shape. As many as seven peak shape functions have been provided in a recent version of the program DBW3.2S. The various profile shape functions have been reviewed by Young and Wiles (69). In the XRS-82 system, however, no analytic function is used. Instead, a single non-overlapping observed peak (standard peak) is selected and analyzed numerically to calculate a peak-profile function ("learned" peak-shape function). The intensity distribution function for an individual peak derived by Hepp and Bärlocher (70) has the form

$$G = \frac{1}{H} G_s(r) [1 - A \cdot G_a(r)]$$

where H is the half width at half height and A the asymmetry parameter. The $G_s(r)$ and $G_a(r)$ are normalized functions representing the symmetric and asymmetric parts of the "learned" peak-shape function, $r = \Delta 2\theta / H = (2\theta - 2\theta_0) / H$ (θ_0 is the Bragg angle). The lower and upper 2θ cutoffs for the standard peak are supplied by the user according to the observed data. These parameters are evaluated from this peak and then the peak shape function generated. This procedure gives an accurate description of the observed peak shape. The dependence of H and A on 2θ is then determined from the entire powder pattern. The XRS-82 system allows more than one peak function.

b. **Peak Profile Parameters**

In the XRS-82 system, these parameters are refined according to the following equations:

$$WD_{cor} = WD_{est} \{ (WD1) + (WD2) \cdot (2\theta) \}$$

$$PA_{\text{cor}} = PA_{\text{est}} \{ (PA1) + (PA2) \cdot (2\theta) \}$$

where (WD1), (WD2), (PA1), (PA2) are variables and WD_{est} and PA_{est} are the estimated peak width (full width at half maximum or FWHM) and peak asymmetry from the standard peak, respectively. Note $PA = A$, and $WD = 2H$ in the Hepp-Bärlocher equation.

c. Least Squares Parameters

The parameters in Rietveld refinement are usually divided into two groups: (1) the profile parameters that define the lattice dimensions, peak half-widths and asymmetries, and preferred orientation; (2) the structure parameters that define the contents of the asymmetric unit cell. In the XRS-82 system, the following parameters are included:

Profile Parameters

Cell parameters: A, B, C, α , β , γ ,

PA1, PA2: peak asymmetry as defined previously;

WD1, WD2: peak half width at full maxima as defined previously;

ZC1, ZC2: 2θ zero correction. $2\theta_{\text{cor}} = 2\theta_{\text{obs}} + (ZC1) + (ZC2) \cdot (2\theta)$;

POF: preferred orientation factor according to $I_{\text{cor}} = I_{\text{obs}} \exp[-(POF)\cos 2\alpha]$ where α is the angle between the scattering vector $h\ k\ l$ and the preferred orientation vector (U V W) (normal of plate-like crystallites).

Structure Parameters

SCL: scale factor (c) defined such that $F_c = F_{\text{relative}}/c$;

UOV: overall isotropic temperature factor defined as the temperature factor correction $T_{\theta} = \exp[-8\pi^2(UOV)(\sin\theta/\lambda)^2]$;

X, Y, Z: fractional coordinates of an atom in the asymmetric unit cell;

PP: population parameter, the fractional occupancy of an atomic site.
Independent of site multiplicity;

U: individual isotropic temperature factor, similar to UOV;

U_{11} , U_{22} , U_{33} , U_{12} , U_{13} , U_{23} : individual anisotropic temperature factors defined as

$$T_{hkl} = \exp[-(h^2\beta_{11} + k^2\beta_{22} + l^2\beta_{33} + 2hk\beta_{12} + 2hl\beta_{13} + 2kl\beta_{23})], \text{ where}$$

$$\beta_i = 2\pi^2 U_i a_i^* a_i^*, \text{ and } a^* \text{ is a reciprocal axis length.}$$

It is possible to use mixed temperature factors in the XRS-82 system.

d. The Least Squares Refinement

The quantity minimized in Rietveld refinement is:

$$M = \sum w_i [Y_i(o) - Y_i(c)/c]^2$$

where $Y_i(o)$ is the observed background-corrected count rate at the i th step of 2θ , and $Y_i(c)$ the calculated count rate including contributions from all Bragg reflections that overlap at the i th step, c is the scale factor, and w_i the weight. The weight to be applied during refinement may be specified in one of four different ways as a user option:

- 1) unit weight (all weights as 1.0);
- 2) weights are accepted as supplied in the binary profile data file;
- 3) weights as supplied in the binary profile file are squared;
- 4) weights are set equal to the reciprocal of $\sigma(Y_{obs})$ and used as Y_{obs} weights.

The program CRYLSP performs the least squares refinement. It is specially structured to accommodate a whole pattern refinement using the numerical peak-shape function of a powder pattern as mentioned above. It also allows the user to employ known interatomic distances and angles as soft restrictions. Two least squares procedures are available: the Gaussian Algorithm and the Variable Metric Algorithm. Dr.

Wieslaw Lasocha stated that his experience indicated that the Gaussian algorithm is more stable than the latter. The original authors suggest the variable metric algorithm is less sensitive toward high correlations.

e. **Goodness of Fit**

The whole pattern plot that includes the observed, calculated and difference patterns is a very informative way of describing the goodness of fit. These plots can reveal discrepancies due to systematic errors such as the systematically lower counts at low angle region in our observed pattern (Figure 12, Page 90), or due to poor peak shape functions or impurity peaks. The difference-Fourier map which can be generated by programs FOURR and PEKPIK is another good way of checking goodness of fit. This map should be relatively flat since random errors typically produce small fluctuations. In addition, bond lengths and angles that can be calculated by program BONDLA in the system can provide more information about the correctness of models and the refined structures.

In the XRS-82 system, four R-values are used to give quantitative descriptions of the refinement. They are discussed briefly here.

Structure Factor R_f

$$R_f = \sum |F_i(o) - F_i(c)| / \sum F_i(o)$$

where $F_i(o)$ and $F_i(c)$ are the observed and scaled calculated structure factors for the i th reflection, respectively. This R_f corresponds to the conventional reliability factor commonly used in single crystal refinements. It measures the agreement between the observed and calculated structure factors.

Integrated Intensity R_i or Bragg Intensity R_b

$$R_i = \Sigma(|I_o - I_c|) / \Sigma I_o = \Sigma|(m_i \cdot F_i(o)^2 - F_i(c)^2)| / \Sigma m_i \cdot F_i(o)^2$$

where m_i is the i th reflection multiplicity and I the integrated intensity. Note $I = m \cdot F^2$.

In a Rietveld refinement both R_i and R_p (or R_w) are biased towards the model because $F(o)$ and I_o are evaluated in proportion to the calculated structure factors.

Profile (or Pattern) R_p

$$R_p = \{\Sigma[Y_i(o) - Y_i(c)/c]^2 / \Sigma Y_i(o)^2\}^{1/2}$$

Weighted Profile R_w

$$R_w = \{\Sigma w_i [Y_i(o) - Y_i(c)/c]^2 / \Sigma w_i \cdot Y_i(o)^2\}^{1/2}$$

These two profile R values indicate how close a calculated profile is to the observed one. From the view point of profile fitting they are more meaningful than R_i and R_p . R_w is the most significant factor since its numerator is the quantity actually minimized.

CHAPTER 3 EXPERIMENTAL

SYNOPSIS

This chapter is divided into two sections. In the first section the synthesis procedure is described as three steps: (1) synthesis of anhydrous individual halides; (2) synthesis of mixed or mixed-valent halide and hydrate precursors; (3) decomposition of precursors at low temperatures. Mixed(-valent) halides $\text{MX}_2\text{-LnX}_3$ were prepared by various methods including partial reduction with hydrogen, thermal decomposition, the ceramic method, and the molten salt method. In the second section X-ray data processing including data collection and the X-ray Rietveld refinement procedure are described.

3.1 Synthesis Procedures

List of Important Chemical Reagents

La_2O_3 : 99.9%, Research Chemicals, Phoenix, AZ;

Nd_2O_3 , Eu_2O_3 and Yb_2O_3 : 99.99%, Research Chemicals;

Sm_2O_3 : 99.9%, Alfa Inorganics, Inc., Beverly, MA;

Gd_2O_3 : 99.9%, Michigan Chemical Corp.,

BaCl_2 : 99.9%, Cerac/Pure, Inc. Milwaukee;

BaBr_2 : synthesized from BaO and NH_4Br ;

$\text{Sr}(\text{OH})_2 \cdot 8\text{H}_2\text{O}$: Baker's Analyzed, J. T. Baker Chemical Co., Phillipsburg, N. J.;

$\text{BaCl}_2 \cdot 2\text{H}_2\text{O}$: Analytic Reagent, Mallinckrodt Chemical Works;

$\text{BaBr}_2 \cdot 2\text{H}_2\text{O}$: Prepurified, Fisher Scientific Company, Fair Lawn, N. J.;

$\text{BaI}_2 \cdot 2\text{H}_2\text{O}$: Prepurified, Fisher Scientific Company;

Sm chips: distilled, 99.9%, Research Chemicals, Phoenix, AZ;

HgI_2 : Mallinckrodt chemical works, distilled;

NH_4Cl : Certified A.C.S. grade, Fisher Scientific Company;

NH_4Br : Baker's Analyzed reagent;

NH_4I : Analytic Reagent, Mallinckrodt Chemical Works;

THF: Baker's Analyzed reagent, purified;

Pyridine: Analytic Reagent, Mallinckrodt Chemical Works, purified;

$\text{H}_2(\text{g})$: Matheson prepurified, >99.999%.

Sample Handling

Due to the moisture sensitivity of the lanthanide halides and some alkaline earth halides, their handling was performed in a glove box continuously purged of both water by 4A molecular sieves (typical moisture content was 3-30 PPMv) and oxygen by heated BASF catalyst (2000-3000 PPMv).

Elemental Analysis

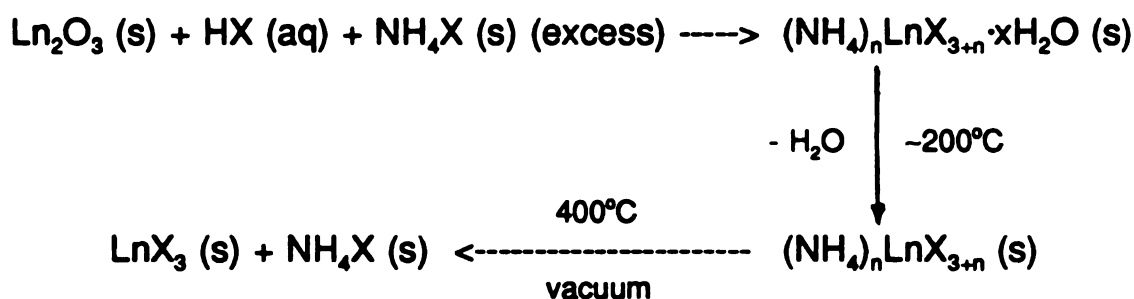
Halide ion contents were determined by titration with NaCl standardized AgNO_3 . 5% K_2CrO_4 solution served as the indicator; Ba^{2+} content was determined gravimetrically by precipitation as BaSO_4 .

Thermal Test for Metastability

To understand the formation mechanism and thermal stabilities of the new structure forms prepared by low-temperature solvolytic decompositions and low-temperature dehydrations, specimens were heated in a high vacuum (10^{-5} - 10^{-6} Torr) at various temperatures and then examined by X-ray powder diffraction for polymorphic transformations.

3.1.1 Synthesis of Individual Halides

LnX_3 ($\text{X}=\text{Cl}, \text{Br}, \text{I}$) One of the principal difficulties encountered in preparing moisture-sensitive anhydrous halides is preventing the formation of oxidehalide impurities. The ammonium halide procedure (10,11,13) is very effective in eliminating oxidehalide impurity and has been used throughout this work. The general procedure is shown schematically below.



NH_4X was removed by sublimation to the cool end of the tube. The part of the tube which contained anhydrous LnX_3 was sealed with a hand-held torch.

EuCl_2 synthesized by hydrogen reduction of EuCl_3 at $500\text{--}600^\circ\text{C}$. For a ~ 1 g sample reduction required ~ 6 h. Samples were placed in pyrolytic graphite boats and transferred between the reaction quartz tube and the glove box under argon. Hydrogen gas first flowed over a Pd catalyst and then through a liquid-nitrogen-chilled trap before being passed over the sample. Heating was effected in tubular furnaces.

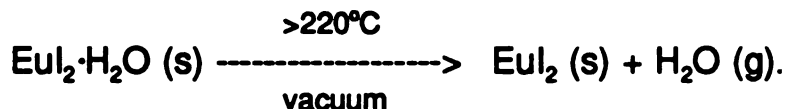
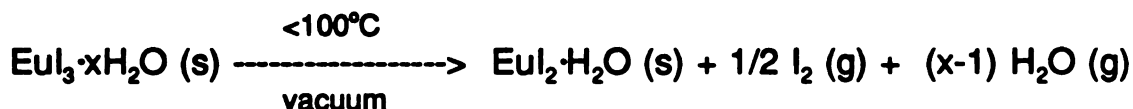
SmCl_2 prepared by hydrogen reduction at $700\text{--}750^\circ\text{C}$.

YbCl_2 The hydrogen reduction product contained a small amount of YbOCl . Pure YbCl_2

was prepared by induction heating of a 2:1 YbCl₃ : Yb mixture in a weld-sealed tantalum tube at 900-1000°C for 10 h. A 1-2 g sample was prepared each time.

SmI₂ prepared by the mercury iodide procedure (71). A stoichiometric mixture of Sm and HgI₂ was sealed into a quartz tube under a 10⁻⁵-10⁻⁶ Torr pressure, heated at 300°C for 1 day, then at 500°C for 2 days.

EuI₂ a direct product of the ammonium halide procedure. Unlike the ammonium halide procedure for other lanthanides where intermediate mixed halides such as (NH₄)₃LnX₆ form, a mixture of Eu₂O₃, HI, and NH₄I was observed to transform to EuI₂·H₂O and NH₄I below 220°C at which temperature NH₄I sublimed out gradually. The reaction is presumed to proceed as follows:



Iodine released in this reaction was condensed in a liquid nitrogen trap. The preparation of EuI₂ by the ammonium iodide procedure is apparently a simple dehydration of EuI₂·H₂O. Thus EuI₂ was also prepared using EuI₃·xH₂O (Eu₂O₃ dissolved in HI and the solution evaporated to dryness) as the reactant.

3.1.2 Synthesis of Precursors (27,72,73)

Ba₁₇La₁₀Cl₆₄ prepared by the ceramic method. ~1 g of an intimately ground mixture of BaCl₂ and LaCl₃ in a 2:1 molar ratio was sealed into a quartz tube under vacuum, heated at 800°C for 5 days, and then quenched.

Ba₁₇Ln₁₀Cl₆₄ (Ln=La, Sm) prepared by the molten salt method. ~1 g of a ground mixture of 40-50% BaCl₂ and LnCl₃ was confined in a pyrolytic graphite boat, heated at ~750°C (molten) for ~0.5-1 h, cooled slowly to 500°C, then quenched. The products contained excess LnCl₃. Note that the formula of the precursors was deduced from crystallographic data as will be discussed in Chapter 4.

Single crystals of Ba₁₇Sm₁₀Cl₆₄ were grown from a 1:1 molar ratio BaCl₂-SmCl₃ melt in a vacuum-sealed quartz tube by melting the mixture (~750°C), cooling it to 500°C at the rate of 3°C/h, and then to room temperature at 10°C/h. The fused salt was crushed with an agate mortar and a pestle in the glove box, then extracted by THF for ~1 h. The crystals were slightly yellowish. They were dispersed in sodium-dried paraffin oil for microscopic examinations. Appropriate specimens were paper-dried and sealed into capillaries.

Ba₉Ln₃Br₃₃ (Ln=La, Nd) prepared by the molten salt method. ~1 g of a ground mixture of 40-50% BaBr₂ and LnBr₃ was treated in the same way as those for the chlorides, but in an argon atmosphere and at 700°C. The products contained excess LnBr₃.

EuCl_x (2<x<3) prepared by partial reduction with hydrogen. ~1 g EuCl₃ was placed in a graphite boat, heated in flowing H₂ at 450-465°C. The sample turned to pale blue

slowly. Reduction was stopped after 3~4 h and the product cooled slowly. It was identified by powder X-ray diffraction as a mixture of two mixed-valence chlorides (35), the vernier type $\text{Eu}_5\text{Cl}_{11}$ (major phase), and the cluster type $\text{Eu}_4\text{Cl}_{33}$ (minor phase) with traces of EuOCl and an unidentified impurity phase. Even though at these temperatures EuCl_3 will be reduced to EuCl_2 eventually, no trace of EuCl_2 was detected by X-ray diffraction. The reaction proceeded slowly enough to prevent complete reduction below 465°C in such a short period of time.

Eu_4Cl_9 prepared by the ceramic method. An intimately ground mixture of EuCl_2 and EuCl_3 in 3:1 molar ratio was sealed into an outgassed quartz tube under vacuum and heated at 500°C for 5 d, then quenched. The X-ray diffraction pattern of this blue powder confirmed the product to be Eu_4Cl_9 .

$\text{Eu}_5\text{Cl}_{11}$ prepared by thermal decomposition or hydrogen reduction. 0.5-1 g of EuCl_3 was heated at 500°C for 5 h in a vacuum of 0.1 to 0.01 Torr; a blue product resulted. The same product was also obtained by reducing EuCl_3 with H_2 at 400°C for 2 d.

$\text{Eu}_4\text{Cl}_{33}$ prepared by thermal decomposition or solid state reaction. Thermal decomposition of EuCl_3 (0.5-1 g sample) in vacuum at 440°C for 12 h yielded a black powder identified as the title compound by X-ray diffraction. The same compound was also obtained when a 3:2 mixture of EuCl_2 and EuCl_3 sealed in quartz under vacuum was heated at 500°C for 5 d and quenched.

$\text{Sm}_{14}\text{Cl}_{33}$ prepared by partial reduction with hydrogen. Slow reduction of 1-2 g SmCl_3 at 650°C for 3 h followed by *in situ* heating to 750°C in flowing H_2 produced a melt which

with subsequent slow cooling in the oven yielded a black rock-like material. The dark brown pulverized material consisted of a mixed-valence phase and unreacted SmCl_3 . This mixed valence compound is the same as that originally formulated as Sm_3Cl_7 (74), but by analogy with $\text{Eu}_{14}\text{Cl}_{33}$ (also originally formulated as Eu_3Cl_7) is formulated as $\text{Sm}_{14}\text{Cl}_{33}$.

$\text{Sm}_9\text{Gd}_5\text{Cl}_{33}$ Reduction of a 1:1 molar ratio mixture of SmCl_3 and the irreducible GdCl_3 at 660°C , above the melting point of GdCl_3 (602°C), for 4-12 h followed by slow cooling produced a black product. It was dark brown after being pulverized. The product was a mixture of $\text{Sm}_9\text{Gd}_5\text{Cl}_{33}$ and GdCl_3 .

$\text{Sm}_9\text{Nd}_5\text{Cl}_{33}$ A mixture of SmCl_3 and NdCl_3 in 9:5 molar ratio was reduced in hydrogen at 660°C for 7 h. The temperature was increased to 850°C to produce a melt, after which it was lowered slowly. Weight loss data suggested complete reduction of the Sm^{3+} ion. The product had a diffraction pattern similar to that of $\text{Sm}_{14}\text{Cl}_{33}$ and was given the title formula.

$\text{SrI}_2 \cdot x\text{H}_2\text{O}$ ($x > 2$) It was crystallized from an aqueous solution of $\text{Sr}(\text{OH})_2 \cdot 8\text{H}_2\text{O}$ neutralized with HI acid.

$\text{EuI}_2 \cdot \text{H}_2\text{O}$ Eu_2O_3 was dissolved in excess hydroiodic acid. The aqueous solution was carefully evaporated to dryness. The obtained yellow powder ($\text{EuI}_2 \cdot x\text{H}_2\text{O}$) was confined in a Pyrex tube connected to the vacuum system and heated slowly at $80\text{--}100^\circ\text{C}$ in a 0.1-0.01 Torr vacuum or at 60°C in a $10^{-5}\text{--}10^{-6}$ Torr vacuum for 4 h. Only the monohydrate was obtained. $\text{EuI}_2 \cdot x\text{H}_2\text{O}$ with $x > 1$ can also be prepared by the hydration procedure described below.

$\text{SmI}_2 \cdot x\text{H}_2\text{O}$ prepared by hydration of **SmI_2** . 0.5-2 g **SmI_2** powder confined in a round bottle was placed in an evacuable glass tube fitted with a stopcock so that samples could be transferred into the glove box for handling. A sufficient amount of **$\text{NiCl}_2 \cdot 6\text{H}_2\text{O}$** powder was confined in another tube. The two tubes were connected through glass ground joints. The system was evacuated, flushed with argon for 3 times, and reevacuated. Hydration took place by water vapor transport from **$\text{NiCl}_2 \cdot 6\text{H}_2\text{O}$** to **$\text{SmI}_2$** . The degree of hydration can be monitored both by the color change of the iodide from deep green to reddish brown and by the weight gain of the sample. For a 0.5 g sample 5-6 h was sufficient to ensure complete hydration ($x > 1$). Over hydration should be avoided since samarium iodide tends to form an aqueous solution and decompose.

3.1.3 Decomposition of Precursors

a. Solvolytic Decomposition (Leaching)

Solvent Purification

Tetrahydrofuran (THF) was refluxed over sodium metal chips (benzophenone as indicator) and distilled prior to use. For the lanthanide (II) halide experiments, it was also deoxygenated repeatedly by first freezing with liquid nitrogen, pumping to 10^{-5} Torr, and then warming to room temperature. Pyridine was refluxed with KOH pellets and distilled prior to use.

Extraction

Solvolytic decompositions were carried out in a modified Soxhlet extractor fitted with Teflon stopcocks and joint sleeves. A powdered sample was placed in the removable

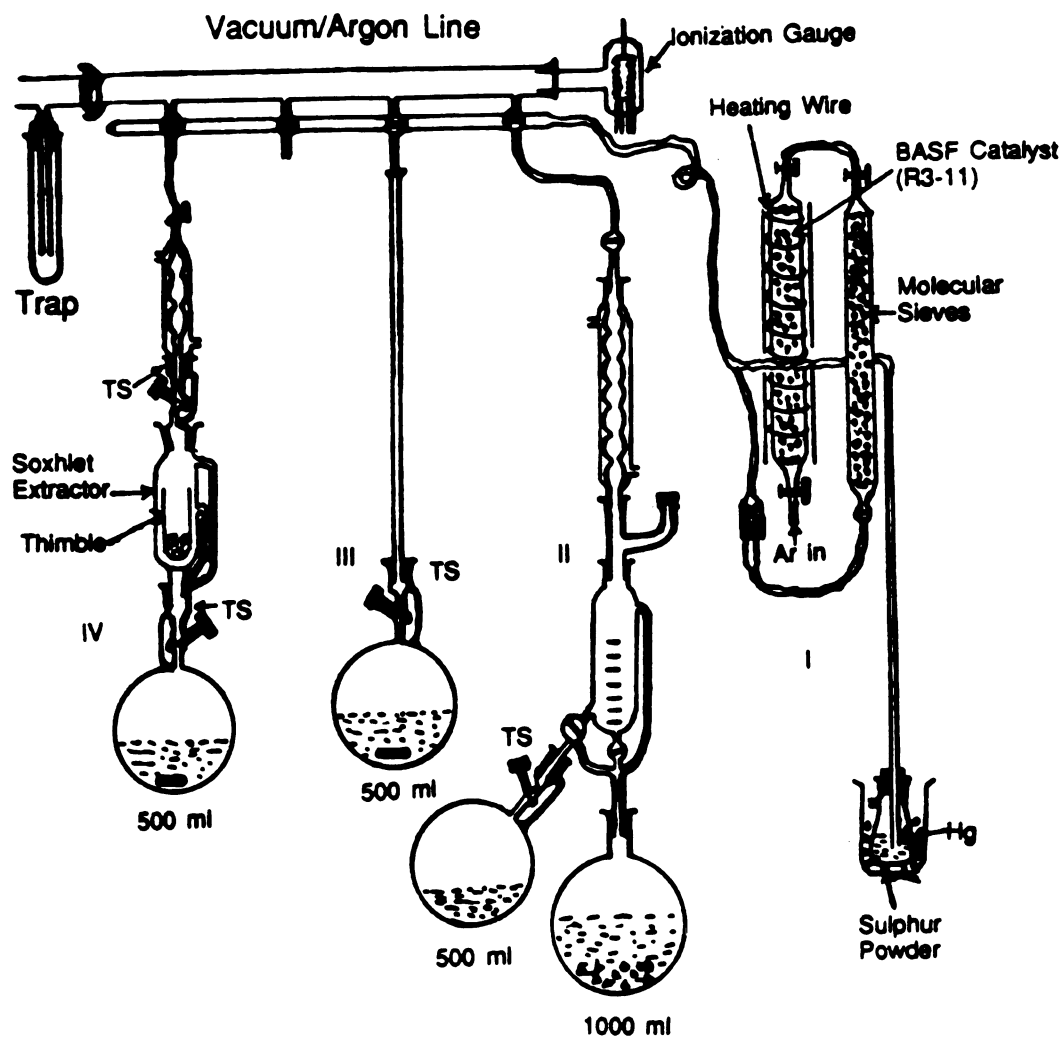
extraction thimble and closed into the extractor under argon. Then the extractor was transferred from the glove box to the extraction apparatus. Extraction was effected in a dry argon atmosphere. The time needed depends on the sample used as will be discussed individually later. When reaction was complete, the leached product was evacuated for 1-3 h, blanketed with argon, and transferred into the glove box for further treatment and analysis.

The solvolytic decomposition and related apparatuses are illustrated schematically in Figure 10.

b. Dehydration

Samples for dehydration were confined in a glass container which was then placed in a quartz tube with a stopcock and a ground joint connecting to the vacuum/argon line. This tube can be transferred into the glove box for moisture sensitive samples, especially dehydrated, fine powders. Heating was effected in a tubular furnace or an oil bath whose temperature was controlled carefully.

Hydrates with more than one mole hydration were kept under a dynamic vacuum at room temperature or heated mildly (below 80°C) overnight. The resulting monohydrates were then dehydrated in a 10^{-5} to 10^{-7} Torr vacuum in the temperature range of 110-125°C for 24 h. Water loss was checked by both weight change and X-ray diffraction.



- I. Argon purification
 - II. Solvent dehydration
 - III. Solvent deoxygenation
 - IV. Extraction
- TS: Teflon Stopcock

Figure 10. Apparatuses for the solvolytic decomposition experiment.

3.2 Instrumentation and Data Processing

3.2.1 Powder X-ray Diffraction Examinations

Due to the moisture sensitivity of most halides we encountered, X-ray diffraction examinations were carried out in an evacuable Guinier-Hägg camera (diameter 114.6mm). Quartz monochromatized Cu K α radiation ($\lambda = 1.54050 \text{ \AA}$) was used with NBS certified silicon powder ($a_0 = 5.43082(3) \text{ \AA}$) as the internal standard. Samples placed on Scotch^R Tape-backed planchets were coated with paraffin oil maintained over sodium chips to protect them from hydrolysis during transfer to the camera.

3.2.2 Automated Powder X-ray Data Collection

X-ray Intensity data suitable for Rietveld refinement were collected with a Philips APD 3720 diffractometer system equipped with a sample spinner and Θ -compensating slit. The extremely moisture-sensitive strontium iodide specimen was gently mixed with "dry" ApiezonTM N grease and spread with a knife onto a Pyrex disk. The diffractometer sample chamber was flushed continuously with nitrogen gas vaporized from liquid N₂.

3.2.3 Data Processing

a. Indexing and Lattice Parameter Refinement

Identification of compounds of known structure types and lattice parameters can be made by comparing the observed patterns with the JCPDS powder files or with calculated patterns (below). Powder patterns of unknown structures were indexed by programs ITO12 (75) and/or TREOR (76). ITO12 requires at least 20 observed reflections and TREOR can work with fewer than 20 reflections as long as the number is

specified by the key word "USE". In general TREOR is better for high symmetry systems and ITO12 for low symmetry systems. Program APPLEMAN (77) was used to perform lattice parameter refinement.

b. Systematic Extinctions and Space Groups

Given a crystal system and lattice parameters, program APPLEMAN lists every possible reflection. Systematic extinctions and subsequently possible space groups were deduced by comparing the observed pattern to that listed by APPLEMAN.

c. Calculated Intensities

Given a correctly-indexed lattice, the chemical formula, and a proper structural model, program POWCOM (78) is used to calculate the theoretical reflection intensities to check the validity of the model structure.

3.2.4 Rietveld Refinement of the SrI_2 -IV Structure

a. Structure Solution

62 interplanar d -spacings were indexed by the program TREOR to an orthorhombic unit cell with figures-of-merit (79,80) $M(20)=19$, $F20=28$; and $M(62)=8$, $F62=14$. Possible space groups determined from systematic extinctions were Pnma (# 62) and $\text{Pn2}_1\text{a}$ (# 33). Both a manual search in the CRYSTAL DATA Determinative Tables effected with lattice parameter ratios and a computer search of the Canadian CRYSTDAT database failed to identify any likely isostructural AB_2 -type compound. Attempts to reduce the observed lattice parameters to those of a known orthorhombic form of SrI_2 and EuI_2 (81,82,83,84) were also unsuccessful. The axial ratios of this new SrI_2 structure

appeared atypical when compared to those of other AB_2 -type compounds, suggestive that this compound may represent a new structure type. It is designated SrI_2 -IV type according to Beck's nomenclature notation (84).

Being interested in the topotactic behavior of low-temperature dehydrations, we also examined the structure of the precursor, $SrI_2 \cdot H_2O$. When a comparison was made between the new phase and $SrI_2 \cdot H_2O$ (85), we noticed an unusual similarity in their lattices. The lattice parameters of SrI_2 -IV derived from the Guinier data, $a = 12.365(2)$, $b = 4.9338(8)$, and $c = 8.408(1)$ Å, were close to those of the well-characterized monohydrate, $a = 12.474(2)$, $b = 4.495(1)$, and $c = 9.741(2)$ Å. Furthermore, both structures even could be assigned to the same space group. These results suggested related atomic arrangements. This was not obvious in their powder patterns, apparently because of their different unit cell dimensions. However, the observed SrI_2 -IV X-ray powder diffraction intensities agreed reasonably well with those calculated with the Sr and I positional and thermal parameters of $SrI_2 \cdot H_2O$. Thus the monohydrate structure devoid of H_2O provided a model for the refinement.

b. Data Reduction

The raw data collected by the diffractometer were stripped of the $Cu K\alpha_2$ component with the APD software (86). All subsequent calculations were effected on a MICROVAX II computer with the program XRS82 (87). Background and the broad absorption band, which spanned $\approx 15 < 2\theta < \approx 26^\circ$ and was caused by the protecting grease, were removed by using the BGVALU command and editing the coded data file manually. Possible systematic 2θ errors due to slight misalignment and displacement of the sample surface from the θ -shaft axis were corrected at the profile refinement level. Observed intensities were multiplied by $(\sin\theta)^{-1}$ to correct for the θ -compensating slit (60).

Lorentz and polarization corrections were applied with the routine STEPCO. Polynomial scattering factors were used with the real and imaginary dispersion correction terms (88). The 2θ -limits of the standard peak were modified until the R-value indicated that an acceptable description ($R < 5\%$) had been achieved. The observed, calculated and the difference profiles of the standard peak are plotted in Figure 11.

c. Refinement

Refinement began with the scale factor; after 3 cycles R_i had decreased to 0.227. Cell parameters were refined next, followed in alternate cycles by scale, profile and the 2θ correction parameters. Unit weights and heavily damped (0.8) structural and profile factors were employed during the entire refinement process. The refinement converged quickly when positional parameters were allowed to vary with an overall temperature factor. Preferred orientation variables and individual isotropic temperature factors were introduced after positional parameter shifts ceased. When refinement under isotropic conditions was complete ($R_i = 0.071$), temperature factors were made anisotropic. That for Sr became non-positive, definite; it was converted isotropic and refinement continued to convergence. The final R_i was 0.069. In the final cycles lattice parameters were not refined.

A difference Fourier after refinement was complete indicated a residual electron density of $\sim 2 \text{ e}\text{\AA}^{-3}$ at 0.63, 0.25, 0.09, and a lesser value close to the I(1) and I(2) sites. A background level of $\sim 1 \text{ e}\text{\AA}^{-3}$ was present at numerous sites. Since the analytical data suggested the presence of up to 1.5 % oxygen, several attempts were made to reduce this residual electron density by introducing trace amounts of oxygen. However, when oxygen atoms were introduced, refinement would not converge. When refinement was effected with the I(1) and I(2) site occupancy set to unity and that of Sr variable, the Sr

occupancy parameter refined to ≈ 1.4 with $R = 0.085$. When the Sr occupancy parameter was set to unity, those of $I(1)$ and $I(2)$ refined to 0.80(4) and 0.78(5), respectively, with $R = 0.065$. Therefore, no further improvement could be made.

It is worth noting that a preferred orientation effect was not observed even though the sample has a thin-plate structure. The ApiezonTM grease thus not only served as an effective protectant during 21 hr of data collection, but also provided a paste in which the randomly oriented crystallites could not stack. However, a potential problem with the grease - X-ray beam absorption - could be a source of error.

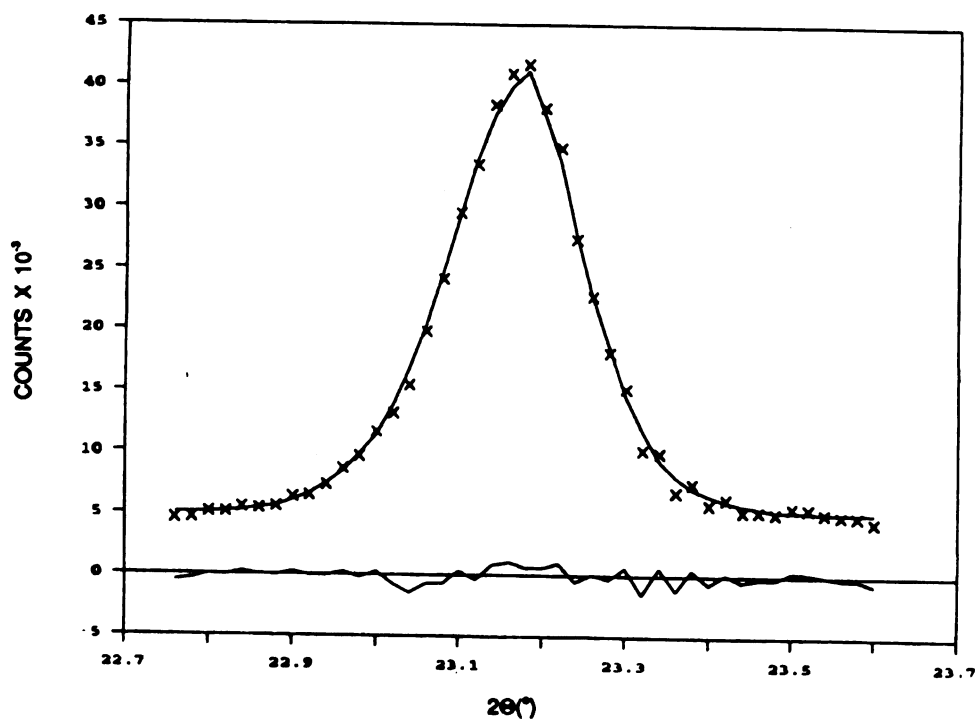


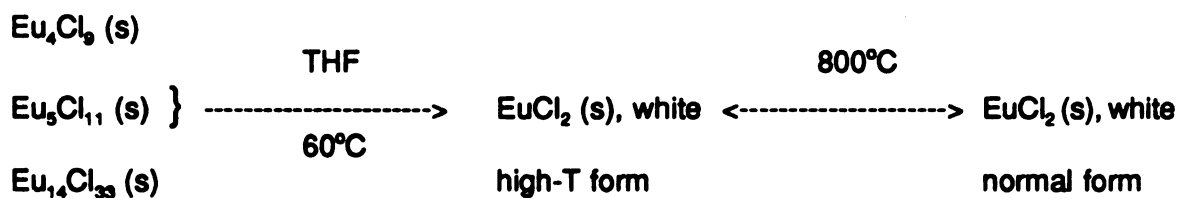
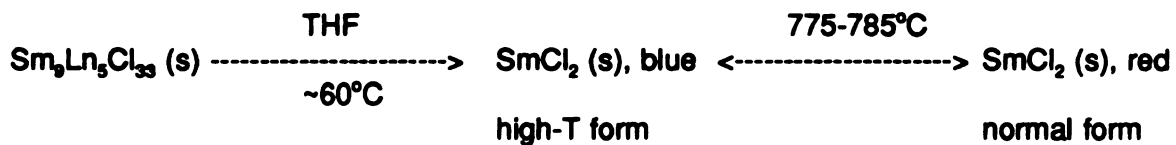
Figure 11. Standard peak for $\text{SrI}_2\text{-IV}$. Top: observed (xx) and calculated (—) profiles (5000 counts offset); bottom: difference (Obsd. - Calc.) profile.

CHAPTER 4 RESULTS

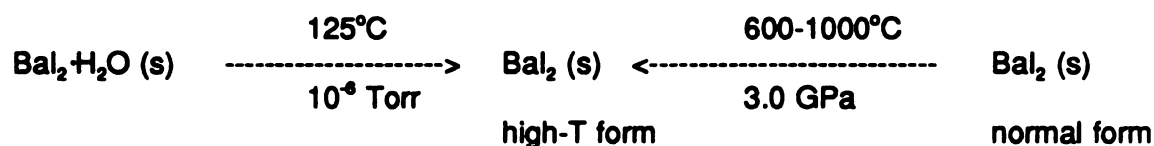
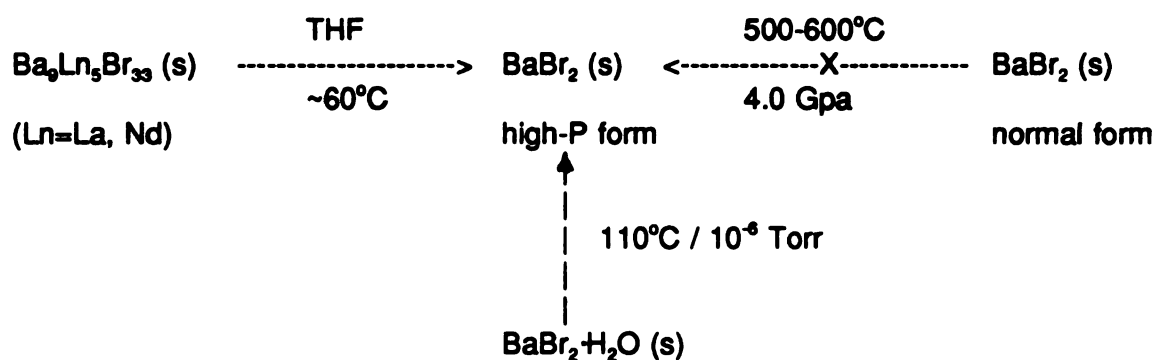
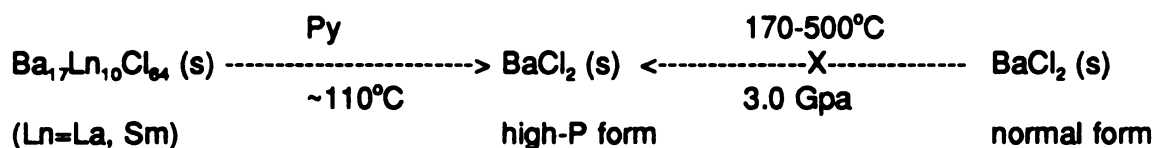
SYNOPSIS

Three types of metastable forms of dihalides were prepared at low temperatures.

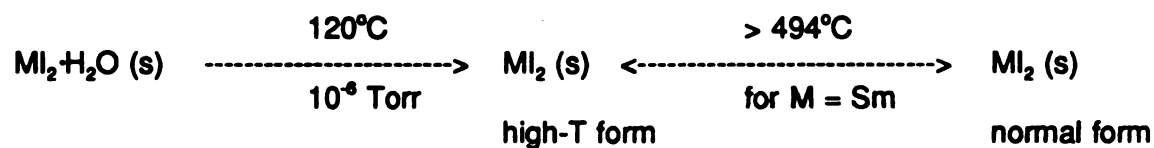
1. Fluorite-type LnCl_2 ($\text{Ln}=\text{Sm}, \text{Eu}$), which were observed previously only at elevated temperatures and are not quenchable, have been prepared by solvolytic decompositions of mixed-valent chlorides.



2. Metastable high-pressure-like forms of BaX_2 ($\text{X}=\text{Cl}, \text{Br}$) with the anti- Fe_2P -type structure, which could not be prepared under high pressures, have been prepared at low temperatures and under normal pressure by solvolytic decompositions of mixed halides and by dehydrations.



3. High temperature forms of MI_2 ($\text{M}=\text{Sr, Sm, Eu}$) which have been observed previously only at high temperatures and are not quenchable have been prepared by low temperature high vacuum dehydrations. This new structure (SrI_2 -IV-type) has been refined by the X-ray Rietveld procedure with $\text{SrI}_2\cdot\text{H}_2\text{O}$ devoid of H_2O as the model structure.



4.1 Precursors and Structures

EuCl_x (2.0 < x < 3.0)

The structures of the phases prepared had been well characterized as described in Chapter 2. The various synthesis procedures are summarized briefly by the following equations. Lattice parameters are summarized in Table 3 (Page 15). Miller indices, observed and calculated d-spacings and intensities of scattered peaks for the three precursors are listed in Tables 7-9.

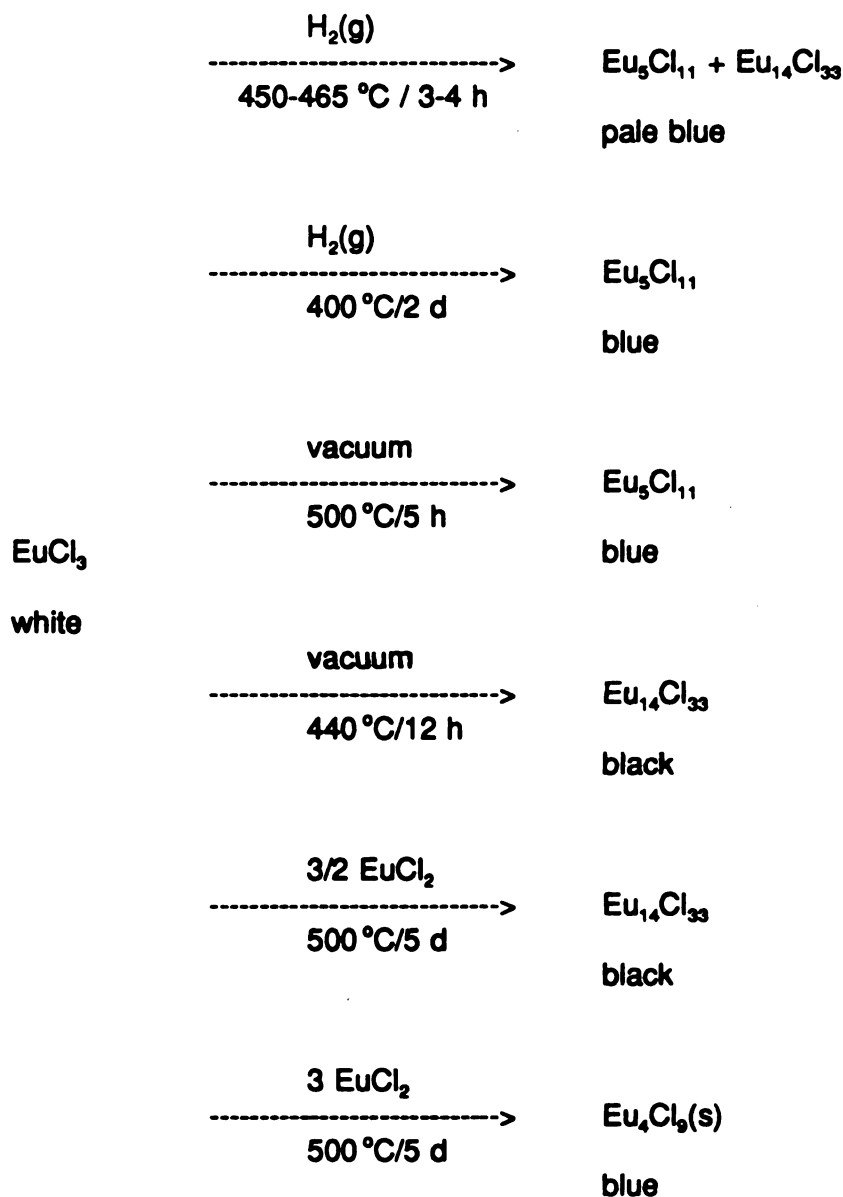


Table 7. Miller indices, and observed and calculated interplanar d-spacings and intensities for Eu_4Cl_9 . *

h	k	l	$d_c(\text{\AA})$	$d_o(\text{\AA})$	I_c	I_o^{**}	h	k	l	$d_c(\text{\AA})$	$d_o(\text{\AA})$	I_c	I_o^{**}
0	2	0	14.143		5	---	1	5	2	2.6673		5	---
0	1	1	6.535		4	---	-2	8	0	2.5678	2.5605	18	w
1	0	1	4.921	4.939	31	w ⁺	2	8	0	2.4895		25	---
0	4	1	4.870		3	---	2	7	1	2.4681	2.4695	3	vw ⁺
0	6	0	4.714		2	---	2	0	2	2.4605	2.4633	33	vw ⁺
-1	4	1	4.080	4.064	100	m	0	8	2	2.4350		57	
1	4	1	4.000	4.024	98	m	-2	2	2	2.4328	2.4370	5	m
2	0	0	3.615	3.615	21	w	1	10	1	2.4303		5	
0	8	0	3.536		28		-2	4	2	2.3392		13	
				3.524		w					2.3266		w, b
-2	2	0	3.529		2		2	4	2	2.3088		18	
-1	6	1	3.441	3.415	4	vw	3	0	1	2.2685		36	
0	0	2	3.358	3.376	21	w				2.2685			w ⁺
							-2	9	1	2.2676		3	
-2	4	0	3.260		9	---	-2	10	0	2.2620		9	---
2	4	0	3.1792		8	---	-3	4	1	2.1786		6	---
-1	1	2	3.0325	3.0470	6	w	-1	12	1	2.1435		19	
											2.1493		vw
-1	8	1	2.9005		13		3	4	1	2.1420		9	
				2.8748		w, b							
1	3	2	2.8873		3		1	0	3	2.1387	2.1300	3	vw ⁺
0	9	1	2.8466		3	---	1	12	1	2.1086	2.1155	23	w
1	8	1	2.8431		9	---	-3	6	1	2.0678		7	
0	10	0	2.8285		8	---	-1	4	3	2.0523		20	
											2.0536		w, b
-2	5	1	2.8072	2.8048	5	w	1	4	3	2.0419		24	
2	5	2	2.7425		8	---	-2	8	2	2.0399		6	
-1	5	2	2.6965	2.7078	11	w							

Note. * Due to poor crystallinity, many relatively weak lines were not observed.

** v = very; w = weak; m = moderate; s = strong; b = broad. + / - means slightly stronger / weaker than.

Table 8. Miller indices, and observed and calculated interplanar d-spacings and intensities for $\text{Eu}_5\text{Cl}_{11}$.

h	k	l	$d_c(\text{\AA})$	$d_o(\text{\AA})$	I_c	I_o	h	k	l	$d_c(\text{\AA})$	$d_o(\text{\AA})$	I_c	I_o
0	2	0	17.585	18.005	5	w	2	12	0	2.2746		5	
0	1	1	6.653	6.667	4	w ⁺	-3	0	1	2.2704	2.2726	11	w ⁺
-1	0	1	4.953		15		-3	1	1	2.2656		6	
1	0	1	4.924	4.937	14	s	3	0	1	2.2619	2.2647	12	w ⁺
-1	4	1	4.316		3		3	1	1	2.2572		6	---
1	4	1	4.296	4.313	2	w	0	12	2	2.2164	2.2184	1	vw
-1	5	1	4.050	4.059	98	vs	-3	4	1	2.1983	2.1965	2	vw ⁻
1	5	1	4.034	4.037	100	vs	2	13	0	2.1643		1	
-1	6	1	3.783		3		-3	5	1	2.1606	2.1627	5	w
1	6	1	3.770	3.784	2	w	-1	0	3	2.1588		2	
2	0	0	3.6069	3.6103	18	m ⁺	3	5	1	2.1533	2.1568	5	w
2	1	0	3.5881		4	---	-1	15	1	2.1192		21	
0	10	0	3.5170	3.5215	27	s ⁻	-3	6	1	2.1171	2.1179	4	s
0	0	2	3.3874	3.3884	21	m	1	15	1	2.1169		21	
2	5	0	3.2096	3.2129	12	m ⁻	3	6	1	2.1103	2.1123	4	w ⁻
1	1	2	3.0477	3.0507	2	w ⁻	-1	5	3	2.0638	2.0641	23	m ⁻
0	12	0	2.9308		3		1	5	3	2.0574	2.0576	24	m
2	7	0	2.9301	2.9323	2	m ⁻	-1	6	3	2.0258		2	
0	11	1	2.8914	2.8926	4	w	-2	10	2	2.0249	2.0254	6	w
-1	10	1	2.8676		9		2	10	2	2.0169	2.0186	8	w
1	10	1	2.8619	2.8651	9	m	-1	16	1	2.0092		2	
-2	6	1	2.8031	2.8067	5	w	1	16	1	2.0072	2.0087	1	w
2	6	1	2.7925	2.7952	5	w	-1	7	3	1.9835	1.9822	1	w ⁻
-1	6	2	2.7218	2.7215	8	w ⁺	1	7	3	1.9778		1	---
1	6	2	2.7121	2.7135	6	w	2	15	0	1.9658	1.9668	10	w ⁺
2	9	0	2.6505	2.6567	2	vw	-2	11	2	1.9579	1.9592	2	vw
2	10	0	2.5181	2.5208	35	s	-3	10	1	1.9074	1.9085	8	w ⁺
-2	0	2	2.4766	2.4779	14	w ⁺	3	10	1	1.9024	1.9037	8	w ⁺
-2	1	2	2.4705	2.4710	5	w ⁻	-3	11	1	1.8511	1.8529	3	w
2	0	2	2.4620		14		3	11	1	1.8465		2	---
2	1	2	2.4559	2.4632	4	m ⁺	0	11	3	1.8446		2	---
0	10	2	2.4398	2.4385	57	vs	4	4	0	1.7667		4	---
2	11	0	2.3926	2.3939	8	w	0	20	0	1.7585	1.7587	8	w ⁺
-2	5	2	2.3360	2.3366	12	m ⁻	4	5	0	1.7470	1.7477	5	w ⁺
2	5	2	2.3237	2.3259	13	m	4	6	0	1.7237	1.7250	3	vw

Table 9. Miller indices, and observed and calculated interplanar d-spacings and intensities for $\text{Eu}_{14}\text{Cl}_{33}$.

h	k	l	$d_c(\text{\AA})$	$d_o(\text{\AA})$	I_c	I_o	h	k	l	$d_c(\text{\AA})$	$d_o(\text{\AA})$	I_c	I_o
1	0	1	10.128		18	---	4	0	4	2.5320		2	
0	1	2	8.265		5	---	2	2	6	2.5309	2.5303	3	vw
0	0	3	8.256		5	---	2	3	2	2.4939		7	
1	0	4	5.407	5.425	2	vw	3	2	-2	2.4939	2.4876	4	s ⁻
1	1	3	5.062		3	---	2	1	-8	2.4910		90	
1	1	-3	5.062		2	---	1	4	0	2.4218	2.4220	76	m ⁺
1	2	-1	4.136		5		1	0	10	2.4173		4	
0	2	4	4.132	4.120	5	w	4	1	-3	2.3239	2.3256	3	vw
0	0	6	4.128		40		2	1	10	2.1328	2.1291	29	w
1	2	2	3.973		5		1	4	6	2.0889		24	
2	1	-2	3.973	3.970	100	s	1	4	-6	2.0889	2.0877	24	m ⁺
3	0	0	3.699		4	---	4	2	2	2.0679		23	
2	0	5	3.695		4	---	0	0	12	2.0640	2.0683	6	w
2	1	4	3.473	3.472	68	m	4	2	-4	1.9865	1.9880	9	vw ⁺
3	0	3	3.376		5	---	5	1	-2	1.9679		2	
2	2	-3	2.9867		7		2	3	8	1.9665	1.9665	2	vw
0	1	8	2.9821	2.9872	3	w	3	2	-8	1.9665		2	
4	0	1	2.7573		4		4	2	8	1.7364	1.7363	20	w ⁺
3	1	-4	2.7563	2.7547	8	w	3	3	9	1.6873	1.6860	2	vw
0	3	6	2.7550		2		2	1	-14	1.6301	1.6287	9	vw ⁺
0	4	2	2.7074		3		4	2	-10	1.6006	1.6003	11	vw ⁺
2	1	7	2.7046	2.7033	7	vw ⁺	0	7	2	1.5726		8	
1	2	-7	2.7046		3		3	5	-2	1.5726	1.5736	8	w ⁻
3	1	5	2.6144	2.6144	7	vw							

$\text{Sm}_9^{2+}\text{Ln}_6^{3+}\text{Cl}_{33}$ (Ln = Nd, Sm, Gd)

All these have the cluster-type structure as discussed previously. Lattice parameters are listed in Table 3 (Page 15). Their powder diffraction patterns are similar to that of $\text{Eu}_{14}\text{Cl}_{33}$ (Table 9) and are not listed.

$\text{BaCl}_2\text{-LnCl}_3$ systems (Ln = La, Sm)

Phase studies on $\text{BaCl}_2\text{-LnCl}_3$ systems by two separate groups have revealed in addition to other miscellaneous phases a common 2:1 compound, Ba_2LnCl_7 , that forms over a wide range of temperatures (89,90). No structural details about these phases were available. The products which resulted from fusion of the approximate 1:1 $\text{BaCl}_2\text{-LnCl}_3$ mixtures were initially thought to be this 2:1 phase with excess LnCl_3 . Earlier powder patterns were indexed on a hexagonal unit cell (72). However, later single crystal X-ray diffraction studies indicated that the true symmetry for " Ba_2SmCl_7 ," is cubic and the composition is probably $\text{Ba}_{17}\text{Sm}_{10}\text{Cl}_{64}$ (below). In fact, the hexagonal lattice parameters can be transformed into pseudo-cubic parameters by $a_c = \sqrt{3} \cdot c_h$ and $a_c = \sqrt{6/2} \cdot a_h$. Program ITO12 also suggested a similar cubic lattice. Indexed lattice parameters from powder patterns, transformed cubic and observed single crystal data are listed in Table 10. The transformed cubic lattice parameter of " Ba_2LaCl_7 " from a_h does not agree well with that transformed from c_h . Therefore the true symmetry of this phase remains in doubt.

Systematic extinctions from single crystal data of " Ba_2SmCl_7 ," correspond to the unique space group $P 6_3$ (# 205). It was noticed that this phase has the same space group and a lattice similar to that of the previously reported mixed-fluoride $c\beta$ -phase $\text{M}^{2+}_{17}\text{Ln}^{3+}_{10}\text{F}_{64}$ (M = Ca, Sr, Sm, Eu, Yb) (29). Thus the mixed chloride phase is tentatively formulated as $\text{Ba}^{2+}_{17}\text{Sm}^{3+}_{10}\text{Cl}_{64}$. Density values are ($\text{g}\cdot\text{cm}^{-3}$): calculated 4.160 with $Z = 4$;

found $4.08(\pm 0.07)$. The theoretical density of Ba_2SmCl_7 (4.098 with $Z = 36$) is also close to that observed, thus the experimental value does not permit one to distinguish between the two formulations. However, the formulation $\text{Ba}^{2+}_{17}\text{Sm}^{3+}_{10}\text{Cl}_{64}$ is more reasonable in view of the crystal chemistry. The cubic lattice is a superlattice corresponding to $3 \times 3 \times 3$ cubic fluorite cells. $a_c/3 = 7.122 \text{ \AA}$ for $\text{Ba}_{17}\text{Sm}_{10}\text{Cl}_{64}$ is very close to the cubic unit cell parameter of BaCl_2 ($a_c = 7.311(1) \text{ \AA}$) (91). Its relation with the fluorite type structure is apparent in the powder X-ray pattern. The "basic reflections" can be indexed as a cubic cell with $a_c = 7.1352(6) \text{ \AA}$. Observed powder diffraction reflections are listed in Table 11. This formulation corresponds to $10 \times 4 = 40 \text{ Sm}^{3+}$ and 40 "extra" Cl^- ions in a unit cell, and thus suggests 8 $\text{BaSm}_5\text{Cl}_{37}$ clusters.

The crystal structure of this phase has not been solved. Direct method procedures did not give useful phase information and the Patterson map is too complicated to interpret.

Table 10. Transformation of " Ba_2LnCl_7 ," hexagonal lattice parameters into cubic lattice parameters. (units in \AA)

Lattice	" Ba_2LaCl_7 ,"	" Ba_2SmCl_7 ,"
a_h, c_h	17.637(6), 12.495(5)	17.471(6), 12.351(6)
derived a_c	21.601, 21.642	21.398, 21.393
observed a_c	-----	21.366(2)

Table 11. Miller indices, observed intensities, and observed and calculated interplanar d-spacings for $\text{Ba}_{17}\text{Sm}_{10}\text{Cl}_{64}$. Cubic $a = 21.406 \text{ \AA}$ (powder); space group $P a 3$.

no.	h	k	l	$d_c(\text{\AA})$	$d_o(\text{\AA})^*$	I_o	no.	h	k	l	$d_c(\text{\AA})$	$d_o(\text{\AA})^*$	I_o
1	2	0	0	10.703	10.683	vw	35	10	2	0	2.0990	2.0987	vw
2	3	0	0	7.1353	7.1239	vw	36	10	2	1	2.0890	2.0916	vw
3	3	1	1	6.4541	6.4535	vw	37	10	2	2	2.0598	2.0601**	w
4	3	2	1	5.7210	5.7149	vw	38	10	3	1	2.0410	2.0411	vw
5	4	1	0	5.1917	5.1898	vw	39	8	7	1	2.0049	2.0065	vw
6	3	3	0	5.0454	5.0556	vw	40	9	6	0	1.9790	1.9790	vw
7	5	1	1	4.1196	4.1092**	vs	41	11	1	0	1.9380	1.9391	vw
8	5	2	0	3.9750	3.9705	vw	42	9	7	2	1.8492	1.8499	vw
9	5	2	1	3.9082	3.9055	vw	43	11	4	2	1.8027	1.8036	vw
10	4	4	1	3.7263	3.7259	vw	44	12	0	0	1.7838	1.7843**	w*
11	6	0	0	3.5677	3.5625**	m	45	12	2	0	1.7596	1.7553	vw
12	6	1	1	3.4725	3.4749	vw	46	10	7	0	1.7536		
13	5	4	0	3.3430	3.3480	vw	47	11	6	1	1.7030	1.7033	vw
14	5	5	0	3.0273	3.0263	vw	48	12	4	1	1.6870	1.6881	vw
15	5	5	1	2.9974	2.9982	vw	49	11	7	1	1.6370	1.6371**	w*
16	6	4	0	2.9685	2.9706	vw	50	13	2	0	1.6275	1.6284	w
17	7	2	0	2.9403	2.9383	vw	51	12	6	0	1.5955	1.5957**	w*
18	7	2	1	2.9130	2.9156	vw	52	10	9	1	1.5867	1.5866	vw
19	7	2	2	2.8353	2.8350	vw	53	11	8	0	1.5738	1.5743	w
20	7	3	1	2.7868	2.7871	vw	54	13	5	0	1.5369	1.5372	vw
21	7	3	2	2.7186	2.7200	vw	55	14	2	1	1.5099	1.5105	vw
22	7	4	0	2.6551	2.6531	w	56	13	6	1	1.4914	1.4917	vw
23	7	4	1	2.6349	2.6339	w	57	13	6	2	1.4807	1.4814	vw
24	8	2	0	2.5959	2.5971	vw	58	14	4	2	1.4565	1.4560**	w*
25	6	6	0	2.5227	2.5213**	vs	59	14	5	0	1.4399	1.4408	vw
26	7	5	0	2.4884	2.4884	w	60	15	2	1	1.4115	1.4114	vw
27	6	6	2	2.4554	2.4551	vw	61	15	3	0	1.3993	1.3992	vw
28	8	3	2	2.4394	2.4410	w	62	15	3	3	1.3732	1.3729**	w
29	9	0	0	2.3784	2.3800	vw	63	13	10	0	1.3051	1.3053	w
30	8	5	0	2.2690	2.2694	vw	64	12	12	0	1.2613	1.2617**	w
31	8	5	2	2.2197	2.2204	vw	65	15	9	3	1.2061	1.2063**	w
32	7	7	1	2.1514	2.1501**	s	66	18	6	0	1.1282	1.1281**	w
33	10	1	0	2.1300	2.1313	vw	67	15	9	9	1.0881	1.0890**	vw
34	10	1	1	2.1195	2.1199	vw							

Note. * powder pattern taken by Guinier camera with ground crystals grown in a melt;

** these lines define the basic fluorite-type structure with the cubic lattice parameter $a = 7.1352(6) \text{ \AA}$.

BaBr₂-LnBr₃ systems (Ln = La, Nd)

The mixed bromide systems have received little attention. The vernier-type lanthanide mixed-valence bromides Nd₄Br₉ (92) Sm_nBr_{2n+1} (n=5,6,11) (93,94); Sr₄LnBr₁₁ and Sr₅NdBr₁₃ (95); Cf₄GdBr₁₁ (43) have been prepared. Reports of other alkaline earth-lanthanide bromides could not be found. Our studies revealed a single mixed bromide phase with excess LnBr₃ present. This phase was identified as the cluster-type Ba₉Ln₅Br₃₃ which is isostructural with Eu₁₄Cl₃₃ (35). Observed and calculated X-ray powder diffraction patterns are in good agreement. The refined hexagonal lattice parameters of rhombohedral Ba₉La₅Br₃₃ and Ba₉Nd₅Br₃₃ are listed in Table 4 (Page 16). Miller indices, calculated and observed interplanar d-spacings and intensities are listed in Tables 12 and 13.

The structural similarity between Ba₉Ln₅Br₃₃ and Eu₁₄Cl₃₃ can be understood in terms of their radius ratio values: $r(\text{Ba}^{2+})/r(\text{Br}) = 0.724$; $r(\text{Eu}^{2+})/r(\text{Cl}) = 0.691$ (VIII coordinated effective cationic radii)(28). Formation of vernier-type mixed bromides such as Ba₃LnBr₉ and Ba₄LnBr₁₁, would also be predicated by analogy with the europium chloride system. Other phases were indeed observed at different compositions but no further effort was made to characterize them in this work.

MI₂·H₂O (M = Sm, Eu, Sr) When diiodide hydrates were evacuated to 0.1-0.01 Torr overnight at room temperature or with heating below 80°C, they were converted to monohydrates with identical orthorhombic structures.

Table 12. Miller indices, and observed (Guinier) and calculated interplanar d-spacings and intensities for $\text{Ba}_9\text{La}_5\text{Br}_{33}$.

h	k	l	$d_c(\text{\AA})$	$d_o(\text{\AA})$	I_c	I_o	h	k	l	$d_c(\text{\AA})$	$d_o(\text{\AA})$	I_c	I_o
1	0	1	11.102	11.198	1	vw	4	0	4	2.7755	2.7799	2	vw
1	1	0	7.049	7.074	4	vw	2	2	6	2.7620	2.7637	9	w
0	2	1	5.951	5.980	2	vw	2	3	2	2.7412	2.7416	14	w ⁺
0	0	6	4.446	4.443	21	w ⁺	3	2	-2	2.7412		5	
2	1	-2	4.361	4.359	47	m	1	1	-9	2.7325		2	---
2	0	5	4.017	4.022	1	vw	1	2	8	2.7029	2.7012	3	vs
2	1	4	3.795	3.800	5	w	2	1	-8	2.7029		100	
3	0	3	3.701	3.709	3	vw	1	4	0	2.6643	2.6639	99	vs
1	2	5	3.4903	3.4908	3	w	1	0	10	2.6063	2.6063	6	vw ⁺
1	3	1	3.3593	3.3546	2		2	3	-4	2.5825	2.5856	1	vw
3	1	-1	3.3593		1	w	4	1	3	2.5522		2	
3	1	2	3.2821		2	---	1	4	3	2.5522	2.5530	1	w
1	3	-2	3.2821		2	---	1	4	-3	2.5522		2	
2	2	3	3.2765	3.2763	3		4	1	-3	2.5522		3	
2	2	-3	3.2765		15	w ⁺	2	3	5	2.4800	2.4800	1	vw ⁺
0	2	7	3.2328	3.2363	2	vw	3	2	-5	2.4800		3	
0	1	8	3.2169	3.2197	2	vw	0	2	10	2.4446	2.4449	2	vw
4	0	1	3.0325	3.0336	11	w	0	5	1	2.4317	2.4329	4	vw ⁺
3	1	-4	3.0194	3.0197	16	w ⁺	3	0	9	2.3960		1	---
3	0	6	3.0021	3.0034	2		0	1	11	2.3788	2.3791	2	vw
0	3	6	3.0021		8	w	3	1	8	2.3760		1	
0	4	2	2.9754	2.9790	3	vw	3	3	0	2.3497	2.3505	2	vw
0	0	9	2.9642	2.9660	3	vw	2	1	10	2.3096	2.3079	24	m
2	1	7	2.9386	2.9371	14		2	4	1	2.2987		1	---
1	2	-7	2.9386		10	m	0	5	4	2.2930		1	---
3	1	5	2.8590	2.8596	16	w ⁺							

Table 12. (continued)

1	4	6	2.2854		18		4	4	0	1.7622		1	---
1	4	-6	2.2854	2.2841	18	m ⁻	2	1	-14	1.7613	1.7612	4	vw ⁺
4	2	2	2.2736		17		3	1	-13	1.7550	1.7549	2	vw ⁻
2	4	-2	2.2736	2.2733	4	w ⁺	4	2	-10	1.7452	1.7448	10	w ⁻
2	0	11	2.2539	2.2552	1	vw ⁻	5	3	2	1.7294		3	
0	4	8	2.2516		1	---	0	7	2	1.7294	1.7288	6	w ⁺
1	5	-1	2.1855		2		3	5	-2	1.7294		6	
5	1	1	2.1855	2.1864	1	vw ⁺	1	5	-10	1.6940		4	
2	3	8	2.1448		1		5	1	10	1.6940	1.6936	4	vw ⁺
3	2	-8	2.1448	2.1449	2	vw ⁺	6	2	-2	1.6796	1.6791	2	vw ⁻
5	1	4	2.0831	2.0846	1	vw	1	6	7	1.6729		1	
0	6	3	1.9836		1		6	1	-7	1.6729	1.6735	2	vw
6	0	3	1.9836	1.9827	1	vw	2	4	-11	1.6717		1	
4	1	-9	1.9815		1		4	4	-6	1.6383	1.6361	3	vw
0	3	12	1.9510		1	---	2	5	9	1.6320	1.6317	1	vw ⁻
5	2	3	1.9094		1		1	5	11	1.6266		2	
5	2	-3	1.9094	1.9084	1	vw ⁻	1	6	-8	1.6257	1.6249	3	w ⁻
4	2	8	1.8974	1.8957	24	w ⁺	6	1	8	1.6257		2	
2	2	-12	1.8803	1.8812	2	vw ⁻	2	1	16	1.5681	1.5672	25	w ⁺
3	3	9	1.8413	1.8409	4	vw	4	5	-1	1.5605		2	
5	2	6	1.7897		2		5	4	1	1.5605	1.5604	3	vw ⁻
2	5	-6	1.7897	1.7885	1	vw ⁺	3	5	-8	1.5455		12	
5	2	-6	1.7897		3		0	7	8	1.5455	1.5446	12	w ⁺
0	0	15	1.7785		1		6	3	0	1.5382	1.5379	11	vw
4	3	7	1.7759	1.7750	2	vw							

Table 13. Miller indices, and observed (Guinier) and calculated interplanar d-spacings and intensities for $\text{Ba}_9\text{Nd}_5\text{Br}_{33}$.

h	k	l	$d_c(\text{\AA})$	$d_o(\text{\AA})$	I_c	I_o	h	k	l	$d_c(\text{\AA})$	$d_o(\text{\AA})$	I_c	I_o
1	0	1	11.049	11.043	2	w ⁻	2	1	7	2.9204	2.9183	13	m
0	1	2	8.955	8.971	<1	vw ⁻	1	2	-7	2.9204		9	
1	1	0	7.019	7.007	5	w	3	1	5	2.8443	2.8423	16	m
0	2	1	5.925	5.928	3	w ⁻	1	3	-5	2.8443		2	
1	0	4	5.814	5.839	<1	vw	3	2	1	2.7739	2.7740	<1	vw
1	1	3	5.495	5.509	<1	vw	2	3	-1	2.7739		<1	
2	1	1	4.528	4.539	<1	vw	4	0	4	2.7622		2	---
1	2	-1	4.528		<1		2	2	6	2.7469	2.7469	9	w ⁻
0	0	6	4.413	4.414	22	m ⁻	2	3	2	2.7293	2.7275	14	m ⁻
2	1	-2	4.341	4.336	49	vs	3	2	-2	2.7293		5	
2	0	5	3.993	3.990	2	vw ⁺	1	1	-9	2.7132		1	---
2	1	4	3.7748	3.7750	6	w ⁺	1	2	8	2.6856	2.6825	3	
3	0	3	3.6830	3.6824	3	vw ⁺	2	1	-8	2.6856		100	vs
1	2	5	3.4707	3.4710	3	w	1	4	0	2.6531	2.6507	99	vs
1	3	1	3.3450	3.3426	1	w	1	0	10	2.5871	2.5865	6	w ⁻
3	1	-1	3.3450		1		2	3	-4	2.5704	2.5708	1	vw
3	1	2	3.2677		2		4	1	3	2.5408		2	
1	3	-2	3.2677	3.2598	1	m ⁻	1	4	3	2.5408	2.5397	1	w ⁺
2	2	3	3.2613		3		1	4	-3	2.5408		2	
2	2	-3	3.2613		14		4	1	-3	2.5408		3	
0	2	7	3.2115	3.2140	2	w	1	3	7	2.5170	2.5164	<1	w ⁻
0	1	8	3.1934	3.1960	2	vw ⁺	3	1	-7	2.5170		<1	
4	0	1	3.0197	3.0188	11	m ⁻	2	3	5	2.4678	2.4672	1	w ⁺
3	1	-4	3.0046	3.0035	16	w ⁺	3	2	-5	2.4678		3	
3	0	6	2.9849	2.9835	2	w	0	2	10	2.4274	2.4291	2	vw ⁻
0	3	6	2.9849		7	---	0	5	1	2.4214	2.4207	4	w
0	4	2	2.9624	2.9643	3	vw	3	0	9	2.3807	2.3826	2	vw ⁻
0	0	9	2.9419	2.9463	3	vw							

Table 13. (continued)

3	1	8	2.3620		1		5	2	6	1.7812		2	
0	1	11	2.3611	2.3610	2	vw	2	5	-6	1.7812	1.7813	1	w
3	3	0	2.3398	2.3393	2	w	5	2	-6	1.7812		3	
2	1	10	2.2941	2.2932	24		4	3	7	1.7672		2	
2	4	1	2.2891		1		0	0	15	1.7651	1.7671	1	w
0	5	4	2.2825	2.2832	1	vw	4	4	0	1.7549		1	---
1	4	6	2.2738		18		2	1	-14	1.7489	1.7490	4	w
1	4	-6	2.2738	2.2711	18	m	3	1	-13	1.7434		2	---
4	2	2	2.2638		18		4	2	-10	1.7354	1.7355	10	w
2	4	-2	2.2638	2.2619	4	m	0	7	2	1.7221		7	
2	3	-7	2.2449	2.2436	<1	vw	3	5	-2	1.7221	1.7214	6	w
0	4	8	2.2387		1		5	3	2	1.7221		3	
2	0	11	2.2380	2.2386	1	vw	1	1	-15	1.7118		<1	
5	0	5	2.2098		<1		1	1	15	1.7118	1.7120	<1	vw
0	0	12	2.2069	2.2101	<1	w	5	1	10	1.6846		4	
1	5	-1	2.1763		2		1	5	-10	1.6846		4	
5	1	1	2.1763	2.1759	1	w	6	2	1	1.6826	1.6826*	1	w
2	3	8	2.1328		1		2	6	-1	1.6826		<1	
3	2	-8	2.1328	2.1332	2	w*	6	2	-2	1.6725	1.6727	2	w
2	4	-5	2.1078		<1		1	6	7	1.6648		1	
1	1	-12	2.1049	2.1062	<1	vw	6	1	-7	1.6648	1.6641	1	w
5	1	4	2.0737	2.0744	1	vw	2	4	-11	1.6620		1	
3	3	6	2.0672	2.0686	<1	vw*	6	2	4	1.6339		1	---
4	0	10	1.9964		<1		4	4	-6	1.6307	1.6314	3	vw
3	4	-1	1.9931	1.9934	<1	vw	2	5	9	1.6235	1.6237	1	vw
0	6	3	1.9750		1		1	6	-8	1.6176		3	
6	0	3	1.9750	1.9755	1	vw	6	1	8	1.6176	1.6169	2	vw*
4	1	-9	1.9702		1	---	1	5	11	1.6173		2	
0	3	12	1.9378		1	---	3	3	12	1.6053	1.6063	1	vw
5	2	3	1.9011		1		2	1	16	1.5569	1.5582	25	w*
5	2	-3	1.9011	1.9023	1	vw	5	4	1	1.5540		3	
4	2	8	1.8874	1.8836	25	m	4	5	-1	1.5540	1.5567	2	v w
2	2	-12	1.8680		1	---	2	6	-7	1.5400		3	
3	3	9	1.8312	1.8320	4	w	3	5	-8	1.5380	1.5374	12	m
1	5	8	1.8227	1.8241	1	w	0	7	8	1.5380		11	

4.2 Decomposition Products and Structures

4.2.1 High-Temperature Forms of LnCl_2 ($\text{Ln} = \text{Sm}, \text{Eu}$)

Fluorite-type EuCl_2 was obtained as a fine white powder when the mixed-valence europium chlorides were extracted by THF. The fluorite-type SmCl_2 that resulted from extraction of both $\text{Sm}_{14}\text{Cl}_{33}$ and $\text{Sm}_9\text{Gd}_5\text{Cl}_{33}$ by THF was a dark blue powder in contrast to the blood red color of the PbCl_2 -type SmCl_2 . Chlorine analysis of this new phase indicated the composition to be $\text{SmCl}_{1.99(1)}$. Extraction of $\text{Sm}_9\text{Nd}_5\text{Cl}_{33}$ also yielded the fluorite modification, but the product was impure and exhibited a reddish color.

Lattice parameters for both EuCl_2 and SmCl_2 and their calculated densities are listed in Table 14 together with values from previously observed high temperature phases. Experimental d values and powder diffraction intensities are in good agreement with the those calculated for a fluorite-type structure (Tables 15 and 16).

Table 14. Lattice parameters and calculated densities of LnCl_2 ($\text{Ln} = \text{Sm}, \text{Eu}$).

Compound	a (Å)	d_x ($\text{g}\cdot\text{cm}^{-3}$)	T (°C)	Reference
SmCl_2	7.1496(2)	3.996(2)	775-785	<u>108</u>
	6.9827(5)	4.3167(9)	23(2)	this work
EuCl_2	7.150(1)	4.073(2)	800	<u>107</u>
	6.961(1)	4.387(2)	23(2)	this work

Table 15. Miller indices, and observed and calculated interplanar d-spacings and intensities for fluorite-type SmCl_2 .

#	h	k	l	$d_c(\text{\AA})$	$d_o(\text{\AA})$	I_c	I_o
1	1	1	1	4.019	4.0339	100	vs
2	2	0	0	3.480	3.4978	14	w
3	2	2	0	2.4608	2.4691	95	vs
4	3	1	1	2.0986	2.1052	58	s
5	2	2	2	2.0092	2.0163	6	w
6	4	0	0	1.7401	1.7460	17	w
7	3	3	1	1.5968	1.6023	26	m
8	4	2	0	1.5564	1.5622	9	w
9	4	2	2	1.4207	1.4257	36	m
10	5	1	1	1.3395	1.3437	15	w
11	3	3	3	1.3395		5	
12	4	4	0	1.2304	1.2343	11	w
13	5	3	1	1.1765	1.1800	20	m
14	4	4	2	1.1600	1.1634	4	vw
15	6	0	0	1.1600		1	
16	6	2	0	1.1005	1.1036	16	w
17	5	3	3	1.0614	1.0642	8	w
18	6	2	2	1.0493	1.0521	3	vw

Table 16. Miller indices, and observed and calculated interplanar d-spacings and intensities for fluorite-type EuCl_2 .

#	h	k	l	$d_c(\text{\AA})$	$d_o(\text{\AA})$	I_c	I_o
1	1	1	1	4.019	4.024	100	vs
2	2	0	0	3.480	3.484	14	w
3	2	2	0	2.4608	2.4610	95	vs
4	3	1	1	2.0986	2.0999	58	s
5	2	2	2	2.0092	2.0117	6	w
6	4	0	0	1.7401	1.7412	17	w
7	3	3	1	1.5968	1.5974	26	m
8	4	2	0	1.5564	1.5578	9	w
9	4	2	2	1.4207	1.4209	36	m
10	5	1	1	1.3395	1.3396	15	w
11	3	3	3	1.3395		5	
12	4	4	0	1.2304	1.2303	11	w
13	5	3	1	1.1765	1.1767	20	m
14	4	4	2	1.1600	1.1598	4	vw
15	6	0	0	1.1600		1	
16	6	2	0	1.1005	1.1001	16	w
17	5	3	3	1.0614	1.0606	8	w
18	6	2	2	1.0493	1.0406	3	vw

4.2.2 High-Pressure Forms of BaX_2 ($\text{X} = \text{Cl}, \text{Br}, \text{I}$)

The mixed chloride precursors $\text{Ba}_{17}\text{Ln}_{10}\text{Cl}_{64}$ were first leached by THF. No apparent change was observed even after 3-4 days of continuous extraction. They were then extracted by pyridine. A new phase was observed after several hours, but solvolysis proceeded exceedingly slowly. With a 0.5-0.8 g reactant ($\text{Ba}_{17}\text{Sm}_{10}\text{Cl}_{64}$ and SmCl_3 mixture) reaction was complete in 5-6 days. The X-ray powder reflections of the white powder that remained agreed well with those previously reported for hexagonal anti- Fe_2P -type BaCl_2 (8). The solvolysis reaction for Ba_2LaCl_7 , incomplete even after 8.5 days, appeared to have stopped, but the same "hexagonal" phase was obviously present.

On the other hand, the mixed-cationic bromides were decomposed rapidly by THF. With 0.5-1.0 g specimens, especially $\text{Ba}_9\text{Nd}_5\text{Br}_{33}$, reaction was apparent after 30 min of extraction and decomposition complete in 2-3 days. The white powder that remained also exhibited the hexagonal anti- Fe_2P -type structure. Elemental analysis for barium confirmed that it was BaBr_2 : calculated Ba% for BaBr_2 , 46.22; found, 45.47. This form was also prepared by dehydrating $\text{BaBr}_2 \cdot \text{H}_2\text{O}$ at 110°C in a high vacuum for 24 h.

Anti- Fe_2P modification of BaI_2 , prepared by Beck under high pressure (46); was also obtained by high vacuum dehydration of $\text{BaI}_2 \cdot \text{H}_2\text{O}$ at $110\text{-}150^\circ\text{C}$. The observed diffraction reflection intensities of the anti- Fe_2P -type BaX_2 ($\text{X} = \text{Cl}, \text{Br}, \text{I}$) prepared in this work are in good agreement with those calculated with the positional and thermal parameters reported for BaI_2 (Tables 17-19).

Lattice parameter and volume per formula data for the anti- Fe_2P -type and normal BaCl_2 and BaBr_2 modifications are presented comparatively in Tables 20 and 21, respectively. From the tables it is obvious that the anti- Fe_2P modification of both BaCl_2 and BaBr_2 is more efficiently packed than the normal modification (the PbCl_2 -type). They are considered the "high-pressure" forms similar to that of BaI_2 . The average volume per

formula unit, V/Z , of our anti- Fe_2P -type form is about 1% smaller than that of the PbCl_2 -type modification. However, the V/Z data on the anti- Fe_2P form of BaCl_2 produced by dehydrating $\text{BaCl}_2 \cdot 2\text{H}_2\text{O}$ (8) at increasing temperatures is slightly larger (at about the same temperature) than that of the normal form. This less dense material could result from poor specimen crystallinity as the lattice parameter standard errors are somewhat large, but more likely results from the matrix environment in which the crystals formed.

The BaCl_2 and BaBr_2 specimens obtained by solvolytic decompositions are relatively pure and fairly well crystallized. The most intense reflection of the PbCl_2 -type modification was frequently observed as a very weak reflection on the Guinier films. This impurity content is estimated to be approximately 3-5% based upon two factors. First, the NdOBr quantitatively determined impurity level in the BaBr_2 sample was 3% (determined by weighing the mass of the water insoluble residue). Second, the intensities of the PbCl_2 -type BaX_2 and the NdOBr X-ray reflections are comparable, the scattering powers are similar, and the symmetries are closely related (orthorhombic and tetragonal, respectively).

It is difficult to eliminate the PbCl_2 form. It probably results from the unreacted barium halide in the mixed-cationic halide precursors. Transformation of the anti- Fe_2P -type to the PbCl_2 type is highly unlikely at the leaching temperatures (60-115°C) because thermal tests (discussed later) demonstrated that the transformation was very slow even at 300°C.

Table 17. Miller indices, and observed and calculated interplanar d-spacings and intensities for anti-Fe₂P-type BaCl₂.

From precursor			Ba ₁₇ Sm ₁₀ Cl ₆₄				"Ba ₂ LaCl ₇ "			
h	k	l	d _c (Å)	d _o (Å)	I _c	I _o	d _c (Å)	d _o (Å)	I _c	I _o
0	0	1	4.616	4.610	8	vw	4.592	4.619	8	vw
1	1	0	4.034	4.029	89	s	4.033	4.032	89	s
1	0	1	3.851	3.849	70	m-s	3.837	3.838	70	m
1	1	1	3.0373	3.0356	39	m	3.0301	3.0289	39	m
2	0	1	2.7854	2.7847	100	s	2.7799	2.7774	100	s
2	1	0	2.6406	2.6399	10	vw	2.6403	2.6443	10	w
3	0	0	2.3287	2.3289	53	m	2.3285	2.3285	53	s
0	0	2	2.3080	2.3073	27	w-m	2.2958		27	---
2	1	1	2.2920	2.2902	71	m	2.2888	2.2883	71	s
3	0	1	2.0791	2.0805	5	vw	2.0767		5	---
2	2	0	2.0167	2.0185	20	w	2.0166	2.0169	20	m
1	1	2	2.0032	2.0038	29	w-m	1.9952	1.9960	29	m
3	1	1	1.7866	1.7876	16	w	1.7850	1.7855	16	w
2	1	2	1.7377	1.7388	5	vw	1.7324		5	---
3	0	2	1.6393	1.6411	34	vw	1.6348	1.6351	34	w
4	1	0	1.5245	1.5248	19	w	1.5244	1.5246	19	w ⁺
2	2	2	1.5187	1.5190	16	vw	1.5151		16	w ⁺
3	2	1	1.5141	1.5140	29	w	1.5131	1.5135	29	w ⁺
1	0	3	1.5026		5	---	1.4950	1.4949	5	vw
4	1	1	1.4479		6	---	1.4467	1.4550	6	vw
1	1	3	1.4376		3	---	1.4309	1.4254	3	vw
2	0	3	1.4081	1.4081	11	vw	1.4018	1.4081	11	w
3	3	0	1.3445	1.3452	5	vw	1.3444		5	---
5	0	1	1.3373	1.3375	8	vw	1.3366	1.3371	8	vw
2	1	3	1.3294		12	---	1.3241		12	---
4	1	2	1.2720	1.2713	20	w	1.2699	1.2695	20	w

Table 18. Miller indices, and observed and calculated interplanar d-spacings and intensities for anti-Fe₂P-type BaBr₂.

From precursor			Ba ₃ La ₅ Br ₃₃				Ba ₃ Nd ₅ Br ₃₃			
h	k	l	d _c (Å)	d _o (Å)	I _c	I _o	d _c (Å)	d _o (Å)	I _c	I _o
1	0	0	7.346		<1	---	7.345		<1	---
0	0	1	4.824	4.833	4	vw	4.839	4.839	4	w
1	1	0	4.241	4.243	21	w ⁺	4.241	4.238	21	m
1	0	1	4.032	4.033	16	w	4.041	4.039	16	w ⁺
2	0	0	3.673	3.679	2	vw	3.672	3.664	2	vw
1	1	1	3.185	3.183	70	vs	3.189	3.187	70	s ⁺
2	0	1	2.9224	2.9206	100	vs	2.9255	2.9208	100	vs
2	1	0	2.7766	2.7762	29	m ⁻	2.7762	2.7738	29	w ⁺
3	0	0	2.4487	2.4484	46	s	2.4484	2.4485	46	s
0	0	2	2.4121	2.4210	31	vw	2.4196	2.4197	31	m ⁺
2	1	1	2.4065	2.4062	49	s	2.4081	2.4067	49	m ⁺
3	0	1	2.1835	2.1843	3	vw	2.1847	2.1861	3	vw
2	2	0	2.1206	2.1213	9	w	2.1203	2.1223	9	w
1	1	2	2.0968	2.0980	7	w	2.1016	2.1017	7	w
3	1	0	2.0374	2.0371	5	w	2.0372	2.0377	5	vw ⁺
2	2	1	1.9414	1.9436	2	vw	1.9421	1.9438	2	vw
3	1	1	1.8769	1.8770	7	w	1.8776	1.8776	7	vw ⁺
4	0	0	1.8365	1.8380	3	vw	1.8363		3	---
2	1	2	1.8210	1.8207	16	w	1.8241	1.8239	16	w ⁺
3	0	2	1.7184	1.7186	31	m	1.7210	1.7207	31	m
3	2	0	1.6853	1.6861	2	vw	1.6851	1.6863	2	vw ⁻
4	1	0	1.6031	1.6032	12	w	1.6028	1.6039	12	w
2	2	2	1.5927		7		1.5947	1.5959	7	vw
3	2	1	1.5910	1.5911	34	w	1.5914	1.5912	34	m ⁻
1	0	3	1.5709		1	---	1.5756		1	---
3	1	2	1.5565	1.5568	4	w	1.5584	1.5591	4	vw
4	1	1	1.5213	1.5215	6	vw	1.5215	1.5214	6	vw
1	1	3	1.5036	1.5037	7	vw	1.5077	1.5076	7	vw ⁺
2	0	3	1.4733		12	w	1.4769	1.4768	12	w
5	0	0	1.4692	1.4713	2		1.4690		2	---
4	0	2	1.4612	1.4628	2	vw	1.4627		2	---
3	3	0	1.4138	1.4139	3	vw	1.4136	1.4137	3	vw ⁻
5	0	1	1.4055	1.4052	8	w	1.4057	1.4063	8	vw
2	1	3	1.3916	1.3929	9	vw	1.3947	1.3948	9	vw ⁺
4	2	0	1.3883	1.3894	2	vw	1.3881		2	---
3	2	2	1.3815		2	---	1.3828		2	---
4	1	2	1.3351		12	w	1.3362	1.3367	12	w ⁺
4	2	1	1.3341	1.3339	6		1.3343	1.3341	6	vw
5	1	0	1.3194	1.3204	2	vw	1.3192		2	---
5	1	1	1.2727	1.2717	8	vw	1.2728	1.2723	8	w

Table 19. Miller indices, and observed and calculated interplanar d-spacings and intensities for anti-Fe₂P-type BaI₂. *

h	k	l	d _c (Å)	d _o (Å)	I _c	I _o	h	k	l	d _c (Å)	d _o (Å)	I _c	I _o
1	0	0	7.917		1	---	4	1	0	1.7277	1.7295	9	vw
0	0	1	5.173	5.197	3	vw	3	2	1	1.7137	1.7149	38	w ⁺
1	1	0	4.571	4.580	3	vw	2	2	2	1.7127		4	
1	0	1	4.3306	4.345	2	vw	3	1	2	1.6739	1.6767	7	vw
2	0	0	3.9586		3	---	4	1	1	1.6387	1.6376	7	vw
1	1	1	3.4253	3.4249	95	s	1	1	3	1.6134	1.6176	10	w ⁺
2	0	1	3.1437	3.1454	100	s	5	0	0	1.5834	1.5854	3	w ⁻
2	1	0	2.9924	2.9935	44	m ⁻	2	0	3	1.5809		13	
3	0	0	2.6391	2.6390	42	m ⁻	4	0	2	1.5719		4	---
2	1	1	2.5903	2.5908	39	m ⁺	3	3	0	1.5237		4	---
0	0	2	2.5865		34		5	0	1	1.5141	1.5162	9	vw
3	0	1	2.3508		2	---	4	2	0	1.4962	1.4977	4	w ⁺
2	2	0	2.2855	2.2898	5	vw ⁺	2	1	3	1.4940		7	
1	1	2	2.2511		1	---	3	2	2	1.4864		3	---
3	1	0	2.1958	2.1985	9	w ⁻	4	2	1	1.4373	1.4381	5	w ⁻
2	0	2	2.1653		1	---	4	1	2	1.4367		9	
2	2	1	2.0906	2.0937	3	vw ⁻	5	1	0	1.4220		3	---
3	1	1	2.0213	2.0257	10	vw ⁺	5	1	1	1.3711	1.3732	9	vw
4	0	0	1.9793	1.9801	4	vw ⁻	3	1	3	1.3562		3	---
2	1	2	1.9568	1.9600	26	w	5	0	2	1.3505		4	---
4	0	1	1.8486		1	---	3	3	2	1.3128		4	---
3	0	2	1.8472	1.8503	29	w ⁺	4	2	2	1.2951	1.2961	5	vw
3	2	0	1.8163		3	---							

* Sample from dehydration of BaI₂·H₂O at 150°C in a 10⁻⁶ Torr vacuum.

Table 20. Structure types and lattice parameters of BaCl₂. *

Structure Type	T (°C)	a (Å)	b (Å)	c (Å)	V/Z (Å ³)	Reference
PbCl ₂	25	7.872(1)	9.425(1)	4.7322(3)	87.78	<u>96</u>
Pnam	25	7.881(1)	9.419(2)	4.7298(8)	87.77	this work
	412	7.879(2)	9.444(2)	4.734(2)	88.06	<u>8</u>
Anti-Fe ₂ P	25	8.069(1)		4.616(1)	86.76	this work
P $\bar{6}$ 2m	12.5	8.103(8)		4.651(5)	88.17	<u>8</u>
	150	8.113(8)		4.675(5)	88.83	<u>8</u>
	200	8.132(7)		4.696(5)	89.63	<u>8</u>

* From Ba₁₇Sm₁₀Cl₆₄ precursor.

Table 21. Structure types and lattice parameters of BaBr₂. *

Structure Type	T(°C)	a(Å)	b(Å)	c(Å)	V/Z(Å ³)	Reference
PbCl ₂		8.276(8)	9.919(8)	4.956(4)	101.7	(<u>97</u>)
Pnam	25	8.266(2)	9.916(3)	4.956(3)	101.6	this work
Anti-Fe ₂ P	25	8.4826(6)		4.824(1)	100.2	this work*
P $\bar{6}$ 2m						

* From Ba₉La₅Br₃₃ precursor.

4.2.3 High-Temperature Forms of MI_2 ($M = \text{Sr, Sm, Eu}$)

The iodides obtained by dehydration of $MI_2 \cdot H_2O$ at 120°C were finely divided powders and were extremely hygroscopic. The anhydrous SrI_2 prepared by dehydration was pure by X-ray diffraction. The crystallinity of these specimens was good as evidenced by the relatively narrow lines on the X-ray diffraction patterns. No oxidehalide was observed. The structure of this new form of strontium iodide (SrI_2 -IV) was refined by the Rietveld refinement procedure (65) and will be described below. The three iodides are isostructural and their X-ray diffraction patterns are similar. Observed patterns are consistent with calculated ones and are listed in Tables 22-24. Some crystallographic data of these metastable phases, together with those of other known modifications and of the iodide monohydrates, are listed in Table 25 for comparison.

It can be seen from the V/Z data in Table 25 that the new forms of these iodides prepared by low temperature dehydration are 2.5% (EuI_2) to 3.8% (SrI_2) less dense than their normal forms. They therefore can be considered the high temperature forms. Wang and coworkers conducted thermal analysis studies on the SmI_2 system (98). Their results revealed for SmI_2 a reversible polymorphic transformation at 494°C . The high temperature X-ray diffraction pattern (99) was not suitable for indexing, but appeared to be the same as that of SrI_2 -IV. They also reported (100) that by dehydrating $SmI_2 \cdot H_2O$ or $SmI_2 \cdot 0.5H_2O$ at 170 - 180°C for 70 min or at 210 - 240°C for 40 min in a 5×10^{-7} Torr vacuum they obtained a new phase isostructural with the orthorhombic form of EuI_2 , *e.g.* the normal form of strontium iodide, SrI_2 -I. However, the compound we prepared by dehydrating $SmI_2 \cdot H_2O$ at 170 - 180°C is the metastable form isostructural with SrI_2 -IV. No polymorphic transformation of this metastable form was observed even at 250°C in a high vacuum within 3-4 hours. Thus the structure of the compound reported by Wang *et al.* (100) is believed to be the same as SrI_2 -IV instead of being isostructural with SrI_2 -I.

Table 22. Miller indices, and observed (Guinier) and calculated interplanar d-spacings and intensities for SrI_2 -IV.

h	k	l	$d_c(\text{\AA})$	$d_o(\text{\AA})$	I_c	I_o	h	k	l	$d_c(\text{\AA})$	$d_o(\text{\AA})$	I_c	I_o
1	0	1	6.953	6.958	7	w	4	2	0	1.9282	1.9279	17	w ⁺
2	0	0	6.183	6.209	<1	vw	6	1	0	1.9016	1.9011	12	w
2	0	1	4.981	4.984	9	w ⁺	3	2	2	1.8906	1.8891	19	m ⁻
0	1	1	4.255	4.256	10	w	4	2	1	1.8794	1.8796	4	vw
1	1	1	4.0237	4.0251	14	w ⁻	2	1	4	1.8456	1.8450	10	w
1	0	2	3.9801	3.9765	13	w	1	2	3	1.8313	1.8320	1	vw ⁻
2	1	0	3.8564	3.8506	49	s	2	2	3	1.7739	1.7744	1	vw ⁻
3	0	1	3.7009	3.7058	3	vw	4	0	4	1.7382	1.7367	12	m
2	1	1	3.5053	3.5105	1	vw	5	1	3	1.7358		2	
1	1	2	3.0978	3.0901	100	vs	3	2	3	1.6891	1.6895	1	vw ⁻
4	0	0	3.0913		35		4	1	4	1.6394 *		6	---
3	0	2	2.9431	2.9417	36	s	7	1	1	1.6315		2	---
4	0	1	2.9014	2.9032	6	w-	7	0	2	1.6285	1.6279	13	w
1	0	3	2.7332	2.7342	1	vw ⁺	0	3	1	1.6140	1.6136	<1	vw ⁻
4	1	0	2.6196	2.6188	13	w	0	2	4	1.5999	1.5993	14	m
2	0	3	2.5525	2.5530	2	vw	0	1	5	1.5916		1	---
3	1	2	2.5276	2.5246	56	vs	2	3	0	1.5893	1.5894	3	w
4	1	1	2.5010	2.5023	<1	vw ⁻	4	2	3	1.5885		2	
0	2	0	2.4669	2.4653	29	m	1	1	5	1.5786	1.5794	<1	vw
0	1	3	2.4368	2.4380	2	vw	7	1	2	1.5464	1.5464	3	vw ⁺
1	1	3	2.3909	2.3920	3	vw ⁺	8	0	1	1.5202	1.5198	1	w ⁺
1	2	1	2.3249		1	---	1	3	2	1.5200		11	
3	0	3	2.3176	2.3206	2	vw	8	1	0	1.4750	1.4750	4	w ⁻
2	2	1	2.2106	2.2118	2	vw	4	3	0	1.4519	1.4521	2	w ⁻
5	1	1	2.1382	2.1244	4	vw	3	3	2	1.4357	1.4359	9	w
0	0	4	2.1019	2.1002	18	m	7	1	3	1.4302		2	---
1	2	2	2.0968		4		4	2	4	1.4209	1.4204	12	m
4	0	3	2.0763	2.0773	2	vw	6	1	4	1.4102	1.4100	8	w ⁺
3	2	1	2.0527	2.0548	1	vw	7	2	2	1.3591 *		13	---
5	1	2	1.9567	1.9558	12	w	1	1	6	1.3400	1.3398	7	w

Note. Sample was annealed in high vacuum at 250°C for 12 hr.

* overlapping with internal standard Si reflections;

Table 23. Miller indices, and observed (Guinier) and calculated interplanar d-spacings and intensities for SrI_2 -IV-type SmI_2 .

h	k	l	$d_c(\text{\AA})$	$d_o(\text{\AA})$	I_c	I_o	h	k	l	$d_c(\text{\AA})$	$d_o(\text{\AA})$	I_c	I_o
1	0	1	6.947	6.991	14	w	5	1	2	1.948	1.948	5	vw*
2	0	0	6.145	6.165	4	vw	4	2	0	1.916	1.921*	16	w
2	0	1	4.964	4.973	20	w	6	1	0	1.890	1.891	10	w
0	1	1	4.236	4.237	21	w*	3	2	2	1.882	1.880	15	w
1	1	1	4.005	4.011	28	w*	4	2	1	1.868		6	---
1	0	2	3.983		1	---	2	1	4	1.845		3	---
2	1	0	3.832	3.834	18	w	6	1	1	1.844		2	---
3	0	1	3.684		9	---	1	2	3	1.826		2	---
2	1	1	3.488		4	---	2	2	3	1.768		3	---
1	1	2	3.091		100	s	4	0	4	1.737		12	---
4	0	0	3.073	3.084	33	s	5	1	3	1.730	1.732	4	w*
3	0	2	2.936	2.930	30	w*	3	2	3	1.683		3	---
4	0	1	2.886	2.893	10	vw	4	1	4	1.637	1.632	10	vw
1	0	3	2.736		3	---	7	1	1	1.622		4	---
4	1	0	2.603	2.605	20	w	7	0	2	1.620	1.619	15	w
2	0	3	2.553		4	---	0	3	1	1.604		2	---
3	1	2	2.519	2.514	72	m	0	2	4	1.597	1.593	16	w
4	1	1	2.487		2	---	0	1	5	1.593		2	---
0	2	0	2.451	2.453	32	w*	1	3	1	1.591		2	---
0	1	3	2.436		4	---	4	2	3	1.582		3	---
1	1	3	2.389	2.386	8	vw*	1	1	5	1.580		2	---
3	0	3	2.316	2.315	4	vw	7	1	2	1.539		3	---
1	2	1	2.311		2	---	1	3	2	1.512	1.511	11	w
2	1	3	2.264		1	---	8	1	0	1.466		4	---
2	2	1	2.198	2.201	5	vw	4	3	0	1.443		3	---
5	1	1	2.126		7	---	3	3	2	1.428	1.427	12	vw*
0	0	4	2.105	2.097	20	w*	4	2	4	1.417	1.414	11	vw
4	0	3	2.072		4	---	6	1	4	1.406	1.403	7	vw
3	2	1	2.041		4	---	7	2	2	1.352	1.351	16	w

Note. Observed lines are broad.

* overlapping with one internal standard Si reflections.

Table 24. Miller indices, and observed (Guinier) and calculated interplanar d-spacings and intensities for SrI_2 -IV-type EuI_2 .

h	k	l	$d_c(\text{\AA})$	$d_o(\text{\AA})$	I_c	I_o	h	k	l	$d_c(\text{\AA})$	$d_o(\text{\AA})$	I_c	I_o
1	0	1	6.911	6.928	14	w	6	1	0	1.8866	1.8883	10	w
2	0	0	6.136	6.142	4	vw	3	2	2	1.8746	1.8760	15	m ⁻
2	0	1	4.947	4.948	20	w	4	2	1	1.8629	1.8646	6	vw
0	1	1	4.218	4.222	21	w ⁺	6	1	1	1.8404		2	---
1	1	1	3.989	3.988	28	w ⁺	2	1	4	1.8342	1.8348	3	w
1	0	2	3.958		1	---	1	2	3	1.8169		2	---
2	1	0	3.822	3.817	18	m	2	2	3	1.7599	1.7627	3	vw ⁻
3	0	1	3.674	3.676	9	vw	4	0	4	1.7277	1.7276	12	m
2	1	1	3.476	3.480	4	vw	5	1	3	1.7236		4	---
1	1	2	3.075		100	vs	3	2	3	1.6759	1.6764	3	vw ⁻
4	0	0	3.068	3.068	33		4	1	4	1.6288	1.6298	10	w
3	0	2	2.924	2.925	30	s ⁻	7	1	1	1.6189		4	
4	0	1	2.880	2.882	10	vw	7	0	2	1.6168	1.6176	15	m ⁻
1	0	3	2.718	2.723	3	vw	0	3	1	1.5984		2	---
4	1	0	2.598	2.601	20	m	0	2	4	1.5883	1.5889	16	m
2	0	3	2.532	2.543	4	vw	1	3	1	1.5850		2	---
3	1	2	2.509	2.508	72	s	0	1	5	1.5824		2	---
4	1	1	2.481		2	---	4	2	3	1.5761	1.5725	3	vw ⁻
0	2	0	2.4426	2.4414	32	m ⁺	1	1	5	1.5694		2	---
0	1	3	2.4212	2.4246	4	vw	7	1	2	1.5349	1.5378	3	vw
1	1	3	2.3754	2.3753	8	w	8	0	1	1.5089		2	---
3	0	3	2.3036		4		1	3	2	1.5059	1.5067	11	m ⁻
1	2	1	2.3030	2.3086	2	w ⁻	4	0	5	1.4696		2	---
2	1	3	2.2522	2.2560	1	vw	8	1	0	1.4635	1.4654	5	vw
2	2	1	2.1902	2.1932	5	w ⁻	4	3	0	1.4383	1.4388	3	vw ⁻
5	1	1	2.1214	2.1244	7	w	3	3	2	1.4227	1.4237	12	w
0	0	4	2.0908	2.0896	20	m	7	1	3	1.4203		3	---
4	0	3	2.0631	2.0657	4	vw	4	2	4	1.4105	1.4118	11	w
3	2	1	2.0342	2.0385	4	vw	6	1	4	1.4006	1.4025	7	w
5	1	2	1.9422	1.9433	5	w	7	2	2	1.3482	1.3498	16	w
4	2	0	1.9109	1.9115	16	w ⁺							

Note. The sample was annealed in a high vacuum at 310°C for 6 h.

Table 25. Comparison of selected crystallographic data of Ml_2 and $\text{Ml}_2\cdot\text{H}_2\text{O}$.

Compound	Structure*	a (Å)	b (Å)	c (Å)	β (°)	V/Z (Å ³)	Reference
$\text{SrI}_2\cdot\text{H}_2\text{O}$	P n m a	12.474(2)	4.495(1)	9.741(2)		136.6	<u>85</u>
		12.501(3)	4.473(1)	9.740(2)		136.2	this work
	$\text{SrI}_2\text{-IV}$	12.365(2)	4.9338(8)	8.408(1)		128.2	this work
SrI_2	$\text{SrI}_2\text{-I}$	15.22(6)	8.22(3)	7.90(3)		123.5	<u>82</u>
	$\text{SrI}_2\text{-II}$	11.23(2)	8.889(10)	4.630(8)		115.5	<u>84</u>
$\text{SmI}_2\cdot\text{H}_2\text{O}$	P n m a	12.472(3)	4.510(1)	9.711(3)		136.6	this work
	$\text{SrI}_2\text{-IV}$	12.290(8)	4.902(3)	8.421(7)		126.8	this work
SmI_2	$\text{Eul}_2\text{-I}$	7.623(2)	8.280(2)	7.903(2)	97.92(2)	123.5	this work
	$\text{SrI}_2\text{-II}$	11.208(6)	8.886(5)	4.579(4)		114.0	<u>84</u>
$\text{EuI}_2\cdot\text{H}_2\text{O}$	P n m a	12.414(2)	4.4867(7)	9.696(2)		135.0	this work
	$\text{SrI}_2\text{-IV}$	12.272(2)	4.8852(8)	8.363(1)		125.4	this work
EuI_2	$\text{Eul}_2\text{-I}$	7.62(2)	8.23(2)	7.88(2)	98.0(5)	122.3	<u>83</u>
	$\text{SrI}_2\text{-I}$	15.12(3)	8.18(2)	7.83(2)		121.0	<u>83</u>
	$\text{SrI}_2\text{-II}$	11.184(3)	8.893(2)	4.575(1)		113.8	<u>84</u>

* Note. The structure types are:

- (1) $\text{SrI}_2\text{-I}$, normal form, orthorhombic, space group P b c a (#61);
- (2) $\text{SrI}_2\text{-II}$, high-pressure form, PbCl_2 -type structure (orthorhombic, space group P b n m (#62);
- (3) $\text{SrI}_2\text{-III}$, high-pressure form, probably orthorhombic. Structure unknown. See reference 84;
- (4) $\text{SrI}_2\text{-IV}$, metastable form, orthorhombic, space group P n m a (#62);
- (5) $\text{EuI}_2\text{-I}$, normal form, monoclinic, space group P 2₁/c (#14).

4.3 The Structure of $\text{SrI}_2\text{-IV}$ by X-ray Rietveld Refinement

Data collection and Rietveld refinement details are summarized in Table 26. The observed, calculated and difference patterns are presented in Figure 12; positional and thermal parameters are listed in Table 27. Estimated standard deviations (ESD's) are calculated according to Scott (101) and are 5-7 times larger than those reported by the XRS82 system in the absence of this option. Selected $\text{SrI}_2\text{-IV}$ and $\text{SrI}_2\text{-I}$ (normal form) bond distances are compared in Table 28.

The $\text{SrI}_2\text{-IV}$ structure is centrosymmetric. Refinement could not be effected in non-centrosymmetric space group $\text{Pn}2_1\text{a}$; the z coordinates exhibited large shift/error ratios even when the x and y coordinates were refined initially. The $\text{SrI}_2\text{-IV}$ lattice parameters derived from Guinier film data are slightly larger than those derived through the Rietveld refinement. Generally the lattice parameters refined in the Rietveld procedure are believed to be more accurate. However, these parameters in our case were not stable and the standard errors were exceedingly small, presumably due to program errors. Since the Guinier data are referenced to NBS certified Si, these values are considered more accurate in this work.

A significance test based on \bar{R} factors with 2623 observations, the number whose intensity is 20 counts above the sum of background and the standard deviation of the count rate at that position, suggests that the iodine anisotropic temperature factors are significant at greater than the 95 % confidence level (102).

An ORTEP drawing of the monocapped trigonally prismatic coordination of Sr is shown in Figure 13(b), and the atomic packing is presented in Figure 14. The Sr coordination polyhedron in $\text{SrI}_2\text{-IV}$ is similar to that of Sr in $\text{SrI}_2\cdot\text{H}_2\text{O}$ (85) when the water molecules are ignored (Figure 13(a)). It is also similar to the metal coordination polyhedron in the normal form of MI_2 (Figure 13(c)) ($\text{M} = \text{Sr, Eu}$) ($\text{SrI}_2\text{-I}$ type) (81,82), and

in the monoclinic EuI_2 structure (83), but with one major difference. In the $\text{SrI}_2\text{-IV}$ coordination polyhedra (Figure 13(b)) a mirror plane coincident with the lattice mirror plane passes through atoms $\text{I}(1)^{\text{II}}$, $\text{I}(2)^{\text{IV}}$, $\text{I}(1)^{\text{V}}$ and Sr^{I} , and relates $\text{I}(1)^{\text{I}}$ to $\text{I}(1)^{\text{II}}$ and $\text{I}(2)^{\text{I}}$ to $\text{I}(2)^{\text{II}}$; the cation coordination polyhedra of the $\text{SrI}_2\text{-I}$ and monoclinic EuI_2 structure types are devoid of symmetry. This mirror plane, which is perpendicular to the b axis, is apparent in Figure 14(a).

The average Sr-I bond lengths of $\text{SrI}_2\text{-IV}$ and $\text{SrI}_2\text{-I}$ are nearly identical. However, the iodine atoms do not relax to fill completely the coordination sites vacated by the H_2O . Thus the metastable form is less dense than is $\text{SrI}_2\text{-I}$ (4.45 vs. 4.59 g cm^{-3} respectively). The openness of the structure is also reflected in the molar volume, 77.3 cm^3/mol , a value close to that of the monohydrate, 82.24 cm^3/mol . Such packing inefficiency might be expected because low preparatory and annealing temperatures mitigate against atomic rearrangement. The capping iodide in $\text{SrI}_2\text{-IV}$, $\text{I}(1)^{\text{V}}$, has a rather long bond distance in comparison to the corresponding $\text{SrI}_2\text{-I}$ distance. The corresponding bond in the hydrate is opposite to those of coordinated water molecules. Its elongation in the hydrate is apparently due both to the decreased acidity of the strontium atom because of the H_2O bonding and the more crowded coordination sphere that results. During the low energy dehydration all the $\text{SrI}_2\text{-IV}$ atoms remain locked in the $4c$ special positions just as they were in the monohydrate; the minor relaxations that occur are insufficient to revert the lattice to the more efficiently packed $\text{SrI}_2\text{-I}$.

Two types of anion coordination are present in the structure. Atom $\text{I}(1)$ is coordinated in a distorted tetrahedral arrangement to four cations, whereas atom $\text{I}(2)$ is coordinated in a capped trigonal arrangement to only three. These can be visualized clearly in Figure 14(b).

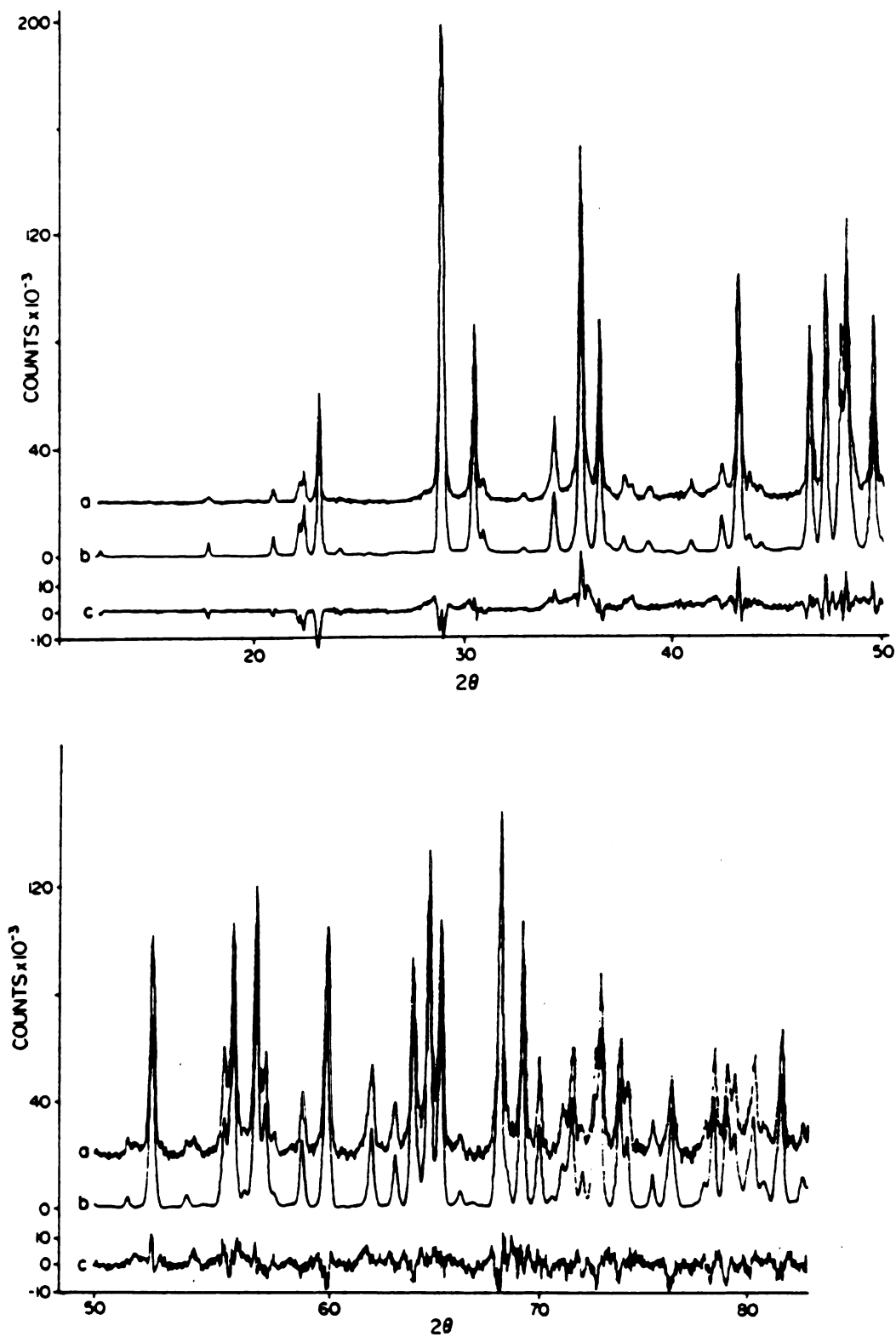


Figure 12. Observed (a), calculated (b), and difference (c) X-ray diffraction patterns for $\text{SrI}_2\text{-IV}$.

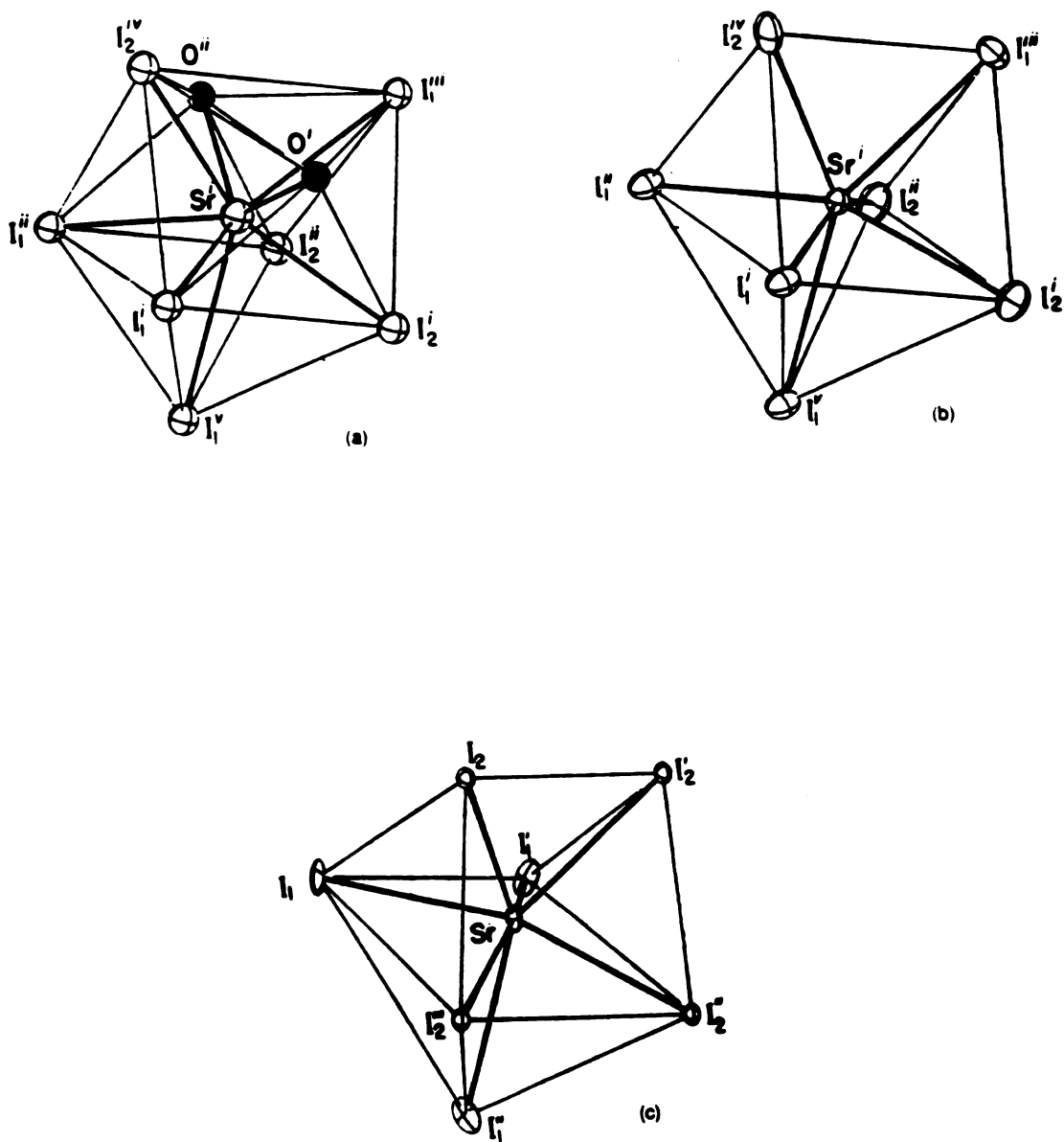


Figure 13. Comparison of several metal coordination polyhedra. (a) $\text{SrI}_2 \cdot \text{H}_2\text{O}$ with H atoms omitted; (b) $\text{SrI}_2 \cdot \text{IV}$; (c) $\text{SrI}_2 \cdot \text{I}$ (normal form).

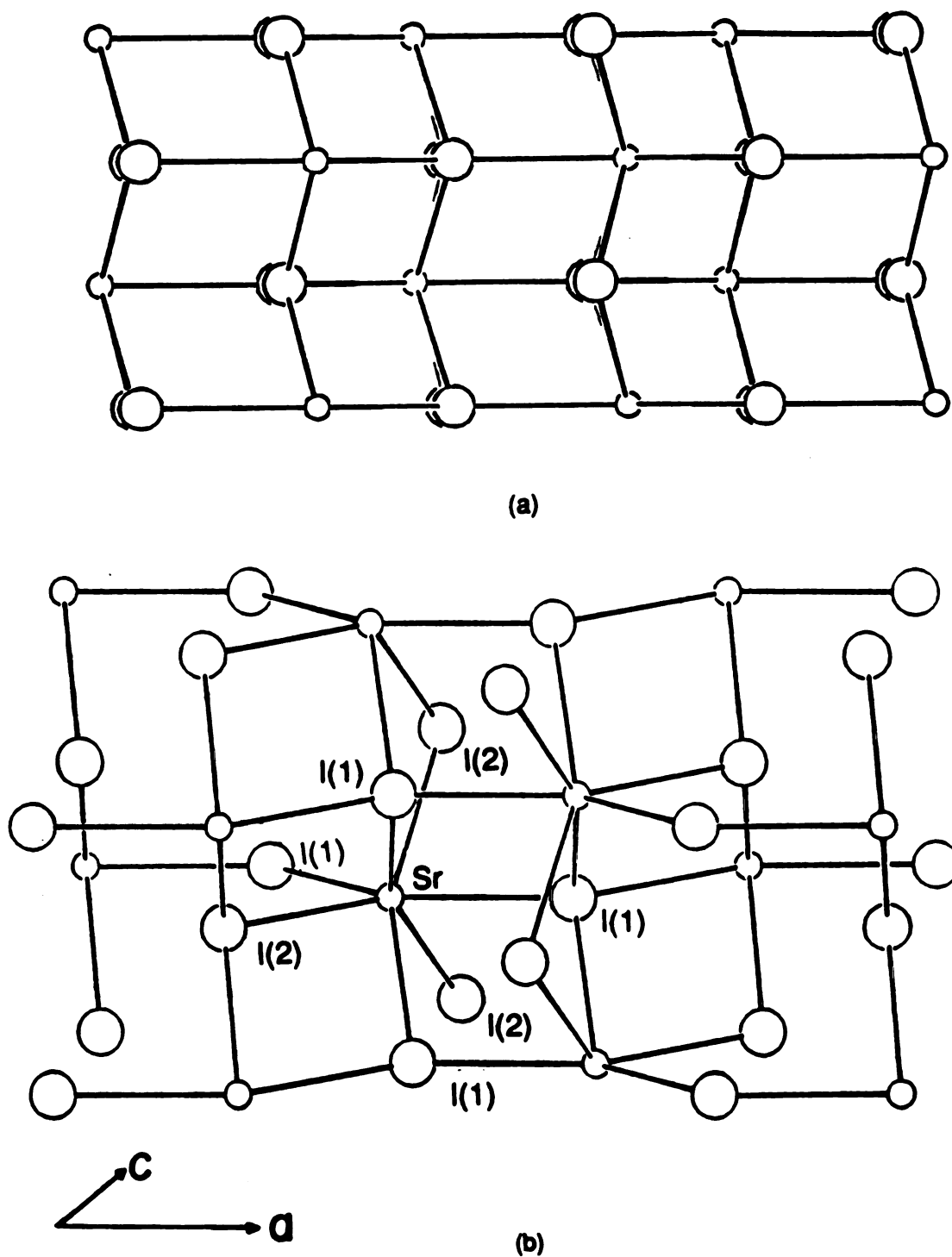


Figure 14. C-axis projection of the $\text{SrI}_2\text{-IV}$ structure illustrating the atomic packing. (a) mirror planes and layer character are shown clearly; (b) the structure is projected and then rotated along the a axis to reveal the coordination polyhedra.

Table 26. Crystallographic and Rietveld refinement data for SrI_2 -IV.

Pattern 2θ (deg)	10-85
Step size 2θ (deg)	0.020
Count time (sec/step)	20
Standard peak: hkl (2θ)	210, (23.10°)
R (standard peak)	0.036
Space group (number), Z	<u>Pnma</u> (62), 4
Systematic extinctions	<u>hk0</u> : $h = 2n+1$ <u>0kl</u> : $k+l = 2n+1$
<u>a</u> (Å)	12.328(2)
<u>b</u> (Å)	4.920(1)
<u>c</u> (Å)	8.384(1)
Volume (Å ³)	509.3
Density (D_x , g·cm ⁻³)	4.452
Number of observations	3682
Number of reflections	196
No. of refined structural parameters	19
No. of refined profile parameters	9 (incl. <u>a</u> , <u>b</u> , <u>c</u>)
$R_f = \Sigma F_o - F_c / \Sigma F_o$	0.069
$R_f = \Sigma (F_o^2 - F_c^2) / \Sigma F_o^2$	0.087
$R_p = \{ \Sigma [y(o) - y(c)/c]^2 / \Sigma y(o)^2 \}^{1/2}$	0.188
$R_{wp} = \{ \Sigma w[y(o) - y(c)/c]^2 / \Sigma w y(o)^2 \}^{1/2}$	0.184
Maximum shift/error	0.09

Table 27. Positional and thermal parameters for Srl₂-IV.

Atom	<u>x</u>	<u>y</u>	<u>z</u>	<u>U</u> ^a	<u>U</u> ₁₁ ^{ac}	<u>U</u> ₂₂ ^{ac}	<u>U</u> ₃₃ ^{ac}	<u>U</u> ₁₂ ^{ac}
Sr	0.170(1)	0.25	0.130(5)	11(4)				
I(1)	0.392(1)	0.25	0.377(3)	[23(4)] ^b	20(9)	27(11)	27(11)	14(14)
I(2)	0.380(1)	0.25	0.883(3)	[32(5)] ^b	37(11)	40(13)	17(12)	13(15)

^a $\times 10^3$ (Å²).

^b from isotropic refinement; form: $\exp\{-8\pi^2 U(\sin\theta/\lambda)^2\}$.

^c Anisotropic factor form: $\exp[-(h^2\beta_{11}+2hk\beta_{12}+...)]$; $\beta_{11} = (2\pi^2 U_{11} a_1^2)$.

Table 28. Comparison of selected Srl₂-IV and Srl₂-I bond distances.

Srl ₂ -IV	Bond distance (Å)	Srl ₂ -I	Bond distance (Å)
Sr-I(1) ⁱ	3.34(3)	Sr-I(2) ⁱⁱⁱ	3.369(8)
Sr-I(1) ⁱⁱ	3.34(3)	Sr-I(1)	3.268(10)
Sr-I(2) ⁱ	3.31(2)	Sr-I(2) ⁱⁱⁱ	3.339(9)
Sr-I(2) ⁱⁱ	3.31(2)	Sr-I(1) ⁱ	3.258(9)
Sr-I(1) ⁱⁱⁱ	3.43(3)	Sr-I(2) ⁱ	3.415(9)
Sr-I(2) ^{iv}	3.31(3)	Sr-I(2)	3.417(8)
Sr-I(1) ^v	3.44(2)	Sr(1) ⁱⁱⁱ	3.390(11)
Average			
Sr-7xl	3.35	Sr-7xl	3.351
I(1)-4xSr	3.38	I(2)-4xSr	3.385
I(2)-3xSr	3.31	I(1)-3xSr	3.305

4.4 Thermal Stabilities of Metastable Phases

The fluorite modifications of EuCl_2 and SmCl_2 are definitely stable toward phase transformations at ambient temperature. After 9 h at 300°C only a very small fraction of the fluorite forms of both chlorides had transformed. Even after 11 h at 360°C or 4 h at 430°C only a portion of the EuCl_2 specimen had transformed to the normal PbCl_2 -type structure. At 440°C the fluorite form of SmCl_2 (blue) changed quantitatively into the thermodynamically stable low-temperature (red) form within hours.

Similarly transformation of the "high pressure" forms of BaX_2 ($\text{X}=\text{Cl}, \text{Br}$) occurs only at temperatures far higher than the solvolytic decomposition temperatures. The anti- Fe_2P -form of BaCl_2 at 350°C and that of BaBr_2 at 300°C evidenced no obvious change in 6 h in a vacuum of 10^{-6} to 10^{-7} Torr. At 400°C about 90% of the former transformed into the PbCl_2 -type (the thermodynamically stable form) within 5 h, and about 50% of the latter transformed in 7 h. All these results confirm that the new forms are metastable phases and their formation is kinetically controlled.

4.5 Solvolytic Decomposition Intermediates

We observed formation of a crystalline intermediate in our early studies (72) when some $\text{Ba}_5\text{Ln}_5\text{Br}_{33}$ ($\text{Ln}=\text{La}, \text{Nd}$) precursors were examined after 30 min of extraction by THF. Later experiments revealed similar behavior in other systems. It is clear now that the intermediates are actually lanthanide trihalide THF complexes.

The triclinic intermediate we reported (72) is $\text{NdBr}_3(\text{THF})_4$. This composition was determined by the weight loss of the complex when it was heated gradually at 130°C for many hours in a high vacuum and the product was identified as the normal form of NdBr_3 . Its powder X-ray diffraction pattern is identical with that of a sample prepared by contacting anhydrous NdBr_3 with THF, and then evacuating to dryness. With 1-3 g of

precursor containing LnBr_3 , the complex was apparently observable in the X-ray diffraction patterns after 3 h of extraction. Miller indices, observed intensities, observed and calculated interplanar d-spacings for $\text{NdBr}_3(\text{THF})_4$ are listed in Table 29.

The $\text{EuCl}_3(\text{THF})_n$ ($1 < n < 2$) complex that formed after 30 min THF extraction of EuCl_{2+x} mixed-valent chlorides containing free EuCl_3 had the same X-ray diffraction pattern as that formed between pure EuCl_3 and THF. This compound was not observed by X-ray diffraction after 6 h. When a pure precursor Eu_4Cl_9 was used the complex was not observable even after 30 min extraction. However, solid state FTIR spectra of these specimens indicated a trace of the THF complex even after 5 h extraction. Fifteen hours later it was not visible by IR. A typical IR spectrum of $\text{EuCl}_3(\text{THF})_n$ is shown in Figure 15.

The mixed-valent chlorides LnCl_{2+x} ($\text{Ln}=\text{Sm}, \text{Eu}$) were decomposed quickly by THF; mixed $\text{Ba}_9\text{Ln}_5\text{Br}_{33}$ was also decomposed quickly, but less rapidly than the LnCl_{2+x} . Extraction of $\text{BaCl}_2\text{-LnCl}_3$ mixed halides proceeded much more slowly. The color change from blue or black to white when EuCl_{2+x} was leached became apparent almost instantly. When the specimens were examined by X-ray diffraction, no trace of the mixed-valent precursor EuCl_{2+x} was observed even after 30 min extraction while the mixed halide precursor $\text{Ba}_{17}\text{Sm}_{10}\text{Cl}_{64}$ disappeared only in a course of 5-6 days. In all the systems examined no trace of any other new phase was observed.

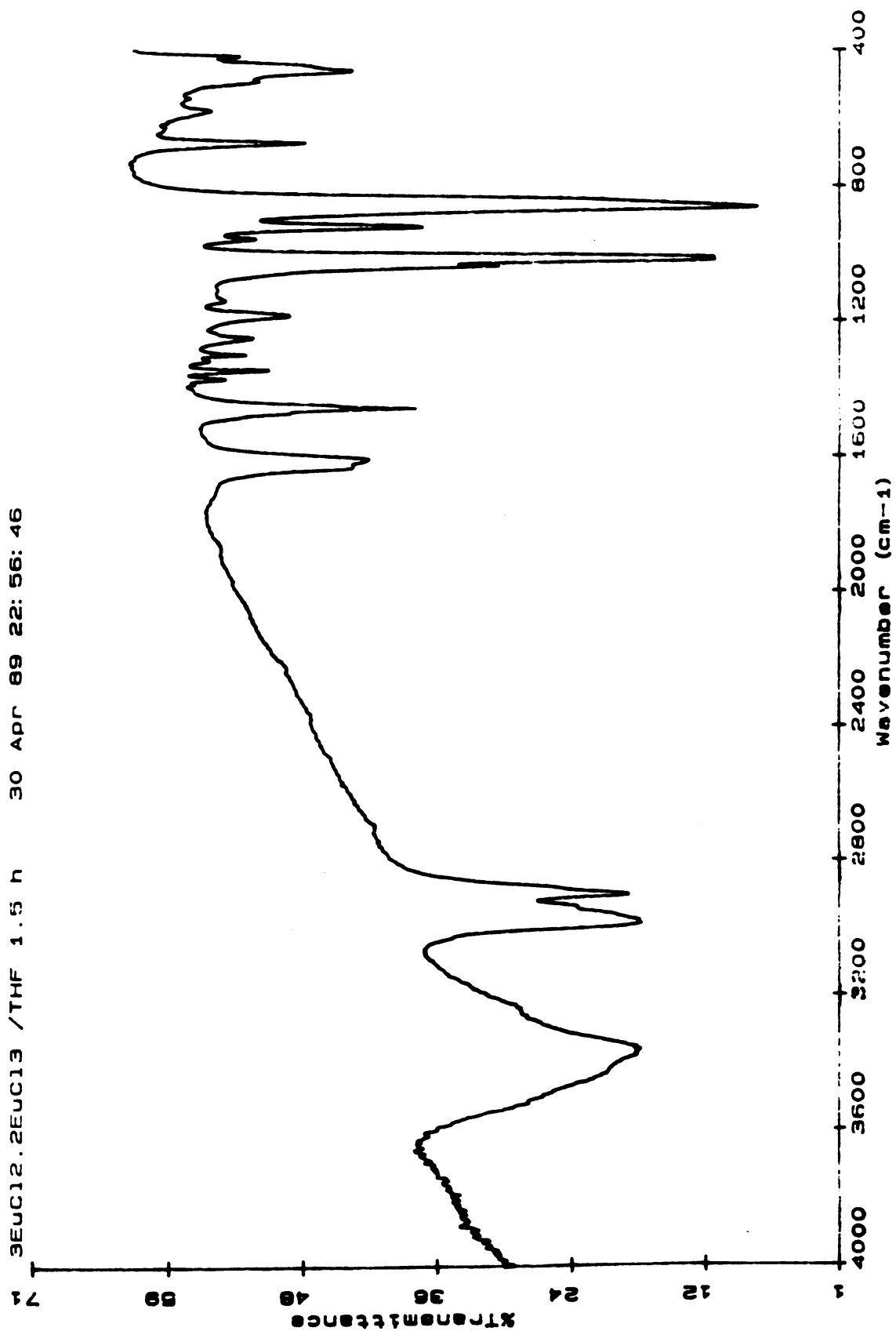


Figure 15. FTIR spectrum of $\text{EuCl}_3(\text{THF})_6$ (KBr pressed pellet).

Table 29. Miller indices, observed (Guinier) intensities, and observed and calculated interplanar d-spacings for triclinic $\text{NdBr}_3(\text{THF})_4$; $a = 8.352(1)$, $b = 15.915(3)$, $c = 9.429(1)$ Å; $\alpha = 100.02(2)$, $\beta = 105.26(2)$, and $\gamma = 87.54(2)^\circ$.

#	h	k	l	$d_c(\text{\AA})$	$d_o(\text{\AA})$	I_o	#	h	k	l	$d_c(\text{\AA})$	$d_o(\text{\AA})$	I_o
1	0	1	0	15.672	15.696	vw ⁺	27	0	3	1	4.2149		
2	0	0	1	8.9660	8.9626	s	28	-1	-2	2	4.1688	4.1707	vw
3	0	-1	1	8.4190	8.4083	s	29	0	1	2	4.1298	4.1306	vw
4	1	0	0	8.0578	8.0438	vs	30	-1	1	2	4.0962		
5	0	2	0	7.8362	7.8352	vs	31	-2	0	1	4.0942	4.0941	m ⁻
6	0	1	1	7.2714	7.2727	m	32	1	-3	1	3.9428		
7	-1	1	0	7.1750	7.1675	vw ⁺	33	-1	3	1	3.9421	3.9414	m ⁺
8	1	1	0	7.1573			34	-2	1	0	3.9049		
9	-1	0	1	6.9595	6.9579	w ⁺	35	2	1	0	3.9992	3.9048	vw
10	-1	-1	1	6.6870	6.6894	w ⁺	36	-2	1	1	3.8915	3.8930	vw
11	0	-2	1	6.4658	6.4666	w	37	0	-4	1	3.8357	3.8369	vw ⁺
12	-1	1	1	6.0777	6.0732	m ⁻	38	-2	-2	1	3.7442	3.7441	vw
13	-1	2	0	5.6263			39	-1	-3	2	3.6976	3.6976	vw
14	1	2	0	5.6092	5.6123	s	40	-1	-4	1	3.6186		
15	-1	-2	1	5.5708	5.5704	vw ⁺	41	-1	2	2	3.6139	3.6151	w ⁻
16	0	3	0	5.2241			42	-2	2	0	3.5875	3.5865	w
17	1	-1	1	5.2230	5.2230	w ⁺	43	1	-1	2	3.5631	3.5619	w
18	1	1	1	4.9054			44	-2	2	1	3.5234		
19	-1	2	1	4.9006	4.9020	w ⁺	45	1	4	0	3.5194	3.5212	w
20	0	-3	1	4.8869			46	1	-2	2	3.4074	3.4058	w ⁻
21	1	-2	1	4.6414	4.6448	w	47	-2	-3	1	3.3449	3.3476	vw
22	0	-1	2	4.5164	4.5166	w	48	-2	-2	2	3.3435		
23	0	0	2	4.4830	4.4851	vw ⁻	49	-2	3	1	3.1126	3.1121	vw ⁺
24	-1	-1	2	4.4684	4.4662	vw ⁻	50	-2	-3	2	3.0846	3.0843	vw
25	-1	-3	1	4.4621			51	1	2	2	3.0781		
26	1	2	1	4.2174	4.2175	w ⁺	52	-1	0	3	3.0748	3.0750	vw

Table 29. (continued)

#	h	k	l	$d_c(\text{\AA})$	$d_o(\text{\AA})$	l_o	#	h	k	l	$d_c(\text{\AA})$	$d_o(\text{\AA})$	l_o
53	-2	2	2	3.0389			72	0	2	3	2.6476		
54	0	-1	3	3.0314	3.0332	vw ⁺	73	-2	-3	3	2.6198	2.6197	vw ⁺
55	-1	-5	1	3.0062	3.0074	vw ⁺	74	1	-1	3	2.6193		
56	0	0	3	2.9887	2.9883	w	75	1	0	3	2.5911	2.5912	vw ⁺
57	0	-2	3	2.9640	2.9651	vw	76	1	5	1	2.5900		
58	-2	-4	1	2.9415	2.9409	w	77	2	1	2	2.5896		
59	0	1	3	2.8486	2.8463	w	78	-3	2	1	2.5797		
60	0	5	1	2.8146			79	1	-2	3	2.5759	2.5768	vw
61	-2	4	0	2.8132	2.8129	w	80	-1	-6	1	2.5558	2.5556	vw ⁺
62	0	-3	3	2.8063	2.8060	vw	81	3	2	0	2.5384	2.5392	vw
63	2	4	0	2.8046			82	-2	-5	2	2.4936		
64	-1	-5	2	2.7867	2.7878	vw	83	-2	2	3	2.4930	2.4929	vw
65	-2	-4	2	2.7854			84	2	-3	2	2.4839		
66	-2	-2	3	2.7477	2.7484	vw ⁺	85	1	6	0	2.4826	2.4830	w
67	2	3	1	2.7464			86	2	4	1	2.4725		
68	-2	3	2	2.7384	2.7382	vw	87	1	-3	3	2.4707	2.4712	w
69	-1	2	3	2.7079	2.7085	vw	88	-3	-3	2	2.4407	2.4405	vw
70	-3	-2	1	2.6609	2.6610	w	89	-3	2	2	2.4196	2.4203	w
71	-3	1	0	2.6487	2.6492	vw	90	-1	-5	3	2.4129	2.4119	w

CHAPTER 5 DISCUSSION

SYNOPSIS

Synthesis conditions are discussed. Reactions that yield metastable phases are analyzed in thermodynamic and kinetic terms and are shown through layer descriptions to be topologically controlled with minimal structural reorganizations. The low-temperature high-vacuum dehydrations do not involve major structural changes while changes that occur during solvolytic decompositions are significant. In-layer atomic rearrangement of the intermediate lattice leads to formation of the fluorite-type structure; further out-of-layer displacement yields the anti-Fe₂P-type structure.

5.1 Solvolytic Decomposition

5.1.1 Energetics

As has been pointed out in Chapter 2, for a solvolytic decomposition reaction that produces a thermodynamically less stable form to occur, the leaching solvent must form a strong complex to compensate for the loss of lattice energy. On the other hand, the stability of the metastable form relative to that of the mixed precursor is also important. The inability to prepare NdCl_2 by solvolytic decomposition of NdCl_{2+x} could be attributed to instability of the assumed fluorite form of NdCl_2 . This fluorite form would be the expected direct product of a leaching experiment because of the similarity of structural properties of neodymium compounds and those of the samarium and europium analogues (ionic radius (28): Nd^{2+} , 1.43; Sm^{2+} , 1.41; Eu^{2+} , 1.39 Å). The normal form of NdCl_2 (PbCl_2 -type), even though preparable by neodymium or lithium reduction, is apparently much less stable than that of LnCl_2 ($\text{Ln} = \text{Sm}, \text{Eu}, \text{Yb}$). The fluorite form of NdCl_2 is thus expected to be highly unstable at ambient conditions. The low solubility of the $\text{NdCl}_3 \cdot x\text{THF}$ solvate in THF, another energetically unfavorable factor, could also contribute to the difficulty of NdCl_2 formation through leaching.

Contamination of mixed(-valent) halide precursors by oxidehalide impurities may also hinder solvolytic decompositions. Many of the mixed halide precursors have cluster-type structures. Given the moisture sensitivity of $\text{M}^{2+}_6\text{Ln}^{3+}_5\text{X}_{33}$ phases and the formation of oxidehalide phase, $\text{Nd}^{2+}_6\text{Nd}^{3+}_6\text{Cl}_{32}\text{O}$, whose structure is almost indistinguishable from that of the Nd_4X_{33} phases, the oxidehalide impurities in the mixed(-valent) halides must be considered. Oxidehalides are expected to have higher lattice energies than those of the mixed halides because $\text{M}=\text{O}$ bonds are stronger than $\text{M}-\text{Cl}$ bonds. In the oxidehalide structure oxygen atoms occupy the cluster centers (38) where the structure undergoes

significant changes upon solvolytic decomposition. Therefore the $M_8Ln_8X_{32}O$ structure is probably too difficult to be decomposed by THF. The fact that the " $Sm_8Gd_5Cl_{33}$ " specimens prepared by the ceramic method could be only partially extracted by THF probably resulted from contamination by oxygen. That is, the specimen may have contained $Sm_8Gd_5Cl_{32}O$ or $Sm_8Gd_5Cl_{32}O$. Oxygen could come from the quartz container.

For the various samarium mixed chlorides prepared by hydrogen reduction, the formulation $Sm_8M_5Cl_{13}$ ($M = Gd$ and Nd) was based upon X-ray and mass balance data since $GdCl_3$ cannot be reduced to a discrete Gd^{2+} ion even when elemental Gd is the reducing agent. $NdCl_3$, on the other hand, can be reduced to $NdCl_2$ with strong reducing agents (103,104) but not with hydrogen (105). Oxidehalide contamination was probably a problem, especially in the $SmCl_2$ - $NdCl_3$ system in which a substantial amount of the " M_4X_{33} " phase was unbreakable even though fluorite-type $SmCl_2$ did form.

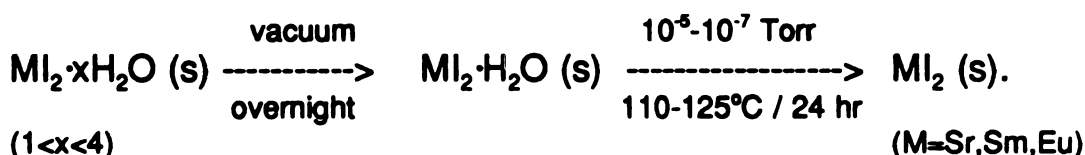
Based on these considerations, efforts should be devoted to the elimination of oxidehalides during the preparation of mixed or mixed-valent halides. Oxygen- and water-free conditions are essential. Lower temperatures and shorter heating times also tend to minimize oxidehalide contamination possibilities. For the europium mixed-valent chlorides the various methods used, partial reduction with hydrogen, thermal decomposition, and even solid state reactions between $EuCl_2$ and $EuCl_3$, did produce fairly pure compounds that could be decomposed completely by THF. For the samarium mixed chlorides, hydrogen reduction of the $SmCl_3$ - $GdCl_3$ 1:1 mixture gave the best result. The barium mixed bromides were not obviously subject to oxygen contamination. But the barium chloride precursors, especially the $BaCl_2$ - $LaCl_3$ system that required reaction temperatures above $800^\circ C$, may have contained some oxidechloride since complete extraction was not achieved. $BaCl_2$ is known to attack quartz at high temperatures (8). $Ba_{17}Sm_{10}Cl_{64}$ is a better precursor than " Ba_2LaCl_7 ".

5.1.2 Solvent Effect

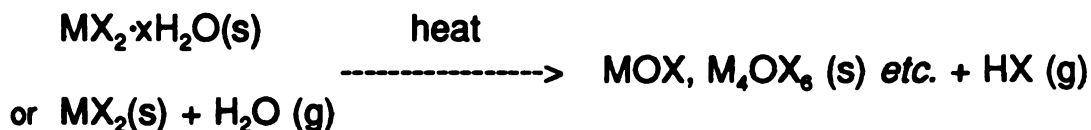
The choice of an appropriate solvent is important to the success of a solvolytic decomposition reaction. However, this choice is usually severely limited by solubility requirements. THF is a good solvent for the lanthanide chlorides and barium bromide. The lanthanide trichlorides are soluble in THF and are expected to form more stable complexes with THF than with pyridine. The reason that the barium mixed chlorides can be leached by pyridine but not by THF is unknown.

5.2 Low-Temperature Dehydration

To monitor the degree of dehydration higher hydrates were always converted first to monohydrates. This step proceeded easily at temperatures lower than 80°C under a dynamic vacuum. Removal of the last mole of water from monohydrates usually requires temperatures higher than 80°C. Previous thermal studies had shown that the $\text{SrI}_2 \cdot \text{H}_2\text{O}$ to SrI_2 conversion occurs at 280°C or even higher temperatures under normal pressure (106). Under the high vacuum conditions of our experiments the dehydration temperature decreases as low as 110°C. At this temperature loss of water is much slower than at 280°C, but dehydration was usually complete within 24 h. The process may be summarized as follows:



Such a low temperature or a high vacuum is not always necessary. For example, $\text{EuI}_2 \cdot \text{H}_2\text{O}$ can be dehydrated at 220-230°C in a 10^{-2} Torr vacuum in 24 h; $\text{SmI}_2 \cdot \text{H}_2\text{O}$ can be dehydrated at 170-180°C in 10^{-7} Torr within about 1 h (98). However, it is important to perform the experiment at a lower temperature to insure that the reaction proceeds slowly. Slow removal of water molecules with minimal disturbance of the crystal lattice is the key to the synthesis of a metastable modification. Fast dehydration at high temperatures can lead to a mixture or to formation of a different modification from that obtained by slow dehydration (8). In addition, low temperature dehydration in a high vacuum will prevent the following hydrolysis reactions that may produce oxidehalides such as EuOCl and Sr_4OCl_6 (9).



5.3 Metastable Structures and Low Temperature Decompositions

Fluorite-type modifications of SmCl_2 and EuCl_2 were observed previously at elevated temperatures by X-ray diffraction (107,108), evidenced transformation temperatures of 768 ± 4 (109) and $745 \pm 5^\circ\text{C}$ (110), respectively, and were not quenchable. The anti- Fe_2P -form of BaX_2 ($\text{X}=\text{Cl}, \text{Br}$) prepared by low-temperature solvolytic decompositions could not be synthesized at high temperatures under high pressures. Nor is the unquenchable high temperature form of SmI_2 , also observed by high temperature diffraction above the polymorphic transformation temperature (99). X-ray diffraction pattern of a EuI_2 specimen heated in a sealed quartz tube to near melting (520°C) and quenched in liquid nitrogen gave no trace of the metastable form even though the metastable form can be synthesized by low temperature dehydration. In view of the need to have stable specimens at ambient temperature to study physical properties, it is significant that the low temperature solvolytic decompositions and dehydrations can both provide convenient mild-condition synthesis routes for some known metastable modifications, and provide possibilities to synthesize compounds not easily accessible by other means.

It was mentioned briefly in Chapter 1 that dehydrating $\text{BaCl}_2 \cdot 2\text{H}_2\text{O}$ could yield the metastable "high-pressure" (anti- Fe_2P) form of BaCl_2 . Since in this reaction the metastable form was observed together with the high-temperature form (8), dehydration is not an appropriate synthesis method for anti- Fe_2P -type BaCl_2 . On the other hand, dehydration is a unique low temperature approach (91) to the high temperature form of BaCl_2 . Our room-temperature high-vacuum dehydration experiment with $\text{BaCl}_2 \cdot 2\text{H}_2\text{O}$ yielded only the high-temperature form (CaF_2 -type). In conclusion, dehydration of $\text{BaCl}_2 \cdot 2\text{H}_2\text{O}$ favors the formation of the fluorite-type high-temperature modification of BaCl_2 while solvolytic decompositions on mixed halide precursors uniquely allow synthesis of the high-pressure

form.

A solvolytic decomposition reaction requires that the two components in the precursor have distinctly different solubilities in the solvent. For this reason solvolytic decomposition becomes difficult or impractical for bromides and iodides since they are soluble. For these systems low temperature dehydration or more generally, low temperature desolvation provides an alternative way of achieving the same goal. Slow removal of solvent molecules from a solvate lattice during desolvation resembles the slow removal of the soluble species from the lattice of a mixed precursor in a solvolytic decomposition. In fact, fluorite-type EuCl_2 was observed during dehydration of $\text{EuCl}_2 \cdot \text{H}_2\text{O}$ (9) and the pure "high-pressure" form of BaBr_2 could be prepared by dehydrating $\text{BaBr}_2 \cdot \text{H}_2\text{O}$. Therefore, the two methods are complementary. The combination is applicable to many more systems than is either individual method.

5.4 Formation Mechanism of the Metastable Forms

5.4.1 Kinetics vs. Thermodynamics

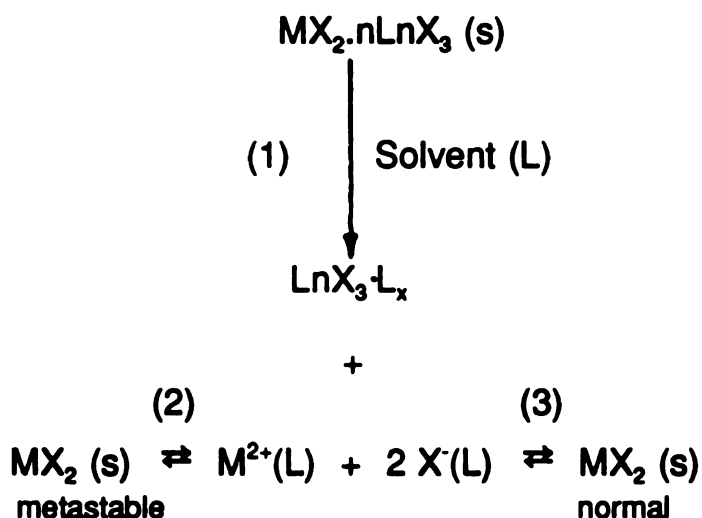
These metastable structures are stable indefinitely at room temperature in the absence of moisture and oxygen. As the thermal results demonstrate, polymorphic transformations into the normal forms take place only at temperatures above 300°C. On the other hand, formation of metastable forms is relatively fast at the reaction temperatures (66-125°C) (see section 4.5). These data indicate fairly low activation energies for the precursor to metastable MX_2 conversions; but high activation energies for the metastable to normal form conversions. Therefore, the metastable forms are trapped as kinetically-controlled products in an energy well.

5.4.2 Topochemical Transformations

Thermodynamic considerations enable us to understand why the metastable modifications are formed, but do not tell us how they are formed and why the precursor to metastable MX_2 conversions have low energy barriers. We must examine our systems at the microscopic level to answer these questions.

At first glance one might speculate that metastable dihalide formation during solvolytic decompositions is a simple dissolution-reprecipitation process. That is, the divalent and trivalent cations with associated anions dissolve together and then the dihalide salts precipitate from solution as metastable solids. Such a mechanism was postulated for the formation of $\gamma\text{-MnO}_2$ when Mn_3O_4 was leached by a mineral acid such as HCl(aq) (23). Mn_3O_4 dissolves into Mn^{2+} and Mn^{3+} ions with the latter disproportionating into Mn^{2+} and $\gamma\text{-MnO}_2$ (s). However, such a dissolution-reprecipitation mechanism for the halides contradicts other experimental results. When $\text{SmCl}_3(\text{THF})_n$ is

reduced in THF, the precipitate, SmCl_2 (s), is the normal (red) (19) rather than the metastable (blue) form. Thus there is a major difference between the mixed halides and Mn_3O_4 . Dihalide salts are only slightly soluble in the solvent, while in Mn_3O_4 both components (MnO and Mn_2O_3) are soluble. Based on thermodynamic considerations, the following equilibria should exist between the solids and the solution:



Were dissolution (1) to occur, the dihalide MX_2 would have to dissolve rapidly since formation of the metastable MX_2 is fast. This is unlikely, if not impossible, because of the very low MX_2 solubility (thus a very small solvation energy), and the need to destroy the entire precursor lattice which would require a high activation energy. Were dissolution of MX_2 rapid and precipitation reaction (2) faster than (3), one would expect a gradual conversion of the metastable form (kinetic product) into the thermodynamically more stable (normal) form. This has not been observed. In addition, if dissolution-reprecipitation is involved, the precipitate should have poor crystallinity because a low temperature rapid precipitation precludes annealing; and the unit cell dimension of the metastable form should be independent of the dimension of the mixed halide precursor. In fact, the

metastable modifications are well crystallized as evidenced by the sharp X-ray reflections. It took only about 30 min for ~1 g Eu_4Cl_6 (s) to be decomposed completely into metastable EuCl_2 (s) and $\text{EuCl}_3(\text{THF})_n$ by THF; no trace of the normal form of EuCl_2 (s) was observed as a result of 24-48 h continuous extraction. In the BaX_2 ($\text{X} = \text{Cl}, \text{Br}$) systems, even though trace amounts of normal forms were observed in the leached product, the fact that lattice parameters of the metastable forms are related to the type of mixed-halide precursor used (Page 117) argues strongly against a dissolution-reprecipitation mechanism.

On the other hand, if the structural changes upon solvolytic decompositions are taken into account, one finds that experimental results can be explained satisfactorily. An important feature of these metastable phases is that they have symmetries higher than those of the corresponding normal forms. The highest symmetry element, the 3-fold inversion axis in the fluorite-related precursors, was retained in both the high-temperature forms of LnCl_2 ($\text{Ln} = \text{Sm}, \text{Eu}$) and the high-pressure forms of BaX_2 ($\text{X} = \text{Cl}, \text{Br}$). It is apparent that the structures of the metastable forms and those of the precursors are closely related. These relationships can be explained in topotactic chemistry terms. The various reactions are discussed separately below.

a. $\text{SrI}_2 \cdot \text{H}_2\text{O}$ to SrI_2 -IV Transformation

The three iodide monohydrates $\text{MI}_2 \cdot \text{H}_2\text{O}$ ($\text{M} = \text{Sr}, \text{Sm}, \text{Eu}$) are isostructural; and so are the metastable iodides MI_2 . To demonstrate the structural changes involved in the monohydrate to anhydrous metastable form transformation, projections of $\text{SrI}_2 \cdot \text{H}_2\text{O}$ and SrI_2 -IV lattices down the shortest (b) axis are shown in Figure 16 and atomic positions of SrI_2 -IV and $\text{SrI}_2 \cdot \text{H}_2\text{O}$ are compared in Table 30.

The $\text{SrI}_2 \cdot \text{H}_2\text{O}$ to SrI_2 -IV transformation is a relatively straightforward topochemical conversion because only water molecules are removed from the precursor lattice. As can be seen in Figure 16, slow removal of coordinated water molecules leaves the frame structure intact except for minor atomic shifts. This can also be seen in Table 30. In fact, it is the topochemical nature of the reaction that allowed us to use $\text{SrI}_2 \cdot \text{H}_2\text{O}$ as a model structure for refinement of the SrI_2 -IV structure.

A significant feature of this topotactic reaction is retention of the mirror planes perpendicular to the b-axis, one of which contains atoms Sr^I , $\text{I}(1)^{\text{III}}$, $\text{I}(2)^{\text{IV}}$ and $\text{I}(1)^{\text{V}}$ in Figure 13 (Page 91), despite the sizable b axis expansion and c axis shortening which resulted from collapse of the parent lattice upon dehydration. Since atomic movements are restricted to the planes, the SrI_2 -IV atoms remain locked in the 4c special positions in the space group as they were in the monohydrate. Since all symmetry transformations are retained, the space group remains unchanged.

Similar features were observed in the topotactic dehydration of the layered oxide hydrates $\text{MO}_3 \cdot \text{H}_2\text{O}$ (3,4). Both $\text{SrI}_2 \cdot \text{H}_2\text{O}$ and SrI_2 -IV also can be viewed as layer-like structures (Figure 14(a), Page 92). The major difference is that the interlayer distance (b axis) of the iodide increases while that of the oxide decreases upon dehydration, a result apparently attributable to the mobility of atoms in the dominantly ionic iodides.

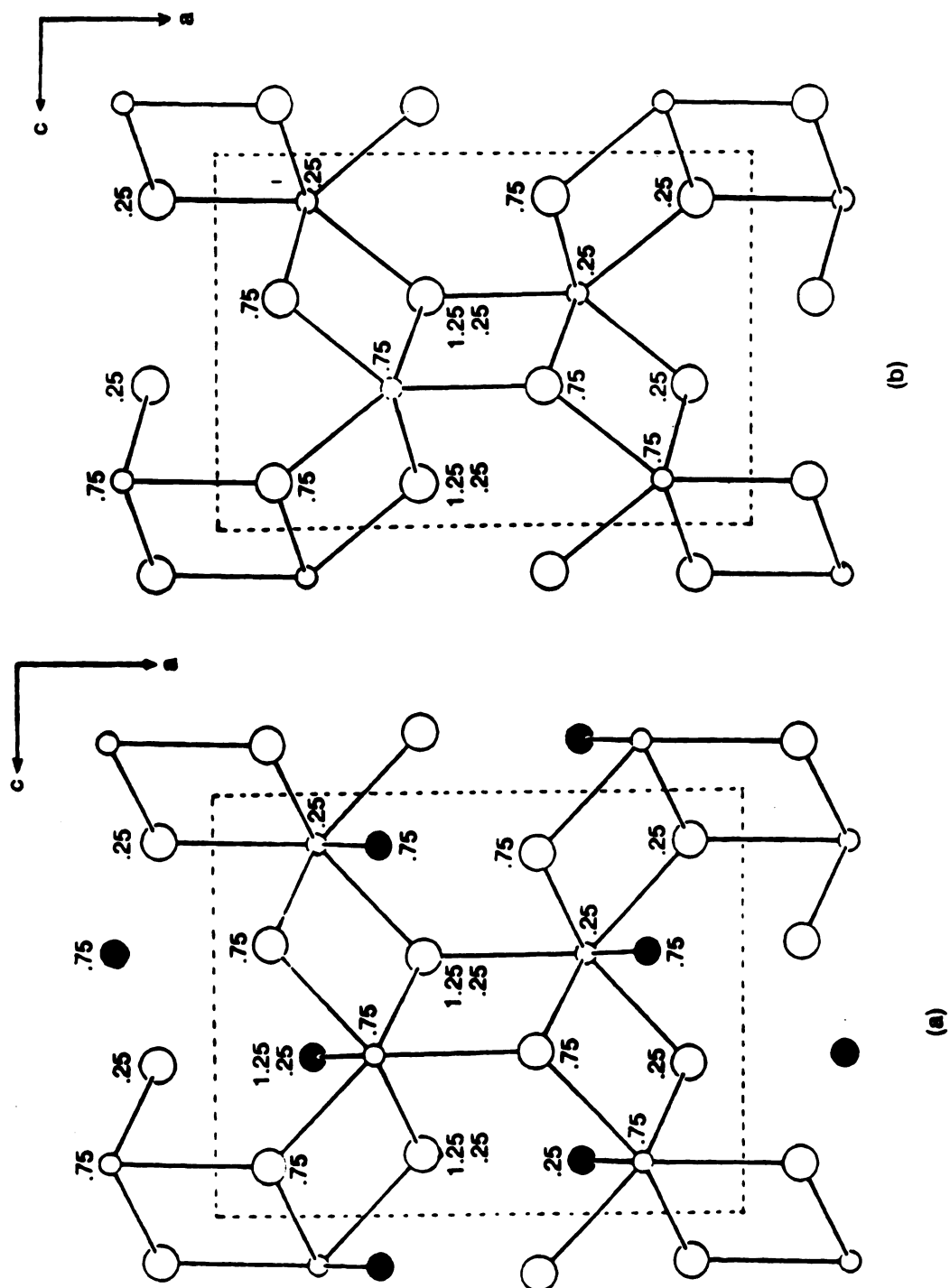


Figure 16. Projection of the $\text{SrI}_2 \cdot \text{H}_2\text{O}$ (a) and $\text{SrI}_2 \cdot \text{IV}$ (b) structures down the b axis. Numbers indicated are y coordinates. Large open circles: I; small open circles: H_2O .

Table 30. Comparison of atomic coordinates of $\text{SrI}_2 \cdot \text{H}_2\text{O}$ (85) and $\text{SrI}_2\text{-IV}$.

Compound		$\text{SrI}_2 \cdot \text{H}_2\text{O}$ (85)	$\text{SrI}_2\text{-IV}$
Space group		Pnma	Pnma
Z		4	4
Sr	x	0.1967(1)	0.170(1)
	y	0.25	0.25
	z	0.1208(2)	0.130(5)
I(1)	x	0.10358(7)	0.108(1)
	y	0.75	0.75
	z	-0.11399(8)	-0.123(3)
I(2)	x	0.10784(7)	0.120(1)
	y	0.75	0.75
	z	0.35664(8)	0.383(3)

b. $\text{Ln}_{14}\text{Cl}_{33}$ to Fluorite-Type LnCl_2 ($\text{Ln} = \text{Sm}, \text{Eu}$) Transformation

The fluorite-type structure of LnX_2 and the fluorite-related structure of $\text{Ln}^{2+}_9\text{Ln}^{3+}_5\text{X}_{33}$ have been described in Chapter 2 where we emphasized layered hexagonal close packing of the cations. It was shown that introduction of the "extra" anions that accompany trivalent cations leads to clustering. In a solvolytic decomposition, the major chemical change is the selective removal of these trivalent cations and accompanying anions from the mixed valent halide lattice. Thus the clusters are the decomposition centers.

When the trivalent cations and associated anions are removed from the layers so gently at low temperatures (Figure 17(a)) that the rest of the lattice is perturbed only slightly, we can assume that the intermediate (LnX_2) lattice (Figure 17(b)) is comprised of Ln^{2+} and Cl^- layers with a large number of vacancies. This intermediate should be highly unstable, and should collapse almost instantly. If the ions simply rearrange in the layers to eliminate the vacancies, each resulting layer is then hexagonally close packed (Figure 17(c)). If the inter-layer stacking sequence (ABCABC.....) is retained, with minimal adjustments the product should be the observed fluorite-type structure. This structural change can be understood better by comparing the layer stackings in Figures 9(a) and 9(b) (Page 36).

Even though direct observations of this microscopic process have not been possible, we believe this is the most likely mechanism for two reasons. Firstly, such a change is nearly a one step process. The intermediate can neither be trapped under the experimental conditions nor be observed easily. This is consistent with our experimental results that no trace of any new phase is seen by X-ray diffraction. Secondly, such an in-layer ion rearrangement involves minimal structural change and should have a low activation energy.

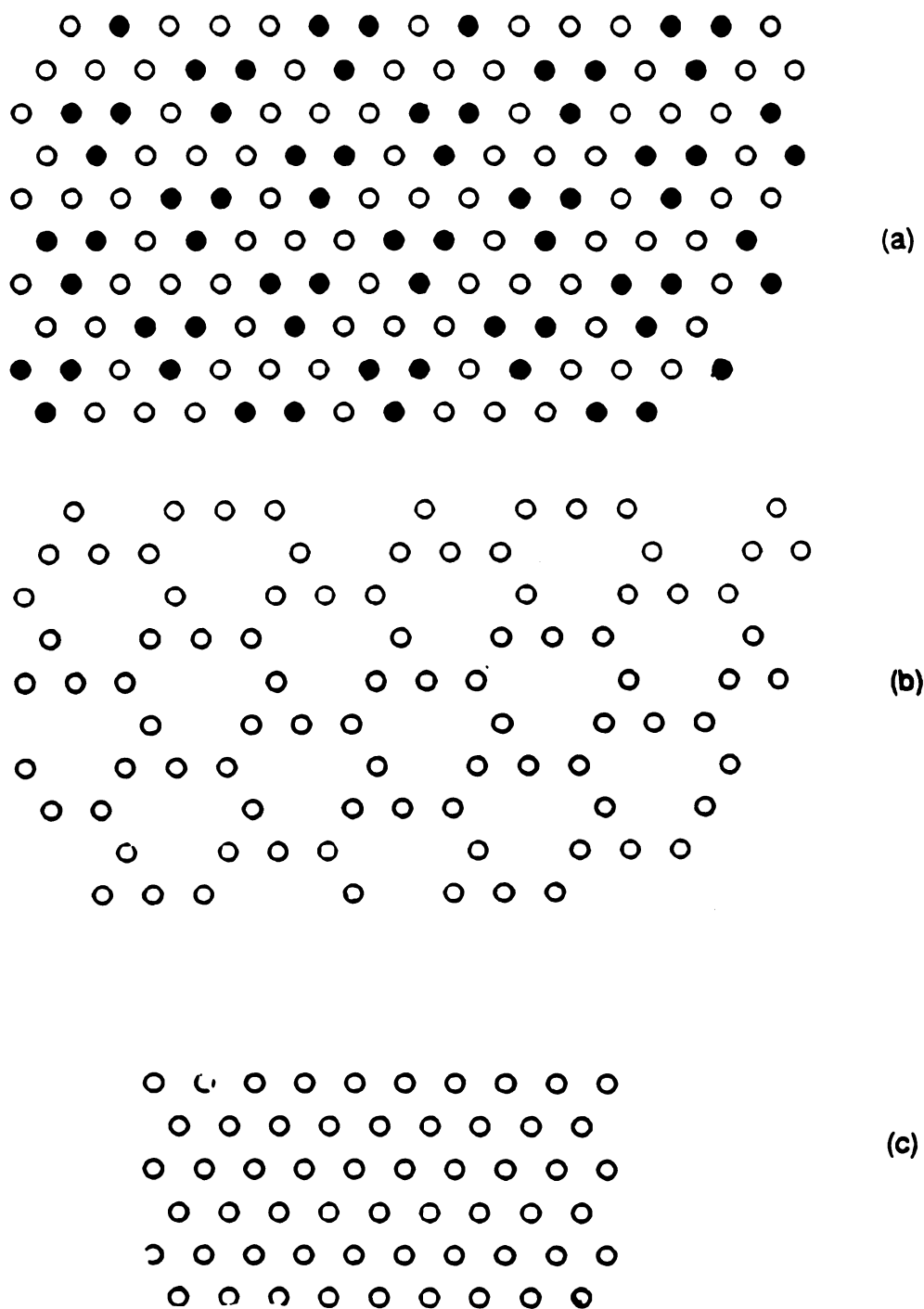


Figure 17. Proposed structural changes during solvolytic decomposition in a single cation layer of $\text{Ln}_{14}\text{Cl}_{33}$. (solid circles: Ln^{3+} ; open circles: Ln^{2+}) (a) Before extraction; (b) proposed intermediate; (c) after reorganized.

c. $\text{Ba}_9\text{Ln}_5\text{Br}_{33}$ to Anti- Fe_2P -Type BaBr_2 ($\text{Ln} = \text{La}, \text{Nd}$) Transformation

The title precursors have the cluster-type $\text{Ln}_{14}\text{Cl}_{33}$ structure. The structure of $\text{Ba}_{17}\text{Ln}_{10}\text{Cl}_{64}$ is unknown, but has been shown to be fluorite-related. The solvolytic decomposition product has the hexagonal anti- Fe_2P -type structure, but not the fluorite-type structure even though the fluorite-type high-temperature form of BaCl_2 can be retained at ambient temperature as described previously. No trace of fluorite-type BaCl_2 or BaBr_2 was observed in either experiment. These results suggest another mechanism.

The major difference between BaX_2 and LnX_2 is their cationic radii (28). Ba^{2+} (1.56 Å) is ~10% larger than both Sm^{2+} (1.41 Å) and Eu^{2+} (1.39 Å). From Table 31 it appears that the $\text{M}^{2+}/\text{Ln}^{3+}$ radius ratio is the major factor in determining product structure.

Thus when LnX_3 species are removed from the mixed halides $\text{BaX}_2\text{-LnX}_3$ the lattice collapses in a way different from that in the mixed valent chlorides $\text{LnCl}_2\text{-LnCl}_3$ presumably due to the larger-sized Ba^{2+} . We demonstrated in Chapter 2 that the cation positions in the anti- Fe_2P -type structure can be derived through displacement of hexagonal close-packed layers. The observed formation of this phase upon solvolytic decomposition suggests that the in-layer rearrangements of the cations to form hexagonal close packing layers is not an energetically favorable process for BaX_2 . Instead, an out-of-layer displacement occurs. Cation displacement leads to the mixing of the cations and anions in the same layers and eventually to the formation of anti- Fe_2P -type structure as can be seen in Figure 9(c) (Page 36).

Metastable phases formed in this way are more densely packed than the normal forms, in contrast to the significantly less closely packed fluorite forms. This result suggests that the barium halides in the mixed halides are probably under internal pressure. The internal pressure may be created by the size incompatibility mentioned above, and is probably the cause of the atomic displacements.

size

dev

Fe

no

br

ar

pr

Ta

—
P

Sy

—
S

—
E

—
B

—
B

—

It is noteworthy that the "high-pressure" forms prepared from precursors of different sized lanthanide cations in $\text{BaX}_2\text{-LnX}_3$ differ slightly. As is shown in Table 32, the c axis deviation appears significant and the precursor with the larger cation produces the anti- Fe_2P -form with the smaller unit cell volume. The deviations are small but are apparently not due to experimental errors since they are reproducible for both the chlorides and the bromides, and are apparent in the observed X-ray diffraction patterns (Table 17 (Page 79) and Table 18 (Page 80)). The larger La^{3+} cation tends to create higher "internal pressures" than the smaller Nd^{3+} and Sm^{3+} cations.

Table 31. Structure-ionic radius ratio relationships for metastable dihalides.

Precursor system	Radius ratio		MX_2 structure type
	X^-/M^{2+}	$\text{M}^{2+}/\text{Ln}^{3+}$	
$\text{SmCl}_2\text{-SmCl}_3$	1.18	1.16	Fluorite
$\text{EuCl}_2\text{-EuCl}_3$	1.20	1.14	Fluorite
$\text{BaBr}_2\text{-NdBr}_3$	1.17	1.28	Anti- Fe_2P
$\text{BaCl}_2\text{-SmCl}_3$	1.07	1.28	Anti- Fe_2P

Table 32. Crystallographic data of metastable BaX_2 (X = Cl, Br) prepared from various precursors

Precursor	a(Å)	c(Å)	V(Å ³)	c/a	Comments
Ba_2LaCl_7	8.066(1)	4.592(2)	258.7	0.5693	room temperature, incomplete reaction
Ba_2SmCl_7	8.069(1)	4.616(1)	260.3	0.5721	room temperature, first trial*
Ba_2SmCl_7	8.0720(7)	4.6305(7)	261.3	0.5737	room temperature, second trial*
$\text{Ba}_9\text{La}_3\text{Br}_{33}$	8.4826(6)	4.824(1)	300.6	0.5687	room temperature
$\text{Ba}_9\text{La}_3\text{Br}_{33}$	8.481(1)	4.845(1)	301.7	0.5713	heated at 400°C, quenched
$\text{Ba}_9\text{Nd}_3\text{Br}_{33}$	8.4814(8)	4.8393(7)	301.5	0.5706	room temperature

- * The precursor in the first trial had been extracted by THF for 3-4 days before being extracted by pyridine.
The product obtained in the second trial is almost the same as that from the first trial heated at 350°C for 6 hours.

5.4.3 Geometric Correlations

The preceding discussions on topochemical relations are based on symmetries of the precursors and the metastable products. Further justifications can be developed from geometric considerations.

a. $\text{Ln}_{14}\text{Cl}_{33}$ to LnCl_2 (Ln = Sm, Eu) Transformation

It has been shown that the fluorite-type LnCl_2 forms from the cluster-type $\text{Ln}_{14}\text{Cl}_{33}$. Correspondingly, the cubic lattice parameter a_c of LnCl_2 can be related to the $\text{Ln}_{14}\text{Cl}_{33}$ hexagonal supercell lattice parameters $a_h(\text{super})$ and $c_h(\text{super})$. Figure 18 illustrates the relation of $a_h(\text{super})$ to a_c in a cation layer. From the Figure we find $\sqrt{2} \cdot a_c / a_h(\text{super}) = 26.5(\text{mm}) / 34.0(\text{mm})$, or $a_c = 0.551 \cdot a_h(\text{super})$. From our previous descriptions we know that $c_h(\text{super})$ is parallel to the cubic body diagonal ($= \sqrt{3} \cdot a_c$) and the supercell is 6 layered while the cubic cell is 3 layered. Thus we have $(6/3) \cdot \sqrt{3} \cdot a_c = c_h(\text{super})$, that is, $a_c = (\sqrt{3}/6) \cdot c_h(\text{super}) = 0.2887 \cdot c_h(\text{super})$. The cubic lattice parameters derived from both $a_h(\text{super})$ and $c_h(\text{super})$ are listed in Table 33. Derived parameters are close to observed values.

b. $\text{Ba}_9\text{Ln}_5\text{Br}_{33}$ to BaBr_2 (Ln = La, Nd) Transformation

Similar derivations can be made. In Figure 18 the relationship between the two sets of lattice parameters are $a_h(\text{BaX}_2) / a_h(\text{super}) = 23.5(\text{mm}) / 36.0(\text{mm})$, or $a_h(\text{BaX}_2) = 0.653 \cdot a_h(\text{super})$, and $c_h(\text{BaX}_2) = c_h(\text{super}) / 6$. Derived parameters are listed in Table 34. Here the metal atoms must undergo significant in-layer reorganization and out-of-layer displacement to form the anti- Fe_2P -type structure (comparing Figures 9(a) and 9(c), Page 36). As a result of the displacement the a_h axis (in-layer) shortens substantially while the c_h axis elongates.

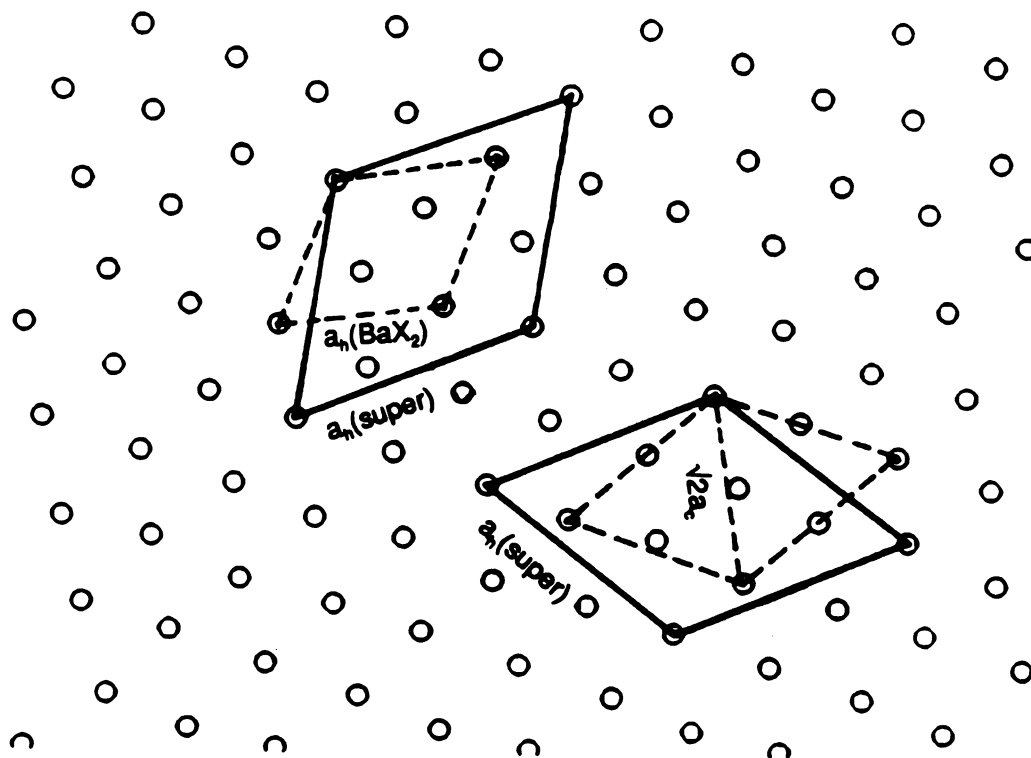


Figure 18. Lattice parameter relationships between the $M_{14}X_{33}$ superstructure and the anti- Fe_2P -type structure (upper left), and between the superstructure and the fluorite-type structure (lower right).

Table 33. Geometrical correlation of the metastable LnCl_2 (cubic) with their precursors $\text{Ln}_{14}\text{Cl}_{33}$ (hexagonal) (units in Å).

Precursor $\text{Ln}_{14}\text{Cl}_{33}$			Metastable LnCl_2 , a_c	
			Derived	Observed
$\text{Sm}_{14}\text{Cl}_{33}$	$a_h(\text{super})$	12.864(2)	7.09	6.9827(5)
	$c_h(\text{super})$	24.72(8)	7.136	6.9827(5)
$\text{Eu}_{14}\text{Cl}_{33}$	$a_h(\text{super})$	12.815(4)	7.06	6.961(1)
	$c_h(\text{super})$	24.768(8)	7.150	6.961(1)

Note. Derived $a_c = 0.551 a_h(\text{super})$, or $a_c = 0.2887 c_h(\text{super})$.

Table 34. Geometrical correlation of the metastable BaBr_2 with its precursors $\text{Ba}_9\text{Ln}_3\text{Br}_{33}$ (both hexagonal) (units in Å).

Precursor $\text{Ln}_{14}\text{Cl}_{33}$			Metastable BaBr_2	
			Derived	Observed
$\text{Ba}_9\text{Nd}_3\text{Br}_{33}$	a_h	14.039(1)	9.17	8.4814(8)
	c_h	26.477(4)	4.413	4.8393(7)
$\text{Ba}_9\text{La}_3\text{Br}_{33}$	a_h	14.098(2)	9.21	8.4826(6)
	c_h	26.678(6)	4.446	4.824(1)

Note. Derived: $a_h(\text{BaX}_2) = 0.653 a_h(\text{super})$; $c_h(\text{BaX}_2) = c_h(\text{super})/6$.

CONCLUDING REMARKS

Low temperature dehydrations and solvolytic decompositions of mixed(-valent) halides have enabled syntheses of metastable phases either not observed previously or observed previously, but not quenchable. Layer structure analysis suggested that the reactions are topologically controlled. Nearly all the low temperature reaction products have symmetries equal to or higher than those of their precursors. The leaching product of $\text{Ba}_9\text{Ln}_5\text{Br}_{33}$ is the anti- Fe_2P -type BaBr_2 but not the PbCl_2 -type BaBr_2 . The latter has a similar layer structure (Page 36) and similar coordination polyhedra but is less symmetric. Symmetry factors apparently are playing significant roles in these low temperature reactions. In the solvolytic decomposition the layers appear to have higher reactivities and the rotational axes orthogonal to the layers are the characteristic symmetry elements retained during reactions. The author believes that the topological analysis developed in this work will help future design for and possibly allow prediction of product structures based on known precursor structures. A combination of the solvolytic decomposition and desolvation reactions can probably be applied to more systems.

PART II

MAGNETIC AND ELECTRICAL PROPERTIES OF OXIDENITRIDES

CHAPTER 1 INTRODUCTION

SYNOPSIS

The possibility of achieving mixed-valent states and making new compounds with potentially interesting magnetic and electrical properties by effectively substituting N^{3-} for O^{2-} is discussed. The chemistry of transition metal oxidenitrides is reviewed and three systems are proposed for studies.

Since the discovery of high T_c ceramic oxide superconductors in 1986 (111) and subsequent characterization of the $T_c = 90$ K '123' phase, $YBa_2Cu_3O_{7-x}$ (112) in 1987, Cu-containing oxides have become the most intensely examined compounds for superconductivity. Numerous compounds of the '123' phase (see, for example, 113,114,115,116,117,118), some of which exhibit superconductivity, and new types of superconductors such as the $T_c \approx 125$ K $Tl_2Ca_2Ba_2Cu_3O_{10+x}$ and related compounds (119,120), and other types of cuprates (see, for example, 121,122,123,124,125) have been synthesized and characterized.

Reports of anion substitution in these ceramic superconductors are far less extensive than those of cation substitution. Such a result is not surprising because not only is it more difficult to synthesize an anion- than a cation-substituted compound, but also the number of possible substitutions is much more limited. Low-temperature fluoridation has been found to passify '123' compounds to hydrolysis (126) with no loss of superconductivity. However, substitution of fluoride and chloride anions for oxide anions in '123'-related compounds suggests that at least for these anions T_c is decreased. The Nd_2CuO_4 -type compounds appear to behave differently to anion substitution. When La_2CuO_4 is treated with $\text{F}_2(\text{g})$ at 200°C a 'new' K_2NiF_4 -type structure forms (127). This new phase has $T_c = 40\text{--}50\text{ K}$, somewhat higher than values reported for O_2 -treated La_2CuO_4 .

On the basis of size and electronegativity considerations, N^{3-} appears to be a likely candidate for O^{2-} substitution. The ionic radius (28) of four-coordinated N^{3-} , 1.32\AA , is only slightly larger than that of four-coordinated O^{2-} , 1.24\AA ; and the electronegativity of N (3.04) and O (3.44) expressed on the Pauling scale, are relatively close. Some metal nitrides have long been known as low T_c superconductors (128). In view of the possibility of achieving a mixed-valence state whose existence in many compounds is an important factor for high T_c superconductivity and uncommon stoichiometries, and of making new compounds with potentially interesting magnetic and electrical properties by effectively substituting N^{3-} for O^{2-} , we initiated an investigation of selected oxidenitrides, mainly lanthanide-containing oxidenitrides.

1.1 An Overview of Transition Metal Oxidenitrides

Previously known transition metal oxidenitrides may be classified into two categories: (1) pseudo-ternary oxidenitrides including perovskite-related $AB(O,N)_3$ where A is an alkali, alkaline earth, Y or lanthanide cation; B is W, Mo, V, Nb, Ta or Ti (129,130,131,132,133); and Scheelite-type $AB(O,N)_4$ including $LnWO_3N$ ($Ln = Nd, Sm, Gd, Dy$) (134), and $MOsO_3N$ ($M = K, Cs$) (135,136) whose structure is closely related to that of $BaSO_4$. (2) pseudo-binary NaCl-type oxidenitrides LnO_xN_{1-x} where Ln is a lanthanide cation and so far $Ln = La-Er$ except for Dy (137,138,139) have been known. The transition metals in these oxidenitrides typically have a lower than maximum oxidation state.

1.1.1 Perovskite-Type

$MTaO_2N$ ($M = Ca, Sr, Ba$) and $BaNbO_2N$ (129) were prepared by one step heating of intimately ground mixtures of $BaCO_3$ and M_2O_5 in NH_3 (g) at $\sim 1000^\circ C$. On the other hand, for synthesis of compounds such as $Ba_{1-x}Sr_xTaO_2N$ and $SrTaO_2N$ the ternary oxides were first prepared and then these oxides were nitridized in NH_3 (130). Structures of some pseudo-ternary oxidenitrides were examined by neutron diffraction. $BaMO_2N$ ($M = Ta, Nb$) compounds were found to remain cubic to the lowest temperature studied (4 K) with N and O atoms distributed statistically over the anion sites (133), while the structure of $SrTaO_2N$ (133) was found to be tetragonal rather than the cubic observed by X-ray diffraction (129), again with O and N atoms distributed statistically in two crystallographic sites. Mixed-cation $Ba_{1-x}Sr_xTaO_2N$ was found to be cubic (130).

Another series of perovskite-type oxidenitrides, $LnWO_xN_{3-x}$ ($0.6 < x < 0.8$), was prepared by heating the mixed oxide $Ln_2W_2O_9$ in $NH_3(g)$ at $700-900^\circ C$ (132). $LnWO_{0.6}N_{2.4}$ was also found to be tetragonal by neutron diffraction (131); the N and O atoms are

dist

an

Th

th

1

b

pe

pr

Eu

Th

inc

for

tra

oxy

sp

Ma

distributed statistically. The W atoms in $\text{LnWO}_{0.6}\text{N}_{2.4}$ exhibited mixed V/VI oxidation states and the compound was semiconducting with powder conductivity values of $10\text{-}15\ \Omega^{-1}\cdot\text{cm}^{-1}$. Thermal power measurements indicated electrons to be the charge carriers. Some of these oxidenitrides are potentially interesting dielectric materials.

1.1.2 NaCl-Type

Structure-composition relationships of the NaCl-type oxidenitrides, $\text{LnO}_x\text{N}_{1-x}$, have been examined for most lanthanides (137,138,139). In most systems the cubic lattice parameter decreases almost linearly as oxygen content increases. Magnetic and transport properties of some of these compounds, primarily $\text{NdO}_x\text{N}_{1-x}$ and the Eu-related systems $\text{Eu}_{1-x}\text{Ln}_x\text{O}_{1-y}\text{N}_y$ ($\text{Ln} = \text{Nd, Eu, Gd}$) (140,141,142), have been studied extensively. The $\text{NdO}_x\text{N}_{1-x}$ phases are ferromagnetic and metallic. Conductivity increases with increasing oxide content and resistivities vary from $10^{-9}\ \Omega\cdot\text{cm}$ for $x = 0.09$ to $10^{-4}\ \Omega\cdot\text{cm}$ for $x = 0.22$. The $\text{Eu}_x\text{Ln}_{1-x}\text{O}_x\text{N}_{1-x}$ compounds are also ferromagnetic. However, their transport properties are apparently different from those of the $\text{NdO}_x\text{N}_{1-x}$ systems. The oxygen-rich $\text{Eu}_x\text{Ln}_{1-x}\text{O}_y\text{N}_{1-y}$ oxidenitrides are semiconductors, while the nitrogen-rich specimens are metallic. Europium is found in both the +2 and +3 oxidation states. Magnetic properties are closely related to the predominantly localized f electrons.

1.2 Goals

Many aspects of the solid state oxidenitride chemistry deserve further studies. Our primary goals in this work include the synthesis, structural characterization, magnetic and electrical property studies of new and interesting known oxidenitrides. Described below are three systems. The $\text{MMo}(\text{O},\text{N})_3$ system presents the importance of NH_3 reductive substitution for the preparation of mixed-valent or lower valent oxidenitrides; the $\text{BaCeLn}(\text{O},\text{N})_4$ system utilizes N^{3-} as a means of introducing mixed valences; the $\text{LaO}_x\text{N}_{1-x}$ system demonstrates the need for the examination and understanding of the magnetic and electrical properties of oxidenitrides.

1.2.1 $\text{MMo}(\text{O},\text{N})_3$

It is worth noting that in the reported pseudo-ternary oxidenitrides described above the transition metals are either at the highest oxidation states or at mixed-valences only slightly lower than the highest oxidation states. These transition metals did not seem to be easily reducible by N^{3-} . Such electronic configurations are not desirable for important magnetic and electrical properties including superconductivity. Since N^{3-} is a fairly strong reducing reagent especially at high temperatures, we expected reductive substitution to be possible under favorable conditions.

It has long been known that MoO_3 can be readily reduced to MoO_2 by both H_2 and NH_3 (143) below 470°C , and MMoO_4 (Mo^{6+} , d^0 ; $\text{M} = \text{Ba}, \text{Sr}, \text{Ca}$) can be reduced by hydrogen to perovskite-type MMoO_3 (Mo^{4+} , d^2) (144). These perovskites are metallic conductors as determined by electrical (145) and magnetic measurements (146). If reductive substitution of MMoO_4 with NH_3 occurs, oxidenitrides with Mo oxidation states higher than that in MMO_3 are expected.

1.2.2 BaCeLn(O,N)₄

Because cerium is known to exhibit multiple valency its nitride and oxidenitride systems seemed of special interest. Room temperature magnetic susceptibility data suggest the Ce⁴⁺ content in CeN may be as high as 89% (147); Ce⁴⁺, as expected, has also been reported in both Li₂CeN₂ and Ce₂N₂O (148). These observations suggest that some cerium ions tend to be in their highest oxidation state even in the presence of reducing N³⁻ ions. On the other hand, cerium forms calcium ferrite-type BaCe₂O₄ that presumably contains Ce³⁺ ions (149) and is probably stabilized by lattice energy. Effectively substituting N³⁻ for O²⁻ in BaCe₂O₄ by fusing CeN with BaCeO₃ thus might both lead to a stable compound and also introduce Ce⁴⁺ into the lattice to give a mixed valence compound.

1.2.3 LaO_xN_{1-x}

Since La³⁺ has neither unpaired nor valence electrons, the LaO_xN_{1-x} oxidenitrides are expected to differ from the other pseudo-binary oxidenitrides mentioned above. Both LaN and LaO have the NaCl-type structure (150,151,152). The nature of the LaN conductivity was still the subject of a recent study (153); it is probably a small band overlap semimetal. It is interesting to note that LaN undergoes a superconducting transition at ~1 K (154) even though the lanthanum ion is probably trivalent (150). LaO prepared under high pressures is also reported to be metallic with trivalent La ions (150,152). Thus LaO is better formulated as La(III)(O,e), where e represents a free electron. Since La(O,e) has a relatively high solubility in LaN (137), substitution of nitrogen by oxygen in LaN should enhance its conductivity by increasing the carrier electron density.

CHAPTER 2 MAGNETIC PROPERTIES OF SOLIDS

SYNOPSIS

Some fundamental magnetic properties of solids are reviewed briefly. The origin and behavior of each of the five basic types of magnetic order, diamagnetism, paramagnetism, ferromagnetism, anti-ferromagnetism, and ferrimagnetism, are described for the convenience of later calculations and discussions.

2.1 Magnetization and Magnetic Susceptibility

When an external magnetic field H is applied to a substance, the magnetic field within the body differs from that surrounding the body. The magnetic induction B is defined as

$$B = H + 4 \pi M$$

which can be rearranged as

$$\frac{B}{H} = 1 + 4 \pi \frac{M}{H}$$

where M is the magnetization (magnetic moment per unit volume).

$$\chi = \frac{M}{H} \quad \text{is the volume magnetic susceptibility (emu}\cdot\text{cm}^{-3}\text{);}$$

$$\chi_g = \frac{\chi}{d} \quad \text{is the gram magnetic susceptibility (emu}\cdot\text{g}^{-1}\text{) where } d \text{ is the density; and}$$

$$\chi_m = \chi_g \cdot M_w = \chi \frac{M_w}{d} \quad \text{is the molar magnetic susceptibility (emu}\cdot\text{mol}^{-1}\text{) with } M_w \text{ the}$$

molecular weight.

2.2 Five Basic Types of Magnetic Order

2.2.1 Diamagnetism

This is a non-cooperative phenomenon associated with closed electron shells. When placed in an inhomogeneous magnetic field, a diamagnetic substance will tend to move towards the weakest region of this field. Its origin can be understood qualitatively by considering Lenz's law of electricity. Shielding currents are induced in atoms of filled electron shells by an applied magnetic field. The shielding magnetic field thus induced will repel the external magnetic field. Some features are summarized as follows:

- (1). Susceptibilities are always negative.
- (2). It is a property of all matter since closed shells exist in all substances.
- (3). It persists only when an external magnetic field is applied.
- (4). Susceptibilities are field-independent and nearly temperature-independent.
- (5). Susceptibilities are very small (10^{-5} - 10^{-6} emu·mol⁻¹).

Theoretical calculation of the diamagnetic susceptibility is possible. Values for many ions can be found in Selwood (155) and other books (see, for example, 156,157).

2.2.2 Paramagnetism

This is also a non-cooperative phenomenon. Atoms with unpaired electrons possess magnetic moments. A substance is paramagnetic if magnetic moments of various atoms in this substance are uncorrelated (randomly oriented) in the absence of an external magnetic field. The dipoles tend to become aligned in an applied magnetic field. Thus a paramagnetic substance will move to the strongest region of the field. Paramagnetic behavior is shown schematically in Figure 19(a) (Page 137). Some

common characteristics are summarized below:

- (1). Susceptibilities are always positive.
- (2). It is a property of substances with unpaired electrons.
- (3). Susceptibilities are field-independent.
- (4). Susceptibilities are significantly higher (for localized electrons, 10^{-3} - 10^{-5} emu·mol⁻¹) than diamagnetic susceptibilities.

a. Curie and Curie-Weiss Laws

Paramagnetic susceptibilities of compounds with localized and unpaired electrons are strongly temperature-dependent. The temperature dependence follows the Curie or Curie-Weiss Law.

Curie Law:

$$\chi_m = \frac{C}{T}$$

Curie-Weiss Law:

$$\chi_m = \frac{C}{T - \theta}$$

where C is the Curie constant and θ the Weiss constant. Deviation from the Curie law is caused by the interaction (exchange coupling) between atomic moments in a magnetic field.

b. Spin-Only

In compounds of the first transition (3d) series, the orbital contribution to the magnetic moment is almost completely quenched by the ligand fields. Only the spins contribute to the effective magnetic moment μ_{eff} (in Bohr magnetons):

$$\mu_{\text{eff}} = 2\sqrt{S(S+1)} = \sqrt{n(n+2)}$$

where S is the total spin quantum number and n the number of unpaired electrons.

c. Spin-Orbital Coupling

For a free, paramagnetic ion such as a lanthanide ion in which spin-orbital coupling causes a splitting of the ground state that is larger than kT , the effective magnetic moment may be calculated from the formulas

$$\mu_{\text{eff}} = g\sqrt{J(J+1)}$$

$$g = 1 + \frac{J(J+1) + S(S+1) - L(L+1)}{2J(J+1)}$$

where g is the electron gyromagnetic ratio, and J , S , and L refer to the ground-state

spectroscopic term L_J^{2S+1} .

d. Temperature-Independent Paramagnetism (TIP)

This arises from the admixing of higher energy states that lie above the ground state by an amount much greater than kT into the ground state. It has been discussed by Jolly (156). Correction for TIP is necessary when it is significant.

e. Pauli Paramagnetism

Metals have unpaired itinerant electrons. Most metallic materials, except those few that are ferromagnetic, are either diamagnetic or feebly paramagnetic with nearly temperature-independent magnetic susceptibilities. This behavior can be understood on the basis of a free electron gas model. In this model it is assumed that the valence

electrons are delocalized. These mobile electrons occupy the conduction band and are thus called conduction electrons. Most conduction electrons do not respond to the applied magnetic field because most states are fully occupied. Only those electrons near the Fermi level E_F within the energy range of $\sim kT$ contribute to the susceptibility. The volume susceptibility is given by the Pauli-Peierls equation

$$\chi = \frac{4\pi m^*}{h^2} \left(\frac{3n}{\pi}\right)^{1/3} \cdot \mu_B^2 \cdot \left(1 - \frac{m_o^2}{3m^{*2}}\right)$$

where μ_B is the Bohr magneton ($= 9.27 \times 10^{-21}$ erg gauss⁻¹), n the electron density, m_o the

electron rest mass, and m^* the electron effective mass. The Landau term $-\frac{m_o^2}{3m^{*2}}$

applies the diamagnetic correction. m^* can be greater or smaller than m_o (157). Many transition metals have values of $m^*/m_o \gg 1$. Hence from the above equation we would expect them to have comparatively large paramagnetic susceptibilities (observed 10^{-4} - 10^{-6} emu·mol⁻¹). A few metals such as Bi, Hg, and Cu have $m^*/m_o \ll 1$.

2.2.3 Ferromagnetism

This is a cooperative phenomenon and exists only in the solid state. In a ferromagnetic solid the spins tend to be aligned parallel below the ferromagnetic Curie temperature T_c . As a result, a spontaneous magnetization (M_s) exists in such materials; that is, even in the absence of a magnetic field there is a magnetic moment. The magnitude of the spontaneous magnetization drops to zero at T_c because thermal energies randomize the spins. Above T_c , the paramagnetic susceptibility obeys the Curie-

Weiss law:

$$\chi_m = \frac{C}{T - T_0}$$

In practice, when a magnetic field is applied to a ferromagnetic specimen, the magnetization may vary from zero to a maximum value called saturation magnetization. According to Weiss' postulation, there exist many domains in a bulk material. Although each domain is spontaneously magnetized, the direction of magnetization may vary from one domain to another. The overall magnetic moment of the specimen is the vector sum of the magnetic moments of individual domains. Thus the average magnetization and magnetic susceptibility of a ferromagnetic material depend on the applied magnetic field. Saturation occurs when the maximum domain alignment is achieved at a certain magnetic field. The magnetic susceptibility of a ferromagnet also depends on the previous magnetic history. Hysteresis, a characteristic behavior of ferromagnetic materials, is not discussed here. The ferromagnetic behavior is illustrated in Figure 19(c) (Page 137).

2.2.4 Anti-ferromagnetism

Anti-ferromagnetism, like ferromagnetism, is a cooperative magnetism of long-range order among identical, spontaneous moments, and exists only in the solid state. Ideally, magnetic ions occupy crystallographically equivalent sites. A simple anti-ferromagnet can be envisaged as composed of two identical sub-lattices of opposite (anti-parallel) spins. The exchange coupling is thus negative. There is overall no spontaneous magnetization.

The temperature dependence of the magnetic susceptibility is complicated. Above the Néel temperature, T_N , where the thermal energy of a moment exceeds the exchange energy, the substance is paramagnetic and follows the Curie-Weiss law

$$\chi_m = \frac{C}{T - T_N}$$

Below T_N in the anti-ferromagnetic range, the susceptibility decreases with decreasing temperature. In an ideal anti-ferromagnet, χ is zero at 0 K.

The anti-ferromagnetic behavior is illustrated in Figure 19(b).

2.2.5 Ferrimagnetism

A ferrimagnetic material may be defined as one which below a certain temperature possesses a spontaneous magnetization that arises from a non-parallel arrangement of the strongly coupled atomic dipoles or from two or more magnetic species that are chemically different. These different species occupy different crystallographic sites. The non-parallel arrangement can be anti-parallel like that in an anti-ferromagnet. However, the net magnetization is not zero because of the difference in magnetic moments of different magnetic species.

The temperature dependence of the magnetic susceptibility is similar to that of a ferromagnet. In a ferrimagnetic material, however, the spontaneous magnetization M_s usually decreases more rapidly than that in a ferromagnet with increasing temperature up to the Néel temperature T_{FN} . In the paramagnetic range there is appreciable deviation from the Curie-Weiss behavior, particularly close to T_{FN} . The ferrimagnetic behavior is shown in Figure 19(d).

In addition to the above five basic types of magnetic order, Hurd (158) recently reviewed nine other types that are derived from these basic types. These relatively new magnetic phenomena are beyond this work and therefore not discussed.

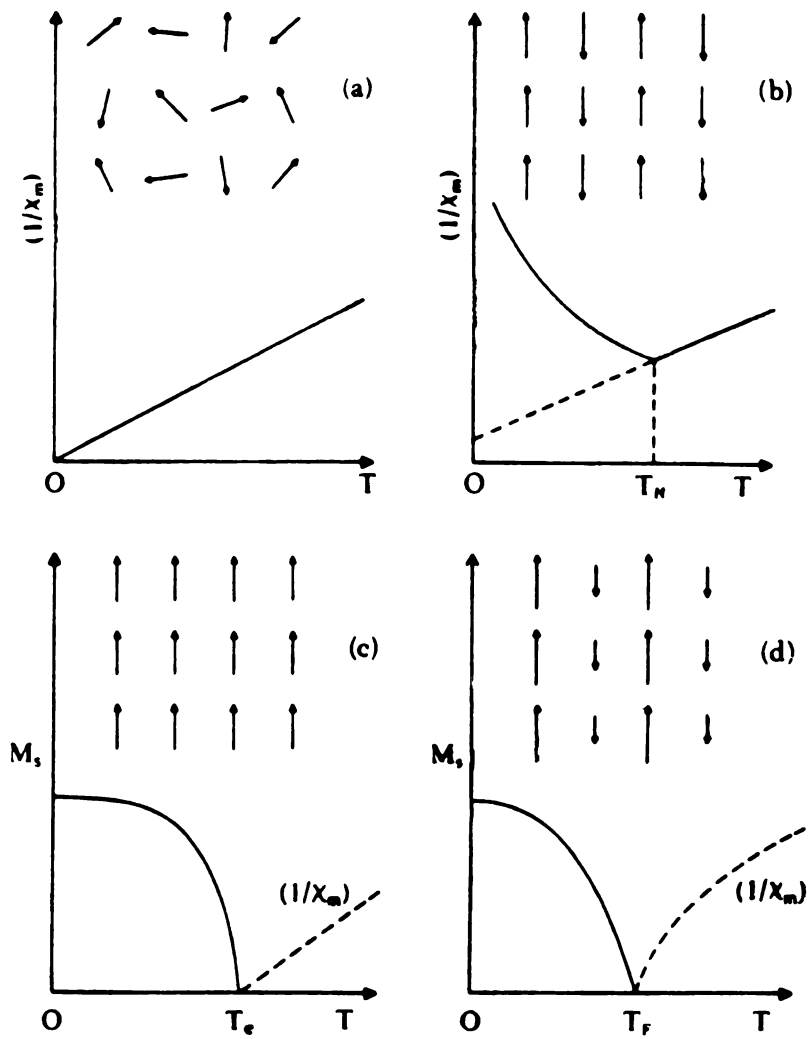


Figure 19. The low temperature ordering (if any) of neighboring dipoles and the consequent behavior of spontaneous magnetization and/or susceptibility, for (a) paramagnetism; (b) anti-ferromagnetism; (c) ferromagnetism; (d) ferrimagnetism.

CHAPTER 3 ELECTRICAL PROPERTIES OF SOLIDS

SYNOPSIS

The classification of electrical materials into metals, semimetals, semiconductors, and insulators according to the Band Theory of solids is reviewed briefly. Typical properties of superconductors and the thermal behavior of electrical conductivity of metals and intrinsic semiconductors are described.

3.1 The Band Theory of Solids

The electronic structures of solid state compounds are usually described by the band theory of Bloch and Wilson developed from molecular orbital theory. In this theory it is assumed that an extremely large number of atomic orbitals of the same symmetry overlap to form an energy band with nearly continuous energy levels. The space between two different bands is called the band gap E_g . The highest filled band (HOMO) is called the valence band, and the lowest empty (LUMO) band the conduction band. The highest occupied energy level in a band is called the Fermi level E_f . In a metal, E_f lies within the partially filled band. In an insulator or a semiconductor, E_f lies between the valence band and the conduction band.

According to this theory, a metal has a strong overlap of the conduction and the valence band. In other words, the highest occupied band is only partially filled with electrons in a metal. An insulator has either completely full or completely empty bands with a large band gap ($E_g > 3.0$ eV); semiconductors can be classified as intrinsic (pure) or extrinsic (doped) depending on the configurations of the energy levels. Extrinsic semiconductors can be further divided into P- (positive or hole) and N- (negative or electron) types according to the nature of carriers. An intrinsic semiconductor is N type and has a completely filled valence band and a completely empty conduction band at 0 K, but has a fairly small band gap ($3.0 \text{ eV} > E_g > 0$). The small thermal population of the conduction band by electrons from the valence band is responsible for the semiconductivity at higher temperatures. The conductivity of extrinsic semiconductors arises either from population of the conduction band by the small number of dopant electrons (electron donor dopant, N-type) or from population of the empty energy levels provided by the electron-accepting dopant (P-type). The band structures of various materials are shown schematically in Figure 20.

It is worth noting that there are several classes of compounds that cannot be described easily as either metals or semiconductors. They are called semimetals because the conduction and valence band overlap is smaller than that in metals.

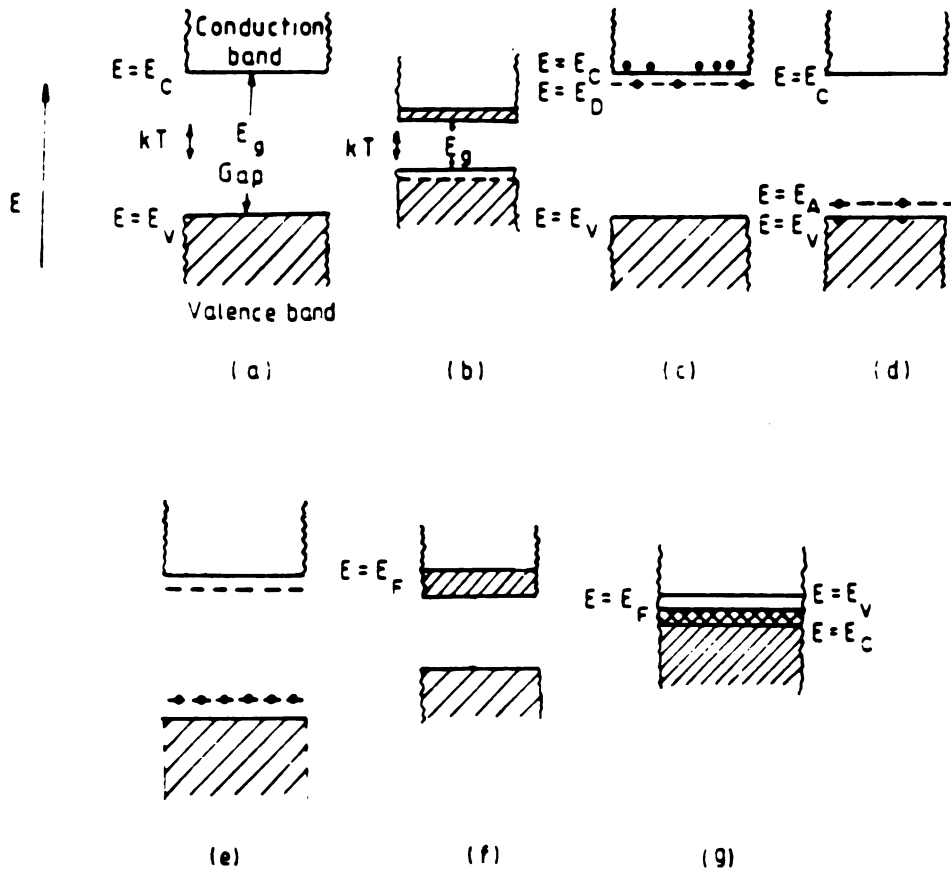


Figure 20. Schematic band structures of solids. (a) insulator; (b) intrinsic semiconductor; (c) and (d) extrinsic semiconductors; donor and acceptor levels in n- and p-type semiconductors are shown respectively. (e) compensated semiconductor; (f) metal; (g) semimetal.

3.2 Electrical Conductivity

The conductivity (σ) of a material is proportional to the carrier density (n) and the carrier mobility (μ):

$$\sigma = n e_0 \mu$$

where $e_0 = 1.602 \times 10^{-19}$ Coulomb is the carrier (electron) charge. $\rho = 1/\sigma$ is defined as the resistivity. Units of the above quantities in both the SI and CGS systems are listed in Table 35. Typical conductivity values for metals, semiconductors, insulators, and superconductors are listed in Table 36.

Table 35. Units of quantities related to electrical conductivity.

Quantity	n	μ	σ	ρ
SI	m^{-3}	$\text{m}^2 \cdot \text{V}^{-1} \cdot \text{s}^{-1}$	$\Omega^{-1} \cdot \text{m}^{-1}$	$\Omega \cdot \text{m}$
CGS	cm^{-3}	$\text{cm}^2 \cdot \text{V}^{-1} \cdot \text{s}^{-1}$	$\Omega^{-1} \cdot \text{cm}^{-1}$	$\Omega \cdot \text{cm}$

Table 36. Typical electrical conductivities for various materials at room temperature.

	Metals	Semiconductors	Insulators	superconductors
$\sigma (\Omega \cdot \text{cm})^{-1}$	$10^4 - 10^6$	$10^{-6} - 10^3$	$10^{-18} - 10^{-6}$	10^{23}

3.2.1 Temperature Dependence of Metallic Electrical Conductivity

The resistivity of a typical metal decreases with decreasing temperature because of weakening lattice vibrations upon cooling. Above a certain temperature, the resistivity is linearly proportional to the temperature, $\rho(T) \propto T$; at very low temperatures, $\rho(T) \propto T^2$ or T^5 . In practice, the resistivity reaches a plateau value controlled by impurities and lattice imperfections at a low temperature. Matthiessen's Rule is often observed: the contribution of impurities and imperfections to resistivity is a constant ($1/\sigma_{\text{imp}}$).

$$\frac{1}{\sigma(T)} = \frac{1}{\sigma_{\text{imp}}} + \frac{1}{\sigma_{\text{pure}}(T)}$$

A typical resistivity vs. T curve for sodium metal (159) is shown in Figure 21 (Page 143).

3.2.2 Semiconductors

For intrinsic semiconductors, the number of conduction electrons is the same as the number of holes. Thus the conductivity is

$$\sigma = n_i e (u_n + u_p)$$

where

$$n_i = \sqrt{N_c \cdot N_v} \exp\left(-\frac{E_g}{2kT}\right)$$

here N_c and N_v are the effective densities of states in the conduction and valence bands, respectively, and u 's are the mobilities. The final expression of the conductivity is

$$\sigma = 2 e u_p (b + 1) \left(2 \pi \sqrt{m_n m_p} \frac{kT}{h^2}\right)^{3/2} \exp\left(-\frac{E_g}{2kT}\right) = \sigma_0 \exp\left(-\frac{E_g}{2kT}\right)$$

where $b = u_n/u_p$. Since the pre-exponential factor (σ_0) is insensitive to temperature, a plot

of $\ln \sigma$ vs. $1/T$ should yield a straight line with slope $= -E_g/2k$, from which the band gap can be estimated.

For extrinsic semiconductors, the temperature dependence of conductivity is complicated because the electron and hole densities, n_n and n_p , are no longer equal. Since it is irrelevant to this work, this subject is not discussed here.

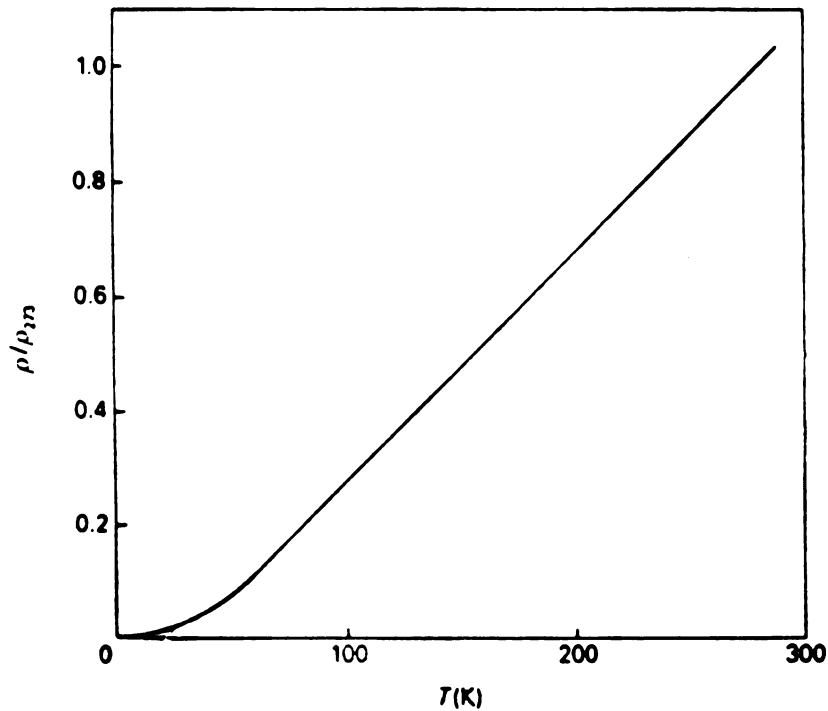


Figure 21. Ratio of the resistivity of metallic sodium at T to that at 273 K vs. T . The essentially linear variation at $T > 100$ K is typical of simple metals.

3.3 Superconductivity

Superconductivity is the loss of electrical resistance below a critical temperature T_c , called the superconducting transition temperature. Typical resistivities in the superconducting state are $\sim 10^{-23} \Omega\text{-cm}$ in comparison to the $\sim 10^{-7} \Omega\text{-cm}$ resistivities of the very good metallic conductors Cu and Au at 100 K. A superconductor must be a good metallic conductor above T_c . Some important features of superconductors are summarized here.

The Meissner-Ochsenfeld Effect

In the superconducting state materials exhibit perfect diamagnetism. The magnetic induction \mathbf{B} inside the specimens is zero.

$$\mathbf{B} = \mathbf{H} + 4\pi \mathbf{M} = 0$$

Thus the volume magnetic susceptibility in the perfect diamagnetic state is

$$\chi = \frac{\mathbf{M}}{\mathbf{H}} = -\frac{1}{4\pi}$$

The result of this diamagnetism can be observed by magnetic field exclusion which causes the levitation phenomenon. Since the Meissner-Ochsenfeld effect is a fundamental property of the superconducting state, it is often used for detecting superconducting transitions.

The interactions of the normal conducting and superconducting states with a magnetic field are illustrated schematically in Figure 22.

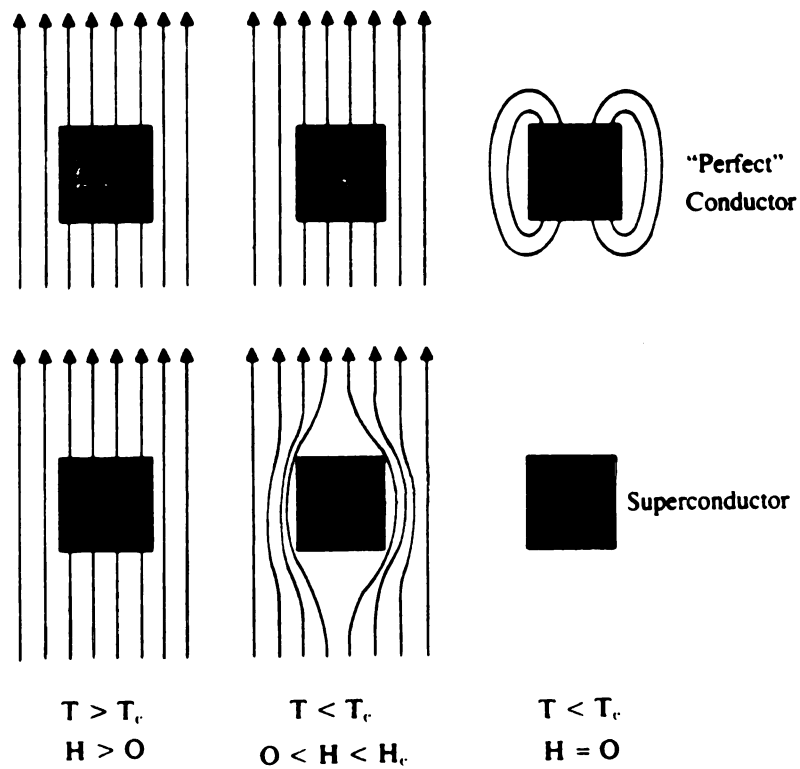


Figure 22. An illustration of the difference between a normal conductor (a) that allows magnetic flux penetration and a superconductor (b) that expels magnetic flux from its interior.

CHAPTER 4 EXPERIMENTAL

SYNOPSIS

Synthesis, magnetic and electrical measurement procedures for various oxidenitrides are described. The oxidenitrides were prepared either by nitridation of oxides with NH_3 (g) or by direct reaction of oxides with nitrides. The four-probe method for the conductivity measurement was used for both pressed pellets and sintered rods of poly-crystalline specimens. Formulas used to elucidate the magnetic and electrical data are listed.

4.1 Synthesis and Structural Characterization of Oxidenitrides

The nitrides and some oxidenitrides are air-sensitive and were handled in the glove box when necessary. Nitrogen content was determined by Galbraith Laboratories, Inc. Powder X-ray diffraction and pattern treatment procedure are as described in Part I of this dissertation.

4.1.1 List of Chemicals

La, Ce chips: Research Chemicals, Phoenix, AZ.

CeO₂: 99.9%, Research Chemicals, Phoenix, AZ.

La₂O₃: 99.9%, Research Chemicals, Phoenix, AZ.

ThO₂: anhydrous, purified, Fisher Scientific Company, Fair Lawn, N. J.

MoO₃: 99.5%, Reagent, Merck & CO. Inc., Rahway, N. J.

BaCO₃: "Baker Analyzed", J. T. Baker Chemical Co., Phillipsburg, N. J.

Sr(NO₃)₂: Certified A.C.S., Fisher Scientific Company, Fair Lawn, N. J.

Ba(NO₃)₂: Reagent A.C.S., Matheson Coleman & Bell, Norwood, Ohio.

NH₃ (g): Matheson Gas Products, E. Rutherford, N. J.

4.1.2 Synthesis Procedure

MMoO₄ (M = Sr, Ba) Precipitated from 1:1 solutions of M(NO₃)₂ and (NH₄)₂MoO₄ (MoO₃ dissolved in NH₃·H₂O) at pH = 9-10, then annealed at 800°C for 2-5h.

BaMO₃ (M = Ce, Th) Perovskite-type BaCeO₃ and BaThO₃ were synthesized by heating intimately ground 1:1 molar mixtures of BaCO₃ and MO₂ (M = Ce, Th) at 950°C for 24 h, then quenching them.

LnN (Ln = La, Ce) 5-6 g of metal chips in corundum crucibles were heated in a slowly flowing ammonia gas stream at 700°C for 12 h. Pulverized CeN was dark brown and contained ~10% CeO₂ by mass; LaN was black and contained ~5% La₂O₃. Both samples are moisture and oxygen sensitive.

BaCeLn(O,N)₄ (Ln = La, Ce) A 0.8-1.0 g intimately ground and nominally stoichiometric mixture of BaCeO₃ and LnN was sealed into an outgassed quartz tube under vacuum or an argon atmosphere, heated at 800°C for 24 h, then quenched by removal from the furnace.

For electrical conductivity measurements ~1.5 g specimens of each product were inserted into 6.35 mm i.d. Ta cylindrical crucibles whose ends were crimped closed. The containers were then heated inductively to 1200-1300 °C for ~2 h in a 10⁻⁵ Torr vacuum to sinter the material. Specimens thus prepared were ~5 mm in diameter and 10 mm long.

LaO_xN_{1-x} Two oxidenitride compositions were prepared by inductively heating intimately-ground mixtures of the LaN and La₂O₃ for 2-3 h in vacuo to 1500-1600°C. The

~15% (I) and ~26% (II) (by weight) La_2O_3 mixtures were confined in closed 6.35 mm i.d. Ta tubes. The products, sintered rods ~4 mm o.d. and 6-8 mm long, were used as synthesized for resistance measurements. Crushed samples were used for magnetic measurements and X-ray characterization. The oxidenitrides are air and moisture sensitive.

$\text{MMo}(\text{O},\text{N})_3$ (M = Sr, Ba) A sample of 0.6-1.2 g MMoO_4 was weighed carefully and contained in a clean platinum or silver crucible, which was then placed in an alumina boat for stability. Reduction was carried out in a flowing NH_3 stream. Reaction conditions vary depending on the system. For SrMoO_4 , heating at 750°C for 48 h appeared to be appropriate; for BaMoO_4 , various temperatures from 650 to 900°C and reaction time from 2 to 6 days have been tried. Reaction products were weighed carefully to check for mass loss.

4.2 Magnetic and Electrical Measurements

Powder samples were contained in plastic capsules and their magnetic moments were measured on a computer-controlled Quantum Design SQUID magnetometer at various magnetic field strengths. Three scans were made and then averaged for each data point. In most of our experiments magnetic moments were measured as a function of both temperature (2 or 5-300 K) and magnetic field strength (200 gauss to up to 5 teslas) by changing the magnetic field at each temperature.

A. C. resistances of pressed pellets of polycrystalline $\text{MMo}(\text{O},\text{N})_3$ ($\text{M} = \text{Sr}, \text{Ba}$) were measured on a Hewlett-Packard 4192A LF Impedance Analyzer by the 4-point arrangement (the van der Pauw method). Specimens were round pellets with a 2.38 mm diameter and a uniform thickness (1.24 mm for $\text{BaMo}(\text{O},\text{N})_3$ and 1.01 mm for $\text{SrMo}(\text{O},\text{N})_3$). Pressure sensitive contacts were employed. Applied voltage was 1.00 V at 1 kHz. Temperatures ranged from 295 K to ~85 K (liquid nitrogen temperature). The probe arrangement is shown in Figure 23(a).

D. C. resistances of sintered $\text{LaO}_x\text{N}_{1-x}$ specimens were measured from 2-300 K by the four-probe method on the Quantum Design SQUID magnetometer. Insulated copper wire probes were spot-welded onto samples in a nitrogen-filled glove bag. To eliminate the thermal e.m.f. contribution to the voltage readings measurements were performed with positive and reversed polarities for 20 seconds each and then averaged. The measurement was also computer controlled with a constant D. C. current supply of 10 mA. Voltage drops ranged from 1.3 to 140 mV in the normal conducting state. The probe arrangement is shown in Figure 23(b).

Conductivity of the sintered $\text{BaCeLn}(\text{O},\text{N})_4$ specimens were checked with a digital ohmmeter.

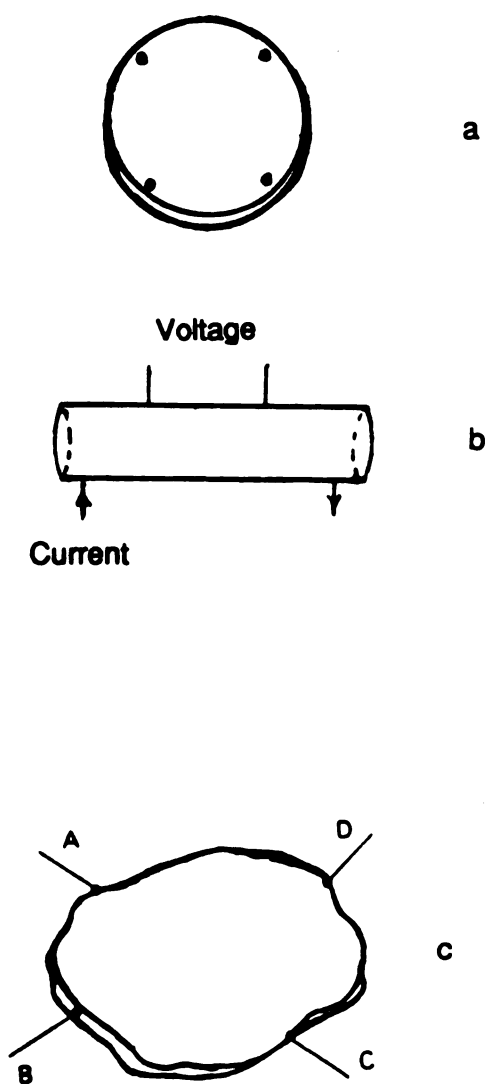


Figure 23. Simple arrangement for four-probe electrical conductivity measurements. (a) Four equally spaced probes on a pressed round pellet of uniform thickness; (b) four probes on a cylindrical sample of uniform diameter; (c) The arrangement for van der Pauw measurements. Note that in (a) and (c) current is driven between two probes and the voltage is measured between other two probes.

4.3 Data Analysis

4.3.1 Magnetic Data

a. Calculations

Directly obtained values of the magnetic measurements were longitudinal magnetic moments in emu units. Molar magnetic susceptibilities were obtained according to the following formula:

$$\chi_m = \frac{\text{mag. moment}}{n \cdot H_o}$$

where n is the number of moles of the material and H_o is the applied magnetic field (gauss). The χ_m 's were plotted against $1/H$ when data in different magnetic fields were available and straight lines were extrapolated to zero reciprocal field ($1/H \rightarrow 0$) to eliminate contributions of ferromagnetic impurities. If necessary, extrapolated susceptibilities χ_m^{ext} were finally corrected for diamagnetism according to the following equation:

$$\chi_m^{\text{corr}} = \chi_m^{\text{ext}} - \chi_m^{\text{dia}}$$

Diamagnetic susceptibilities were estimated by the following procedure developed by Pascal:

$$\chi_m^{\text{dia}} = \sum_i n_i \cdot \chi_i(A) + \sum_j n_j \cdot \chi_j(B)$$

where n_i is the number of atoms of type i in a molecular formula, χ_i the ionic (or atomic) gram diamagnetic susceptibility, and χ_j is the susceptibility associated with n_j structural features such as double or triple C-C bonds. In this work $n_j = 0$. Diamagnetic susceptibilities were taken from Selwood (155). It is worth noting that the correction also

included the diamagnetism of the capsule containers used in this experiment.

Because the diamagnetic contribution is always negative, the corrected molar susceptibility is always greater than the uncorrected value.

For a paramagnetic substance that obeys the Curie or Curie-Weiss Law, the effective magnetic moment μ_{eff} (in Bohr magnetons) can be calculated with the formula:

$$\mu_{\text{eff}} = 2.828 \sqrt{\chi_m^{\text{corr}} \cdot (T - \theta)}$$

$\theta = 0$ when the Curie Law is obeyed.

(Numerous computer programs for the above calculations have been written in FORTRAN-77 and are available in directory [LIU] in the CEMVAX system. If sufficiently good data are available, computer extrapolation of χ_m vs. $1/H$ can be used.)

b. Plotting

χ_m^{corr} vs. $1/T$.

If a straight line is observed the data follow the Curie Law. The slope of the straight line is the Curie constant C ; the line should pass through the origin.

If a straight line which intercepts the positive χ_m axis at $1/T = 0$ is obtained, temperature-independent paramagnetism may be present, or the diamagnetic correction may have been over-estimated.

If a straight line which intercepts the negative χ_m axis at $1/T = 0$ is obtained, the diamagnetic correction probably has been underestimated.

$1/\chi_m^{\text{corr}}$ vs. T

If the χ_m^{corr} vs. $1/T$ plot is not linear, then plot $1/\chi_m^{\text{corr}}$ vs. T . A straight line indicates that the data follow the Curie-Weiss Law. The intercept of the line is the Weiss constant θ ; the slope is still the Curie constant.

χ_m^{corr} vs. T

Sometimes magnetic susceptibilities do not have a simple temperature dependence. For example, an anti-ferromagnetic transition will have a complex magnetic feature. In this case, a straightforward plot of χ vs. T is probably most informative.

4.3.2 Electrical Resistivities

For the sintered $\text{LaO}_x\text{N}_{1-x}$ specimens, D.C. resistivities ($\Omega\cdot\text{cm}$) can be calculated with the formula:

$$\rho = R \frac{A}{l} = R \frac{\pi r^2}{l}$$

where R is the resistance (Ω) obtained by the method shown in Figure 23(b) (Page 151), A is the cross sectional area of the sample rod, l the distance (cm) between the two voltage probes, and $r = d/2$ is the radius (cm) of the rod. Resistivity errors are estimated to be less than 5% and are mainly from inaccuracies in the size measurement of the irregular-shaped specimens.

For powder samples of $\text{MMo}(\text{O},\text{N})_3$ ($M = \text{Ba}, \text{Sr}$), the conductivity σ ($\Omega^{-1}\cdot\text{cm}^{-1}$) can be calculated according to the following van der Pauw equation (159) that is derived for arbitrarily positioned contacts with an irregularly shaped sample of uniform thickness d (cm) (Figure 23(c), Page 151).

$$\sigma = \frac{\ln 2}{\pi d} \left(\frac{2}{R_{AB,CD} + R_{BC,DA}} \right) \cdot F \left(\frac{R_{AB,CD}}{R_{BC,DA}} \right)$$

where R s are the resistances (Ω) between the designated probes, and F is a slowly varying function of its argument. In our experiment, the samples were round disks and the four probes were equally spaced, thus

$$R_{AB,CD} = R_{BC,DA} \quad \text{and} \quad F(R_{AB,CD}/R_{BC,DA}) = 1,$$

and the van der Pauw equation is simplified as

$$\sigma = \frac{\ln 2}{\pi d R} \quad \text{or} \quad \rho = R \frac{\pi d}{\ln 2}$$

CHAPTER 5 RESULTS AND DISCUSSION

SYNOPSIS

Crystal structures derived from X-ray powder diffraction data, chemical analysis results, and magnetic and electrical properties of various oxidenitrides are presented and discussed. Perovskite-related $\text{MMo}(\text{O},\text{N})_3$ ($\text{M} = \text{Ba}, \text{Sr}$) exhibit complex magnetic behavior at low temperatures and are probably metallic; $\text{CaFe}_2(\text{O},\text{N})_4$ -type $\text{BaCeLn}(\text{O},\text{N})_4$ ($\text{Ln} = \text{La}, \text{Ce}$) are insulating and paramagnetic with Ce exhibiting mixed-valent states; NaCl-type $\text{LaO}_x\text{N}_{1-x}$ are metallic above 6 K for $x = 0.45$ and above 5 K for $x = 0.28$ and become superconducting below these temperatures.

5.1 Pseudo-Ternary BaCeLn(O,N)₄ Systems (Ln = La, Ce)

5.1.1 Chemical Characterization

Reddish-colored BaCeLn(O,N)₄ (Ln = La, Ce) powders were obtained both by quenching and upon slow cooling. They gave similar X-ray powder diffraction patterns, decomposed quickly upon contact with water, and evolved ammonia gas that was easily detected both by its smell and by moist pHydrion paper. They also decomposed slowly in air with a weight gain and a color change first to light yellow and eventually to brown.

Duplicate nitrogen analyses were performed on two identical but separately packaged (i.e., A,B) BaLaCe(O,N)₄ specimens. Found for A: 1.60, 1.55%; for B: 1.62, 1.49%. (The second member of each pair is lower than the first as would happen if hydrolysis occurred between analyses and may indicate a slightly low analysis result.) Combining all four results yields %N = 1.56 ± 0.05. If all anion sites are occupied, the formula is BaCeLaO_{3.47(2)}N_{0.53(2)}. The nitrogen content is slightly higher than this; as is indicated below, the specimen contained ~10% BaLa₂O₄.

Duplicate nitrogen analyses were also performed on comparably packaged BaCe₂(O,N)₄ specimens. Found for specimen A: 1.23, 1.56%; for B: 2.35, 2.41%. In lieu of the data on the Ln = La compound, the disparity between the two A results, and the magnetic data, the A set is rejected. The remaining analytical data suggest the formula, BaCe₂O_{3.18(1)}N_{0.82(1)}.

5.1.2 Magnetic and Electrical Properties

Both oxidenitrides are strongly paramagnetic between 10-300 K. In the high temperature region they obey the Curie law as is illustrated in the Figure 24 plot of $\chi(\text{BaCeLa}(\text{O,N})_4)$ vs T^{-1} . For BaCeLa(O,N)₄, the presence of Ce³⁺ is thus clear. Observed

magnetic moments are lower than those calculated on the basis of an f^1 localized configuration for Ce^{3+} , indicative that the cerium ions exhibit mixed valence states. The observed magnetic moments of 1.83 and $1.70 \mu_B$ at 300 K for $\frac{1}{2} \text{BaCe}_2(\text{O,N})_4$ and $\text{BaCeLa}(\text{O,N})_4$, respectively, correspond to about 1.44 Ce^{3+} in $\text{BaCe}_2(\text{O,N})_4$ and 0.68 Ce^{3+} in $\text{BaCeLa}(\text{O,N})_4$. Approximately 70% of the cerium ions in each compound are in the trivalent state.

Magnetic data suggest the formulas $\text{BaCeLaO}_{3.68}\text{N}_{0.32}$ and $\text{BaCe}_2\text{O}_{3.44}\text{N}_{0.56}$, again on the assumption of complete anion site occupancy. They support the mixed anion composition, partial reduction of Ce^{4+} in both CeN and BaCeO_3 by N^3 when the latter reacts with CeN at 800°C , and a greater Ce^{3+} ion content in the oxidenitride than in the reactant CeN . For $\text{BaCeLa}(\text{O,N})_4$ the magnetic data also underestimate the N-content because of the BaLa_2O_4 impurity.

Conductivity tests with sintered specimens indicated insulating properties of these oxidenitrides. The resistances of both sintered specimens at room temperature exceeded 2 megohms. Unidentified impurity reflections were observed in the X-ray powder diffraction patterns of the sintered specimens. These resistivities are so large that even in the presence of a small impurity level the products must be insulators. Although precise resistivities could not be obtained, these data suggest localized trivalent and tetravalent cations.

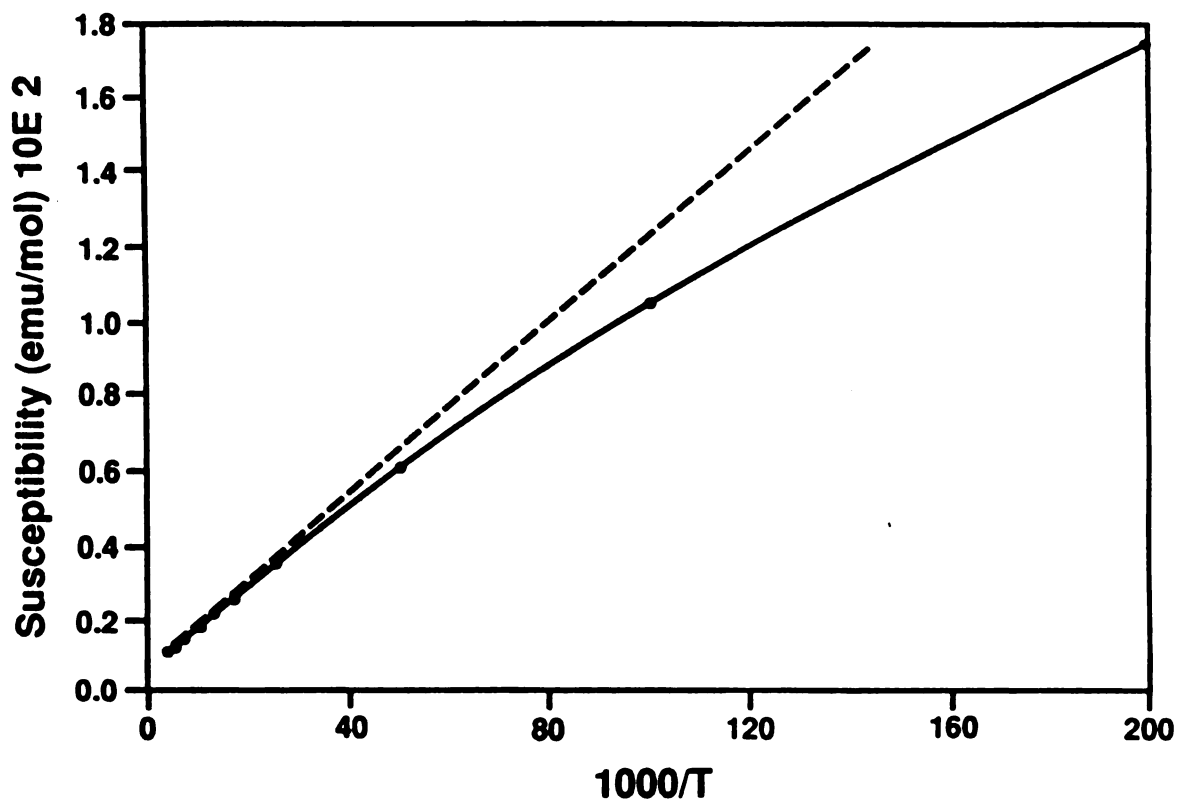


Figure 24. The magnetic susceptibility of BaCeLa(O,N)₄ plotted against reciprocal temperature at 5-300 K.

5.1.3 Crystal Structures

The $\text{BaCe}_2(\text{O,N})_4$ product contained a trace unidentified impurity—two very weak reflections in the X-ray powder diffraction photograph. The powder X-ray diffraction pattern can be indexed on orthorhombic symmetry with figures-of-merit, $F(20) = 26$ and $F(31) = 23$. Lattice parameters of both $\text{BaLn}_2(\text{O,N})_4$ compounds are listed in Table 37. Systematic extinctions consistent with space groups Pbnm (# 62, centrosymmetric) or $\text{Pbn}2_1$ (# 33, noncentrosymmetric) suggest the CaFe_2O_4 -type structure (160). Intensities calculated using the atomic parameters for CaSc_2O_4 (161) and isotropic temperature factors of 1.5, 1.0, and 0.9, respectively, for O^{2-} , Ba^{2+} , and Ce^{3+4+} agree well with observed values. Miller indices and observed and calculated interplanar d-spacings and intensities for $\text{BaCe}_2(\text{O,N})_4$ are presented in Table 38.

Table 37. Lattice parameters for selected (Pbnm , $Z=4$) CaFe_2O_4 -type oxides and oxidenitrides.

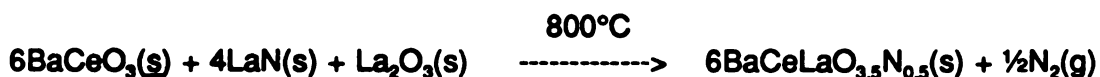
Formula	$a(\text{\AA})$	$b(\text{\AA})$	$c(\text{\AA})$	$V(\text{\AA}^3)$	Reference
BaCe_2O_4	12.584	10.641	3.676	492.2	(149)
$\text{BaCe}_2(\text{O,N})_4$	12.565(1)	10.644(1)	3.6593(4)	489.4	this work
$\text{BaCeLa}(\text{O,N})_4$	12.573(3)	10.637(3)	3.657(1)	489.1	this work
BaLa_2O_4	12.652(2)	10.686(2)	3.7077(6)	501.3	this work
	12.662	10.675	3.705	500.8	(149)

Table 38. Miller indices, and observed and calculated interplanar d-spacings and intensities for Pbnm CaFe_2O_4 -type $\text{BaCe}_2(\text{O,N})_4$.

<u>h</u>	<u>k</u>	<u>l</u>	<u>d_c</u> (Å)	<u>d_o</u> (Å)	<u>I_o</u> ^a	<u>I_c</u>	<u>h</u>	<u>k</u>	<u>l</u>	<u>d_c</u> (Å)	<u>d_o</u> (Å)	<u>I_o</u> ^a	<u>I_c</u>
0	2	0	5.322	5.331	vw	3	3	4	1	1.9142		-	2
2	2	0	4.061	4.065	w	9	0	0	2	1.8297	1.8283	w	20
1	0	1	3.513	3.513	w	11	1	5	1	1.8207	1.8210	vw	1
1	1	1	3.336	3.338	w	9	6	3	0	1.8035	1.8031	w	14
4	0	0	3.141	3.142	m	45	6	1	1	1.7916	1.7911	w	17
2	3	0	3.089	3.086	vs	100	4	4	1	1.7754			20
2	1	1	3.031	3.029	s	67				1.7734		m	
0	2	1	3.015			32	0	6	0	1.7740			12
4	1	0	3.013	3.013	m	8	2	5	1	1.7659			14
1	2	1	2.932	2.932	w	7				1.7623	1.7651	w	4
2	2	1	2.718	2.711	w	2	4	5	0				
3	1	1	2.6677	2.6677	m	26	6	2	1	1.7200	1.7202	w	6
1	3	1	2.4965	2.4963	w	9	3	5	1	1.6487	1.6846	vw	2
2	4	0	2.4503			4	2	2	2	1.6681	1.6687	vw	2
3	2	1	2.4471	2.4483	w	2	6	4	0	1.6457	1.6459	vw	3
2	3	1	2.3606		-	3	5	4	1	1.6346		-	4
4	1	1	2.3259	2.3257	w	8	7	1	1	1.5934	1.5931	vw	3
3	3	1	2.1764			11	1	6	1	1.5836			2
4	2	1	2.1453	2.1748	m	31				1.5806		w	
0	4	1	2.1521	2.1510	w	21	4	0	2	1.5810			14
1	4	1	2.1212	2.1208	w	12	2	3	2	1.5743			33
5	0	1	2.0716	2.0713	vw	6	8	0	0	1.5706	1.5731	m	2
2	4	1	2.0360	2.0344	vw	2	4	1	2	1.5639	1.5638	vw	3
6	2	0	1.9487	1.9486	w	12	8	1	0	1.5538	1.5536	vw	5
5	2	1	1.9305	1.9301	w	5	4	6	0	1.5447			12
							7	2	1	1.5424	1.5442	w	1
							8	2	0	1.5064			1
							6	4	1	1.5009	1.5012	vw	5

The product of the BaCeO₃-LaN reaction is a mixture of two CaFe₂O₄-type structures: BaCeLa(O,N)₄ and BaLa₂O₄ (149). The data compiled in Table 37 illustrate the close relationship between the lattice parameters of BaCeLn(O,N)₄ (Ln = La, Ce) and BaLn₂O₄. The unit cell volume of BaCe₂(O,N)₄ is slightly less than that of BaCe₂O₄. This result would not be expected from oxidation number and ionic radii considerations. The Ce³⁺, La³⁺ and Ce⁴⁺ CN VI ionic radii are 1.01, 1.03, and 0.87 Å, respectively; O²⁻ and N³⁻ CN IV ionic radii are 1.38 and 1.46 Å (28). If the compounds are considered ionic the number of N³⁻ and Ce⁴⁺ ions must be equal. The volume of a N³⁻ ion is 2.028 Å³ larger than that of the O²⁻ ion while a Ce⁴⁺ ion is 1.557 Å³ smaller than a Ce³⁺ ion. We would thus expect a unit cell volume increase of 0.470 Å³/N atom. The volume decrease therefore must reflect either more efficient lattice packing (which is unlikely), a smaller size for the nitrogen atom than its 'ionic' radius indicates, or the presence of a greater quantity of Ce⁴⁺ than is required for charge balance. Magnetic and analytical data suggest the nitrogen atom is smaller than predicted by its ionic radius.

The oxygen needed to substitute for loss of nitrogen came from the small amount of La₂O₃ or CeO₂ present in the reactants. In reactions which involved CeN this contaminant disappeared during reaction. In those which involved LaN the product contained a BaLa₂O₄ impurity, an indication of insufficient La₂O₃ to allow the reaction to go to completion. The reaction can typically be illustrated by the following equation



Gas evolution indeed occurred; quartz tubes which contained the products were pressurized when they were opened in the glove box. When research was initiated the

reaction was envisioned a 1:1 BaCeO₃:LnN combination and oxide was not considered necessary. The results indicate that the (BaCe₂O₃N) 3:1 O:N product is less stable than less nitrogen-rich compounds; additional oxide is therefore necessary for reaction.

Reduction of Ce⁴⁺ by N³⁻ also occurred in the CaO-CeO₂-CeN system when we attempted to prepare CaCe₂(O,N)₄ at 950°C. The quartz tubes again contained a gas under pressure and a Ce₂O₃-like phase (presumably Ce₂(O,N)₃) resulted; CaCe₂(O,N)₄ did not form. The Ca²⁺ ionic radius is presumed too small to stabilize the compound.

Efforts to synthesize BaThCe(O,N)₄ using the difficultly reducible Th⁴⁺ to substitute for Ce⁴⁺ in BaCeO₃ were unsuccessful even though perovskite-type BaThO₃ could be prepared (162). The 0.94 Å Th⁴⁺ ionic radius is very close to that of Ce⁴⁺ (0.87 Å) and reasonably close to that of Ce³⁺ (1.01 Å) (28), suggestive that a mixed valence Ce-compound might form. However, a BaThO₃ - CeN reaction did not occur even at 950°C, a temperature higher than that for the BaCeO₃-CeN reaction (800°C) --- the only product was again a Ce₂O₃-like phase which resulted from reaction between CeN and the CeO₂ impurity. This observation suggests mixed valence to be an important factor for the formation of BaM₂(O,N)₄-type oxidenitrides -- for cerium to exhibit both 3+ and 4+ oxidation states the related central cation must exhibit some degree of trivalency.

It is noteworthy that the cerium oxidenitrides characterized so far have structures and lattice parameters closely related to those of their oxide counterparts. The X-ray diffraction pattern previously reported for the (Ce⁴⁺-containing) oxidenitride, Ce₂N₂O (148), said to be isostructural with Th₂N₂O, is almost identical to that of Ce₂O₃ prepared by H₂ reduction of CeO₂ at 1200°C (163). This similarity can be demonstrated better by comparison of their hexagonal lattice parameters : "Ce₂N₂O": \underline{a} = 3.880 Å, \underline{c} = 6.057 Å vs. Ce₂O₃: \underline{a} = 3.891 Å, \underline{c} = 6.063 Å. Given the essentially identical X-ray scattering powers of N³⁻ and O²⁻, the small size difference between them, and the counter-balancing size

difference between Ce^{4+} and Ce^{3+} , it is difficult to distinguish $\text{Ce}_2\text{N}_2\text{O}$ (Ce^{4+}), Ce_2O_3 (Ce^{3+}) and Ce_2NO_2 (Ce^{3+} and Ce^{4+}) and other mixed valence states by X-ray diffraction. Similarly, the possibility that the reported Li_2CeN_2 (148) with Ce^{4+} could be a mixed valent $\text{Li}_2\text{Ce}(\text{O},\text{N})_2$ cannot be dismissed. Since anion ordering has been observed in the cerium oxidenitride $\text{CeO}_x\text{N}_{1-x}$ (138), the true symmetries of these oxidenitrides may differ from predictions based upon X-ray diffraction data. Further studies, e.g., neutron diffraction, appear necessary to characterize these compounds definitively.

5.2 Pseudo-Ternary $\text{MMo}(\text{O},\text{N})_3$ Oxidenitrides ($\text{M} = \text{Sr}, \text{Ba}$)

5.2.1 Crystal Structures

$\text{SrMo}(\text{O},\text{N})_3$ This product was obtained as dark blue to deep purple fine powders. Its color is in sharp contrast to the deep red of SrMoO_3 . The X-ray diffraction pattern of the oxidenitride is essentially indistinguishable from that of SrMoO_3 . Both are perovskite-types with $a = 3.9765(3) \text{ \AA}$ for $\text{SrMo}(\text{O},\text{N})_3$, and $a = 3.9751(3) \text{ \AA}$ (145) for SrMoO_3 ($3.9761(5) \text{ \AA}$ from our result). Repeated experiments indicated that the weight loss upon NH_3 reduction corresponds to an empirical formula very close to SrMoO_2N . Found N (%): 3.09 ± 0.03 . Derived chemical formula is $\text{SrMoO}_{2.49}\text{N}_{0.51}$. Thus Mo appears to be in a mixed-valent state; its average oxidation number is +4.51.

$\text{BaMo}(\text{O},\text{N})_3$ It was obtained as a black powder, also distinctly different from the dark red of BaMoO_3 . Samples prepared between 700-950°C were mixtures of at least three phases. A typical sample contained in addition to $\text{BaMo}(\text{O},\text{N})_3$ 5-10% perovskite-type BaMoO_3 , and ~5% of another unidentified impurity which shows broad reflections at $d \approx 2.500$ and 2.465 \AA . Found N (%): 3.66 ± 0.15 . Derived chemical formula is $\text{BaMoO}_{2.27}\text{N}_{0.73}$. The real composition of the major phase, typically about 90% in the mixture, while uncertain, obviously has a high nitrogen content. This result suggests for molybdenum a higher oxidation state than that in SrMoO_3 .

The X-ray powder pattern of the $\text{BaMo}(\text{O},\text{N})_3$ phase has been indexed successfully by the program TREOR on a rhombohedral lattice with the refined hexagonal parameters $a = 5.9701(8)$ and $c = 21.510(4) \text{ \AA}$. Possible space groups deduced from systematic

extinctions include $R32$, $R3m$, and $R\bar{3}m$. While the structure of this new rhombohedral phase remains a mystery, a possible model structure BaRuO_3 , better described as a nine-layer close packing of BaO_3 layers (164). It has the space group $R\bar{3}m$. Recently $\text{Ba}_9\text{Ir}_{3.2}\text{Mn}_{5.8}\text{O}_{27}$ has been shown by single crystal studies (165) to be isostructural with BaRuO_3 . The model structure can be derived by a rhombohedral distortion of the cubic perovskite structure. Calculated diffraction reflection intensities based on this model generally matched those observed. Miller indices, observed and calculated interplanar d spacings and intensities are listed in Table 39. However, the structure of $\text{BaMo}(\text{O},\text{N})_3$ could not be refined to a satisfactory degree by the X-ray Rietveld procedure. Refinements have been tested with both programs XRS-82 and DBW32S (mentioned in Part I). Refinement did converge; final R_i was 14%. However, the isotropic temperature factor of Mo(1) at (0.0, 0.0, 0.5) was unusually high ($U=0.42$ compared to ~ 0.01 for Mo(2)). Alternatively, when it was allowed to refine with a fixed overall temperature factor, the occupancy factor of the Mo(1) site refined to ~ 0.1 . Such a low occupancy suggests a chemical formula close to $\text{Ba}_9\text{Mo}_6(\text{O},\text{N})_{27-x}$, which appears to contradict mass loss data obtained upon NH_3 reduction of BaMoO_4 .

Table 39. Miller indices, and observed and calculated interplanar d-spacings and intensities for BaMo(O,N)₃.

h	k	l	d _c (Å)	d _o (Å) ¹⁾	I _c ²⁾	I _o ³⁾	h	k	l	d _c (Å)	d _o (Å)	I _c	I _o
0	0	3	7.1701	7.1737	7	<1	2	0	11	1.5596	1.5614	0	1
1	0	1	5.0396	5.0396	4	<1	3	0	6	1.5533		----	20
0	1	2	4.6598	----	6	0	2	2	0	1.4925	1.4929	23	23
1	0	4	3.7293	3.7293	3	1	0	1	14	1.4728	1.4741	<1	2
0	0	6	3.5851	----	5	<1	2	1	10	1.4464	1.4464	29	34
0	1	5	3.3070	3.2995	67	98	0	0	15	1.4340	1.4343	2	5
1	1	0	2.9850	2.9802	100	100	3	0	9	1.3979	1.3991	<1	2
1	1	3	2.7558	----	5	0	2	2	6	1.3779	----	2	<1
1	0	7	2.6415	----	3	<1	3	1	5	1.3604	1.3607	12	22
2	0	2	2.5135	2.5150	0	5	2	0	14	1.3208	1.3215	<1	1
0	2	4	2.3299	2.3302	10	7	1	0	16	1.3011	----	2	0
1	1	6	2.2940	2.2931	11	1	1	1	15	1.2926	1.2924	10	23
2	0	5	2.2159	2.2136	46	57	2	2	9	1.2660	1.2667	0	3
1	0	10	1.9860	1.9854	40	35	4	0	4	1.2568	1.2570	1	2
0	2	7	1.9782	----	3	0	0	4	5	1.2379	1.2382	7	10
1	1	9	1.8657	1.8662	3	4	1	2	14	1.2078	1.2082	<1	2
2	0	8	1.8635	----	2	0	1	3	10	1.1932	1.1932	15	16
1	2	5	1.7792	1.7787	24	56	2	3	5	1.1435	1.1434	7	12
3	0	0	1.7234	1.7234	22	27	4	1	0	1.1282	1.1281	12	12
0	2	10	1.6535	1.6533	25	27	4	0	10	1.1079	1.1065	7	6
1	2	8	1.5808	1.5816	<1	1	2	1	16	1.1076	----	2	0

Note. 1) d_o Guinier data;
 2) I_c calculated from the BaRuO₃ model;
 3) I_o diffractometer data.

5.2.2 Reaction Conditions

Two independent reactions can be described as follows:



(1) is a reductive substitution that yields Mo^{5+} ; (2) is a simple reduction similar to the hydrogen reduction that produces Mo^{4+} perovskites. Apparently both reactions occurred for BaMoO_4 since BaMoO_3 was observed. If partial reductive substitution occurs, a mixed-valent oxidenitride with Mo^{4+x} will be obtained. It is not clear whether $\text{SrMo}(\text{O},\text{N})_3$ is a mixed-valent compound or simply a mixture of SrMoO_3 and SrMo_2N . But $\text{BaMo}(\text{O},\text{N})_3$ must either be a mixed-valent compound or a reductively substituted oxidenitride BaMoO_2N with Mo^{5+} . For the NH_3 reactions with BaMoO_4 temperature appears to be a very important factor in determining the relative reaction rates. Numerous experiments at various temperatures performed to synthesize the pure oxidenitride met with little success. Too high a reaction temperature ($\geq 750^\circ\text{C}$) increases the yield of BaMoO_3 . When the temperature was $700\text{--}900^\circ\text{C}$, not only was BaMoO_3 formed but another unknown reaction also occurred. When it was lowered to 650°C , the reaction proceeded slowly with the formation of essentially a single phase; that is, the rhombohedral oxidenitride. However, the reaction was incomplete even in 6 days; it seemed to have stopped after the first 2~3 days of reaction, probably because of a diffusion problem. Subsequent regrinding and heating or raising the temperature unavoidably lead to formation of impurity phases. Efforts to synthesize mixed metal oxidenitrides $\text{Ba}_x\text{Sr}_{1-x}\text{Mo}(\text{O},\text{N})_3$ produced mixtures of the cubic and rhombohedral phases. The relative composition varies with the reaction

temperature and the Ba/Sr ratio. The cubic phase predominates even with Ba/Sr up to 3. Preparation of a single cubic phase at a small Ba/Sr ratio appeared possible, however, the weight loss indicated that unlike SrMoO_4 in which nearly one mole of oxygen can be substituted by nitrogen simple reduction predominates for $\text{Ba}_x\text{Sr}_{1-x}\text{MoO}_4$.

5.2.3 Magnetic and Electrical Properties

Both $\text{SrMo}(\text{O},\text{N})_3$ and $\text{BaMo}(\text{O},\text{N})_3$ are feebly paramagnetic and magnetic susceptibilities are field dependent. The extrapolated and diamagnetically corrected susceptibilities are plotted against the temperature in Figures 25 and 26. Room temperature susceptibilities of $\text{SrMo}(\text{O},\text{N})_3$ and $\text{BaMo}(\text{O},\text{N})_3$ are 1.23×10^{-4} and 5.80×10^{-5} $\text{emu} \cdot \text{mol}^{-1}$, respectively, and increase only about 5% down to 90 K. These values are significantly lower than those expected for localized d^1 or d^2 electronic configurations and are also lower than susceptibilities of the metallic oxides (146), SrMoO_3 (2.01×10^{-4}) and BaMoO_3 (2.15×10^{-4} $\text{emu} \cdot \text{mol}^{-1}$). The difference in magnetic behavior between the oxidenitrides and oxides becomes more apparent in the low temperature range. Susceptibilities of the oxides are constant to within 3% from room temperature to that of liquid helium; the oxidenitrides exhibit interesting features below 90 K. First, there is a peak around 50 K on curves of both $\text{SrMo}(\text{O},\text{N})_3$ and $\text{BaMo}(\text{O},\text{N})_3$. It was suspected to be from liquified molecular oxygen (mp 54.35, bp 90.18 K, from reference 166). However, repeated experiments with samples carefully purged prior to measurements indicated that the peak results from the specimens. It probably represents an anti-ferromagnetic transition. $\text{BaMo}(\text{O},\text{N})_3$ has another weaker peak around 30 K. Since among the three phases present in the $\text{BaMo}(\text{O},\text{N})_3$ mixture BaMoO_3 has a temperature-independent paramagnetism, the different magnetic behavior observed is probably principally that of the oxidenitride. Secondly, the magnetic susceptibility of $\text{SrMo}(\text{O},\text{N})_3$

increases rapidly with decreasing temperature below the transition point and appears to obey the Curie law as shown in Figure 27. The susceptibility of $\text{BaMo}(\text{O,N})_3$ at the lower temperature region is only slightly higher than that at higher temperatures.

The feeble and nearly temperature-independent paramagnetic susceptibilities of $\text{BaMo}(\text{O,N})_3$ and $\text{SrMo}(\text{O,N})_3$ above 90 K suggest metallic behavior. Typical powder resistivity values are: for $\text{SrMo}(\text{O,N})_3$, $1.50 \times 10^{-2} \Omega\cdot\text{cm}$ at 294 K and $1.77 \times 10^{-2} \Omega\cdot\text{cm}$ at 86 K; for $\text{BaMo}(\text{O,N})_3$, $0.416 \Omega\cdot\text{cm}$ at 295 K and $0.652 \Omega\cdot\text{cm}$ at 85 K. The resistivity of both samples increases with decreasing temperature. This is a typical feature of a semiconductor. However, the non-linear relationships between $\ln \sigma$ and $1/T$ shown in Figures 28 and 29 do not support the semiconducting model. It is believed that observed resistances are predominately contact resistances, especially for the $\text{BaMo}(\text{O,N})_3$ specimen because it contained a small amount of insulating BaMoO_4 . Since sintering tends to decompose the oxidenitrides, we have not been able to get more accurate data. When all the experiments are considered, the fairly low resistivities of $\text{SrMo}(\text{O,N})_3$ are considered an indication of metallic conductivity.

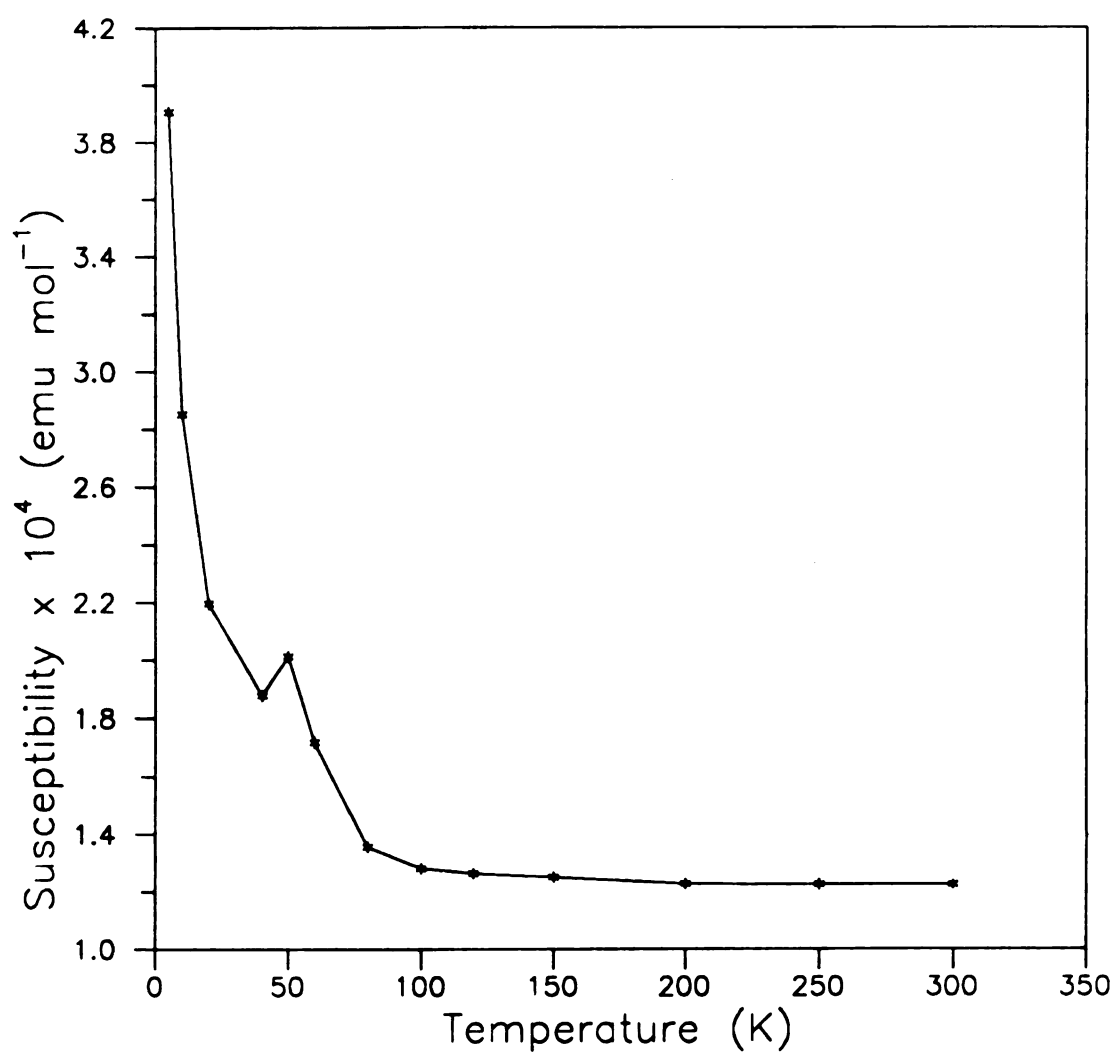


Figure 25. Magnetic behavior of $\text{SrMo}(\text{O,N})_3$ at 5-300 K.

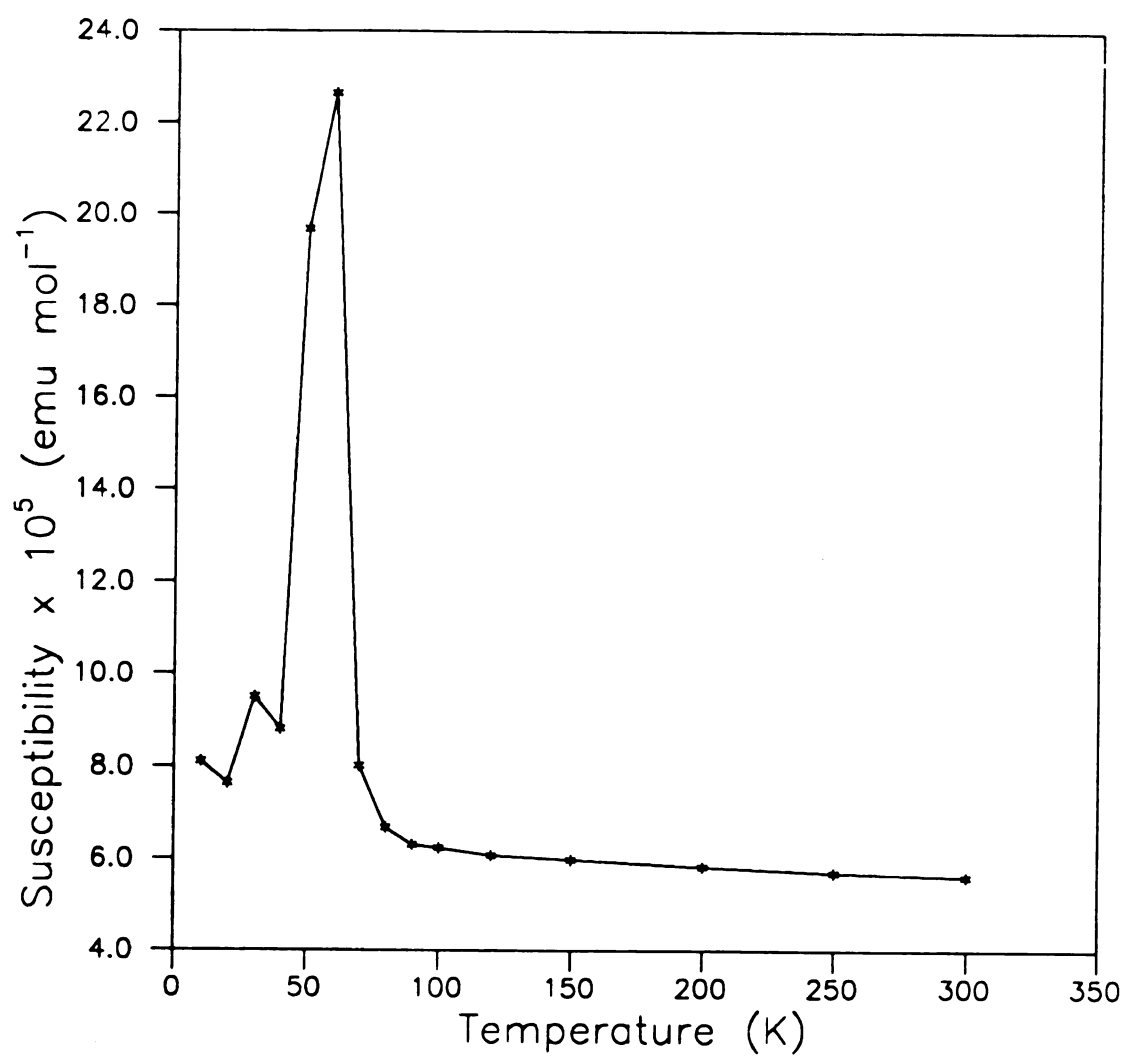


Figure 26. Magnetic behavior of BaMo(O,N)₃ at 10-300 K.

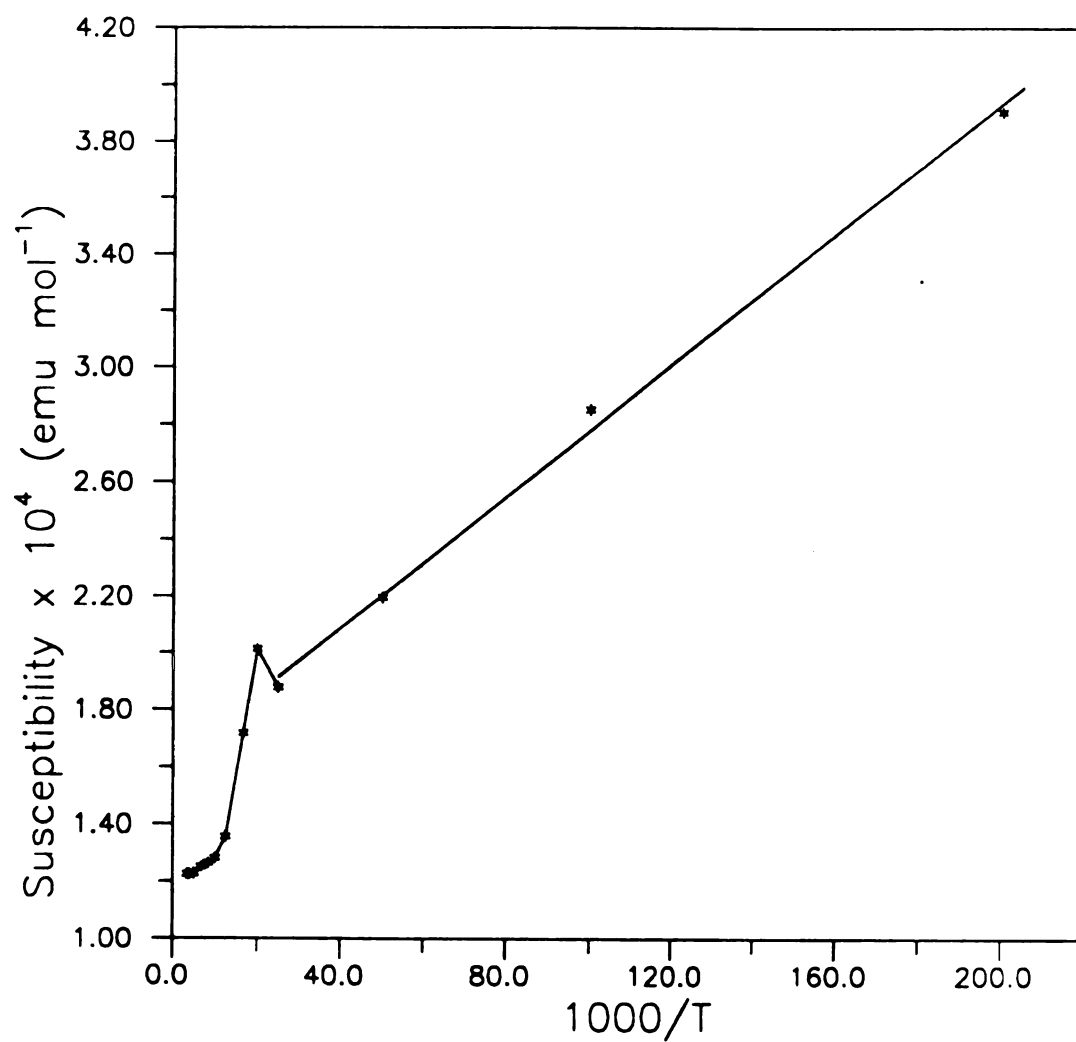


Figure 27. Magnetic susceptibility of $\text{SrMo}(\text{O,N})_3$ vs. reciprocal temperature.

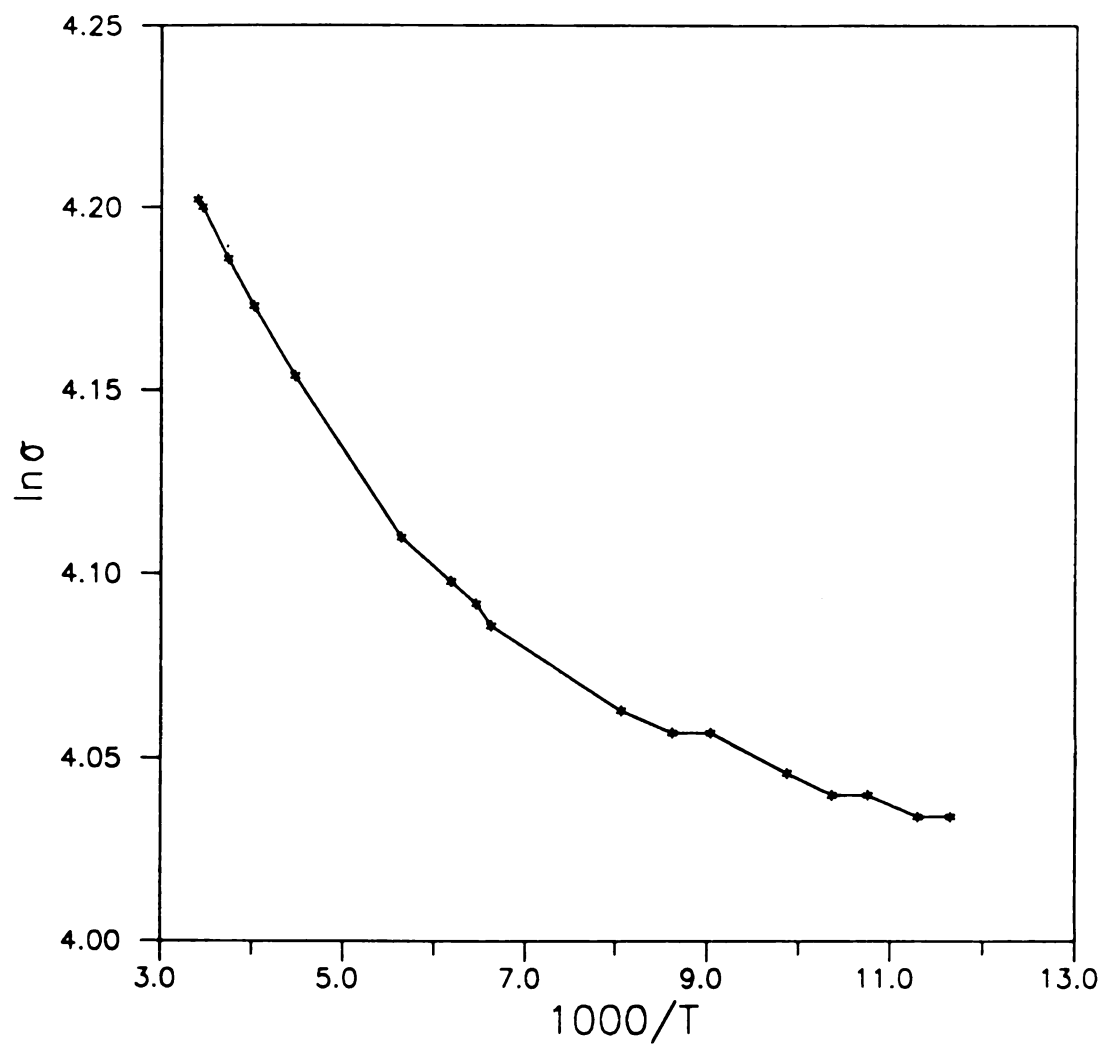


Figure 28. Conductivity data of $\text{SrMo}(\text{O,N})_3$ at 86-294 K plotted as $\ln \sigma$ against reciprocal temperature.

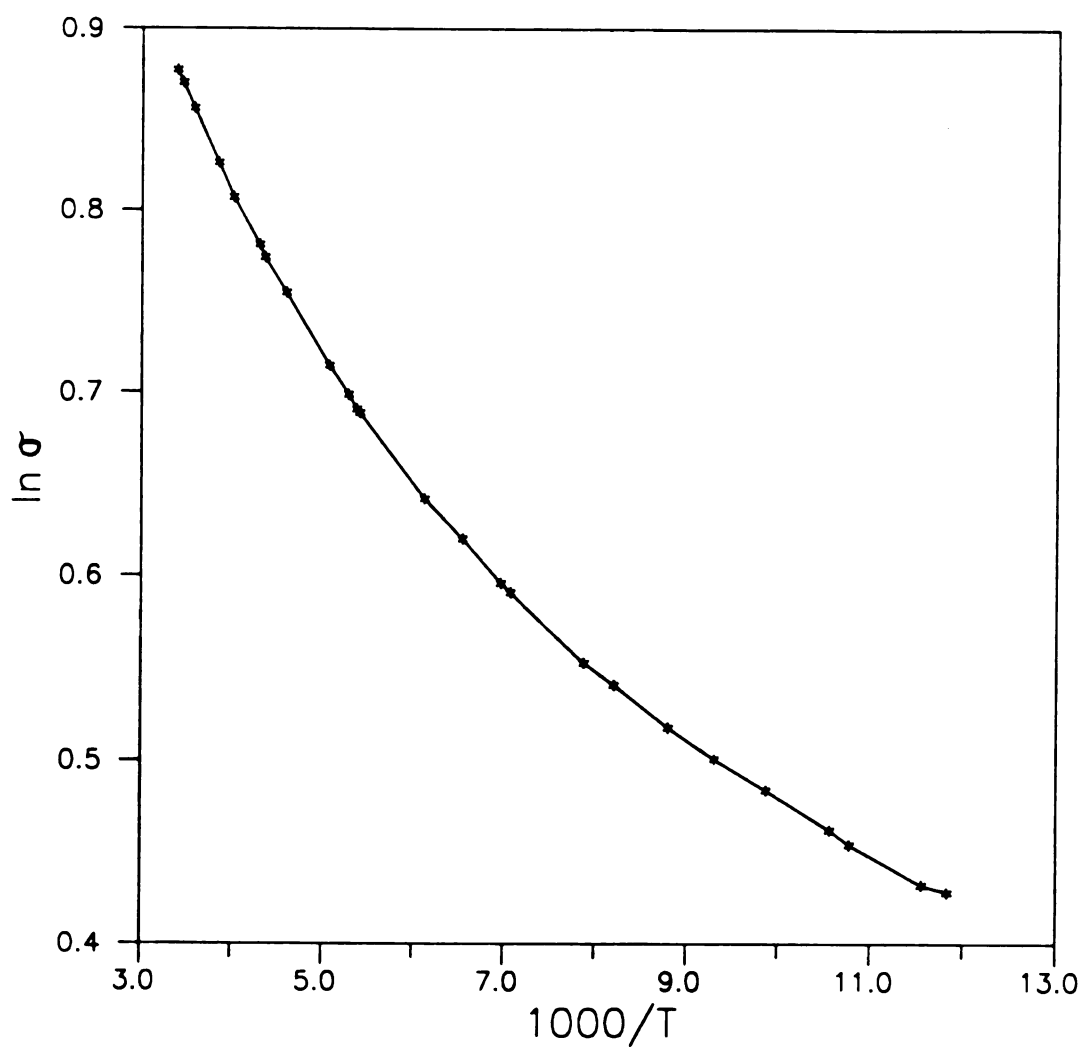


Figure 29. Conductivity data of $\text{BaMo}(\text{O},\text{N})_3$ at 85-295 K plotted as $\ln \sigma$ against reciprocal temperature.

5.3 Pseudo-Binary $\text{LaO}_x\text{N}_{1-x}$ Oxidenitrides

Both compositions (Page 149) yielded cubic single-phase products; specimen I was dark blue with $a = 5.2540(5) \text{ \AA}$ while II was deep red with $a = 5.2273(8) \text{ \AA}$. Similar colors were reported by Brown and Clark (137). Upon exposure to air the products decomposed gradually with evolution of $\text{NH}_3(\text{g})$. The X-ray powder diffraction lines were fairly broad, indicative of inhomogeneous solid solutions over a certain range of compositions. Approximate compositions deduced from a Vegard-law plot of $\text{LaO}_x\text{N}_{1-x}$ - lattice parameter data (137) indicated the formulas $\text{LaO}_{0.28}\text{N}_{0.72}$ (I) and $\text{LaO}_{0.45}\text{N}_{0.55}$ (II), respectively. Since the lattice parameter remained invariant at $a = 5.223 \text{ \AA}$ when $x \geq 0.46$ in $\text{LaO}_x\text{N}_{1-x}$, the oxygen content in II, whose lattice parameter is slightly less than this invariant value, may be actually higher than 0.45.

5.3.1 Electrical Properties

The resistivity-temperature data of I and II are shown in Figures 30 and 31, respectively. Both samples exhibit characteristic metallic conductivity similar to that of sodium (Figure 21, Page 143) in the temperature regions 6-300 K. In this normal conducting state the resistivities of both specimens decrease linearly with decreasing temperature to the superconducting transition point where a sharp transition occurs at $T_c = 5.6\text{-}6 \text{ K}$ for $\text{LaO}_{0.45}\text{N}_{0.55}$ and at $T_c = 4\text{-}5 \text{ K}$ for $\text{LaO}_{0.28}\text{N}_{0.72}$. Comparison of these values to the $\text{LaN } T_c$, 1.3 K (154) suggests that the superconducting transition temperature increases with increasing oxygen content.

The $\text{LaO}_{0.45}\text{N}_{0.55}$ specimen is more conducting than $\text{LaO}_{0.28}\text{N}_{0.72}$ at the normal conducting state. At room temperature the resistivity of the former is nearly two orders of magnitude less than that of the latter, while $\text{LaO}_{0.28}\text{N}_{0.72}$ has a greater thermal coefficient than $\text{LaO}_{0.45}\text{N}_{0.55}$. The greater conductivity value with higher oxygen content suggests that

an increase in the oxygen content increases the number of electrons in the conduction band and thus confirms the formulation $\text{La}^{3+}\text{O}_x\text{N}_{1-x}\underline{\text{e}_x}$. Similar behavior has been observed for $\text{NdO}_x\text{N}_{1-x}$ (139).

Even though powder resistivities are usually greater than single crystal resistivities, our data on sintered samples are considered quantitative because the temperature and composition dependences and even the zero resistance behavior at the superconducting state are well resolved. Therefore contact resistances are negligible. Based on the deduced compositions, the lattice parameters and the free electron formulation, electron mobilities can be estimated as discussed Chapter 3. Mobilities calculated for the two samples at three different temperatures are listed in Table 40. These data suggest that $\text{LaO}_{0.45}\text{N}_{0.55}$ is nearly a free carrier conductor. The reason for the substantially lower mobilities of the less oxygen-rich $\text{LaO}_{0.28}\text{N}_{0.72}$ is not clear.

Table 40. Estimated Mobilities of Oxidenitrides $\text{LaO}_x\text{N}_{1-x}$.

Compound	Electron dens. electrons·cm ⁻³	Mobility (cm ² ·volt ⁻¹ ·sec ⁻¹)		
		10 K	150 K	300 K
$\text{LaO}_{0.28}\text{N}_{0.72}$	7.72×10^{21}	3.04	0.376	0.168
$\text{LaO}_{0.45}\text{N}_{0.55}$	1.26×10^{22}	23.3	13.4	8.39

The temperature dependence curves of the resistivities of both samples are linear but describable as two straight lines of different slopes above the T_c 's. The cross point of the two straight lines is ~50 K for $\text{LaO}_{0.28}\text{N}_{0.72}$ and ~85 K for $\text{LaO}_{0.45}\text{N}_{0.55}$. Below these temperatures the thermal coefficients are smaller than those above it. This transition is probably related to a structural change, such as an anion ordering as was observed in $\text{CeO}_x\text{N}_{1-x}$ by electron diffraction (138) or a cubic to tetragonal transformation as was

observed in $\text{NdO}_{0.08}\text{N}_{0.94}$ (139). Structural studies, especially using neutron or electron diffraction as a function of temperature, are necessary to reveal the changes.

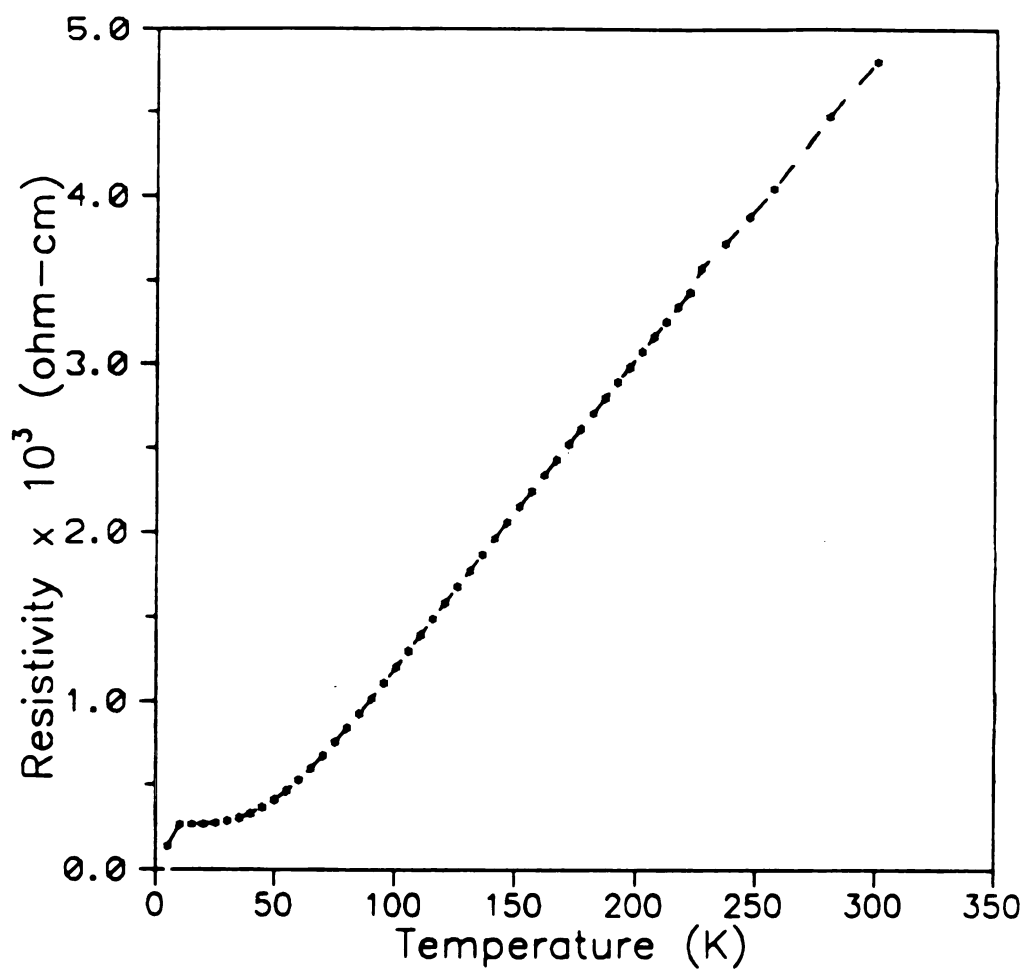


Figure 30. Electrical resistivity of $\text{LaO}_{0.28}\text{N}_{0.72}$ vs. temperature at 5-300 K.

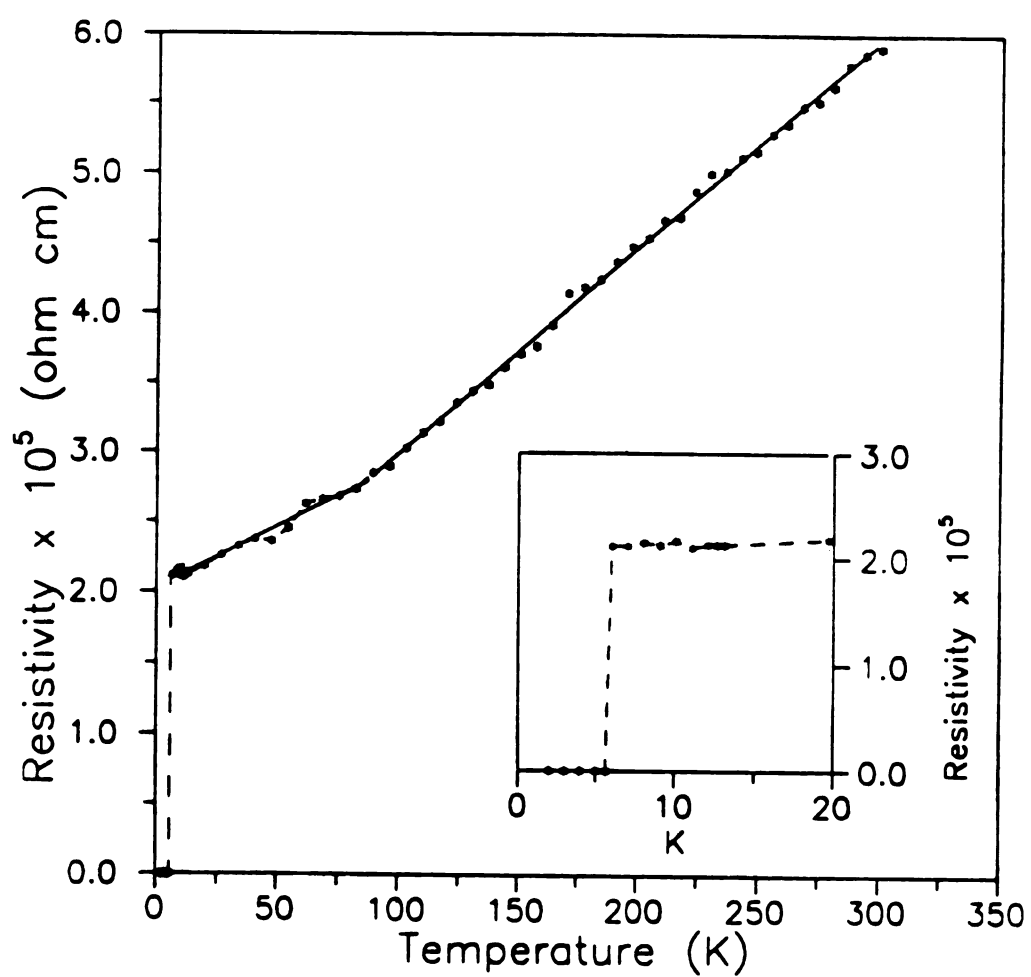


Figure 31. Electrical resistivity of $\text{LaO}_{0.45}\text{N}_{0.55}$ vs. temperature at 2-300 K.

5.3.2 Magnetic Properties

The molar susceptibility-temperature curves for $\text{LaO}_{0.28}\text{N}_{0.72}$ and $\text{LaO}_{0.45}\text{N}_{0.55}$ are depicted in Figures 32 and 33, respectively. The flux exclusion phenomenon is observed at the superconducting state with transition temperatures consistent with those observed in the electrical measurements.

The temperature dependence of the susceptibility in the normal conducting state appears complicated. It remains almost constant above ~ 40 K for $\text{LaO}_{0.28}\text{N}_{0.72}$, and above ~ 80 K for $\text{LaO}_{0.45}\text{N}_{0.55}$ as can be seen from Figures 32 and 33; between these temperatures and the superconducting transition temperatures Curie behavior is observed as shown in Figures 34 and 35. However, the susceptibility is apparently field-dependent, indicating the presence of ferromagnetic impurities in the sample. Such a dependence is illustrated for II in Figure 36 together with the diamagnetically-corrected and zero reciprocal field-extrapolated susceptibilities, which should be the true paramagnetic susceptibilities of the samples. The Curie type susceptibilities in the low temperature regions probably result from a very small amount of paramagnetic impurity. The nearly constant and small extrapolated susceptibilities in the higher temperature regions are in agreement with a Pauli-type electron gas model of metallic materials. However, the susceptibility values of $7 - 10 \times 10^{-5} \text{ emu}\cdot\text{mol}^{-1}$ are significantly higher than expected. Using the electron densities given in Table 40, we can estimate the magnetic susceptibility from the Pauli-Peierls equation discussed in 2.2.2e (Page 134). Even neglecting the diamagnetic term ($-m_e^2/3m^2$) in the computation, with a volume of $21.50 \text{ cm}^3\cdot\text{mol}^{-1}$, the molar Pauli susceptibility for $\text{LaO}_{0.45}\text{N}_{0.55}$ would be about 1.1×10^{-5} , at least seven times lower than the observed value. The observed high susceptibilities are probably an indication of a narrow $5d\ t_{2g}$ band structure (146).

Metal nitride superconductors with the NaCl-type structure have long been known.

Among them, NbN has the highest T_c (~18 K) (128). Phillips applied the bond length anomalies arising from anharmonic stabilization of harmonic lattice instabilities (128) and three golden coordinates, the suitable averaged valence-electron numbers N_v , the orbital radii differences ΔR , and the metallic electronegativity differences ΔX (167), to analyze the superconducting transition temperatures. The above described oxidenitrides $\text{LaO}_x\text{N}_{1-x}$ are a group of new materials. It appears that the increase of superconducting transition temperature of $\text{LaO}_x\text{N}_{1-x}$ is due to the increased electron densities. Further studies on related oxidenitrides and measurements of the electronic and magnetic properties of La(III)O_x at low temperatures are necessary to facilitate our understanding of the superconductivity of oxidenitrides and to search for ways of increasing the transition temperatures.

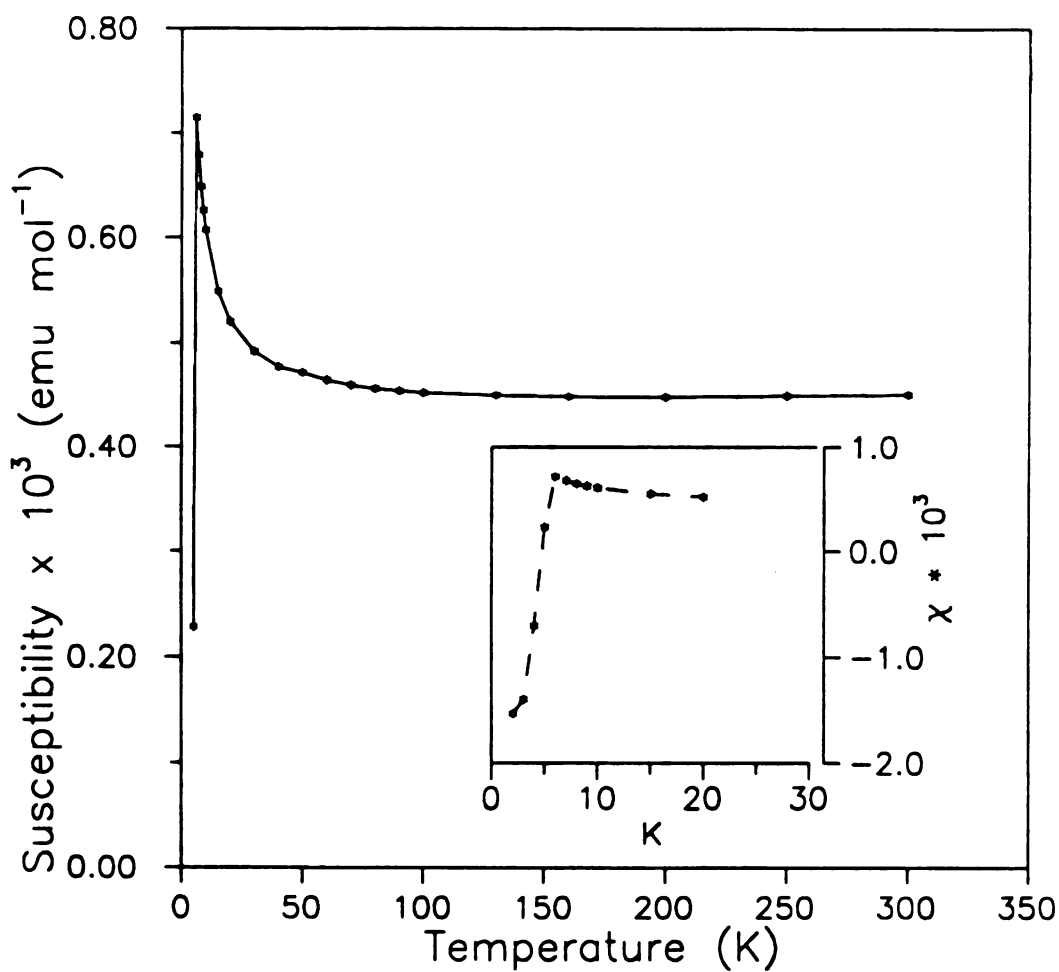


Figure 32. Magnetic susceptibility of $\text{LaO}_{0.28}\text{N}_{0.72}$ vs. temperature at 2-300 K ($H_0 = 200$ gauss).

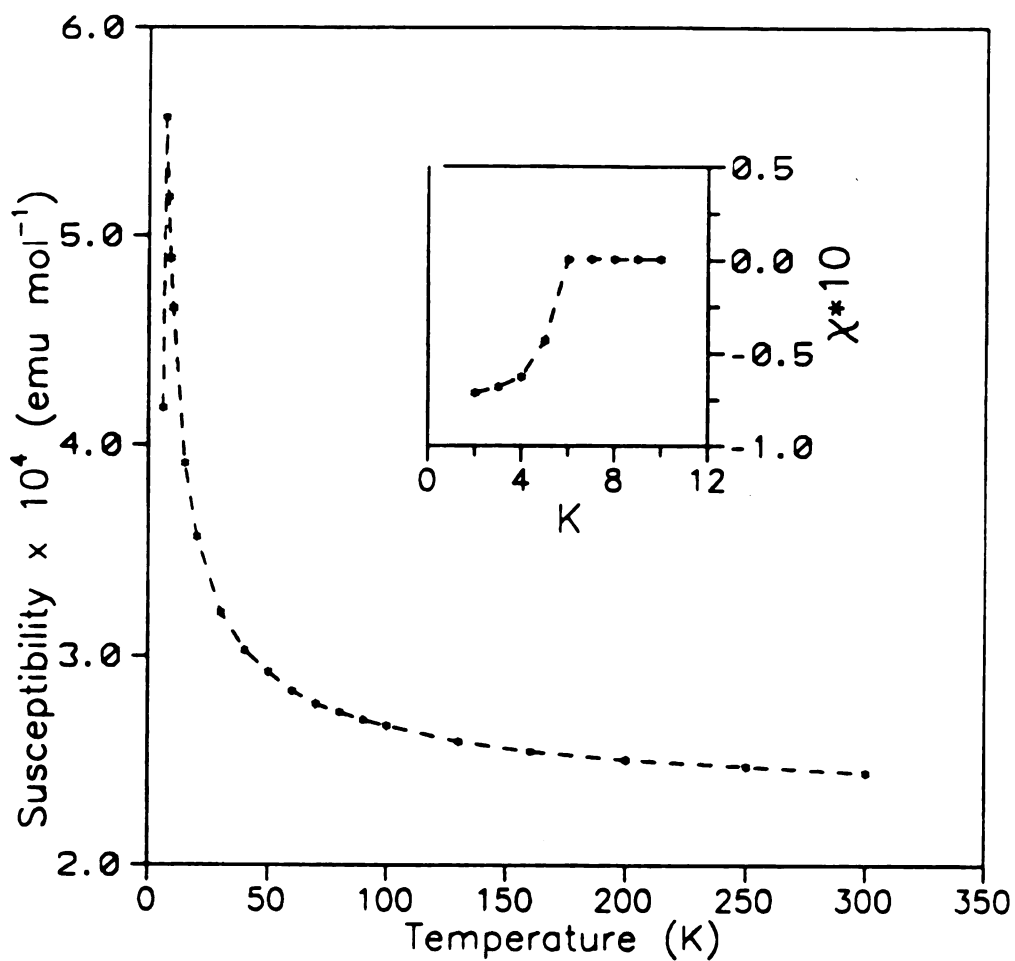


Figure 33. Magnetic susceptibility of $\text{LaO}_{0.48}\text{N}_{0.55}$ vs. temperature at 2-300 K ($H_0 = 200$ gauss).

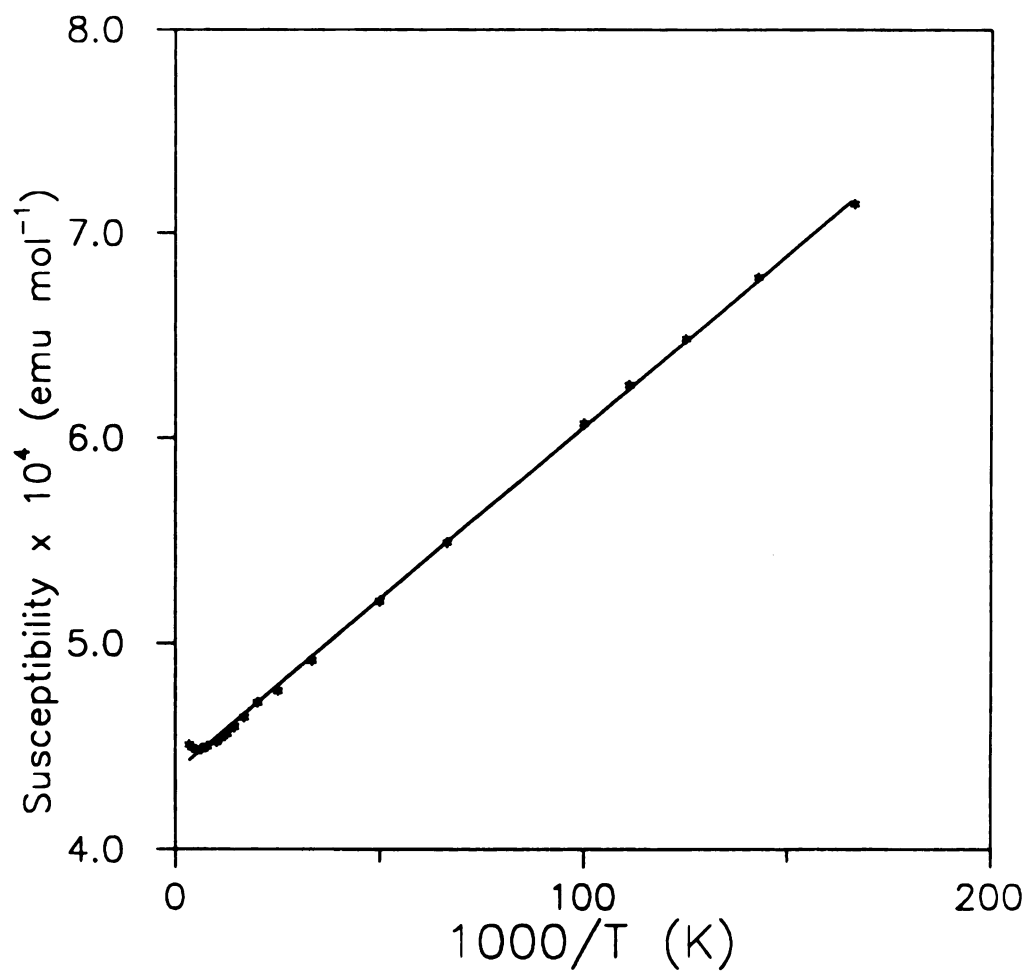


Figure 34. Magnetic susceptibility of $\text{LaO}_{0.28}\text{N}_{0.72}$ plotted against reciprocal temperature to illustrate the Curie behavior at low temperatures ($H_0 = 200$ gauss).

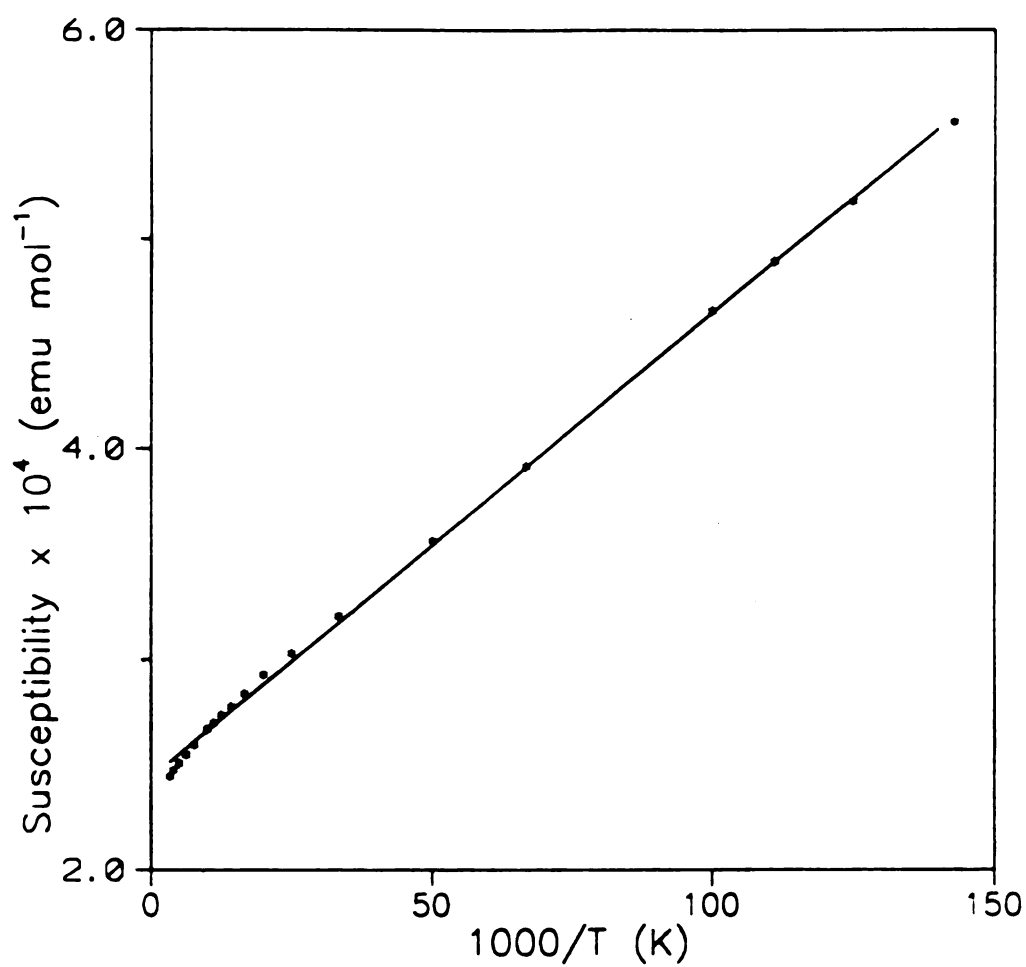


Figure 35. Magnetic susceptibility of $\text{LaO}_{0.45}\text{N}_{0.55}$ plotted against reciprocal temperature to illustrate the Curie behavior at low temperatures ($H_0 = 200$ gauss).

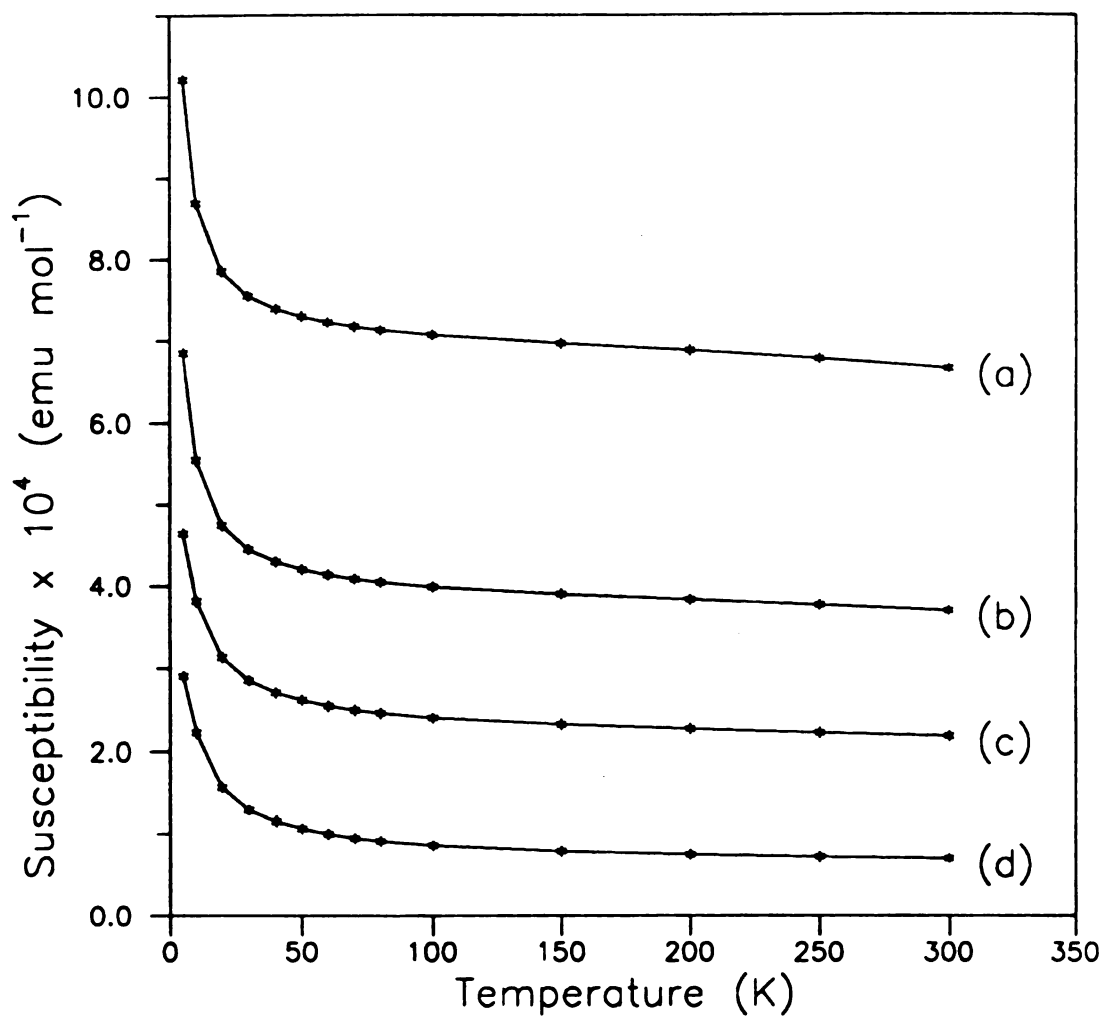


Figure 36. Magnetic field and temperature dependences of the magnetic susceptibility of $\text{LaO}_{0.45}\text{N}_{0.55}$ above T_c . Applied magnetic field is: (a) 5000 gauss; (b) 1 tesla; (c) 2 teslas; (d) extrapolated to $H \rightarrow \infty$.

CONCLUDING REMARKS

Oxidenitrides are potentially interesting magnetic, electrical, or dielectric materials. The preliminary results presented in this work indicate some possible directions of this research area. $\text{LaO}_x\text{N}_{1-x}$ are especially interesting because of their superconducting transitions at low temperatures. Oxidenitrides of non-lanthanide elements without f valence electrons such as $\text{YO}_x\text{N}_{1-x}$ and $\text{ScO}_x\text{N}_{1-x}$, if they exist, are expected to have interesting electrical and magnetic properties similar to those of $\text{LaO}_x\text{N}_{1-x}$ if the "free electrons" are responsible for these properties. Further studies are necessary to understand the superconducting mechanism and to increase the superconducting transition temperature T_c . Transition elements such as Re, Mn, Fe, and Os exhibit multiple valences and form perovskite-type BaMO_3 oxides. These oxides are likely candidates for nitrogen substitutions. Neutron diffraction studies are desirable for structural studies of these oxidenitrides.

GENERAL REFERENCE BOOKS

1. C. N. R. Rao and J. Gopalakrishnan, "New Directions in Solid State Chemistry. *Structure, synthesis, properties, reactivity and materials design*", Cambridge University Press, 1986.
2. A. K. Cheetham and P. Day, "Solid State Chemistry. *Techniques*", Clarendon Press, 1987.
3. D. Brown, "Halides of the Transition Elements. *Halides of Lanthanides and Actinides*", John Wiley & Sons Ltd., 1968.
4. M. F. C. Ladd and R. A. Palmer, "Structure Determination by X-Ray Crystallography", Plenum Press, Second Edition, 1985.
5. G. H. Stout and L. H. Jensen, "X-Ray Structure Determination. *A Practical Guide*", 1972.
6. B. D. Cullity, "Elements of X-Ray Diffraction", Addison-Wesley Publishing Company, Second Edition, 1978.
7. H. D. Megaw, "Crystal Structures: *A Working Approach*", W. B. Saunders Company, 1973.
8. R. W. G. Wyckoff, "Crystal Structures", Vol. 1, Interscience Publishers, Second Edition, 1963.
9. J. S. Blakemore, "Solid State Physics", Cambridge University Press, Second Edition, 1985.

REFERENCES

- 1 M. S. Whittingham, *Prog. Solid State Chem.* **12**, 41-99 (1978).
- 2 W. A. England, J. B. Goodenough, and P. J. Wiseman, *J. Solid State Chem.* **49**, 289 (1983).
- 3 J. R. Günter, *J. Solid State Chem.* **5**, 354-359 (1972).
- 4 L. Ganapathi, A. Ramanan, J. Gopalakrishnan, and C. N. R. Rao, *J. Chem. Soc., Chem. Commun.*, 62-63 (1986).
- 5 T. Kudo, A. Ishikawa, H. Okamoto, and K. Miyauchi, *J. Solid State Chem.* **77**, 412-415 (1988).
- 6 A. K. Ganguli, L. Ganapathi, J. Gopalakrishnan, and C. N. R. Rao, *J. Solid State Chem.* **74**, 228-231 (1988).
- 7 A. Le Bail, C. Jacoboni, M. Leblanc, R. De Pape, H. Huroy, and J. L. Fourquet, *J. Solid State Chem.* **77**, 96-101 (1988).
- 8 A. Haase and G. Brauer, *Z. Anorg. Allg. Chem.* **441**, 181-195 (1978).
- 9 A. Haase and G. Brauer, *Z. Anorg. Allg. Chem.* **450**, 36-44 (1979).
- 10 M. D. Taylor and C. P. Carter, *J. Inorg. Nucl. Chem.* **24**, 387-390 (1962).
- 11 G. Meyer and P. Ax, *Mater. Res. Bull.* **17**, 1447-1455 (1982).
- 12 G. Meyer, T. Staffel, S. Dötsch, T. Schleid, *Inorg. Chem.* **24**, 3505-3507 (1985).
- 13 G. Meyer, S. Dötsch and T. Staffel, *J. Less-Common Metals* **127**, 155-160 (1987).
- 14 M. M. Banaszak Holl, M. Kersting, B. D. Pendley and P. T. Wolczanski, *Inorg. Chem.* **29**, 1518-1526 (1990); M. M. Banaszak Holl, P. T. Wolczanski, G. D. Van Duyne, and A. T. Harrison, 1990 ACS meeting, Boston, Inorg Chem Division, abstract no. 143.
- 15 G. Davies, B. C. Giessen and H. L. Shao, 1990 ACS meeting, Boston, Inorg Chem Division, abstract no. 351.

- 16 J. G. Brennan, T. Siegrist, S. M. Stuczynski, and M. L. Steigerwald, *J. Am. Chem. Soc.* **111**, 9240-9241 (1989).
- 17 M. L. Steigerwald, *Chem. Mater.* **1**, 52-57 (1989).
- 18 K.-W. Kim, S. Dhingra and M. G. Kanatzidis, 1990 ACS Meeting, Boston, Inorg. Chem. Division, abstract no. 142.
- 19 K. Rossmanith, *Monatsh. Chem.* **110**, 109-114 (1979).
- 20 A. F. Clifford and K. J. Hughes, In *Rare Earth Research III*; L. Eyring, Ed., Gordon and Breach, 1965.
- 21 A. F. Clifford, in *Rare Earth Research II*, K. S. Vorres, Ed.; Gordon and Breach, New York, 1963; pp. 45-50.
- 22 G. Brauer and B. Pfeiffer, *J. Less-Common Met.* **5**, 171-176 (1963).
- 23 R. Giovanoli, W. Feitknecht, R. Maurer, and H. Haeni, *Chimia* **30**, 307-309 (1976).
- 24 M. M. Thackeray and A. De Kock, *J. Solid State Chem.* **74**, 414-418 (1988).
- 25 R. Chevrel, M. Sergent and J. Prigent, *Mater. Res. Bull.* **9**, 1487 (1974).
- 26 K. Rossmanith and C. Auer-Welsbach, *Monatsh. Chem.* **96**, 602-605 (1965).
- 27 G. Liu and H. A. Eick, *Inorg. Chem.* **27**, 2161-2163 (1988).
- 28 R. D. Shannon, *Acta Cryst.* **A32**, 751-767 (1976).
- 29 O. Greis and J. M. Haschke, Rare Earth Fluorides, in *Handbook on the Physics and Chemistry of Rare Earths*, Vol. 5, Chapter 45, pp 387-460, Eds. K. A Gschneidner, Jr. and L. Eyring, North-Holland, 1982.
- 30 S. E. Ness, D. J. M. Bevan, H. J. Rossell, *Eur. J. Solid State Inorg. Chem.* **25**, 509-516 (1988).
- 31 D. J. M. Bevan, M. J. McCall, S. E. Ness, and M. R. Taylor, *Eur. J. Solid State Inorg. Chem.* **25**, 517-526 (1988).
- 32 D. J. M. Bevan, S. E. Ness, and M. R. Taylor, *Eur. J. Solid State Inorg. Chem.* **25**, 527-534 (1988).
- 33 C. Rinck, *Ph.D. Dissertation*, University of Karlsruhe, 1982, and references therein.
- 34 D. M. Laptev, V. F. Goryushkin, I. S. Astakhova and G. G. Polyakova, *Russ. J. Inorg. Chem. (Engl. Transl.)* **24**, 730-733 (1979).
- 35 H. Bärmighausen, J. M. Friedt and J. P. Sanchez, Int. Rare Earth Conf., ETH Zürich, Switzerland March 3-8, 1985; private communication. J. F. Sanchez, M.

- Malki, J. M. Friedt, and H. Bärnighausen, *Hyperfine Interactions* **28**, 811-814 (1986).
- 36 S. A. Hodorowicz, M. Olejak-Chodan, and H. A. Eick, *J. Solid State Chem.* **71**, 205-213 (1987).
- 37 M. Olejak-Chodan, S. A. Hodorowicz, and H. A. Eick, *Cryst. Res. Tech.* **22**, 285-289 (1987).
- 38 U. Löchner, *Dissertation*, Universität Karlsruhe, 1980.
- 39 H. Bärnighausen, *Proc. Rare Earth Res. Conf.*, 12th, **1**, 404-413 (1976).
- 40 U. Löchner, H. Bärnighausen, and J. D. Corbett, *Inorg. Chem.* **16**, 2137 (1977).
- 41 H. Lüke and H. A. Eick, *Proc. Rare Earth Res. Conf.*, 12th, **1**, 424 (1976).
- 42 H. Lüke and H. A. Eick, *Inorg. Chem.* **21**, 965 (1982).
- 43 G. J. McCarthy, J. J. Rhyne and H. B. Silber, *The Rare Earths in Mod. Sci. and Tech.*, Vol. 2, Plenum Press, New York, 1978.
- 44 M. Eitel, *Ph.D. Dissertation*, University of Karlsruhe, 1985.
- 45 H. Bärnighausen, *Rev. Chim. Min.* **10**, 77-92 (1973).
- 46 H. P. Beck, *J. Solid State Chem.* **47**, 328-332 (1983).
- 47 D. J. M. Bevan, J. Strähle and O. Greis, *J. Solid State Chem.* **44**, 75-81 (1982).
- 48 H. M. Rietveld, *Acta Cryst.* **22**, 151-152 (1967).
- 49 H. M. Rietveld, *J. Appl. Cryst.* **2**, 65-71 (1969).
- 50 A. K. Cheetham and J. C. Taylor, *J. Solid State Chem.* **21**, 253-275 (1977).
- 51 A. Albinati and B. T. M. Willis, *J. Appl. Cryst.* **15**, 361-374 (1982).
- 52 G. Malmros and J. O. Thomas, *J. Appl. Cryst.* **10**, 7 (1977).
- 53 J. O. Thomas, N. O. Fresson and Y. Anderson, *J. Appl. Cryst.* **13**, 605-607 (1980).
- 54 K. E. Johansson; T. Palm and P. E. Werner, *J. Phys. E.* **13**, 1289-1291 (1980).
- 55 P.-E. Werner, *Chem. Scripta A26*, 57-64 (1986).
- 56 J. O. Thomas, *Chem. Scripta A26*, 7-10 (1986).
- 57 P. Thompson and I. G. Wood, *J. Appl. Cryst.* **16**, 458-472 (1983).

- 58 A. Clearfield, L. B. McCusker, and P. R. Rudolf, *Inorg. Chem.* **23**, 4679-4682 (1984).
- 59 P. Rudolf and A. Clearfield, *Acta Cryst.* **B41**, 418-425 (1985).
- 60 W. Lasocha and H. A. Eick, *J. Solid State Chem.* **75**, 175-182 (1988); and **77**, 90-95 (1988).
- 61 Ch. Bärlocher, Proc. of the 6th Int. Conf. on Zeolites, Reno, U.S.A. P. 823. Eds. D. Olson and A. Bisio, Butterworths, London, 1984.
- 62 J. Paul Attfield, *Acta Cryst.* **B44**, 563-568 (1988).
- 63 A. G. Casado, A. Mendiola and I. Rasines, *Inorg. Chem.* **21**, 2902-2903 (1982).
- 64 D. E. Smith, J. E. Maskasky, and L. R. Spaulding, *J. Appl. Cryst.* **15**, 488-492 (1982).
- 65 G. Liu and H. A. Eick, *J. Less-Common Metals* **156**, 237-245 (1989).
- 66 J. E. Berg and P. E. Werner, *Z. Kristallogr.* **145**, 310-320 (1977).
- 67 Y. Laligant, A. Le Bail, G. Ferey, M. Hervieu, B. Raveau, A. Wilkinson and A. K. Cheetham, *Eur. J. Solid State Inorg. Chem.* **25**, 237-247 (1988).
- 68 P. Lightfoot, A. K. Cheetham and A. W. Sleight, *Inorg. Chem.* **26**, 3544-3547 (1987).
- 69 R. A. Young and D. B. Wiles, *J. Appl. Cryst.* **15**, 430-438 (1982).
- 70 A. Hepp and Ch. Bärlocher, *Aust. J. Phys.* **41**, 229-236 (1988).
- 71 S. H. Wang, G. King, S. H. Lin and T. Brown, *J. Solid State Chem.* **69**, 224-229 (1987).
- 72 G. Liu and H. A. Eick, *J. Less-Common Metals* **149**, 47-53 (1989).
- 73 G. Liu and H. A. Eick, to be published.
- 74 I. S. Astakhova, V. F. Goryushkin, and D. M. Laptev, *Russ. J. Inorg. Chem. (Engl. Transl.)* **24**, 1096-1097 (1979).
- 75 J. W. Visser, *J. Appl. Cryst.* **2**, 89-95 (1962).
- 76 P. E. Werner, L. Eriksson and M. Westdahl, *J. Appl. Cryst.* **18**, 367-370 (1985).
- 77 D. E. Appleman, D. S. Handwerker and H. T. Evans, Program X-ray, Geological Survey, U. S. Department of Interior, Washington, DC, 1966.

- 78 D. K. Smith, M. C. Nichols and M. E. Zolensky, "A FORTRAN IV Program for Calculating X-Ray Powder Diffraction Patterns, Version 10." The Pennsylvania State University, University Park, PA., 1983.
- 79 P. M. de Wolff, *J. Appl. Cryst.* **1**, 108-113 (1968).
- 80 G. S. Smith and R. L. Snyder, *J. Appl. Cryst.* **12**, 60-65 (1979).
- 81 H. Bärnighausen and E. Th. Rietschel, *Z. Anorg. Allg. Chem.* **354**, 23-26 (1967).
- 82 E. Th. Rietschel and H. Bärnighausen, *Z. Anorg. Allg. Chem.* **368**, 62-72 (1969).
- 83 H. Bärnighausen and N. Schultz, *Acta Cryst.* **B25**, 1104-1110 (1969).
- 84 H. P. Beck, *Z. Anorg. Allg. Chem.* **459**, 81-86 (1979).
- 85 H. D. Lutz, W. Buchmeier and B. Engelen, *Acta Cryst.* **B43**, 71-75 (1987).
- 86 J. Ladell, A. Zagofsky, and J. S. Pearlman, *J. Appl. Cryst.* **8**, 499-506 (1975).
- 87 Ch. Bärlocher and A. Hepp, "The X-Ray Rietveld System," Institut f. Kristallogr. u. Petrographie, ETH, Zürich, Switzerland, 1982.
- 88 J. A. Ibers and W. C. Hamilton, Ed, "International Tables for X-Ray Crystallography," Vol. IV, Kynoch Press, Birmingham, England, 1974.
- 89 G. Vogel and A. Schneider, *Inorg. Nucl. Chem. Lett.* **8**, 513-521 (1972).
- 90 R. Blachnik, G. Alberts and E. Enninga, *Z. Anorg. Allg. Chem.* **522**, 207-216 (1985).
- 91 *JCPDS Powder diffraction File No. 24-95*, International Centre for Diffraction Data, 1601 Park Lane, Swarthmore, PA 19081.
- 92 R. Bachman, *Diplomarbeit*, Universität Karlsruhe, 1980.
- 93 J. M. Haschke, *Inorg. Chem.* **15**, 298-303 (1976).
- 94 H. Bärnighausen and J. M. Haschke, *Inorg. Chem.* **17**, 18-21 (1978).
- 95 W. Martin, *Diplomarbeit*, Universität Karlsruhe, 1976.
- 96 *JCPDS Powder diffraction File No. 24-94*, International Centre for Diffraction Data, 1601 Park Lane, Swarthmore, PA 19081.
- 97 *JCPDS Powder diffraction File No. 24-89*, International Centre for Diffraction Data, 1601 Park Lane, Swarthmore, PA 19081.
- 98 S-H. Wang, S-B. Jiang, Z-X. Tang, H-Z. Yang, X-M. Li, *Huaxue Tongbao*, 654-656 (1981).

- 99** S-H. Wang, private communication; 1989.
- 100** X-M. Li and S-H. Wang, in *New Front. Rare Earth Sci. Appl.*, Proc. International Conf. on Rare Earth Development and Applications, Vol. 1, pp.338-341. Scientific Press; 1985.
- 101** H. G. Scott, *J. Appl. Cryst.* **16**, 159-163 (1983).
- 102** W. C. Hamilton, *Acta Cryst.* **18**, 502-510 (1965).
- 103** L. F. Druding and J. D. Corbett, *J. Am. Chem. Soc.* **83**, 2462-2467 (1961).
- 104** G. Meyer and T. Schleid, *Z. Anorg. Allg. Chem.* **528**, 55-60 (1985).
- 105** L. R. Morss, in *Standard Potentials in Aqueous Solution*; A. J. Bard, R. Parsons and J. Jordan eds; Dekker: New York, 1985; pp 587-629.
- 106** H. D. Lutz, H. J. Kluppel, F.-J. Marner, and H.-J. Kesterke, *Z. Naturforsch.* **28B**, 8-11 (1973).
- 107** D. M. Laptev, I. S. Astakhova, N. M. Kulagin and N. F. Bomko, *Russ. J. Inorg. Chem. (Engl. Transl.)* **21**, 643-644 (1976).
- 108** D. M. Laptev and I. S. Astakhova, *Russ. J. Inorg. Chem. (Engl. Transl.)* **26**, 914-915 (1981).
- 109** D. M. Laptev, V. F. Goryushkin, N. M. Kulagin, and E. S. Vorontsov, *Russ. J. Inorg. Chem. (Engl. Transl.)* **21**, 1438-1441 (1976).
- 110** D. M. Laptev, N. M. Kulagin and I. S. Astakhova, *Russ. J. Inorg. Chem. (Engl. Transl.)* **20**, 1108-1109 (1975).
- 111** J. G. Bednorz and K. A. Müller, *Z. Phys.* **B64**, 189 (1986).
- 112** M. K. Wu, J. R. Ashburn, C. J. Torng, P. H. Hor, R. L. Meng, L. Gao, Z. J. Huang, Y. Q. Wang, and C. W. Chu, *Phys. Rev. Lett.* **58**, 908 (1987).
- 113** J. M. Tarascon, W. R. McKinnon, L. H. Greene, G. W. Hull, and E. M. Vogel, *Phys. Rev. B* **36**, 226-234 (1987).
- 114** Y. LePage, T. Siegrist, S. A. Sunshine, L. F. Schneemeyer, D. W. Murphy, S. M. Zahurak, J. V. Waszczak, W. R. McKinnon, J. M. Tarascon, G. W. Hull, and L. H. Greene, *Phys. Rev. B* **36**, 3617-3621 (1987).
- 115** S. A. Hodorowicz, W. Lasocha, A. Lasocha, and H. A. Eick, *J. Solid State Chem.* **77**, 145-148 (1988).
- 116** W. Kang, H. J. Schulz, D. Jerome, S. S. Parkin, J. M. Bassat, and Ph. Odier, *Phys. Rev. B* **37**, 5132-5138 (1988).

- 117 J. M. Tarascon, L. H. Greene, P. Barboux, W. R. McKinnon, G. W. Hull, T. P. Orlando, K. A. Delin, S. Foner, and E. J. McNiff, Jr., *Phys. Rev. B* **36**, 8393-8400 (1987).
- 118 D. M. de Leeuw, C. A. H. A. Mutsaers, H. A. M. Van Hal, H. Verweij, A. H. Carim, and A. C. A. Smoorenburg, *Physica C* **156**, 126-132 (1988).
- 119 S. S. P. Parkin, V. Y. Lee, E. M. Engler, A. I. Nazzal, T. C. Huang, G. Gorman, R. Savoy, and R. Beyers, *Phys. Rev. Lett.* **60**, 2539 (1988).
- 120 S. S. P. Parkin, V. Y. Lee, A. I. Nazzal, R. Savoy, T. C. Huang, G. Gorman, and R. Beyers, *Phys. Rev. B* **38**, 6531-6537 (1988).
- 121 F. A. M. Van Woerden and D. M. Deleeuw, *Physica C* **165**, 221 (1990).
- 122 M. A. Subramanian, J. Gopalkrishnan, and A. W. Sleight, *J. Solid State Chem.* **84**, 413 (1990).
- 123 I. Felner, U. Yaron, Y. Yeshurun, E. R. Yacoby, and Y. Wolfus, *Phys. Rev. B* **40**, 11366 (1989).
- 124 Y. K. Tao, M. Bonvalot, Y. Y. Sun, R. L. Meng, P. H. Hor, and C. W. Chu, *Physica C* **165**, 13 (1990).
- 125 E. A. Early, N. Y. Ayoub, J. Beille, J. T. Markert, and M. B. Maple, *Physica C* **160**, 320 (1989).
- 126 A. Tressaud, B. Chevalier, B. Lepine, K. Amine, J. M. Dance, L. Lozano, J. Darriet, J. Etourneau, R. Tournier, A. Sulpice, P. Lejay, J. L. Diot, and P. Maestro, *Solid State Ionics* **32/33**, 1109 (1989).
- 127 B. Chevalier, A. Tressaud, B. Lepine, K. Amine, J. M. Dance, L. Lozano, E. Hickey, and J. Etourneau, *Physica C* **167**, 97 (1990).
- 128 J. C. Phillips, *Phys. Rev. Lett.* **26**, 543-546 (1971).
- 129 R. Marchand, F. Pors, and Y. Laurent, *Rev. Int. Hautes Tempér. Réfract., Fr.* **23**, 11-15 (1986).
- 130 F. Pors, P. Bacher, R. Marchand, Y. Laurent, and G. Roult, *Rev. Int. Hautes Tempér. Réfract., Fr.* **24**, 239-246 (1987-1988).
- 131 P. Bacher, P. Antione, R. Marchand, P. L'Haridon, Y. Laurent, and G. Roult, *J. Solid State Chem.* **77**, 67-71 (1988).
- 132 P. Antoine, R. Marchand, Y. Laurent, C. Michel, and B. Raveau, *Mater. Res. Bull.* **23**, 953-957 (1988).
- 133 F. Pors, R. Marchand, Y. Laurent, P. Bacher, and G. Roult, *Mater. Res. Bull.* **23**, 1447-1450 (1988).

- 134** P. Antoine, R. Marchand, and Y. Laurent, *Rev. Int. Hautes Tempér. Réfract., Fr.* **24**, 43-46 (1987).
- 135** Y. Laurent, R. Pastuszek, P. L'Haridon, and R. Marchand, *Acta Cryst. B* **38**, 914-916 (1982).
- 136** R. Pastuszek, P. L'Haridon, R. Marchand, and Y. Laurent, *Acta Cryst. B* **38**, 1427-1430 (1982).
- 137** R. C. Brown and N. J. Clark, *J. Inorg. Nucl. Chem.* **36**, 2287-2290 (1974).
- 138** R. C. Brown and N. J. Clark, *J. Inorg. Nucl. Chem.* **36**, 1777-1782 (1974).
- 139** C. Mourgout, B. Chevallier, J. Etourneau, J. Portier, P. Hagenmuller and R. Georges, *Rev. Int. Hautes Tempér. Réfract., Fr.* **14**, 89-96 (1977), and references therein.
- 140** B. Chevallier, J. Etourneau, and P. Hagenmuller, *Mater. Res. Bull.* **12**, 473-479 (1977).
- 141** J. Etourneau, B. Chevallier, P. Hagenmuller, and R. Georges, *J. Phys. Colloq. C* **5**, 193-204 (1980).
- 142** B. Chevallier, J. Etourneau and P. Hagenmuller in *The Rare Earths in Mod. Sci. and Tech.*, Eds. G. J. McCathy, J. J. Rhyne, and H. B. Silber, 1980, pp 403-408.
- 143** F. A. Cotton and G. Wilkinson, "Advanced Inorganic Chemistry," 4th ed, John Wiley & Sons, Inc., 1980, p 847.
- 144** R. Scholder and L. H. Brixner, *Z. Naturforsch.*, **10 b**, 178-180 (1955).
- 145** L. H. Brixner, *J. Inorg. Nucl. Chem.* **14**, 225-230 (1960).
- 146** G. H. Bouchard, Jr., and M. J. Sienko, *Inorg. Chem.* **7**, 441-443 (1968).
- 147** U. Von Essen and W. Klemm, *Z. Anorg. Allg. Chem.* **317**, 25-34 (1962).
- 148** M. G. Barker and I. C. Alexander, *J. Chem. Soc. Dalton Trans.* (20), 2166-2170 (1974).
- 149** N. M. Maister and I. M. Lopato, *Inorg. Mater.* (Eng. Transl.) **9**(1), 57-60 (1973).
- 150** G. L. Olcese, *J. Phys. F.* **9**, 569-78 (1979).
- 151** J. M. Leger, N. Yacoubi, and J. Lories in *The Rare Earths in Mod. Sci. and Tech.*, Eds. G. J. McCathy, J. J. Rhyne, and H. B. Silber, 1980, pp 203-208.
- 152** J. M. Leger, N. Yacoubi, and J. Lories, *J. Solid State Chem.* **36**, 261-270 (1981).

- 153** M. R. Norman, H. J. F. Jansen, D. D. Keolling, and A. J. Freeman, *Solid State Commun.* **52**, 739-741 (1984).
- 154** J. J. Veyssie, D. Brochier, A. Nemoz, and J. Blanc, *Phys. Lett.* **14**, 261-262 (1965).
- 155** P. W. Selwood, "Magnetochemistry," 2nd ed., Interscience Publishers, Inc., New York, N.Y. 1956, p 78.
- 156** W. L. Jolly, "The Synthesis and Characterization of Inorganic Compounds," Prentice-Hall, Inc., Englewood Cliffs, N.J., 1970.
- 157** A. H. Morrish, "The Physical Principles of Magnetism," John Wiley & Sons, Inc., 1965.
- 158** C. M. Hurd, *Contemp. Phys.* **23**, 469-493 (1982).
- 159** A. K. Cheetham, and P. Day, "Solid State Chemistry, Techniques," Clarendon Press, Oxford, 1987, p. 289-290.
- 160** R. W. G. Wyckoff, "Crystal Structures," Vol. 3, 2nd Ed, Interscience, 1965, pp 87-91.
- 161** H. Müller-Buschbaum and H. G. Schnering, *Z. Anorg. Allg. Chem.* **336**, 295-305 (1965).
- 162** *JCPDS Powder Diffraction File No. 3-1102*, International Centre for Diffraction Data, 1601 Park Lane, Swarthmore, PA 19081.
- 163** *JCPDS Powder Diffraction File No. 23-1048*, International Centre for Diffraction Data, 1601 Park Lane, Swarthmore, PA 19081.
- 164** P. C. Donohue, L. Katz, and R. Ward, *Inorg. Chem.* **4**, 306-310 (1965).
- 165** Ch. Lang and Hk. Müller-Buschbaum, *J. Less-Common Metals* **157**, 301-306 (1990).
- 166** N. N. Greenwood, and A. Earnshaw, "Chemistry of the Elements," 1st ed, Pergamon Press, 1984, (reprinted with corrections in 1986), p. 706.
- 167** P. Villars and J. C. Phillips, *Phys. Rev. B* **37**, 2345-2348 (1988).

MICHIGAN STATE UNIV. LIBRARIES



31293009146030